2015

Formation of micro-structural banding in hot-rolled medium-carbon steel

Masoud Said Al Gahtani
University of Wollongong

UNIVERSITY OF WOLLONGONG

Formation of Micro-Structural Banding in Hot-Rolled Medium-Carbon Steel

A thesis submitted to fulfil the requirements
for the award of the degree of

Doctor of Philosophy

from

University of Wollongong

by

Masoud Said Al Gahtani
B.Sc. (Mech. Eng.), M.Sc. (Adv. Met.)

School of Mechanical, Materials and Mechatronics Engineering

August 2015

Thesis Certification

I, Masoud S. Al Gahtani, declare that this thesis, submitted in fulfilment of the requirements for the award of Doctor of Philosophy, in the School of Mechanical, Materials and Mechatronic Engineering, University of Wollongong, is wholly my own work unless otherwise referenced or acknowledged. The document has not been submitted for qualifications at any other academic institution.

Masoud S. Al Gahtani

August 2015

ABSTRACT

Micro-structural banding in steel is defined as a manifestation of alternating bands of different microstructural constituents aligned parallel to the rolling direction. These alternating bands of different microstructure affect the directional homogeneity of the mechanical properties and the formation of such bands should be avoided. Micro-structural banding is a particular problem in medium-carbon steels that are produced by continuous casting techniques.

It is well established that delta-ferrite dendrites grow roughly perpendicular to the casting direction during the initial solidification of steel in a continuous caster. Most of the alloying elements of interest in the production of medium carbon steel segregate to inter-dendritic regions during the solidification of the last liquid. Hence primary and secondary dendrites of low carbon content are interspaced by almost spherical pockets of high solute content and these regions of high solute content are retained during the delta-ferrite to austenite phase transition. It is also well established that these pockets of high solute content as well as the dendrites are elongated during subsequent hot-rolling. Earlier researchers have shown that these micro-chemical bands are a pre-requisite to microstructural band formation, but that it is actually the kinetics of the austenite decomposition that is responsible for the formation of alternating bands of ferrite and pearlite (microstructural banding). Although earlier research has shown that alternating elongated bands of high and low alloy content form during hot-rolling, the exact way in which the cast structure, consisting of delta-ferrite primary and secondary dendritic arms interspaced with almost spherical pockets of high alloy content, are transformed into almost continuous bands of low and high allow content has not been clarified as yet. It is this question that prompted the design of the present study, which aimed to provide an improved quantification of the mechanism by which these elongated micro-chemical bands form.

Because of its industrial significance, a medium-carbon steel with a manganese content of 1.28 *wt.* % and very low in other alloying elements was selected to conduct a series of hot-rolling tests in order to study the response of a typical cast-structure comprising primary and secondary dendrites as well as micro-segregated regions, to hot-rolling. Hot-rolling was conducted in a laboratory-scale rolling mill and the progressive

rotation of the primary and secondary dendrite arms as well as the associated inter-dendritic regions were studied experimentally and an attempt was made to model these respective progressive rotations in order to provide quantitative information. Some specimens were subjected to full rolling to different degrees of reduction in thickness, while others were only partially rolled so that the rotation of the micro-structural components could assessed by conducting cross-sectional metallographic examinations. Optical as well as electron-probe micro-analyses revealed that primary dendrite arms rotated progressively around the transverse axis during hot-rolling while the secondary dendrite arms, with their adjacent areas of inter-dendritic segregation, elongated progressively parallel to the rolling direction. When the reduction exceeds 80% the primary as well as the secondary dendrite arms, with their associated inter-dendritic regions, align parallel to the rolling direction, thereby forming layers of low and high concentration of alloying elements respectively.

The mechanical properties at room temperature of the dendritic and inter-dendritic regions respectively of the as-cast medium-carbon steel under investigation were determined by the use of instrumented indentation techniques (nano-hardness measurement). In addition, hot-tensile tests, at typically hot-rolling temperatures, were conducted on specimens selected from the as-cast slab in such a way that they represent the primary and secondary dendrite arms or the inter-dendritic regions respectively. In this selection of specimens, it was assumed that an area of the slab close to the surface represent dendrite structures, while an area close to the centre-line represent inter-dendritic regions. There was a discernible difference in mechanical properties between the dendritic and inter-dendritic regions in a continuously-cast slab at room temperature as well as at high temperatures.

Two-dimensional symmetric finite element (FE) models were employed to simulate the behaviour of the dendritic and inter-dendritic regions respectively during hot-rolling with a view to determining the microstructural changes leading to micro-chemical banding. In this modelling study the equivalent plastic strain and von-Mises equivalent stress distributions were determined as a function of rolling reduction. During hot rolling, the secondary arms experienced larger elongations than the segregated regions within strain bands due to the lower yield point of the dendrite arms. The primary dendrite arms rotated about the rolling direction and align with the

rolling direction at rolling reductions of more than 70% while secondary dendrite arms located between two (harder) segregated regions experience significant thinning during rolling until the segregated regions latch onto each other at a rolling reduction of about 70%. At rolling reductions between 65 and 75%, the primary and secondary dendrite arms as well as the inter-dendritic regions (roughly spherical) pre-existing in the as-cast structure, were destroyed and transformed into distinctive elongated micro-chemical bands that align parallel to the rolling direction.

In order to further explore how banding originates, an attempt was made to directly observe the formation of micro-structural bands by the use of high-temperature laser-scanning confocal microscopy. These observations have been made in real time and at temperatures typically used in industrial hot-rolling practice. During cooling from the austenite phase field, ferrite nucleates on austenite grain boundaries and grows progressively into the austenite grains. Pearlite/ferrite band formation could clearly be observed *in-situ* when care was taken to prevent surface decarburisation. The banding observed *in-situ* in the high-temperature microscope was similar to that detected by optical microscopy following the same heat treatment that was used in the microscope.

This study provided new insights with respect to the origins and alignment of bands of different chemical composition, which eventually results in the formation of microstructural banding.

ACKNOWLEDGEMENTS

I would like to thank the people who supported me throughout the preparation of this thesis possible. First and foremost, I would like to express my deepest sense of gratitude to my supervisor Professor Rian Dippenaar for his continuous encouragement, guidance, understanding, patience, important suggestions and valuable comments throughout my Ph.D.

My sincere thanks go to Dr. Mark Reid for his unlimited support and valuable advice, ideas and suggestions during my study.

I am also grateful for the help provided to me by Dr. Cheng Lu and Dr. Yu Hai-liang (Finite Element Modelling), Mr. Greg Tillman (Metallography), Mr. Joe Abbott (Rolling Laboratory), workshop staff in the University of Wollongong.

I wish to deeply thank Dr. Karen Privat, University of New South Wales, for her assistance with the Electro-Probe Micro Analysis and valuable discussion.

My thanks also go to my fellow students, especially Stefan Griesser and Salar Niknafs for their great assistance in laser-scanning confocal microscopy experiments.

I would like to express my gratitude to my employer and sponsor, Saudi Basic Industries Corporation (SABIC), for sponsoring my graduate studies.

Finally, I would like to convey my deepest regards and appreciation to my parents, Saeed and Muharah, for their unconditional love and support, to my wife Nuha for her patience, love and support, to my lovely children, Shaden, Abdullah and Abdulrahman, and to my brothers and sisters. I dedicate this thesis to them.

TABLE OF CONTENTS

LIST OF FIGURES

LIST OF TABLES

Chapter 1. Introduction

1.1 Overview

Micro-structural banding, often simply referred to as banding, in steel is defined as a manifestation of alternating bands of different microstructures aligned parallel to the rolling direction [1-14]. These alternating bands of different microstructure affect the directional homogeneity of mechanical properties and the formation of such bands should be avoided [7, 15]. Banding is a particular problem in medium carbon steels that are produced by continuous casting techniques.

Continuous casting of steel has been developed into a sophisticated technology over the past 60 years. The conventional casting of steel slabs, typically 200-300mm-thick, are cast at a rate of about one meter per minute. One specific development that has transformed the continuous casting industry was the introduction of thin-slab continuous casting, which typically produces slabs 60-100 mm thick at casting speeds of more than 4 m/min. One of the latest developments in continuous casting technology, the innovative high-speed strip-casting technology, integrates casting and rolling and renders possible the casting of the liquid steel directly into thin sheet [16]. For the sake of comparison a brief outline of several different continuous casting technologies is shown in Figure 1.1.

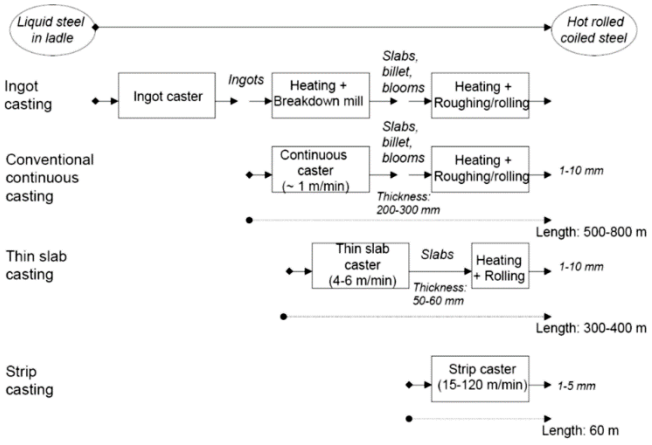

Figure 1.1: A comparison of the casting and rolling stages of different continuous casting techniques [16].

During the conventional and thin-slab continuous casting processes, liquid steel partially solidifies in a water-cooled copper mould. On exiting the mould, the surface of the strand is rapidly cooled with water sprays and the thickness of the shell increases progressively as the material solidifies. A steep temperature gradient is established in

the through-thickness of the strand and it is this temperature gradient that is primarily responsible for the formation of different microstructural morphologies in the through-thickness. The typical microstructural development upon solidification of steel slabs occurs in sequence in three steps: a fine-grained chill zone forms at the mould walls due to the very high cooling rate in this zone. These crystals grow into the liquid, initially with random orientations. As the growth proceeds, the initial planar solid/liquid interface becomes unstable and due to constitutional super cooling dendrites grow ahead of the advancing solid/liquid interface to eventually form a columnar structure, the second zone, progressing towards the centre in preferred crystallographic directions. This dendritic growth leads to the segregation of alloying elements across the slab thickness. The concentration of these solute elements increases ahead of the growing columnar dendrites. The alloying elements having partition coefficients less than unity (e.g. manganese) are rejected from the first formed delta ferrite dendrites, resulting in inter-dendritic regions of high solute content. The segregation between dendrites is shown schematically in Figure 1.2 (b). This solidification sequence and morphological development is well understood and credible theories have been developed for the relationship between the morphology of growing crystals, the temperature gradient, cooling rate, the extent of segregation of solute elements and the rate of solidification [17]. As the dendrites approach the centre-line of a slab, the thermal gradient is diminished and the dendritic growth rate is retarded. Due to the convective movement of liquid steel perpendicular to the dendrite growth direction, tips of the growing dendrites are fractured and float in the liquid metal ahead of the solid/liquid interface. These floating crystals act as nuclei for further solidification and as a result, an equiaxed structure is formed (the third zone). These three zones are shown schematically in Figure 1.2(a). Dendrites, consisting of primary and secondary arms are illustrated in more detail in Figure 2(b).

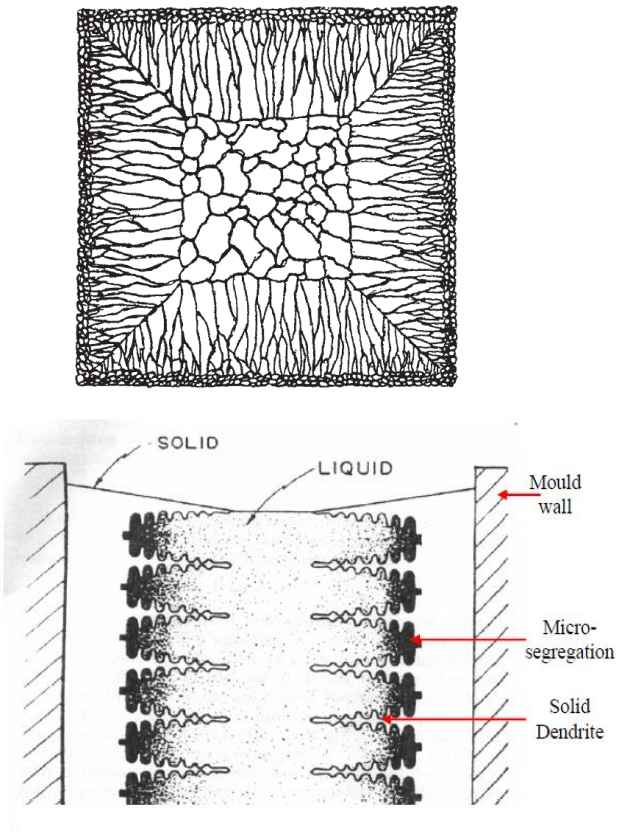

Figure 1.2: (a) Schematic diagram of zones of crystal morphologies in an as solidified section of steel [2] (b) Sketch of Solidification in mould showing liquid, solid and dendrites.[18]

Subsequent hot rolling in the austenitic phase field leads to the formation of layers of high and low solute content respectively. This variation in alloying element concentration may cause an inhomogeneous distribution of carbon in the austenite during subsequent heat treatment. Certain elements (e.g. manganese) effectively attract carbon, while other elements reject carbon (e.g. silicon). Due to its relatively high diffusivity, carbon in the austenite can be assumed to be distributed according to thermodynamic equilibrium. On the other hand, the variations in the concentration of other solutes such as silicon and manganese will not be eliminated due to the low diffusivity of these elements and hence, the local A_3 transition temperature, at which the austenite reverts to ferrite in the local regions, will depend on the extent of manganese segregation. Silicon will increase the local A_3 transition temperature while this temperature will be decreased by manganese [19, 20]. It is this inhomogeneous distribution of alloying elements that leads to the formation of alternating bands of ferrite and pearlite in medium carbon steel during hot-rolling and subsequent heat treatment following casting of the strand. The ferrite-pearlite bands are intimately

related to the occurrence of micro-segregation of alloying elements to the extent that Offerman *et al.* argued that the formation of micro-chemical bands is a prerequisite for micro-structural band formation. However, these authors have provided convincing experimental proof that the kinetics of the austenite-to-ferrite phase transformation determines the actual occurrence of these microstructural bands [20].

Much research has been undertaken to investigate the kinetics of formation of ferrite-pearlite micro-structural banding in hot-rolled medium carbon steel [2, 4, 9, 20-26], but fewer research efforts have been devoted to a study of the mechanisms by which micro-chemical banding forms in the first instance. The mechanism by which carbon and solute depleted dendrites and solute enriched inter-dendritic regions develop into microstructural bands parallel to the rolling direction has not been studied in detail and is poorly understood [19, 27]. This dearth of information prompted the present study and an attempt was made to establish exactly how dendrites and solute-rich regions, originally perpendicular to the rolling direction, are transformed into microstructural bands parallel to the rolling direction.

1.2 Thesis Objectives

The arguments advanced above indicated that there is a need to better understand the mechanism or mechanisms that leads to the formation of micro-structural bands parallel to the rolling direction from microstructural features that were originally orientated perpendicular to the rolling direction.

The approach taken in the present research was to examine in detail samples of medium carbon steel that were cast in an operating thin-slab caster under normal industrial operating conditions. The microstructure at various positions in the through-thickness of the slab was determined and in addition, some of these samples were further subjected to laboratory heat treatments and rolling studies. In an attempt to better interpret the outcomes of the experimental observations, a finite element model was developed and implemented to study the rotation of dendrites and inter-dendritic regions in the course of hot-rolling.

The specific objectives for this study were as follows:

- To study the response of dendritic structures in medium-carbon steel to hot-rolling and specifically to determine how dendrites, originally orientated perpendicular to the rolling direction, are transformed by hot-rolling into bands parallel to the rolling direction.

- To investigate the mechanism or mechanisms by which hot-rolling transforms discontinuous inter-dendritic segregated regions, originally perpendicular to the rolling direction, into continuous segregated bands parallel to the rolling direction.
- To study the variation in high-temperature mechanical properties of dendritic and inter-dendritic regions of a continuously cast medium-carbon steel and the behaviour of these different regions during hot-rolling.
- To predict the response of dendritic and inter-dendritic regions to isothermal hot-rolling and specifically to predict the pertaining stress and strain distributions by using Finite Element Modelling techniques.
- To observe *in-situ* the formation of microstructural banding during heat treatment of hot-rolled medium-carbon steel by using advanced high-temperature laser-scanning confocal microscopy.
- To study by using Electron Probe Micro Analyses (EPMA), the change in alloying element distributions in the course hot-rolling.

The high-temperature mechanical properties of selected specimens were determined by the use of a thermo-mechanical simulator (Gleeble 3500). Finite element (FE) models to simulate the behaviour of dendritic and inter-dendritic regions during hot rolling of the medium-carbon steel were developed using ANSYS LS-DYNA software. *In-situ* heat treatments and observations of the actual formation of microstructural banding during heat treatment were accomplished by using a 1LM21H laser-scanning confocal microscope, supplied by Lasertec Corporation, Japan.

1.3 Thesis Organisation

The remainder of the thesis is structured as follows:

Chapter 2: Review the available literature, starting with a definition and outline of the formation of micro-segregation during solidification of steel. Following the discussion of micro-segregation a detailed discussion of the literature pertaining to banding is given. The theories of microstructural band formation are then examined and subsequently a number of factors effecting the formation of microstructural bands are discussed. These include, steel composition, cooling rate during the austenite to ferrite transformation and the austenite grain size prior to transformation. Moreover, the effects of microstructural banding on the

mechanical properties of hot-rolled steels are discussed. The variation of micro-mechanical properties of inhomogeneous steel microstructures at room temperature and the nano-indentation techniques are discussed. The high temperatures mechanical properties and behaviour of various bulk steels are outlined. The chapter also discusses theories of plasticity and available hot and cold rolling Finite Element Models.

Chapter 3: Presents the behaviour of dendritic structures during hot-rolling of medium-carbon steel. It also investigates the variation of chemical composition between dendritic and inter-dendritic regions which were obtained from EPMA line-scan measurement and map observations.

Chapter 4: Includes an investigation of the variation of mechanical properties of dendritic and inter-dendritic regions at high temperature. The mechanical properties include elastic modulus, tensile strength and ductility. It also provides empirical equations for these properties of each region separately at high temperatures.

Chapter 5: Simulates the behaviour of dendritic and inter-dendritic regions during hot-rolling of medium-carbon steel. It uses (FE) models to provide effective stress and strain distributions through inhomogeneous dendritic structures. This analysis is based on the high-temperature mechanical properties obtained from the experimental investigation discussed in Chapter 4.

Chapter 6: Deals with the *in-situ* heat treatment of hot-rolled medium-carbon steel using the advanced techniques of laser-scanning confocal microscopy. It also provides details of the high-temperature laser-scanning confocal microscopical techniques employed. In addition, it includes observations of ferrite-pearlite banding during heat treatment of a hot-rolled sample.

Chapter 7: Summarises the main results as well as suggests the areas for future research.

Chapter 2. Literature Review

2.1 Introduction

Microstructural banding is a common occurrence in hot-rolled steels which can be defined as alternation of layers of ferrite and pearlite [1-14]. The banding has been studied extensively due to its detrimental impact on mechanical properties [1, 3, 7, 10, 28-31]. Microstructural banding is strongly related to the micro-segregation of alloying elements during solidification, and the subsequent deformation of the segregated structure during hot-rolling. In addition, the formation of banded structures is influenced by two other main factors; the cooling rate during the austenite to ferrite transformation and the austenite grain size [2, 4, 9, 19, 22, 24, 27, 32].

Due to its fundamental importance to the process of band formation, this review begins with a detailed discussion on the formation of chemical in-homogeneities during the dendritic solidification in the course of the continuous casting of steel (micro-segregation on the scale of the dendrites, as opposed to macro-segregation which is on the scale of the half thickness of the casting, a phenomenon that is beyond the scope of the present study).

Modelling of micro-segregation is discussed followed by a brief discussion of dendrite arm spacing (DAS), a factor intimately related to the development of micro-segregation. The final part of the discussion of micro-segregation is concerned with some aspects of the transformation of austenite to ferrite on cooling is briefly discussed as again it is intimately linked to the formation of microstructural bands.

Following the discussion of micro-segregation, a more detailed discussion is provided of the literature pertaining to banding. The theories of microstructural band formation are then examined and subsequently a number of factors effecting the formation of microstructural bands are discussed. These include steel composition, cooling rate during the austenite to ferrite transformation and the austenite grain size prior to transformation. In addition, the effects of microstructural banding on the mechanical properties of hot-rolled steels are discussed.

The variation of micro-mechanical properties of inhomogeneous steel microstructures at room temperature and the nano-indentation techniques used to assess these are discussed. Finally, the simulation by Finite Element Modelling of hot-rolling processes and the associated plasticity theories and models are discussed in detail.

2.2 Solidification in Continuous Casting of Steel

During continuous casting of steel, the surface of the cast strand is cooled rapidly and the thickness of the shell increases progressively as the material solidifies. A steep temperature gradient is established along the thickness of the strand, which causes the formation of a fine, equiaxed microstructure on the surface and oriented columnar dendritic towards the centre. This dendritic growth leads to the segregation of alloying elements in the through-thickness of the slab.

The solubility of solute elements is usually lower in the solid state than in molten steel. These solute elements are discharged into the molten steel at the growing front of the columnar dendrites of the solidifying shell, which grows as solidification proceeds. The alloying elements having partition coefficients less than unity (e.g. manganese) are rejected from the first formed delta ferrite dendrites, resulting in inter-dendritic regions of high solute content, which is retained during the transformation from δ-ferrite to austenite. Subsequent hot-rolling in the austenitic phase field leads to elongated high solute regions. The variation in alloying element concentrations may cause an inhomogeneous distribution of the carbon in the austenite. Certain elements (e.g. manganese) effectively attract carbon, while other elements reject carbon (e.g. silicon). Due to its relatively high diffusivity, the carbon in the austenite can be distributed according to thermodynamic equilibrium. Calculations of Verhoeven [19] and Offerman [20] have shown that variations in manganese concentration result in variations in carbon concentration, which can significantly alter the local A_3 transition temperature. The variation in alloying element concentration by itself also raises (e.g. silicon) or lowers (e.g. manganese) the A_3 transition temperature. These solute elements concentrate, to form what is called micro-segregation. The segregation between dendrites is shown schematically in the right hand side of Figure 2.1. This micro-segregation occurs during the final stages of solidification between the branches of columnar dendrites and also at the centre-thickness of the cast strand. Solidification theories have been established for the relationship between the morphology of growing crystals and the temperature gradient and cooling rate, the segregation of solute elements near the front of solidifying shell and the rate of solidification which affects this segregation [17].

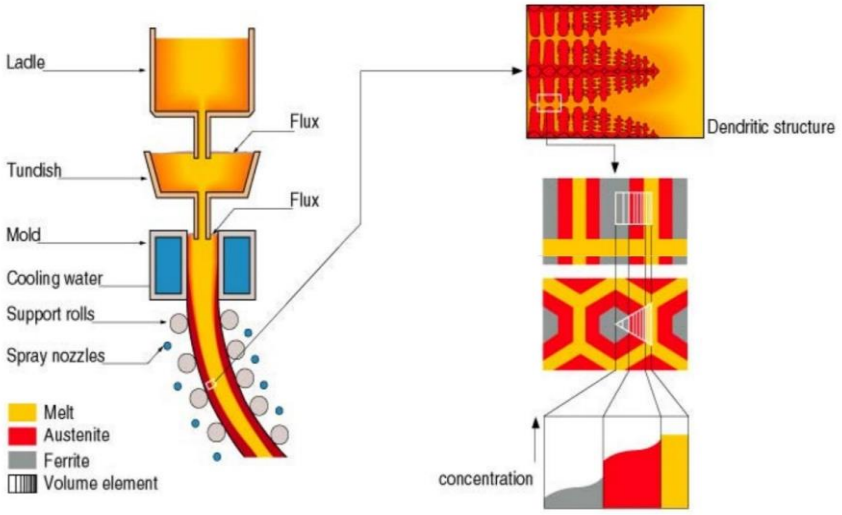

Figure 2.1: Simulation of solidification and segregation in continuous casting [17].

2.3 Micro-segregation

Since micro-segregation has the most significant impact on band formation, experiments and models have been developed for determining the extent of micro-segregation of alloying elements across the slab as influenced by the steel composition and operating parameters.

2.3.1 Micro-segregation during Dendritic Solidification

A necessary condition for the formation crystals in a liquid metal melt, is that the liquid temperature is lower than the melting point T_m or liquidus line T_L of the solid. Initially solidification occurs by the formation of small nuclei (nucleation) on the mould wall and develops a layer separating the mould and liquid metal. Further growth of the solid occurs through the progression of the solid/liquid interface into the liquid metal as heat is extracted through the solid. Initially the shape of the solid/liquid interface is planar or parabolic. Given in Figure 2.2 is the low-carbon high-temperature section of the iron-carbon phase diagram. Reference to this diagram illustrates an extremely important effect in the solidification of alloys: solute rejection during solidification. Following the path of the solidification of a Fe 0.2% C alloy, the initial solid that forms has a composition of ~0.05% C with the resultant rejection of carbon in to the remaining liquid at the interface. Under the right conditions this leads to constitutional undercooling of the liquid at the interface. This is the situation where the rejected solute at the interface reduces the solidus temperature of the liquid at the interface to below the temperature of the solid/liquid interface hence, preventing planar growth

from continuing. The solid/liquid interface then becomes unstable and lead to the formation of protrusions that grow from the interface into the liquid (past the constitutionally undercooled liquid). A similar mechanism occurs on the sides of the protrusions resulting in secondary branches that grow perpendicular to the primary cells to form dendrites as shown in Figure 2.3.

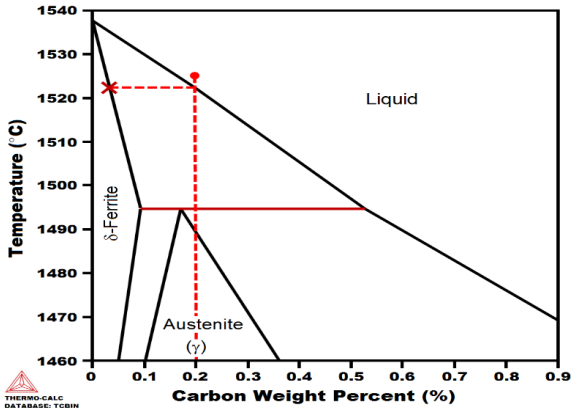

Figure 2.2: Low carbon, high temperature section of the iron-carbon phase diagram.

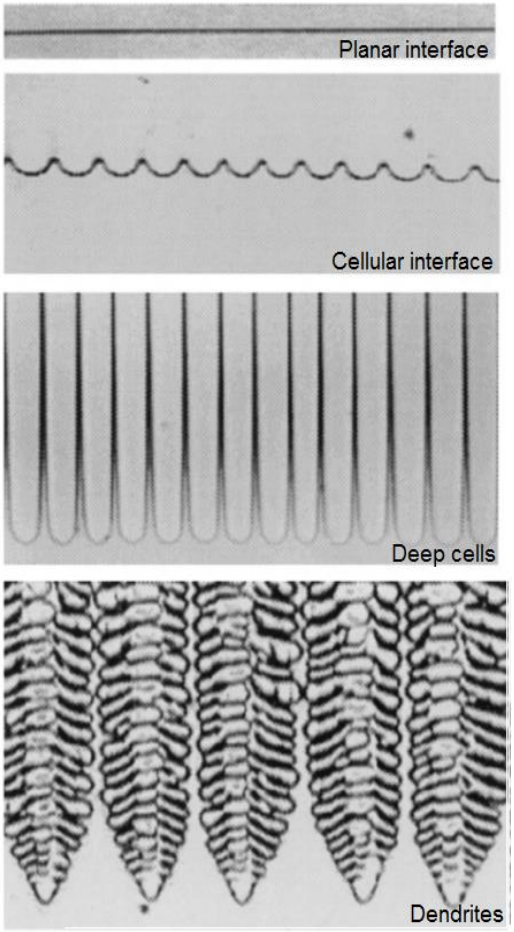

Figure 2.3: Steady-state patterns formed at the solid/liquid interface of a binary alloy of succinonitrile and coumarin 152 during directional solidification [33].

The result of this type of growth is the entrapment of solute rich liquid between the primary and secondary (and in some cases ternary) arms of the dendrites. The rejection of solute elements occurs for all elements mixed with iron to form steel (all have a lower solubility in solid iron than in liquid iron). The formation of pockets of solute rich liquid between dendrites is called micro-segregation. The dendrite growth direction is orientated in certain specific crystallographic directions and depends on the crystal structure of the solidifying metal as listed in Table 2.1. For example, dendrites in steel always prefer to grow in the direction <100>. This growth direction also corresponds to the direction of highest thermal conductivity, for obvious reasons [34-37].

Table 2.1: Dendritic Growth in Various Crystal Structures [38].

Crystal Structure	**Dendritic Growth Direction**
Face-centred cubic	<100>
Body-centred cubic	<100>
Hexagonal close-packed	$<10\bar{1}0>$
Body-centred tetragonal	<110>

2.3.2 Modelling of Micro-segregation

Due to the significant influence of micro-segregation on the properties of steel, including the formation of banding, considerable effort has been expended in attempts to understand and predict the occurrence of segregation during casting. The earliest approximation to this problem was to completely neglect solid state diffusion, which was done by Scheil [39] where the problem was reduced to one dimension by considering only a volume element perpendicular to the growth direction of the dendrite as shown in Figure 2.4. The shape of the dendrite was simplified and assumed to be plate-like. Further assumptions in the Scheil model included infinitely fast diffusion in the liquid state, no undercooling, no difference in density between solid and liquid, and linear solidus and liquidus lines. This last assumption implies a constant equilibrium partition coefficient *k*, given by the ratio of the equilibrium solidus concentration to the equilibrium liquidus concentration as:

$$k = \frac{C_s}{C_L} \qquad 2.1$$

The Scheil equation described the concentration in the solid at the solid/liquid interface C_S^* for a given fraction solid f_S and partition coefficient.

$$C_s^* = kC_0(1 - f_s)^{k-1} \qquad 2.2$$

C_0 here is the average concentration of the alloy. The dependence of C_S on the fraction of solid is shown for several models in Figure 2.5. Although Scheil's model does not provide an accurate estimate of the degree of micro-segregation, it gives, in conjunction with the lever rule the lower and upper limit of possible segregation profiles.

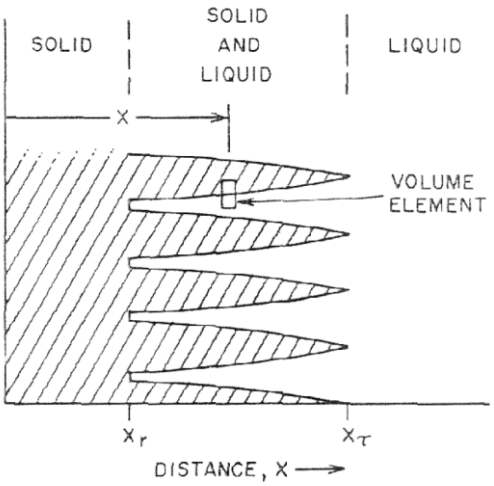

Figure 2.4: Schematic representation of growing dendrites with the volume element that is considered in the model [40].

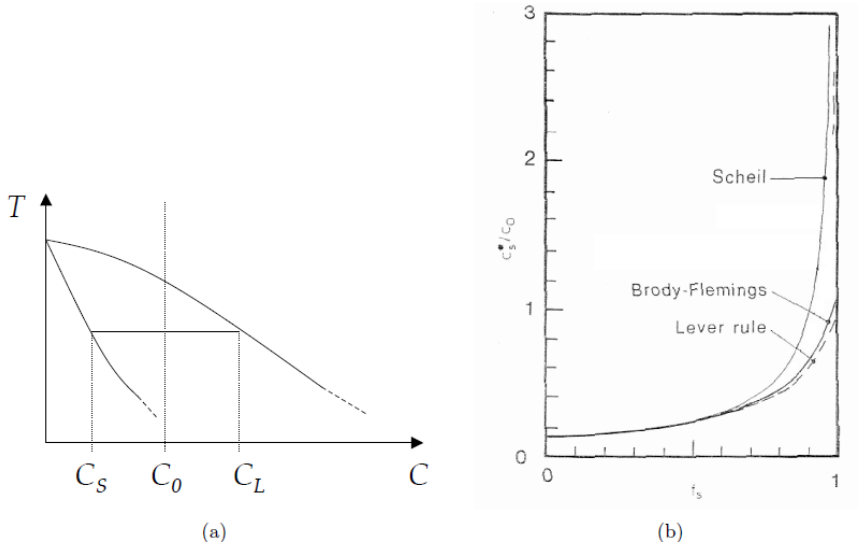

Figure 2.5: an example partial phase diagram showing the solidus and liquidus concentrations C_S and C_L for a given average concentration C_0. (b) The dependence of the concentration of the solid at the solid-liquid interface on the fraction solid f_s, for different segregation models [41].

Brody and Flemings [40] developed a model that included solid-state diffusion. The same geometry and approximations were used as in the Scheil model, except for diffusion in the solid. Diffusion was described by Fick's second law and two different interface velocity dependencies were assumed: constant velocity and parabolic growth. It was assumed that solid state diffusion does not change the concentration gradient at the interface, so the interface concentration as a function of the fraction solid can be calculated. The ratio of the diffusion coefficient in the solid state, ω, was defined as:

$$\omega = \frac{D_s t_f}{L^2} \qquad 2.3$$

where D_S is the diffusion coefficient, t_f is the local solidification time and L is the half of the dendrite spacing. The interface concentration for a constant solidification velocity is given by

$$C_s^* = kC_0\left(1 - \frac{f_s}{1+\omega k}\right)^{k-1} \qquad 2.4$$

The extent of micro-segregation depends on the ratio of t_f to L_2. It is apparent that the cooling rate influences the dendrite spacing, but this model was not able to describe this behaviour. Even though the Body-Flemings model was a major improvement on the Scheil model, it still was very limited. Therefore, other models [42-45] were proposed in attempt to resolve the limitations of Schiel and Brody and Flemings models including the assumption of the dendrite geometry: cylinders, hexagons and other 2-D geometries, peritectic solidification with two moving phase boundaries, finite diffusion or convection in the liquid state, differences in density between solid and liquid, undercooling at the dendrite tip, variable partition coefficient, various cooling conditions such as constant heat flow or input of an experimental cooling curve, and many other assumptions. Over the last 20-30 years, with the rapid increase in computing power, a new generation of physical models, relying on numerical solutions, have been developed to solve the underlying heat and mass transfer equations required to describe physical phenomena such as solidification and solid state phase transformations.

2.3.3 Dendrite Arm Spacing

During metal solidification, a consequence of constitutional undercooling and destabilisation of solid-liquid interface is the formation of dendrites. The distance between dendrite arms that evolve during solidification is a major factor in the calculation of the degree of micro-segregation and also the segregation profile that leads to banding. There is still a lack of information in the literature regarding the link between the degree of microstructural banding in steel and the primary and secondary dendrite arm spacing. It is clear that the dendritic arm spacing increase from the surface towards the centre of a casting while most studies have assumed one degree of banding across the slab. Verhoeven [19] argued that there is a relationship between the band-width and primary dendrite arm spacing (PDAS), which is defined as the distance between two adjacent dendrites. On the other hand, Krauss [8] argued that the secondary dendrite arm spacing (SDAS), which is defined as the distance between two adjacent secondary arms of a dendrite, as the most important measure of the degree of inter-dendritic segregation. Primary and secondary dendrite arm spacing are dependent, to different extents, on cooling rate [46]. It was experimentally shown that there is an exponential relationship between secondary dendrite arm spacing and local solidification time. This relation was described by the empirical equation:

$$\lambda_2 = K t_f^h \qquad 2.5$$

Where λ_2 is secondary dendrite arm spacing, t_f is the local solidification time and K is an empirical parameter with the exponent h ranging from 0.3 to 0.6 [2, 47].

It was found experimentally by Kattamis *et al.* [48] that the final dendrite spacing is mainly dependent on the coarsening kinetics and not on the initial spacing. Pierer and Bernhard [49] have experimentally investigated the effect of carbon on the secondary dendrite arm spacing. Solidification experiments were performed using a Submerged Split Chill Tensile test with a series of carbon steels containing 0.08, 0.12, 0.16, 0.30, 0.50, and 0.70 wt.% carbon with other alloying elements of 0.28 wt.% Si, 1.32 wt.% Mn, 0.007 wt.% P, and 0.007 wt.% S. From a very large number of λ_2-values measured for the steels under consideration, they were able to derive the secondary dendrite arm spacing for steels containing carbon between 0.08 and 0.7 wt.% by the empirical λ_2-relation:

$$\lambda_2 = (23.7 - (13.1 \times (wt.\%C)^{\frac{1}{3}})t_f^{\frac{1}{3}} \quad 2.6$$

λ_2 is expressed in μm.

Figure 2.6 shows the experimental values of λ_2 as a function of local solidification time for different carbon content steels.

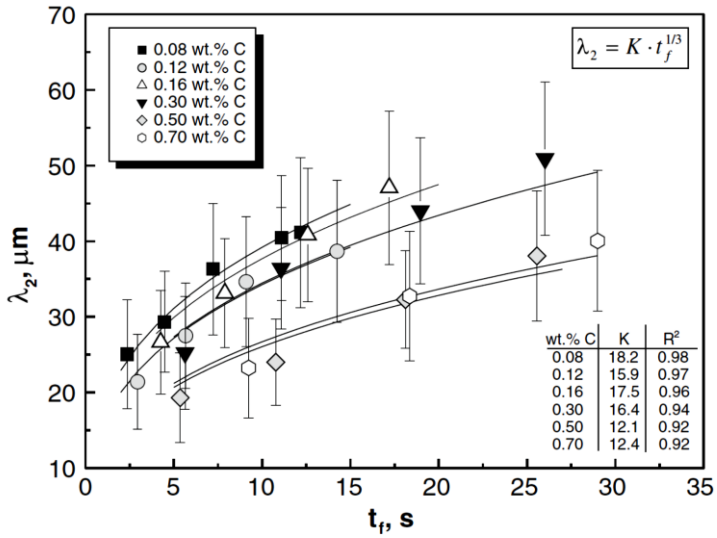

Figure 2.6: Secondary dendrite arm spacing as a function of local solidification time for steel of different carbon content [49].

Preßlinger [50] measured and calculated manganese segregation as a function of distance from the strand surface for conventionally-cast high-strength structural steels. Model calculations agreed well with the experimental findings and they found that the secondary dendrite arm spacing increases with distance from the surface as shown in Figure 2.7.

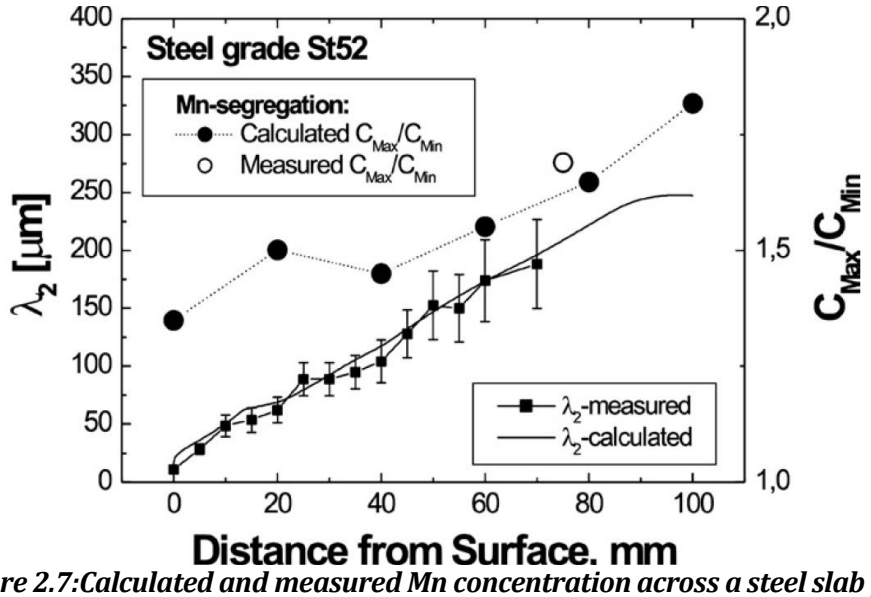

Figure 2.7:Calculated and measured Mn concentration across a steel slab [50].

Micro-segregation of alloying elements in the cast slab has been identified by many earlier researchers as an important factor on the formation of microstructure of consisting of alternating bands of ferrite and pearlite in medium carbon steel (or sometimes martensite in other steels) during subsequent hot-rolling. These ferrite pearlite bands are strongly related to the micro-segregation of alloying elements as Grossterlinden *et al.* [23] and Thompson and Howell [9] have shown by the use of electron probe microanalysis (EPMA). Offerman *et al.* [20] also reported that ferrite/pearlite bands show that microstructural banding in hot rolled medium carbon steel is related to the micro-chemical banding of manganese and silicon. Their experiments showed that the degree of banding decreases as the isothermal transformation temperature decreases, since the relative difference between the ferrite nucleation rates in regions with a low and a high A_3, transition temperature decreases. It was shown that the formation of micro-chemical bands is a prerequisite to band formation, but that the kinetics of the phase transformation determines the actual existence of microstructural bands.

2.4 Microstructural banding in Steels

Microstructural banding, more commonly simply referred to as banding, is a common phenomenon in hot-rolled alloy steels. Research on banding has been conducted since the beginning of the last century [1-14, 51-53] and is still ongoing, which led Verhoeven [19] to describe this phenomena as an "ubiquitous microstructure". Microstructural banding has been defined as the manifestation of alternating bands of

different microstructures parallel to the rolling direction of hot-rolled steel [1-14, 20]. These bands are mainly ferrite and pearlite, but could in some cases be ferrite and martensite, ferrite and bainite, two kinds of bainite, high-cementite as well as low-cementite and other combinations [2, 3, 7, 19]. An example of a banded microstructure of 1020 steel and a 3-D optical micrograph of a banded microstructure is shown in Figure 2.8 (a) and (b) respectively.

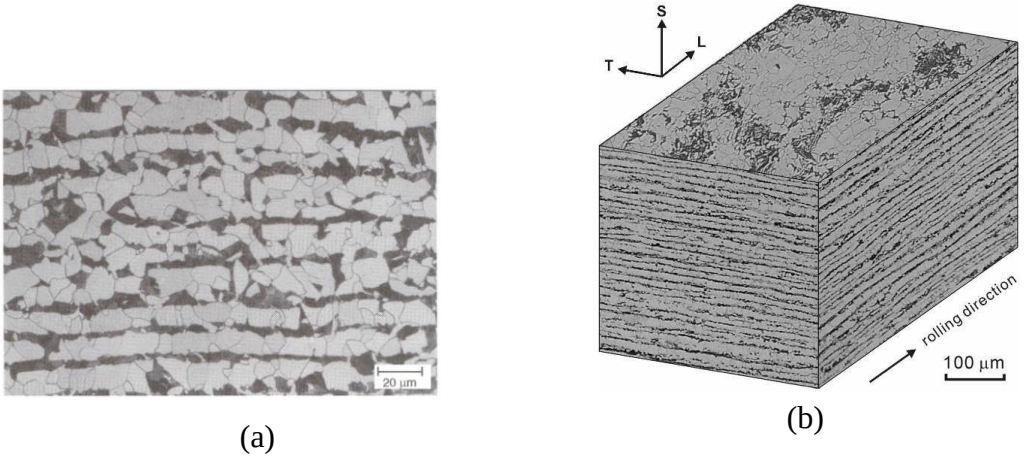

(a) (b)

Figure 2.8: (a) Ferrite and Pearlite bands in 1020 steel hot-rolled plate. [3] (b) 3-D Banded ferrite-pearlite microstructure shown by optical micrography [54].

2.4.1 Effect of deformation on Inter-dendritic Segregation

As has been previously explained, during the solidification of steel, regions of high solute content are retained after the completion of solidification. The subsequent hot-rolling of the steel in the austenite phase field results in the formation of bands of alternating high and low solute content parallel to the rolling direction. The mechanism by which this occurs is poorly understood and little studied [19, 27]. The effect of this distribution of solutes and the subsequent transformation to ferrite has been studied in detail by a number of researchers and their results are summarised as follows.

Due to the importance of ferrite nucleation in determining the formation of banding, Offerman *et al.* [20] identified the influence of the micro-segregation of certain alloying elements in hot-rolled medium carbon steel on austenite decomposition. The principal aim of their study was to identify aspects of the austenite to ferrite/pearlite transformation that leads to microstructural banding. They measured the ferrite fraction formed as a function of time during isothermal annealing using a neutron depolarization (ND) technique in addition to using EPMA to quantify the segregation of solute elements. Two main criteria, that were earlier identified and employed by

Rivera-Díaz-del-Castillo *et al.* [25] to quantify the formation of bands, were used in their experiments to guarantee that banding occurs. The first was that the rate of nucleation of ferrite in the region with a high A3 temperature must be more than 6-8% higher than the rate in the regions with low A3 temperature. The other criterion was that the annealing temperature and time above the A_1 transition temperature must be enough to allow carbon to diffuse over one half of the segregation wavelength during the heat treatment process. These criteria were successfully implemented by Offermann *et al.* [20] who found that the presence of chemical bands and the isothermal transformation temperature were critical in determining the formation of ferrite/pearlite banding. Ferrite/pearlite bands that formed at a relatively low fluctuation of only 8K in A_3 temperature between the bands are shown in Figure 2.9. By contrast Grossterlinden *et al.* [23] found in a similar study that a difference of 50K was required to induce banding when the steel was cooled continuously. Offerman *et al.* [20] predicted that a critical cooling rate is required to induce band formation as shown in Figure 2.10.

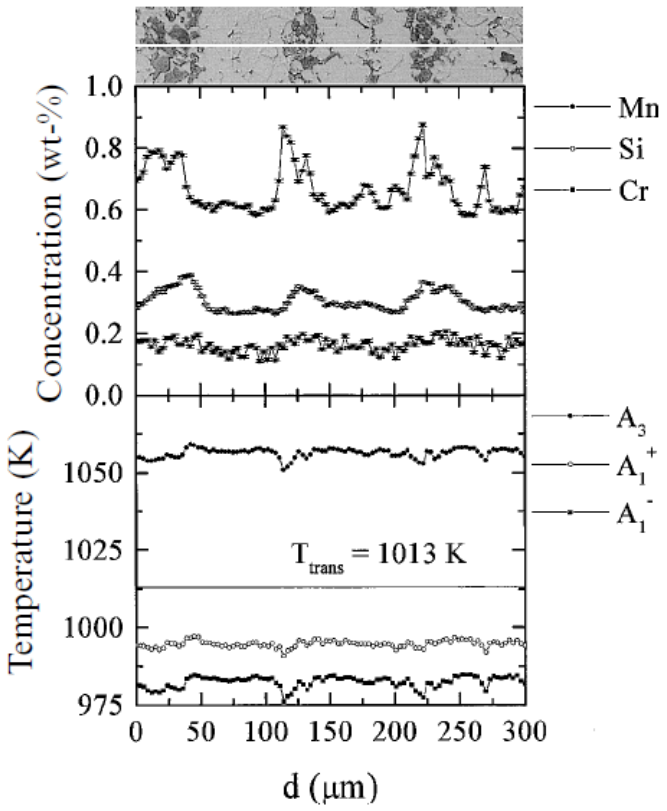

Figure 2.9: Concentration profiles of Mn, Si and Cr measured by EPMA corresponding banded microstructure and calculated local calculated A3 temperature [20].

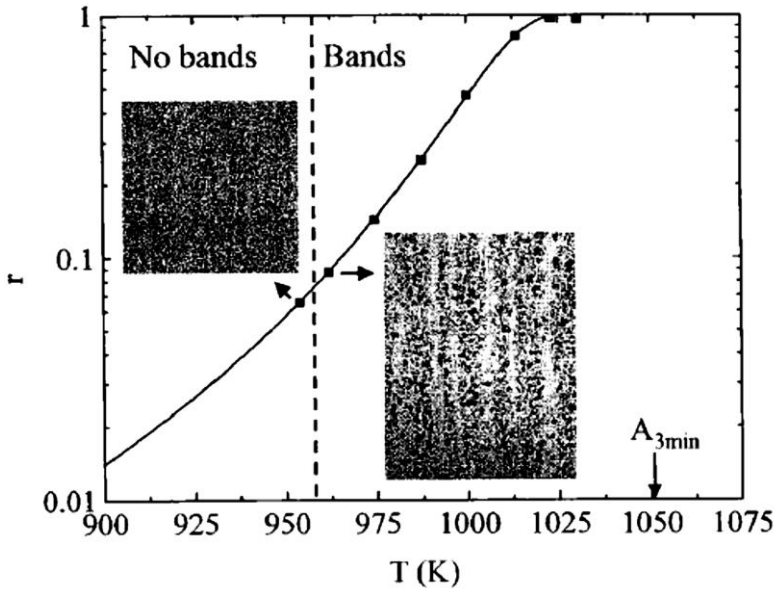

Figure 2.10: Difference in nucleation of ferrite rat r as function of isothermal transformation temperature and critical undercooling for band formation [20]

Preßlinger *et al.* [55] studied the development of micro-segregation in cast and rolled structures of slabs, hot-rolled strip and cold-rolled strip of two different steels (DP and S355) of by using EPMA concentration mapping of alloying elements. They found that the orientation of primary dendrites aligned parallel to the direction of heat flow in the cast structure. During subsequent hot-rolling the distributions of silicon, manganese, phosphorus, and chromium evolved with increasing deformation from the initial dendrites to a banded structure at 70% reduction, as shown in Figure 2.12. The alloying elements segregation did not change during rolling as illustrated in Figure 2.13.

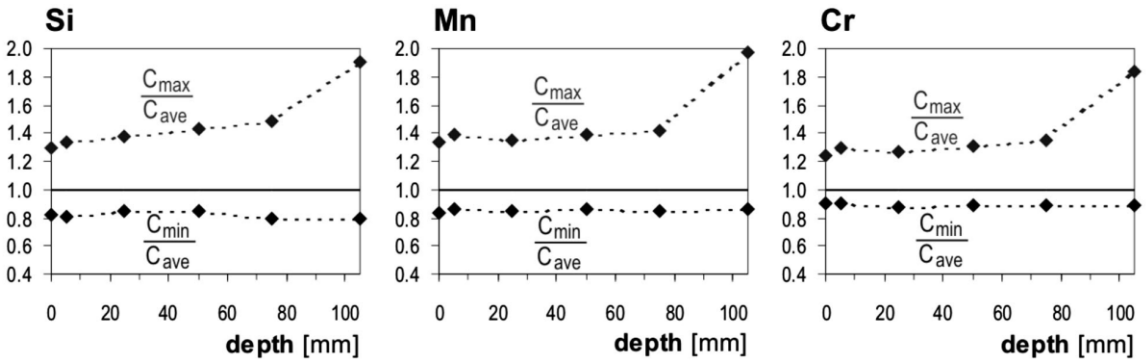

Figure 2.11: Segregation intensities as function of depth from slab surface [55]

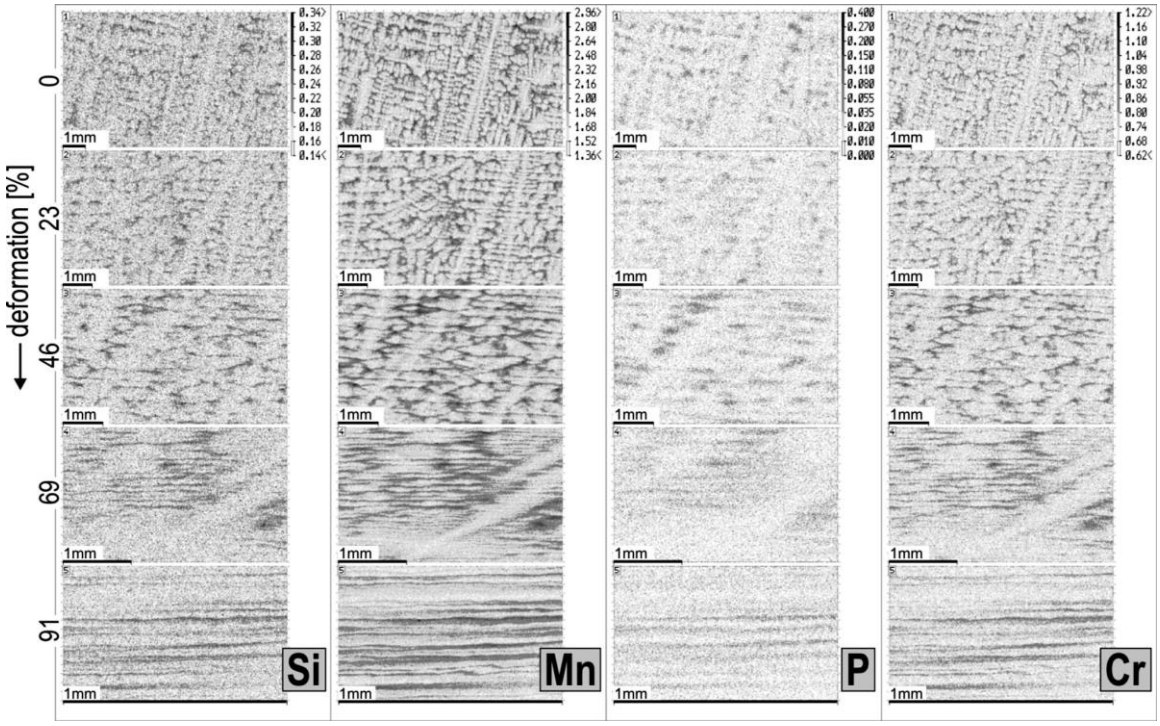

Figure 2.12: Change of Alloying element segregation structures with increasing deformation in hot rolling [55] .

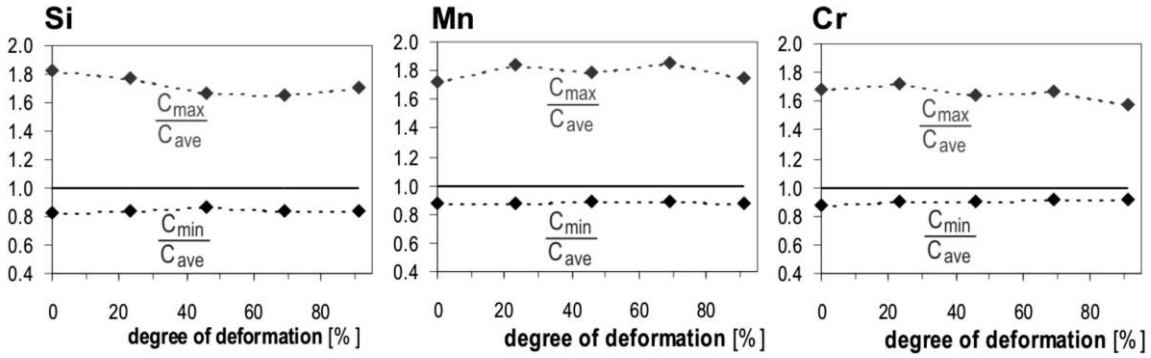

Figure 2.13: Segregation intensities as function of the degree of deformation [55].

2.4.2 Mechanisms of Microstructural Band Formation

The mechanism through which microstructural bands are formed in hot-rolled steels has been extensively studied and two broad theories have been proposed (as opposed to the mechanism by which micro-chemical bands form, which has received far less attention). In 1956 Jatczak *et al.* proposed two mechanisms through which microstructural banding may occur, these are, "Pre-segregation" and "Trans-segregation". Subsequently numerous authors have referred to these two mechanisms [2, 3, 7, 12, 19, 21, 24, 27, 32].

Pre-segregation is related to the differences in carbon concentration present in the microstructure before the transformation from austenite to ferrite occurs and which are responsible for the location of ferrite nucleation. Segregated alloying elements either

lower or raise the activity of carbon in iron in localized regions. The carbon concentration attains equilibrium due to its high diffusivity in austenite. Where the equilibrium concentration of carbon is low (due to an elevated carbon activity) ferrite nuclei will form in preference to those areas with higher carbon content [19]. As shown in Figure 2.14, highly mobile carbon homogenizes during cooling in the austenite phase field but as the carbon maintains a uniform chemical potential in the austenite, slight variations occur corresponding to the location of the manganese segregation. Manganese lowers the activity of carbon and hence the manganese rich regions are associated with higher carbon concentration. The spatial distribution of carbon depends on the concentration of substitutional solutes in austenite and these differences in concentration have been implicated as being the cause of banding.

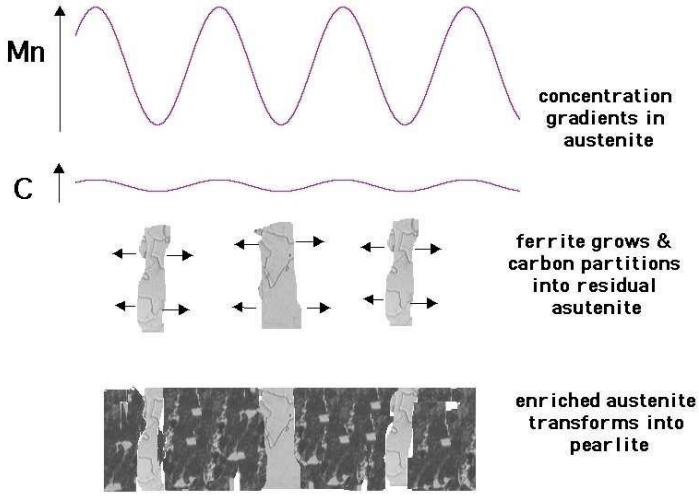

Figure 2.14: An illustration of the pre-segregation mechanism of banding. [12]

The trans-segregation theory relates to the effect of alloying elements on the local Ar_3 temperature, which determines where ferrite is nucleated first. In regions with a high content of ferrite stabilizing elements such as phosphorus or silicon (that increase the Ar_3 temperature) ferrite nuclei will form at higher temperatures than in regions with a high content of austenite stabilizers such as manganese, nickel and chromium [19].

To determine which one of these mechanisms dominates the formation of bands, Kirkaldy *et al.* [32] simulated a segregated microstructure by welding a disc of alloyed steel (with various alloying elements) between two discs of plain carbon steel with the same carbon content. After a heat treatment process, the microstructures were analysed by light microscopy to detect in which part of the sample ferrite formed first. Nickel was used as the alloying element and as nickel lowers the A_3 temperature this leads to

ferrite bands in the plain carbon steel as nucleation of ferrite occurs in the higher A_3 plain carbon steel than the nickel rich alloy steel.

A third mechanism of microstructural band formation is described in the literature relating to steels containing high sulphur concentrations. In these situations manganese-sulphides precipitate in the regions with a high concentration of manganese. The manganese is then bound in the sulphide which is surrounded by a manganese depleted zone, which then promotes the formation of ferrite (due to the associated higher A_3 temperature). The ferrite transformation then partitions carbon into the higher manganese neighbouring zones which transformed to pearlite as shown in Figure 2.15 [7, 12, 32].

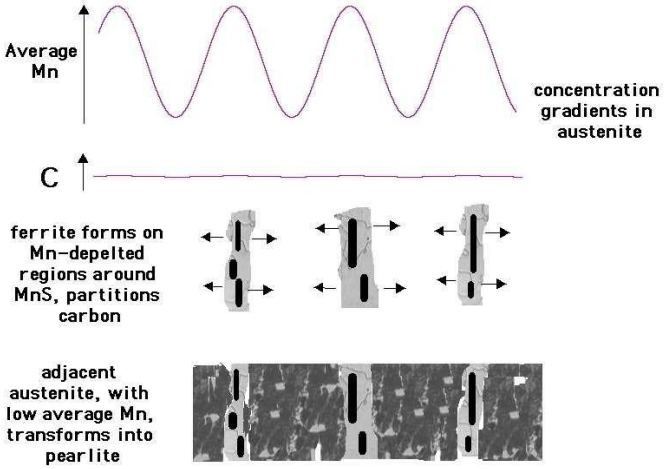

Figure 2.15: The mechanism of banding in steels containing manganese [12].

2.4.3 Factors Influencing the Development of Microstructural Banding

Formation of microstructural banding in hot rolled steel depends on many factors. The main factors that influence formation of microstructural banding are; steel composition, cooling rate and austenite grain size.

2.4.3.1 Steel Composition

The most common form of banded microstructures is the ferrite/pearlite banding, which occurs widely in plain carbon steels and in slow cooled low alloy AISI steels. In such structures, longitudinal micrographs display alternating bands of ferrite and pearlite lined up in the rolling direction wrought steel products. Figure 2.16 shows four different AISI steels with different types of banding. The variation in concentration of carbon and alloying elements leads to variation in segregation and subsequently banding [19].

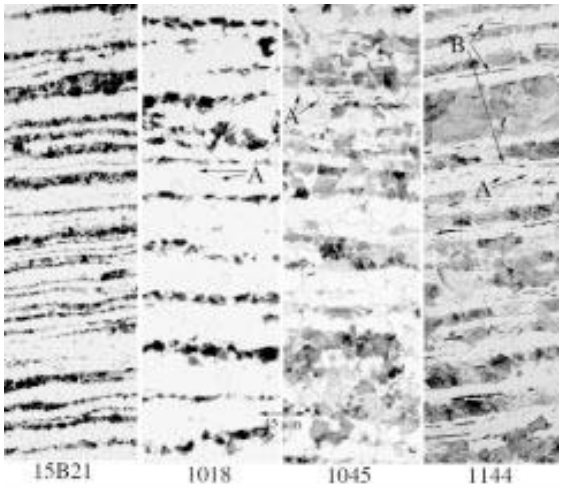

Figure 2.16: Banded microstructure of four steels after austenitization and furnace cooling [19].

2.4.3.2 Cooling Rate

The cooling rate applied after heat treatment in the austenite phase field of steel plays a critical role in the austenite to ferrite transformation and the subsequent formation of microstructural bands. Under slow cooling conditions, banded ferrite/pearlite microstructures appear. However, at higher cooling rates, there is not enough time for carbon diffusion and therefore, no banded microstructures result [22, 56]. Thompson and Howell [9] showed that banding is less severe in a sample from the edge of a hot rolled sheet where the cooling rate is higher than in the centre of the sheet as shown in Figure 2.17. While fast cooling can suppress the formation of a banded microstructure, it cannot remove the micro-segregation and bands may result again with reheating and slow cooling.

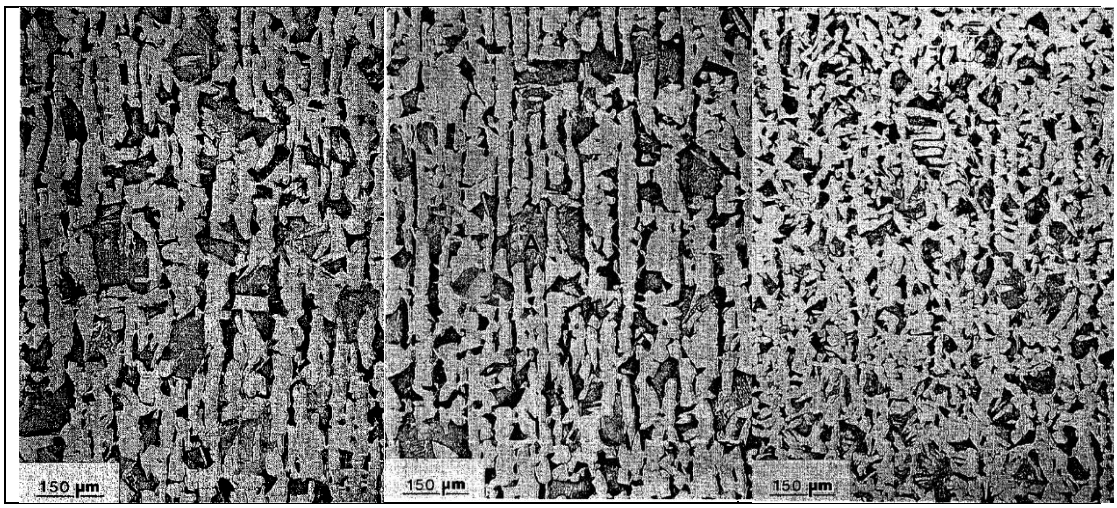

(a) Center of transver plane *(b) Center of longitudinal plane* *(c) Edge of longitudinal plane*

Figure 2.17: Optical micrographs of specimens taken from different locations of a hot rolled steel sheet. The steel contained 1.5 wt.% Mn and 0.15 wt.% C [9].

2.4.3.3 Austenite Grain Size

An important factor that significantly influences microstructural banding is the austenite grain size prior to the austenite-to-ferrite transformation. Thompson and Howell [9] have discussed this in detail and found that when ferrite grains nucleate at austenite grain boundaries. If the austenite grains are small compared to the wavelength of micro-segregation, sufficient nucleation sites are present and ferrite will nucleate in regions of low manganese concentration. If the austenite grain size is two or three time larger than the micro-segregation wavelength, there are not enough nucleation sites for ferrite available and banding is not possible. The process by which a small austenite grain size can produce banding is illustrated in Figure 2.18.

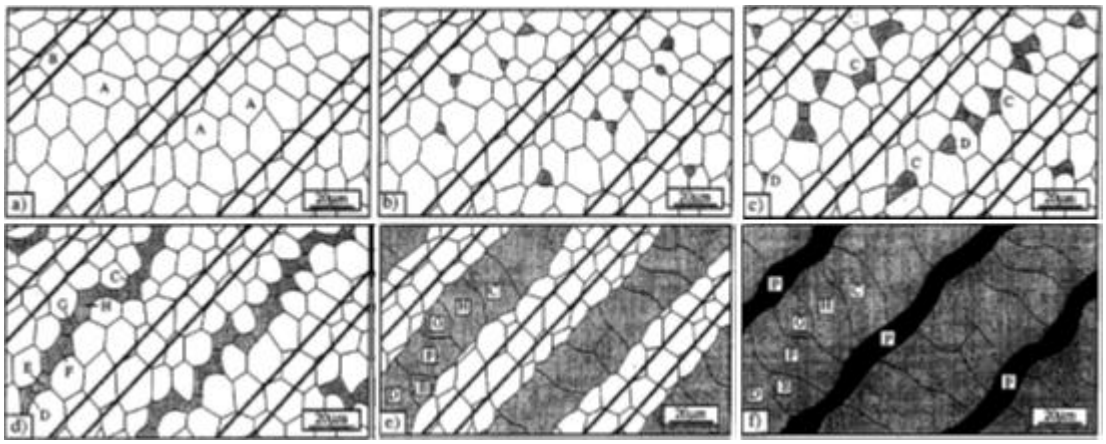

Figure 2.18: Model illustration of the growth processes leading to banding [9]

2.4.4 Effects of Microstructural Banding on Mechanical Properties

The mechanical properties of hot-rolled steel are significantly influenced by the heterogeneity caused by microstructural banding. The impact of banding varies among different types of alloys. Schwartzbart investigated the mechanical properties of a 0.21 *wt.*% carbon, 1.47 *wt.*% manganese steel which exhibited severe microstructural banding. The transverse mechanical properties of the bulk material improved through manganese homogenization. Working on a highly banded carbon steel, 0.3%C, Jatczak *et al.* [24], however, concluded that homogenization causes little alteration in longitudinal mechanical properties, and only slight, commercially insignificant, improvements in the transverse ductility and impact strength. Owen *et a1*[57] compared the behaviour of low-carbon steel with banded and homogenized microstructures and found no difference in impact properties below the ductile to brittle transition temperature. However, in the testing temperature range for ductile

fracture, both longitudinal and transverse energy absorptions were higher in homogenized specimens. Grange [29] concluded that both microstructural banding and elongated inclusions cause anisotropy in mechanical properties in wrought steel containing 0.25 *wt.*%C and 1.5 *wt.*%Mn. Elimination of banding was effective in reducing anisotropy but resulted in only slight improvement of anisotropy in the steel containing many elongated inclusions. Heiser and Hertzberg [58, 59] found that the ductility and impact-resistance anisotropy in banded steel was controlled by the delamination which occurred by inclusion/matrix interface separation in the mechanically fibred material. When delamination occurs normal to the crack growth direction, they are beneficial, by increasing the fracture energy and ductility, but when they bands occur in the growth direction and on the fracture plane, they are detrimental. Rao [60] studied the influence of banding on the impact and fatigue properties of a high strength SAE steel and concluded that the elimination of banding brought about an increase in impact strength and fatigue properties, and this was more pronounced at lower temperatures than at higher temperatures. The endurance limit was also raised by 8% by the removal of banding. Stauffer *et al.* [30] examined low alloy steels. The presence of significant amounts of manganese, chromium, and molybdenum were found in the inter-dendritic regions thus causing the segregated bands. Tensile testing of specimen oriented in the short transverse direction of the plate showed low ductility and a large variation in failure strains, depending on the continuity of the bands as well as the presence of large precipitate particles within the bands. Crack initiation in line pipe service failures has been traced to martensitic or hard segregation bands intersecting the pipe surface. In order to study the effect of continuity of banded structures on mechanical properties Tasan [61] and others have carried out a local *in situ* analysis of the deformation of two distinct banded microstructures of dual phase (DP) steel, coupled with micro-scale strain field measurements. The behaviour of continuous hard band regions was compared with discontinuous softer band regions in the same microstructure. Analyses from digital image correlation of in-situ electron microscopy micrographs showed that effects of band continuity yield a clear detrimental influence especially, for hard bands with a continuous morphology. Figure 2.19 shows the local strain evolution in martensitic and ferritic grains in the DP steel.

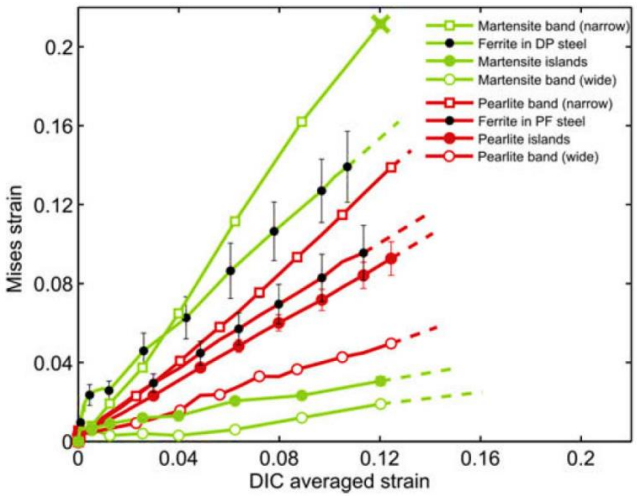

Figure 2.19: Local strain evolution in martensitic and ferritic grains in DP [61].

The previous studies show the significant influence of banding on the mechanical properties of different steels. However, Majka [3-5] showed that there is no evidence of the effect of banding when he evaluated the tensile properties of laminated specimens that simulate banding with sharp differences in chemistry and systematic variations in band spacing. Spitzig *et al.* [62] concluded that, banding had no effects on tensile or impact properties, while the shape and number of the inclusions had a large influence.

2.5 Mechanical Properties at High Temperature

Segregation of alloying elements occurs during solidification, which results in an inhomogeneous microstructure and variations in mechanical properties of the material. The variation in mechanical properties between segregated regions and other phases greatly affect the mechanical behaviour of the materials. Mechanical properties of each phase are of significant importance for the understanding mechanical behaviour of the material of this variation during subsequent process such as hot rolling. It is hard to determine mechanical properties on micro-scale by use of traditional methods [63]. Thus, various methods [64-66] have been developed to quantitatively determine the micro-scale mechanical properties of materials at such as weld materials. An important example of these methods is nano-indentation technique.

2.5.1 Nano-indentation

Nano-indentation technique has been widely adopted to evaluate the characterization of mechanical behaviour of materials at small scales [67-70]. As a relatively new form of mechanical testing that expands on the capabilities of traditional hardness testing,

the load-depth curve can be derived from the depth-sensing indentation technique without measuring contact area, so both the hardness and elastic modulus can be obtained. Detailed investigation of materials on micro-scale and nano-scale can be measured because of its ultra-low loads (on the μN scale). For this reason, the method has become a primary technique for determining elastic modulus, hardness, creep resistance, residual strain, and fatigue properties of thin films, single grains, individual phases and small structural features [70-72]. Furthermore, because of its high sensitivity, nano-indentation can be a powerful tool determine physical and mechanical properties of materials [72, 73]. Thus, however, nano-indentation testing has most commonly been conducted at room temperature [72-74]. This is in spite of the fact that materials and micro-devices are often employed at elevated temperatures and deformation physics are usually thermally activated. However, characterizing deformation requires the ability to test over as wide a range of temperatures as possible to enable the study of properties under operating conditions [73-75]. Although this is complicated by the difficulties encountered at elevated temperatures, nano-indentation has recently been also performed at elevated temperatures. However, in the studies on oxidizing materials such as metals, it is either required a sufficiently low test temperature to retard oxide growth, or involved flowing inert gas to dilute oxygen content in the atmosphere around the sample. Besides oxidation, another major issue in elevated temperature nano-indentation is thermal drift. Thermal drift occurs when any component in the load frame expands or contracts in response to changing thermal gradients, resulting in the measurement of apparent displacement that is not a true reflection of a material's force-displacement response. During testing at room temperature, thermal drift is generally low and assumed to be constant throughout the test, allowing it to be subtracted from the material response in a straightforward manner. Other difficulties are also encountered at elevated temperatures such as degradation of the tip material and geometry and heating of electronic components [73-75]. Of those experiments carried out at high temperatures, most are carried out in air, resulting in either a limitation of the temperatures or materials tested. This can be adequately managed for steel and other metals during testing in air up to 400°C with appropriate equilibration [73-75].

At macro-scale, it has been found for bulk steel that the deterioration of mechanical properties such as yield strength and elastic modulus of various steels grades at

elevated temperature (dependent on steel grades), is generally insignificant up to 400°C [76-84]. Since the significant deterioration of mechanical properties of steel occurs at higher temperatures, hot nano-indentation becomes inappropriate test to study micro-mechanical properties of steel features at high temperatures.

Various mechanical properties such as the elastic modulus and yield strength of pure iron and different steel grades have been determined with different techniques with range up to 723°C where primary phase is ferrite (α-phase). Mechanical properties of different steel grades have been also determined at higher temperatures.

2.5.2 Elastic Modulus at High Temperature

Above this temperature steel undergo a phase transformation to mixture of ferrite and austenite (γ-phase), or austenite at about 910°C [85]. Köster [86] provided data for calculating elastic modulus, E_γ at higher temperatures in austenite phase (γ-phase) in the range between 910°C and 1000°C using the following equation:

$$E_\gamma(T) = \gamma_1(1 - (T - \gamma_2)\gamma_3) \qquad 2.7$$

The value of γ_1 is *216 GPa,* γ_2 is *26.85* °C and γ_3, is 4.7×10^{-4} °C^{-1}. *T* is temperature expressed in degrees Celsius.

In the two-phase field, ranging between 723°C and 910°C, it is more difficult to evaluate the modulus as a function of temperature. Thus, a simple method [85] for approximating the elastic modulus, $E_{\alpha\text{-}\gamma}$ in the two-phase region was used by interpolating between the two phases as the following equation:

$$E_{\alpha-\gamma}(T) = E_\alpha(A_1) + \frac{E_\gamma(A_3) - E_\alpha(A_1)}{A_3 - A_1}(T - A_1) \qquad 2.8$$

Where A_1= 723°C and A_3= 910°C

Different calculations of these elastic moduli of structural steels are also shown in Figure 2.20.

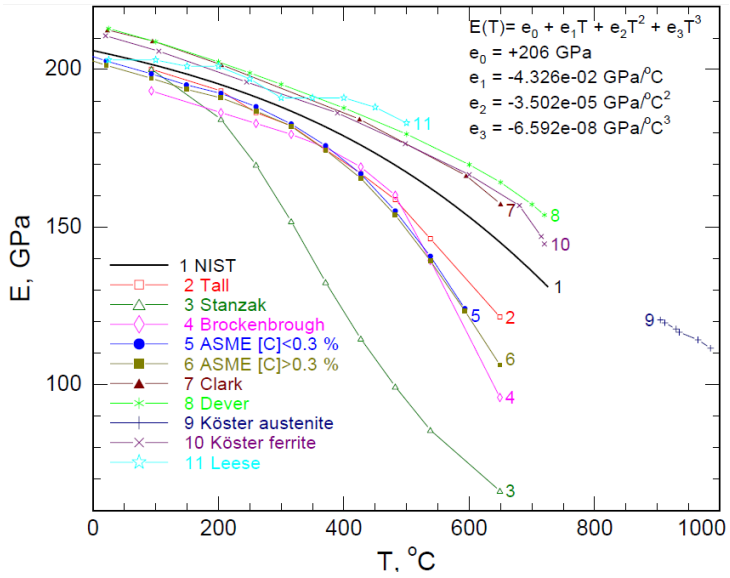

Figure 2.20: Elastic moduli at high temperature of some structural steels [85].

2.5.3 Yield Strength at High Temperature

A useful and often recognized relation is that the yield strength of steel as a function of temperature, normalized to the room-temperature value. It was found that the normalized curve for yield strength drops rapidly from unity beyond about 400 °C. An equation was developed to represent the yield strength behaviour up to 800 °C for some structural steels as following:

$$\sigma_{y_T} = \sigma_{y_{RT}} \left\{ (1 - A_2) \exp\left(-\frac{1}{2} \left[\left(\frac{T}{s_1} \right)^{m_1} + \left(\frac{T}{s_2} \right)^{m_2} \right] \right) + A_2 \right\} \qquad 2.9$$

T is the temperature in °C and $\sigma_{y_{RT}}$ is the yield strength at room temperature and A_2, s_1, s_2, m_1 and m_2 are yield reduction parameters. Figure 2.21 shows the ratio, f, of high-temperature yield strength (σ_{y_T}) to room-temperature yield strength ($\sigma_{y_{RT}}$) for all steels characterized [85].

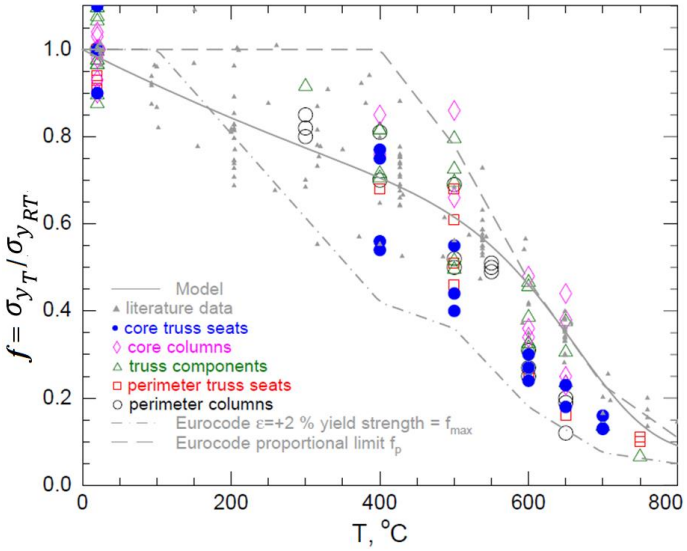

Figure 2.21: ratio of high-temperature yield strength to room temperature yield strength [85].

For temperatures above 800°C, studies [76-80, 87-93] were also conducted for a number of different steels. The yield strength at these temperatures was similarly calculated by using the ratio, *f*, of high-temperature yield strength to room-temperature yield strength. This reduction factor (*f*) of the yield strength of these steels is shown in Figure 2.22 and Figure 2.23.

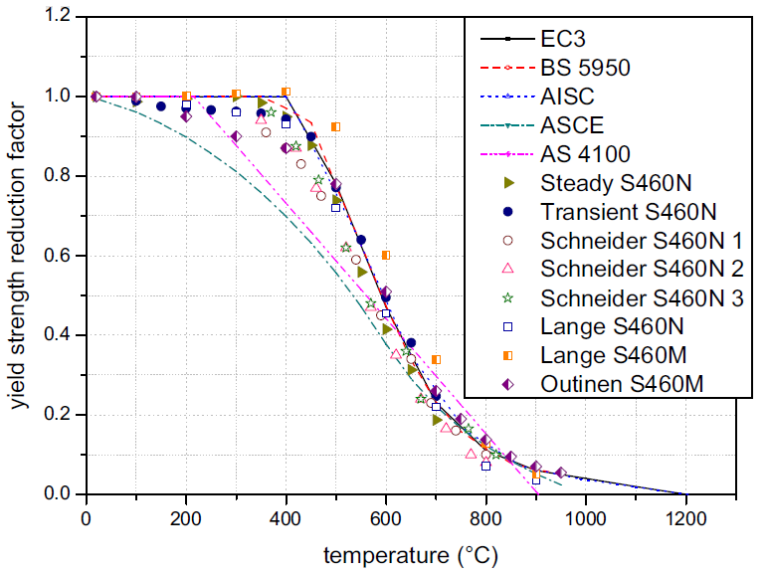

Figure 2.22: High-temperature yield strength behaviour for various structural steels [77].

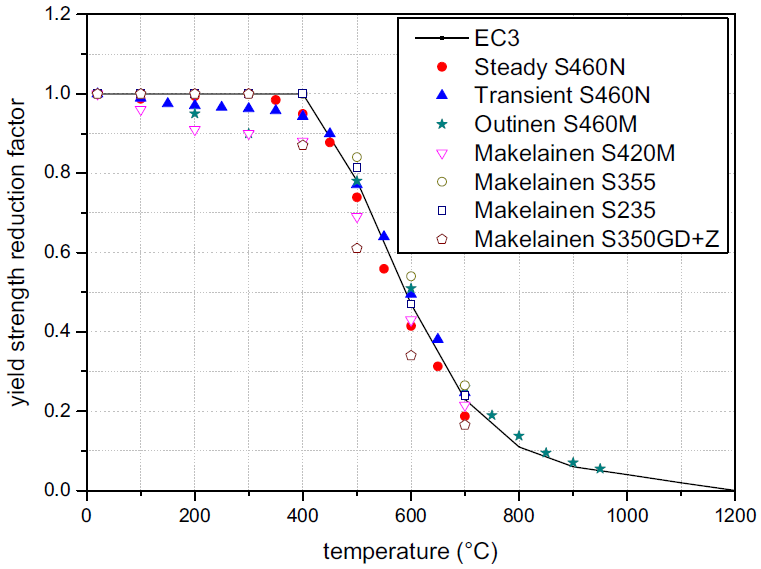

Figure 2.23: High-temperature yield strength behaviour for various mild steels [77].

Qiang [80] developed an empirical equation representing the yield strength behaviour of high strength structural steels at higher temperatures up to 1000°C. The equation is:

$$\sigma_{y_T} = \sigma_{y_{RT}}\{1.8 \times 10^{-8}T^3 - 4.03 \times 10^{-5}T^2 + 2.74 \times 10^{-2}T - 4.711\} \quad 2.10$$

where $650\,℃ < T < 1000\,℃$

2.6 Rolling Process

It is important for understanding the mechanism of micro-chemical and microstructural banding formation during hot rolling, to understand rolling process and behaviour of material during rolling. The rolling process can be defined as a continuous process of plastic deformation for long parts of constant cross section, in which a reduction of the cross sectional area is achieved by compression between two rotating rolls (or more) [94]. In cold rolling the material is deformed at room temperature (but it can be slightly higher with heat dissipation due to plastic work) and in hot rolling the temperature is high (more than half of the absolute melting temperature).

Another important distinction is made according to geometric considerations. Flat rolling is performed with cylinders: this is also the case for sheet rolling or strip rolling (in which the thickness is very small, of the order of millimetres or less), or slab rolling (in which the slab thickness is of the order of 0.1 m) and any inter-mediate situation.

Shape rolling allows the production of more complex work-specimen by using appropriate roll geometries: the cross section of the part can be a round, an oval, various beams, a rail, and so on. Figure 2.24 represents the general principle for flat rolling and two examples of geometries in a vertical cross section by a plane parallel to the rolling direction.

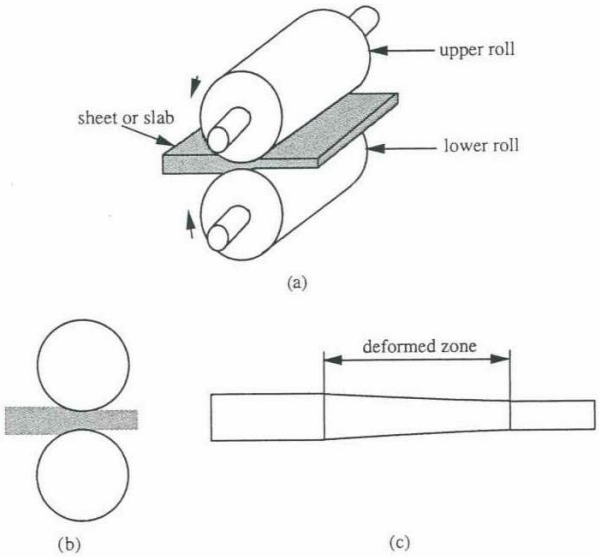

Figure 2.24: Flat rolling: (a) general, (b) cross section for slab rolling, (c) cross section for rolling strip [94].

For hot or cold rolling of any geometry, the desired reduction of cross-sectional area is too large to be feasible in one pass. The final deformation is progressively applied by using several stands so that several pairs of cylinders successively deform the same part as shown in Figure 2.25. There are thus interacting forces between two successive stands, which induce tension (in plane loads) either in the direction of rolling or in the opposite direction. In Figure 2.25, the smaller rolls are in contact with the sheet and produce successive reductions of thickness. The small diameters limit the width of the deforming region and thus the roll-separating force. The larger diameter rolls are designed to prevent excessive bending of the work roll [94]. Traditionally, the initial material form for rolling is an ingot or slab. Figure 2.26 gives a summary of the main rolling processes.

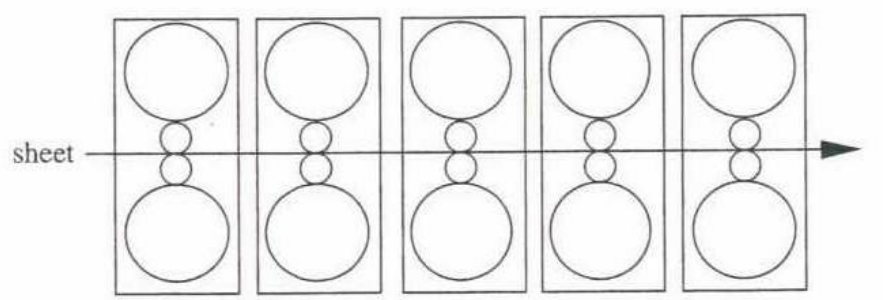

Figure 2.25: Schematic of a five-stand rolling mill [94].

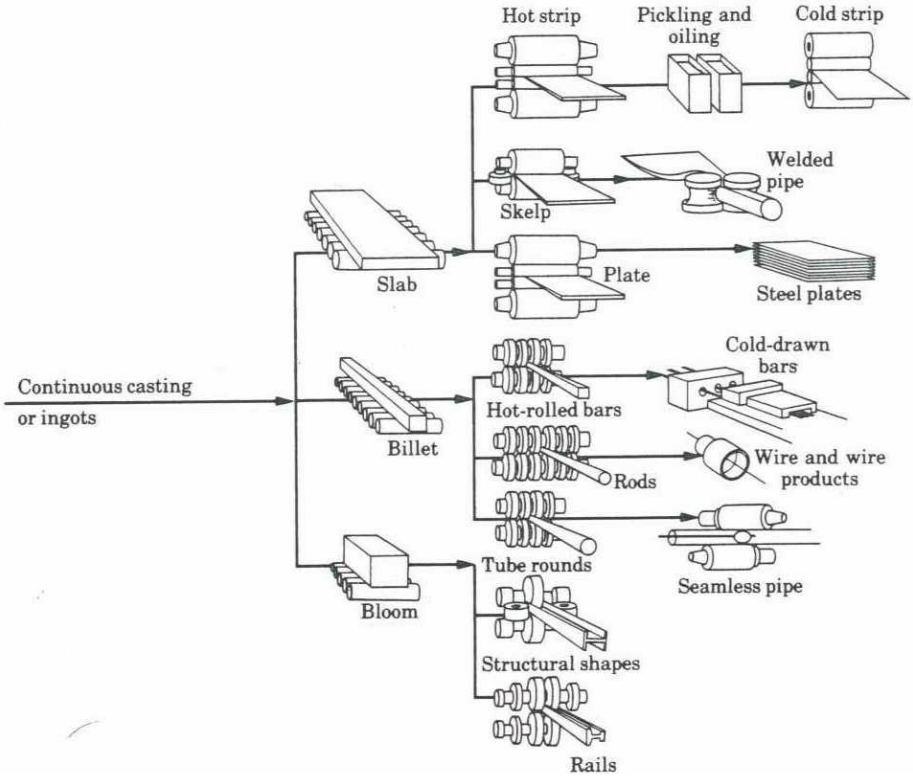

Figure 2.26: Schematic of various flat-and-shape rolling processes [95].

A schematic illustration of the flat rolling process is shown in Figure 2.27. A strip thickness h_o enters the roll gap and is reduced to h_f by a pair of rotating rolls, each roll being powered through its own shaft by electric motors. The surface speed of the roll is V_r. The velocity of the strip increases from its initial value V_o as it moves through the roll gap, just as fluid flows faster as it moves through a converging channel. The velocity of the strip is highest at the exit of the roll gap and is denoted as V_f. Since the surface speed of the roll is constant, there is relative sliding between the roll and the strip along the arc of contact in the roll gap, L. At one point along the contact length, the velocity of the strip is the same as that of the roll. This is called the neutral, or no slip, point. To the left of this point, the roll moves faster than the strip, and to the right

of this point, the strip moves faster than the roll. Hence, the frictional forces, which oppose motion, act on the strip as shown in Figure 2.27 (b).

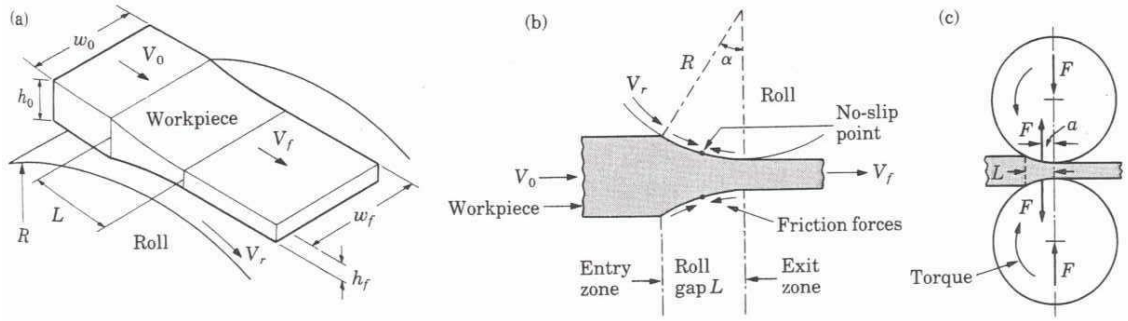

Figure 2.27: (a) Schematic Illustration of the flat-rolling process, (b) Friction forces acting on strip surfaces, (c) Roll force F and torque acting on the rolls [95].

2.7 The Finite Element Method

The Finite Element Method (FEM) is a numerical analysis procedure used to obtain approximate solutions to boundary value problems, which are found in every field of engineering. Difficulties found in everyday industrial applications do not have typical single solution. Due to incapability to overcome many difficult structural mechanics, material behaviour, heat transfer analysis, and fluid mechanics problems, the Finite Element Method became an essential tool in the field of engineering mechanics and materials

The FEM was initially applied to the structural analysis area and its associated theory of elasticity. Then the FEM expanded to cover fluids heat diffusion equation. After these successive development with the advances in computer technology, researchers began to focus develop more complicated materials and behaviours such as fluids and plastic/visco-plastic materials, whose behaviour is described by the theories of plasticity, and visco-plasticity materials, which are used to explain the permanent deformations that occur in the metal forming processes [96-98].

Finite element analysis, particularly nonlinear, facilitates the simulation of metal forming processes in a more realistic manner than ever before, especially in the hot rolling industry where the behaviour of steel at high temperatures needs more understanding.

2.8 Plasticity

Steel and most metals and behave more likely perfectly plastic material follow plasticity theories when they are subjected to hot deformation. During hot rolling, very

large strains and deformations involved, thus elastic strains can be disregarded during the analysis of such processes [99].

Models of special limit theorems of plasticity have been developed and are usually employed to overcome these type of problems. For formulation of basic plasticity theories, the following assumptions are usually made:

1. **The response is independent of rate effects**: plastic deformations are normally rate independent, i.e. the stresses induced are independent of the rate of deformation (or rate of loading).
2. **The material is incompressible in the plastic range:** after plastic deformation, the material will undergo negligible volume change.
3. **There is no Bauschinger effect:** the presence of the Bauschinger effect complicates any plasticity theory.
4. **The yield stress is independent of hydrostatic pressure**: experiments show that, for metals, the yield behaviour is independent of hydrostatic pressure. i.e, stress state $\sigma_{xx} = \sigma_{yy} = \sigma_{zz} = -p$ has negligible effect on the yield stress of a material to very high pressures.
5. **The material is isotropic**

These assumptions can be made on the type of hardening and on whether elastic deformations are significant. For example, consider the models illustrated in Figure 2.28, commonly used for metals in theoretical analyses. In Figure 2.28 (a) both the elastic and plastic curves are assumed linear. In Figure 2.28 (b) work-hardening is neglected and the yield stress is constant after initial yield. In Figure 2.28 (c) the elastic curve is assumed linear and plastic curve is assumed exponential. Such perfectly-plastic models are particularly appropriate for studying processes where the metal is worked at a high temperature such as hot rolling where work hardening is small [100-105].

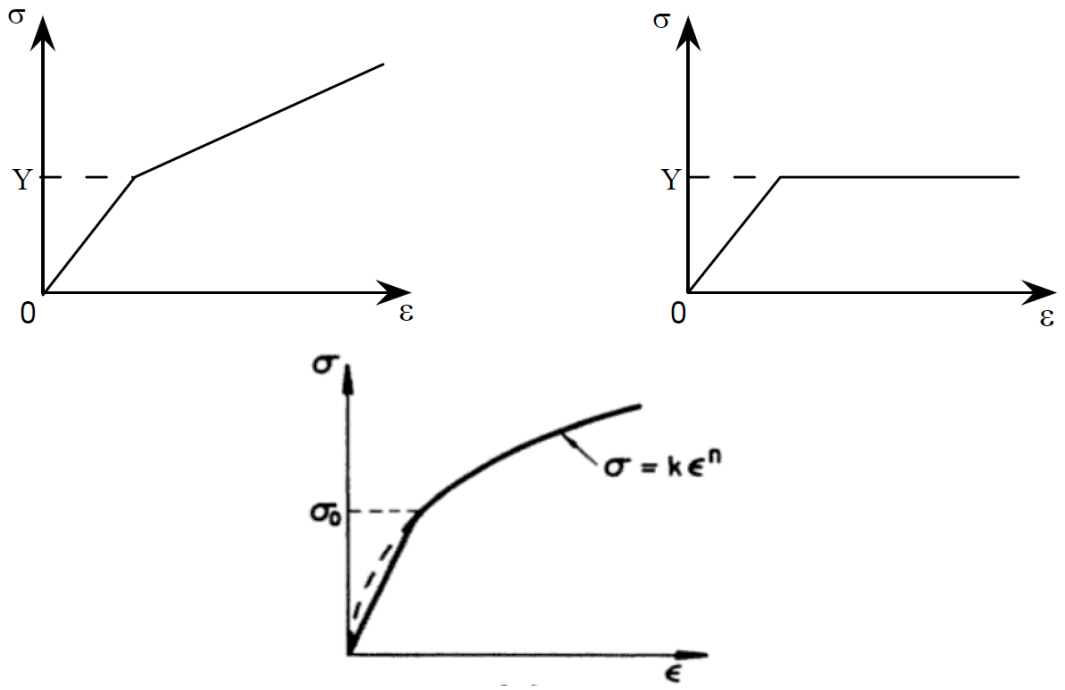

Figure 2.28: Common models of elastic and plastic deformation of metals. (a)Linear Elastic-Plastic Model (b) Elastic-Perfectly-Plastic Model [102]; and (c) Elastic-Exponential (Power-law) Hardening Model, [101].

With the assumption of that the behaviour of steel under compression (rolling) is generally similar to that under tension and the true stress and strain are used, then the two curves would coincide.

Stress and strain are related in the elastic region through

$$\sigma = E\varepsilon \qquad 2.11$$

where *E* being the Young's modulus.

In the plastic region, a commonly used relation to define the relation between stress and strain is given by

$$\sigma = K\varepsilon^n = H\varepsilon^m \qquad 2.12$$

The strength coefficient, *K* or *H*, is the stress when ε =1; and *m* or *n* is the strain hardening exponent, 0 < n < 1 (0 is perfectly plastic and 1 is perfectly elastic) .

The tangent modulus *K* , as shown in Figure 2.29, is the slope of the stress-strain curve in the plastic region and will in general change during a deformation. At any instant of strain, the increment in stress $d\sigma$ is related to the increment in strain $d\varepsilon$ through

$$d\sigma = Kd\varepsilon \qquad 2.13$$

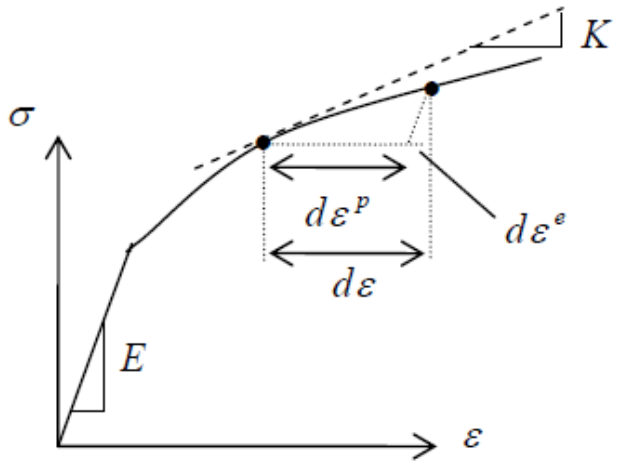

Figure 2.29: The tangent modulus [102].

After yield, the strain increment consists of both elastic, ε^e, and plastic, $d\varepsilon^p$, strains:

$$d\varepsilon = d\varepsilon^e + d\varepsilon^p \qquad 2.14$$

The stress and plastic strain increments are related by the plastic modulus *H*:

$$d\sigma = H\, d\varepsilon^p \qquad 2.15$$

and it follows that

$$\frac{1}{K} = \frac{1}{E} + \frac{1}{H} \qquad 2.16$$

The phenomenon whereby yield stress increases with increasing plastic strain is known as work hardening or strain hardening introduced by symbol *k* as hardening parameter. As the elastic and inelastic behaviour is usually separated by the *yield strength* of the material in the ductile materials such as most common metals, the hardening rules are applied [100-105].

The yield stress is usually determined in a tensile test, where a single uniaxial stress acts. However, the actual structure of material usually exhibits multi-axial stress state which can be predicted in general multi-dimensions. This is done by use of a theory called yield criterion which defines the limit of elasticity in a material and the onset of plastic deformation under any possible combination of stresses. The yield criterion provides a scalar invariant measure of the stress state of the material which can be compared with the uniaxial case [100-105].

There are several possible yield criteria. However, the two most commonly used and successful yield criteria for isotropic metallic materials are the Tresca and Von Mises criteria [100-102].

In general, a stress state can be separated into two components; hydrostatic stress that generates volume change, and deviatoric stress that generates angular distortion as schematically shown in Figure 2.30.

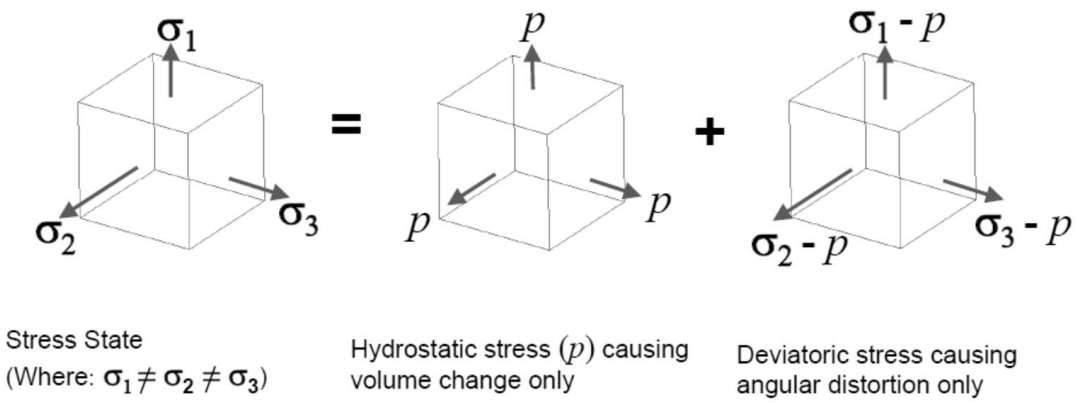

Figure 2.30: Stress state, hydrostatic stress, and deviatoric stress [106].

A purely hydrostatic stress $\sigma_1 = \sigma_2 = \sigma_3 = p$ will lie along the vector [111] in principal stress space. For any point on this line, there can be no yielding, since in metals, it is found experimentally that hydrostatic stress does not induce plastic deformation [106]. If $\sigma_1 = Y$, $\sigma_2 = \sigma_3 = 0$ then yielding will occur, where Y is a uniaxial stress [100-105]. Therefore, there must be a surface, which surrounds the hydrostatic line and passes through (Y, 0, 0) that defines the boundary between elastic and plastic behavior. This surface will define a yield criterion. Such a surface has also to pass through the points: (0, Y, 0), (0, 0, Y), ($-Y$, 0, 0), (0, $-Y$, 0) and (0, 0, $-Y$).

The plane defined by the three points (Y, 0, 0), (0, Y, 0) and (0, 0, Y) is parallel to the plane defined by the three points ($-Y$, 0, 0) (0, $-Y$, 0) and (0, 0, $-Y$).

The Tresca yield criterion states that a material will yield if the maximum shear stress reaches some critical value

$$max\left\{\frac{1}{2}|\sigma_1 - \sigma_2|, \frac{1}{2}|\sigma_2 - \sigma_3|, \frac{1}{2}|\sigma_3 - \sigma_1|\right\} = k \qquad 2.17$$

The value of k can be obtained from a simple experiment. For example, in a tension test,

$\sigma_1 = \sigma_0, \sigma_2 = \sigma_3 = 0$ and failure occurs when σ_0 reaches Y, the yield stress in tension. It follows that

$$k = \frac{Y}{2} \qquad 2.18$$

The Von Mises yield criterion predicts that yielding will occur whenever the distortion energy in a unit volume equals the distortion energy in the same volume when uni-axially stressed to the yield strength. The Von Mises criterion states that yield occurs when the principal stresses satisfy the relation

$$\sqrt{\frac{(\sigma_1-\sigma_2)^2+(\sigma_2-\sigma_3)^2+(\sigma_3-\sigma_1)^2}{6}} = k \qquad 2.19$$

from a uni-axial tension test, k can be found as

$$k = \frac{Y}{\sqrt{3}} \qquad 2.20$$

the Von Mises Stress in terms of Y is

$$\sigma_{VM} = \frac{1}{\sqrt{2}}\sqrt{(\sigma_1 - \sigma_2)^2 + (\sigma_2 - \sigma_3)^2 + (\sigma_3 - \sigma_1)^2} = Y \qquad 2.21$$

Thus, when the Von Mises Stress reaches the yield stress in pure tension, the material begins to deform plastically.

The hydrostatic line and the yield surfaces for the Tresca yield criterion and the von Mises yield criterion in plane stress are shown in Figure 2.31 (a) and (b) respectively:

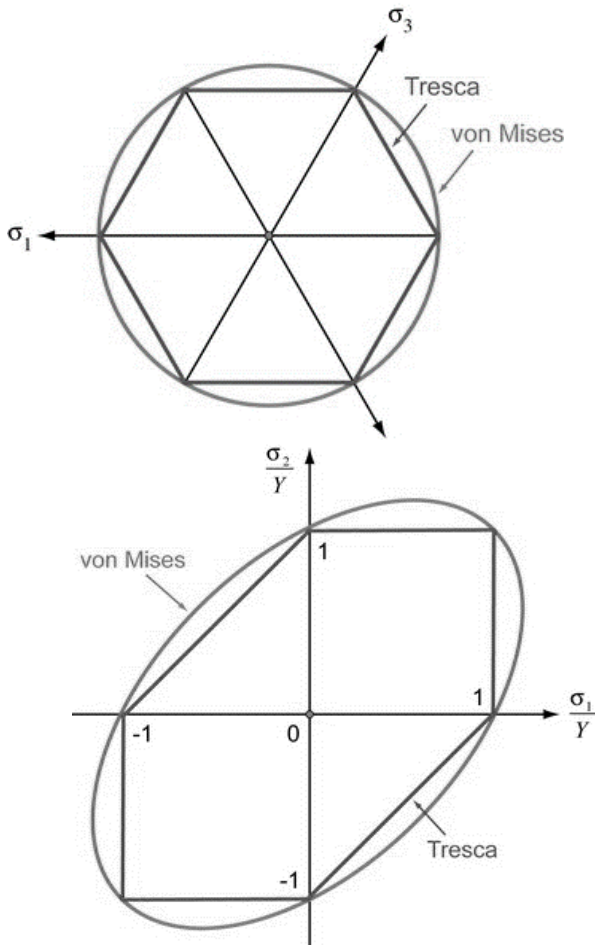

(a) (b)

Figure 2.31: (a) The hydrostatic line and (b) the yield surfaces for the Tresca yield criterion and the von Mises yield criterion in plane stress [106]***.***

Experiments suggest that the von Mises yield criterion is the one which provides better agreement with observed behavior than the Tresca yield criterion. However, the Tresca yield criterion is still used because of its mathematical simplicity [105, 106].

It is very common to interpret yield criteria geometrically in a principal stress space. The two non-zero principal stresses for plane stress, σ_1 and σ_2, so that σ_3=0. The criteria can then be presented in (σ_1, σ_2) 2-D principal stress space. Therefore, with σ_3=0, the Tresca criteria condition reduces to

$$\max\{|\sigma_1 - \sigma_2|, |\sigma_2|, |\sigma_1|\} = Y \qquad 2.22$$

and the Mises criteria condition reduces to

$$\sigma_1^2 + \sigma_1\sigma_2 + \sigma_2^2 = Y^2 \qquad 2.23$$

These are plotted on the yield surface and some stress states are shown in Figure 2.32 in the stress space: point *A* corresponds to a uniaxial tension, *B* to *A* equi-biaxial tension and *C* to a pure shear τ. The points inside these surfaces represent an elastic stress state. Any combination of principal stresses which push the point out to the yield surfaces results in plastic deformation.

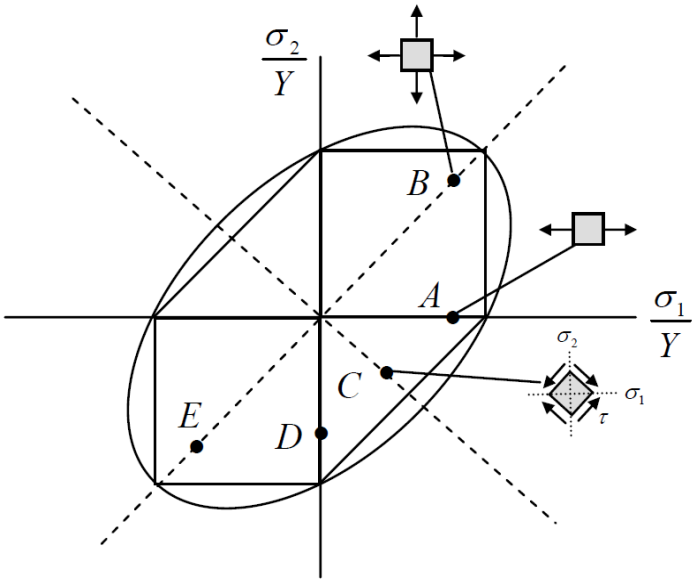

Figure 2.32: Yield surface in 2D principal stress space [102].

As explained experiments show that under uniaxial loading, the strain at a given stress has two parts: a small recoverable elastic strain, and a large, irreversible plastic strain. However, for multi-axial loading, a general strain increment, $d\varepsilon_{ij}$ is generalized by decomposing it into elastic and plastic parts, as

$$d\varepsilon_{ij} = d\varepsilon_{ij}^{e} + d\varepsilon_{ij}^{p} \qquad 2.24$$

In cases of the criteria, the yield stress, *Y*, that may increase during plastic straining, so it is used as function of a measure of total plastic strain.

To predict the plastic strains induced by stressing the material beyond the yield point, plastic strain increments are determined rather than total accumulated strain.

For **Von Mises yield criterion with isotropic hardening,** the small plastic strain increments are determined from

$$d\varepsilon_{ij}^{p} = d\bar{\varepsilon}^{p}\frac{\partial f}{\partial \sigma_{ij}} = d\bar{\varepsilon}^{p}\frac{3}{2}\frac{S_{ij}}{Y} \qquad 2.25$$

where

$$f(\sigma_{ij}, \bar{\varepsilon}^p) = d\bar{\varepsilon}^p \frac{\partial f}{\partial} = \sqrt{\frac{3}{2} S_{ij} S_{ij}} - Y(\bar{\varepsilon}^p) \quad 2.26$$

where S_{ij} is components of the deviatoric stress tensor (MPa)

$$S_{ij} = \sigma_{ij} - \frac{1}{3}\sigma_{kk}\delta_{ij} \quad 2.27$$

the Von-Mises yield criterion, and $d\bar{\varepsilon}^p$ is determined from the condition that the yield criterion must be satisfied at all times during plastic straining. This shows that

$$f(\sigma_{ij} + d\sigma_{ij}, \bar{\varepsilon}^p + d\bar{\varepsilon}^p) = f(\sigma_{ij}, \bar{\varepsilon}^p) + \frac{\partial f}{\partial \sigma_{ij}} d\sigma_{ij} + \frac{\partial f}{\partial \bar{\varepsilon}^p} d\bar{\varepsilon}^p = 0 \quad 2.28$$

$$\frac{\partial f}{\partial \sigma_{ij}} d\sigma_{ij} - \frac{\partial Y}{\partial \bar{\varepsilon}^p} d\bar{\varepsilon}^p = 0 \quad 2.29$$

$$\bar{\varepsilon}^p = \frac{1}{h}\frac{\partial f}{\partial \sigma_{ij}} d\sigma_{ij} = \frac{1}{h}\frac{3}{2}\frac{S_{ij} d\sigma_{ij}}{Y} \quad 2.30$$

where $h = \frac{dY}{d\bar{\varepsilon}^p}$

where Latin subscripts (*i, j, k*) have the range (1, 2, 3) and $h = \frac{\partial Y}{\partial \bar{\varepsilon}^p}$ is the slope of the plastic stress-strain curve.

2.9 Mathematical Models of the Rolling

Mathematical models of the flat rolling process are numerous. In each, the equations of motion, thermal balance, material properties and roll deformation are used to calculate the stress, strain, strain rate, velocity and temperature fields, the roll pressure distribution, roll separating forces and roll torques [107, 108].

The accuracy of these models depends on the quality of the assumptions made. In the conventional models, most researchers assume the existence of homogeneous compression of the strip, considered to be made of an isotropic and homogeneous material that is incompressible in the plastic state. Further, plane strain conditions are assumed to exist and either a constant friction factor or Coulomb friction conditions apply at the roll-strip interface. Assumptions and simplifications vary broadly when

finite element methods are employed. The same applies to the material models the main models used being the elastic plastic and rigid plastic ones [107].

A general mathematical model of the flat rolling process should include [107]:

a) Equations of motion of the deformed metal,

b) Heat balance of the roll/strip system,

c) Equations of equilibrium of the work roll,

d) Description of the frictional forces between the work roll and the metal,

e) Description of the material properties.

As the strip enters the roll gap it is first deformed elastically. It speeds up; the relative velocity between the roll and the strip is such that friction draws the metal in. The criterion of plastic flow governs the manner in which the transformation from elastic to plastic happens in what is known as the elastic-plastic interface. The strip proceeds through the roll gap and more plastic flow occurs until finally at the exit roll pressure is removed. The strip is unloaded and it returns, through an elastic state to the original, load free condition. It is observed that during rolling, the relative velocities of the roll and the strip change and as the strip is accelerating forward it reaches the roll surface velocity at the no-slip or neutral point. From then on, as further compression occurs, the strip speeds up and the direction of friction changes in such a way that it now retards motion. Exit velocity of the strip is often larger than that of the roll and the difference between the two velocities is determined by the forward slip [107, 108].

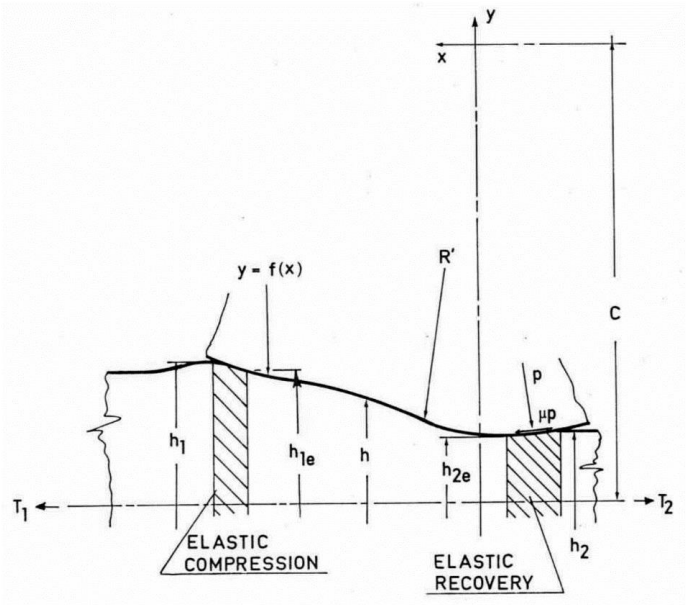

Figure 2.33: Schematic Diagram of the Flat Rolling Process [107].

Thermal events occurring during the strip's passage through the roll gap are also of importance. In fact, it is the thermal events that contribute most to the metallurgical developments of the final structure of the rolled material. Surface conditions, roll wear and thus roll life are also affected by thermal conditions. Heat is generated because of the work done on the strip, increasing its temperature. Interfacial friction forces also cause the temperature to rise. Contact with the cold and often water-cooled rolls also causes heat losses. Metallurgical transformations also contribute to temperature changes. A complete mathematical model should account for both thermal and mechanical events, which occur in the deformation zone during the rolling process. Several assumptions regarding material behaviour must be made. The material is usually assumed to be, and to remain, isotropic and homogeneous; it is considered to be elastic-plastic even though as gross plastic straining takes place, elastic deformations may be quite small in comparison to plastic strains. During forming the volume of the plastic region is taken to remain constant, and finally, a plane state of strain is assumed to exit [107, 108].

2.10 Finite Element Model and Plasticity

The equations relating stress, strain, stress rate (increase of stress per unit time), and strain rate are called the constitutive equations, since they depend upon the material properties of the medium under discussion. In the case of elastic solids, the constitutive equations take the form of generalized Hooke's law, which involves only stress and strain and is independent of the stress rate or strain rate. In plasticity however, the constitutive equations have a more difficult formulation, as they need to describe more complex phenomena. According to Lenard & Pietrzyk, functions describing the constitutive behaviour of metals at high temperatures can be divided into several groups [107, 108].

Group I: functions, $\sigma = f(\varepsilon)$, which account for the current strain (ε) , and in some cases, for the initial stress (σ_Y) or initial strain (ε_0),

Group II: functions $\sigma = f(\varepsilon, \dot{\varepsilon}, T)$, which account for an influence of the current temperature (T), strain rate $(\dot{\varepsilon})$ and strain (ε) ,

Group III: functions, $\sigma = f(\varepsilon, \dot{\varepsilon}, T, \sigma_w)$, which in addition to the temperature, strain, and strain rate, account for the influence of an internal state variable of the material(σ_w),

Group IV: functions, $\sigma = f(\varepsilon, \dot{\varepsilon}, T, t)$, which also account for the time in addition to the current temperature (T) in degree Celsius, strain rate $(\dot{\varepsilon})$ and strain (ε),
Group V: functions, which account for an influence of strain directions.
The basic factors that affect the magnitude of yield stress are the temperature and the rate of deformation. Their influence is different in cold and hot deformation [94].

Metal undergoes strain hardening and the yield stress increases with the amount of cold deformation. The rate of increase falls off as the degree of cold work increases. Finally, a degree of cold work is reached, beyond which no increase in strain hardening can be observed.

In hot deformation, the strain hardening and re-crystallization take place simultaneously. Therefore, the effects of strain hardening are not very apparent. Assuming that the deformation temperature is constant, it can be concluded that the yield stress should also remain constant. The determination of the yield stress at temperatures above 700 ºC is a challenge. The stress-strain curve does not show any great change of direction on reaching the yield stress. Some researchers make the assumption that at these high working temperatures the yield stress differs very little from the ultimate tensile stress, and this value is sometimes defined as the constrained yield stress, $S = 2\tau_Y = 1.15\sigma_Y$. The temperature of the specimen has great influence on the strain rate. In order to study it, we will distinguish the following temperature ranges [94, 108, 109]:

Lower temperature range: brittleness can occur on applying large strain rates to metals which are ductile at low strain rates,
The cold deformation range (below recrystallization temperature): the influence of strain rate is very small but the mechanical factors introduced due to the increase of strain rate can be of importance,
Higher temperature range (above recrystallization temperature): while the phenomena of cold work occurs at high strain rates, hot working takes place at low strain rates,
Hot deformation range: The strain rate has an important influence. The higher the strain rate, the higher the yield stress. At very high temperatures, as the strain rate increases, the heat has no time to be dissipated and remains in the metal, causing a rise in temperature. This results in lowering the range of fusion temperature of the metal at

high strain rates, and hence the permissible temperature range for hot working becomes narrower. Therefore, low strain rates are necessary in hot rolling.

The basic factor that decides the degree of plastic deformation of metal is the yield stress, which is dependent on the condition of the metal at the moment of deformation.

a) For deformation and forming problems under conditions insufficient for recrystallization – cold working, the yield stress depends on: the properties of material, the amount of cold deformation or initial strain hardening, the strain and the strain rate to a very small degree which is almost negligible.

b) Deformation above the temperature of recrystallization processes (hot working), the yield stress depends on: the properties of material, the strain, the strain Rate and the temperature of deformation.

Therefore functions in group I are effective in the simulation of cold deformation processes, and functions in groups II, III, IV, and V are the ones used to simulate hot forming processes.

For cold rolling hot rolling, the most common and at the same time accurate constitutive equation is given by the well-known power law (Eq. 2.12)

In the literature we find some variations of the power law such as:

Dasko

$$\sigma = K(\varepsilon_0 + \varepsilon)^n \qquad 2.31$$

ε_0 = pre-existing amount of strain hardening

Ramberg-Osgood

$$\sigma = \sigma_Y + K\varepsilon^n \qquad 2.32$$

σ_Y= yield stress

Haslach and Armstrong [110] reported that the larger the hardening exponent, the easier the metal is to cold work. Experiments have shown that the strain hardening coefficient, *K*, is proportional to the square root of the density of dislocations in the material.

2.10.1 Basic Model of Flat Rolling

Figure 2.34 illustrates the stresses acting upon a differential elemental vertical section of the flat specimen between the rolls. It has been reported to analyse the plastic deformation of the specimen an infinitesimal element in the specimen of thickness *dx* to be selected, and all normal and friction forces acting on the element have been identified. Then the appropriate differential equation can be derived from which a solution is obtained by integration of the equation using appropriate boundary conditions and then assumptions are made [107-109, 111-115].

The assumption includes:

a) The direction of the applied load and planes perpendicular to this direction define principal directions,
b) The principal stresses do not vary on these planes,
c) The frictional forces do not produce the internal distortion of the metal and do not change the orientation of the principal directions,
d) Plane vertical sections remain plane and therefore, the deformation is homogeneous in regard to determination of induced strain,
e) Elastic deformation of the specimen is negligible in comparison with the plastic deformation,
f) There is no elastic deformation of the tool in the contact zone,
g) The compressive strength is constant throughout the contact length,
h) The specimen does not spread laterally as we assume a state of plane strain,
i) There is no roll flattening in the arc of contact,
j) The peripheral velocity of the rolls is constant,
k) Material does not undergo work-hardening during its passage between the rolls,
l) The compression rate from point along the arc of contact does not have any effect on the magnitude of the compression strength,
m) The vertical component of the friction force is negligible.

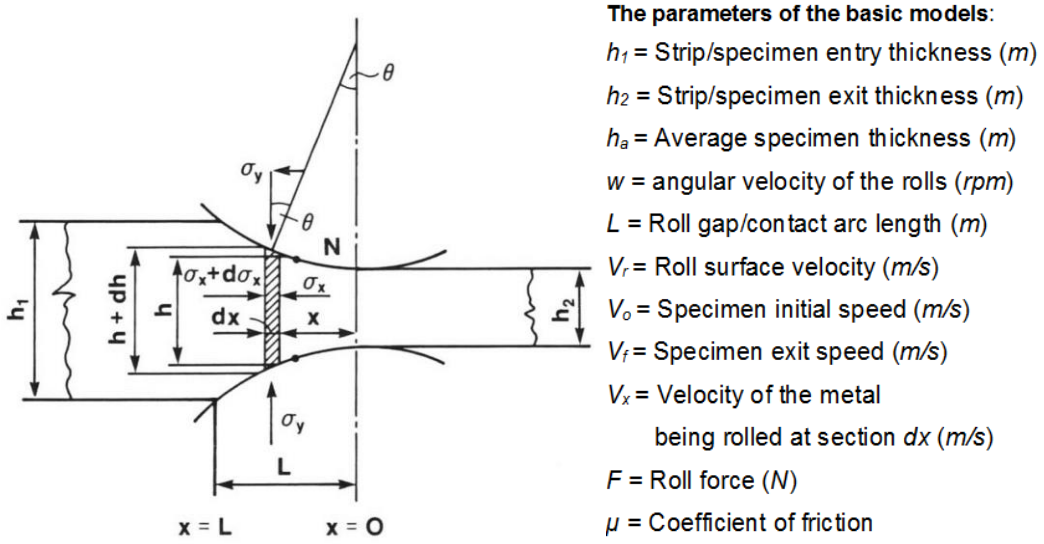

Figure 2.34: A schematic of the deformation zone in flat rolling [111].

The horizontal forces acting on vertical faces of the section *dx* produce compressive stresses $\sigma_x + d\sigma_x$ acting on the face of the section of height $h+dh$ and compressive stresses σ_x acting on the face of height *h*.

The equilibrium of the horizontal forces acting on section *dx* may be expressed as:

$$(\sigma_x + d\sigma_x)(h + dh) \pm 2\mu\sigma_y\, dx - 2\sigma_y\, tan\theta dx - \sigma_x\, h = 0 \qquad 2.33$$

$$Or \quad 2\sigma_y\, (tan\theta \pm \mu)dx = d(h\sigma_x) \qquad 2.34$$

where the (-) sign corresponds to the sections *dx* located between the entry and neutral planes and sign (+) corresponds to the sections *dx* located between the neutral and exit planes.

Since, $tan\theta = \frac{1}{2}\frac{dh}{dx}$, then

$$\sigma_y \frac{dh}{dx} \pm 2\mu\sigma_y = \frac{d[h\sigma_y]}{dx} \qquad 2.35$$

Ginzburg [111] analysed it as the theory of homogeneous deformation using the yield criterion for plane strain, $\sigma_y - \sigma_x = 2\tau_y$, and $P = \sigma_y$ as

$$P\, \frac{dh}{dx} \pm 2\mu P = \frac{d[h(P-2\tau_y)]}{dx} \qquad 2.36$$

However, these type of models have a lot of limitations because they are based on the inaccurate assumption that a plane vertical section of the rolled material remains plane

during rolling. However, this contradicts the facts obtained from numerous experiments and FEM simulations. Another limitation of the theories of homogeneous deformation arises from the assumptions that the yield stress of the material and the coefficient of friction remain constant. Further, the homogeneous theories of rolling give a simplistic description of the deformation zone that can be improved if such factors as roll flattening and elastic recovery of the rolled strip are taken into consideration. These models have been improved afterwards by implementing more assumptions. The development assumptions include nature of frictional forces and contact between roll and specimen to include for example deformable-rigid contact, deformable-deformable contact and, stick, shear and sliding friction [115, 116].

2.10.2 Plane Strain Model

The 2-D plane strain of rolling models is designed to predict the main flat rolling parameters, namely, the rolling loads, temperature and velocity fields, the overall geometric changes of deformed specimen, and the metal flow under different temperatures, as well as the optimum conditions for the flat rolling process. The process can be modelled as a two-dimensional or a three-dimensional problem. Both have their advantages and trade-offs. The 3-D model is more accurate in its description of the process because it takes into account the spread (deformation in the direction of the thickness) that the specimen undergoes. This important factor is ignored by the 2-D plane strain models where $\varepsilon_z = 0$. The 3-D method is however more computationally expensive as the number of elements is increased. One of the most efficient approaches to the simulation of the flat rolling process is the plane-strain method.

The thermo-mechanical interactions such as transient heat transfer & dynamic mechanical during rolling process can be modelled as a coupled thermo-mechanical transient dynamic problem

There are three assumptions to model the plane-strain flat-rolling:

1. **Deformable-Rigid coupled analysis:** where the slab is modelled as a deformable body and the rolls as rigid.
2. **Deformable-Rigid with heat transfer coupled analysis:** where the slab is again modelled as a deformable body, but the rolls are modelled as a rigid body with heat transfer (this approach utilizes a special kind of element)
3. **Deformable-Deformable Coupled analysis:** where both the steel strip and the rolls are modelled as deformable bodies.

The cold rolling model uses the work hardening material model that is implemented using the elastic-plastic material formulation. However, hot rolling model uses rigid-visco-plastic flow formulation so no hardening is necessary.

2.10.2.1 Elastic-Plastic Flow Model

The elastic-plastic or elasto-plastic solid formulation is more realistic than the rigid-plastic approximation, as it takes into account the elastic contribution to the total strain rate

$$\dot{\varepsilon} = \dot{\varepsilon}^e + \dot{\varepsilon}^p \qquad 2.37$$

This approach is necessary when analysing processes in which the elastic effects play significant role. Similar to the cold rolling process, the strip enters the roll gap and deformed elastically first. As the strip proceeds through the roll gap plastic flow occurs until finally at the exit the roll pressure is removed. The strip is, at that time, unloaded and it returns through an elastic state to the original load free condition. The elasto-plastic approach is also necessary for processes where residual stresses are existent.

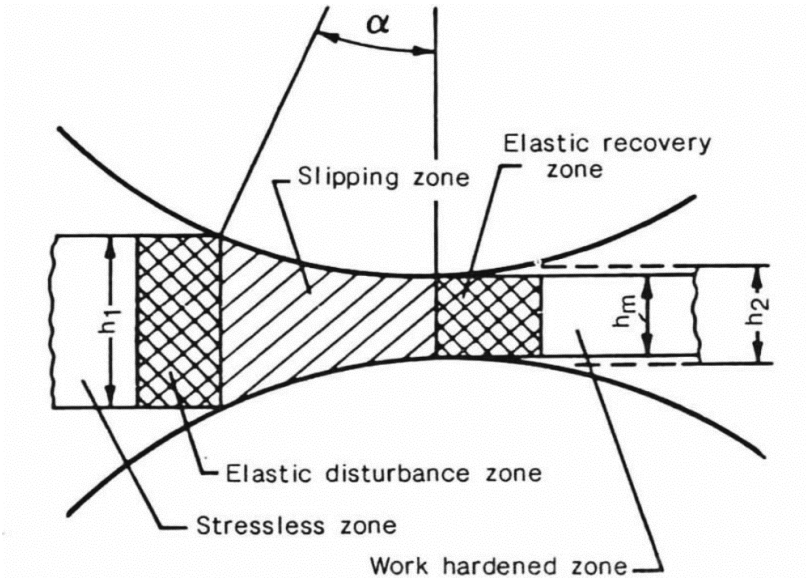

Figure 2.35: Schematic Illustration of the strip elastic recovery [111].

The finite element method for metal forming problems are based on the use of the Prandtl-Reuss equations for elastic-plastic materials [111]. The formulation is given in the rate form and assumes the infinitesimal theory of deformation

$$\dot{\varepsilon}_{ij}^p = \dot{\lambda}_{ij} \qquad 2.38$$

$$\dot{\lambda}_{ij} = \frac{1}{\tau_Y}\sqrt{\dot{\varepsilon}_{ij}\,\dot{\varepsilon}_{ij}} \qquad 2.39$$

where $\dot{\lambda}$ is flow rule nonnegative factor of proportionality.

2.10.2.2 Visco-Plastic Flow Model

The experimental tests show that the deformed metals exhibit temperature, strain and strain rate sensitivity. A material behaviour that exhibits rate sensitivity is called visco-plastic [117].

There are several materials that prone visco-plastic behaviour such as most of metals at high temperature. When there is large deformation, most of materials are considered to be rigid-visco-plastic which is the case of the hot rolling process.

In cold rolling processes, the strain is the major factor affecting the yield stress, while the influence of the other two parameters is negligible. Thus, an elastic-plastic description of the material's resistance to deformation is the most suitable for these processes. The yield stress σ_Y in the Levy-Mises flow rule is given in the form of a strain-hardening curve.

In hot rolling processes, metals are also sensitive to changes of temperature and strain rate, and the influence of these parameters is often much stronger than the influence of strain. The behaviour of these materials is well described by rigid-plastic flow and also by the visco-plastic flow rule, which is expressed by a visco-plastic potential [107].

Since the hot rolling models are rigid-visco-plastic and assume negligible elastic response during the deforming. The flow formulation of the finite element method for metal forming processes is based on the Levy-Misses plasticity model for rigid-plastic materials, which assumes that work hardening is negligible, and is given by

$$\dot{\varepsilon}_{ij} = \dot{\lambda}\frac{\partial f(\sigma_{ij})}{\partial \sigma_{ij}} = \frac{3}{2}\frac{\dot{\bar{\varepsilon}}}{\bar{\sigma}}S_{ij} \qquad 2.40$$

$$\dot{\lambda} = \frac{3}{2}\frac{\dot{\bar{\varepsilon}}}{\bar{\sigma}} \qquad 2.41$$

$$\dot{\bar{\varepsilon}} = \sqrt{\frac{2}{3}\dot{\varepsilon}_{ij}\,\dot{\varepsilon}_{ij}} \qquad 2.42$$

$$\bar{\sigma} = \sqrt{\frac{2}{3}S_{ij}\,S_{ij}} \qquad 2.43$$

For both the hot and cold rolling models, the von Misses yield are usually used when building and analysing Finite Element Models.

2.10.3 High Temperature Model for Steel Rolling

Shida's model for behaviour of carbon steels at high temperature using a cam-plasto-meter was reported by Pietrzik & Lenard [108]. Shida [118] tested about 200 low, medium and high carbon steels and developed a comprehensive set of empirical equations, which describe the metal resistance to deformation as a function of the temperature, strain rate, strain, and the carbon content. The equations also take into account the behaviour of the steels in the austenitic, ferritic and in the two-phase regions.

Shida's model is given by the relations:

$$\sigma = \sigma_f f \left(\frac{\dot{\varepsilon}}{10}\right)^m \left(\frac{kg}{mm^2}\right) \qquad 2.44$$

Where for

1. $\bar{T} \geq 0.95\frac{C+0.41}{C+0.32} \quad \Rightarrow \quad \sigma_f = 0.28e^{\left(\frac{5}{\bar{T}}\left(\frac{0.01}{C+0.05}\right)\right)}$,

$$m = (-0.019C + 0.126)\bar{T} + (0.075C - 0.05)$$

2. $\bar{T} \leq 0.95\frac{C+0.41}{C+0.32} \quad \Rightarrow \quad \sigma_f = 0.28q(C,\bar{T})e^{\left(\frac{C+0.32}{0.19(C+0.41)} - \frac{0.01}{C+0.05}\right)}$,

$q(C,\bar{T}) = 30(C+0.9)\left[\bar{T} - 0.95\left(\frac{C+0.49}{C+0.42}\right)\right]^2 + \frac{C+0.06}{C+0.09}$, $m = (0.018C - 0.154)\bar{T} - 0.019C + 0.207 + \left(\frac{0.027}{C+0.32}\right)$

Where

$f = 1.3(5\varepsilon)^n - 1.5\varepsilon$

$n = 0.41 - 0.07C$

$\bar{T} = \frac{T + 273}{1000}$

T= temperature in °C, 700<T<1200

C= carbon weight percent, C<1.2%

$\dot{\varepsilon}$= strain rate, 0.1< $\dot{\varepsilon}$<100 s^{-1}

ε= strain < 70%

All constitutive equations that are dependent on the temperature are part of what is known as temperature dependent plasticity. As seen in Figure 2.36, as the temperature increases, the stress-strain curve becomes more relaxed, i.e. the slope of the elastic and plastic part decreases.

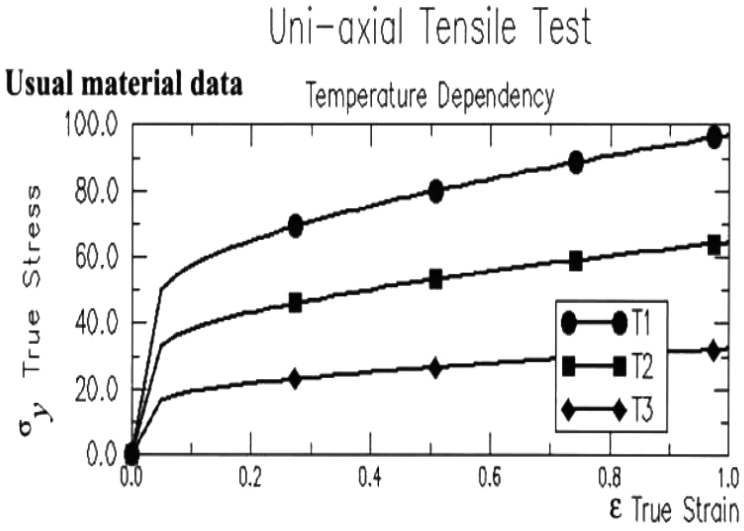

Figure 2.36: Temperature Dependent Stress-Strain Diagrams (T3>T2>T1) [115].

The above behaviour is perfectly captured by Shida's model for high temperature steel. The graphical representation of this equation is obtained by plotting the flow stress versus the strain, the strain rate and the temperature for the following ranges for each of the three independent variables:

$$0 \leq \varepsilon \leq 1, \qquad 1 \leq \varepsilon \leq 50\dot{} \ (s^{-1}) \qquad \text{and} \qquad 700 \leq T \leq 1200$$

This model is particularly convenient for the hot rolling process where as the specimen deforms, the strain, strain rate, and temperature all change simultaneously.

2.11 FE Models for Rolling Simulations

Many models have been proposed for simulation of hot rolling based on the finite element method. FEM has been widely developed of rolling processes to predict different physical phenomena such as metal flow occurring in the strip during cold and hot rolling together with its thermo-metallurgical evolution and the thermal. FEM allows calculations and observations of stress strains, strain rates, metal flow and thermal characteristics through the cross section using two-dimensional or three-dimensional rolling simulation, either steady or non-steady-state [119-126].

2.11.1 Simulations of Rolling Process

During hot rolling, numerous thermal and mechanical interactions between the strip as it contacts the rolls. Prediction of the detailed thermal behaviour of the strip has been of great interest of many researchers for a variety of reasons. The metal flow is influenced by the temperature and stress, distribution in the specimen, since the flow stress is strongly dependent on temperature. The temperature distribution in the specimen is affected by heat generation due to plastic deformation and interface friction and also by the velocity field in the specimen, resulting in a strong correlation between the mechanical and thermal phenomena in the specimen.

Chen *et al.* [127] and Tseng and Wang [128] developed the two-dimensional finite difference method (FDM) to predict the temperature profiles in the specimen and the roll and the two-dimensional FEM to predict the mechanical behaviour in the specimen. Pietrzyk and Lenard [107] applied the two-dimensional FEM to analyse the thermo-mechanical behaviour of the specimen and the thermal behaviour of a contact area of the roll. Grober [119] showed the FEM predictions of strain on the cross-sectional side. The predicted strains were not uniform for reductions greater than 20% and the non-uniformity increased with increasing reduction. Micari [120] was performed a three dimensional analysis on hot steel rolling of the head of specimen. The total strain was predicted on the lateral side and on the top side but not through the cross section. This was done for two assumptions: an initial *w/h* ratio of 2 and a reduction in height of 18%, and an initial *w/h* ratio of 5 and a reduction in height of 27%. The analysis showed that the largest total strain was occurring at the corner of the specimen at the head for both simulations. The strain at the corner was reported to be 1.1 compared to 0.9 for the centre of the top surface and 0.2 for the centre of the lateral surface as illustrated in Figure 2.37. Zhou [126] developed a FEM simulation model for hot rolling of steel strips integrating different phenomena such as the mechanics and the heat transport in the strip and the roll, and the metallurgical behaviour of the strip. The inhomogeneity of strain rate and strain across the strip thickness were demonstrated as shown in Figure 2.38 (a) and (b) respectively.

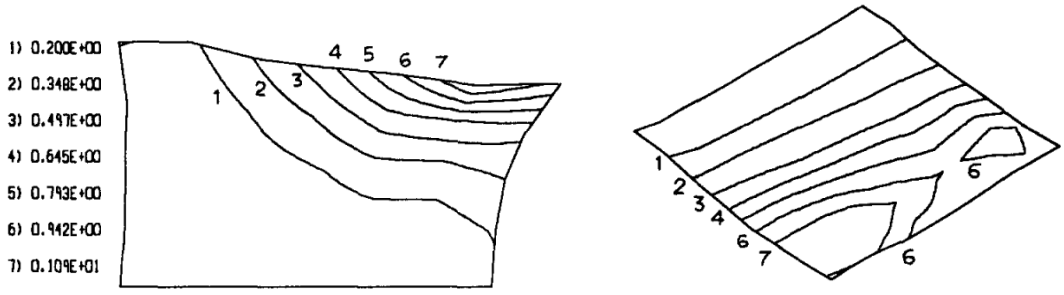

Figure 2.37: Plastic strains on the lateral and on half of the upper surface of the specimen [120].

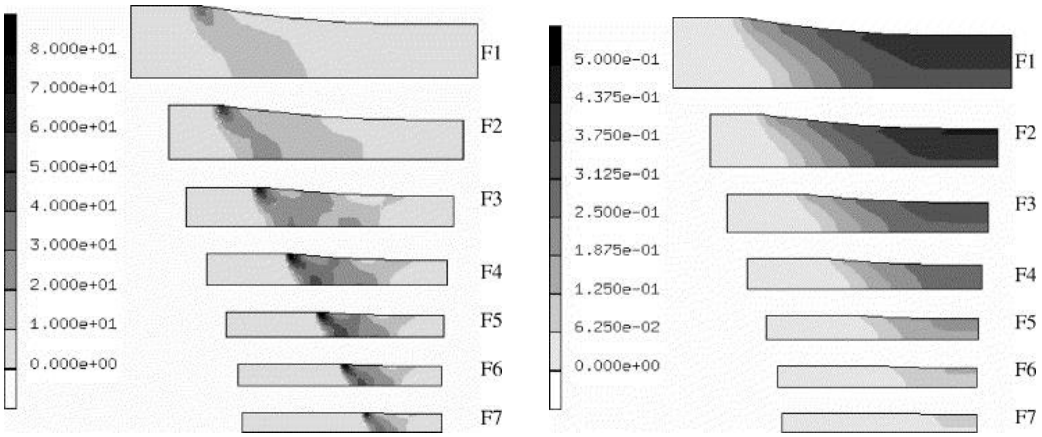

Figure 2.38: (a) Effective strain rate (1/s) (b) Effective strain at different reductions [126].

2.11.2 Modelling of Microstructures Behaviour

Microstructural behaviour and evolution of various carbon steels during hot rolling and their effects on materials flow, have been studied in order provide fundamental information to optimise conditions of hot rolling processes for better products quality. The microstructural evolution under hot deformations generally involves strain hardening, recovery, re-crystallisation and grain evolution, all of which are highly temperature and deformation rate-dependent.

A number of mathematical models, which are adopted to predict microstructural and mechanical properties of steel products during hot rolling, have been developed in the past decade. The models either concentrate on separate dynamic and static re-crystallisation [129], stress–strain relationships coupled with dynamic re-crystallization [130, 131], or low deformation rate at high temperature [132]. Liu [133] developed a visco-plastic model based on experimental data to predict the evolution of dislocation density, re-crystallisation and grain size, and their effects on visco-plastic flow of a C–Mn steel.

However, efforts have been spent investigating the various aspects and deformation behaviour at macroscopic level. Since the macroscopic mechanical behaviours of inhomogeneous materials including steel significantly depend on the microstructures, modelling of steel behaviour during deformation needs to be accomplished on the microstructure level to understand local deformation mechanisms [134, 135]. Choi *et al.* developed a FEM to study the ultimate ductility and failure modes of TRIP steel under different loading conditions. Paul [136] employed a micromechanics based approach to predict the flow behaviour, plastic strain localization and plastic instability of DP steels. Sun *et al.* [135] and [137] predicted ductile failure of DP steels in the form of plastic strain localization resulting from the incompatible deformation between the harder martensite phase and the softer ferrite matrix. Uthaisangsuk *et al.* [138] used the Gurson–Tvergaard–Needleman (GTN) model with two void nucleation mechanisms, in ferrite to capture ductile damage and cohesive zone model in ferrite–martensite interface to capture decohesion of interface. Nygårds [139] modelled two-phase ferritic/pearlitic steels using a finite element two-dimensional micromechanical model based on the stress–strain curves of the pure phases. The model evaluated local stresses and strains and the plastic behaviour by applying uniaxial tension tests on pure ferrite and pearlite specimens, as well as on materials containing 25 and 58% pearlite. The FEM has also been widely used for analysing of rolling of inhomogeneous internal structures of steel by mean of inclusions in steel matrix. Luo and Ståhlberg [140] and [141] developed a rigid-visco-plastic 2D FE Model, and obtained the shape along rolling direction of the oxidized inclusions and the MnS inclusions in flat rolling process at different rolling conditions. Melander [142] simulated the behaviour of short cracks between the inclusions and the matrix under rolling contact fatigue load was by and investigated the effects of the inclusion shape on the behaviour of cracks. Hwang and Chen [143] simulated the void generation and development around the inclusion which was assumed to be rigid, and found out that the void length in front of inclusion was larger than that in rear of inclusion under different rolling conditions. Yu *et al.* [144] used a FE model with a transition layer between the inclusion and the strip matrix was established for analysing the inclusion deformation and the crack generation. Yu *et al.* [145] developed a 2D FEM model to predict and analyse behaviour the deformation of inclusion during multi-pass cold rolling. The strain distribution was

calculated during cold rolling between various sizes and type of inclusions (soft and hard) and steel matrix using a 3D FEM by Yu *et al.* [146].

Although, FEMs coupled with other simulation techniques have been also effectively used for better understanding of dendritic structures formation and growth during solidification[36, 42, 147], FEM have not been used study the behaviour of dendritic structures and inter-dendritic segregations of steel during hot rolling.

Chapter 3. Behaviour of Dendritic Structures during Hot-rolling of Medium-Carbon Steel

3.1 Introduction

During the continuous casting of steel, the main solidification structures that form are primary dendrite arms, secondary dendrite arms, and areas of inter-dendritic segregation (micro-segregation). These three features, or dendritic structures, strongly control the formation of micro-chemical banding during subsequent hot-rolling which leads to formation of microstructural banding upon subsequent heat treatment processes.

These microstructural developments were analysed by optical, SEM and EPMA analyses. EPMA was used to detect and quantify quantification segregation of alloying elements, mainly manganese, silicon, phosphorus and sulphur [148-150]

A series of hot-rolling tests were conducted on as-cast medium-carbon steel to study the behaviour of dendritic structures, including micro-segregation during hot-rolling. The changes of the dendritic structures subjected to different amounts of full and partial deformation at 25%, 50%, 75% and 90% reduction using lab rolling mill, were analysed using optical microscopy with picric acid etchant and EPMA. Macro and microscopic behaviour of dendritic and inter-dendritic structures and mechanisms leading to micro-chemical banding, the main source of micro-chemical banding, during hot-rolling were observed. The effects of deformation and reheating prior hot-rolling on the concentration of alloying elements contained in dendritic structures were examined. In addition, the variation in chemical compositions of the dendritic and inter-dendritic regions was also assessed.

3.2 Experimental Work

Table 3.1 shows the composition of the steel used in the experimental work. This medium-carbon steel was continuously cast in conventional casting machine and has relatively high manganese content with very low contents of other alloying elements. Manganese in this steel increases the strength and hardness, which renders it suitable for case hardening. and it is used for parts which require a hard wear-resistant surface and a soft core, for example, small shafts, plungers, and lightly loaded gears in a wide range of industries such as the , agricultural and automotive industries [151]. This steel was selected in this study specifically because of its tendency to form a severe degree of micro-structural banding following subsequent hot-rolling and heat treatment.

Table 3.1: Steel composition used in this study (Concentrations are given in percentage by mass).

%C	%Mn	%S	%P	%Si
0.316	1.27	0.0073	0.0078	0.01

3.2.1 Sample preparation

Blocks, 100×80×70 mm, were initially cut from 220-mm-thick continuously-cast slab as in order to include the chill and columnar zones and avoid centreline region of the slab as shown in Figure 3.1. For as-cast metallographic examination, samples 10×10×10 mm in size were cut from the top surface of the block to the bottom as follows: One set of samples were cut every 10 mm in transverse direction perpendicular to the casting direction and another set were cut every 5 mm parallel to the casting direction.

For hot-rolling experiments, samples of 70×10×15 mm with inclined head were cut from the bottom region of the block as shown in Figure 3.1. The bottom region of the block was selected for the rolling tests because the dendritic structures in this region are coarse and well-oriented in a direction perpendicular to the rolling direction. The samples were then cut after rolling, tested along rolling direction and prepared for metallographic analysis.

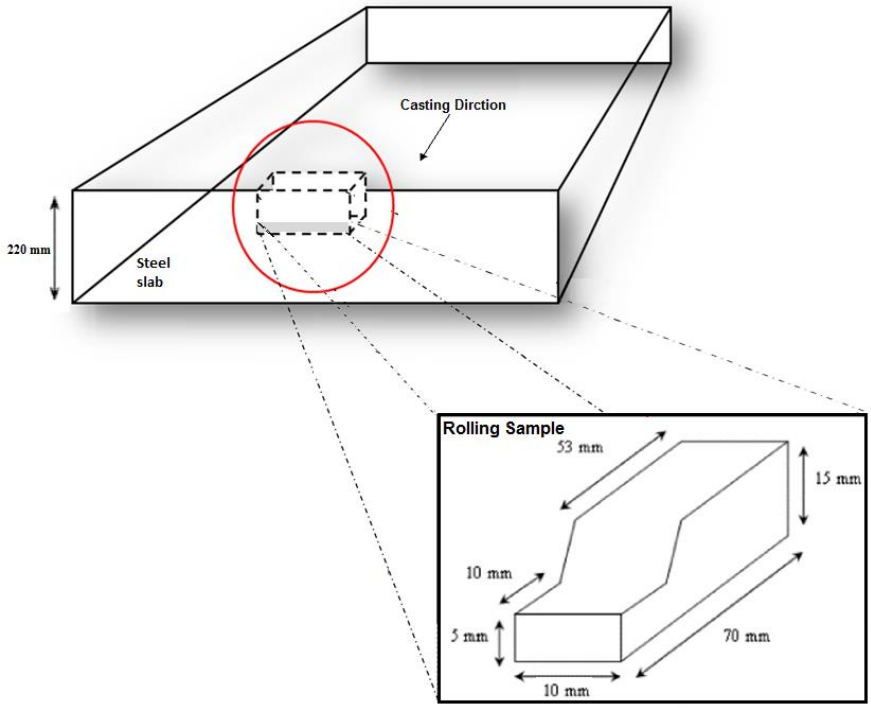

Figure 3.1: Preparation of samples from plant slab to lab hot-rolling.

3.2.2 Hot Deformation Test

Hot-deformation tests were performed on a laboratory-scale rolling mill (Hille Mill). The mill can be used to carry out single-pass forward-forward or forward-reverse, rolling. The mill has a three-phase 7.5 hp (5592.75 Watts) induction motor for the main drive, reduction gears for roll speed adjustment (between 5-30 rpm from the feed motor speed of 1400 rpm) and two rolls with a diameter of 55mm. The maximum torque of the Hille mill is 1700 Nm and the maximum load of 250 kN. The roll gap is adjusted by a 0.5 hp (372.85 Watts) motor via a worm-wheel screw down mechanism linked to the top roll.

Samples of as-cast medium-carbon steel from the bottom region of the columnar zone (near the centre of the slab – see Figure 3.1) which have coarse, stable and well-oriented dendrites, were heated to 1100°C in a tube furnace and held for 30 minutes with injection of argon. Two types of test were then performed in single-pass forward rolling: full deformation and partial deformation as shown in Figure 3.2 of the specimen shown in Figure 3.1. The thermal and mechanical treatments used simulated the actual industrial rolling process.

The full deformation tests were conducted as follows: the samples were soaked at a temperature of 1100°C and then subjected to four different single-pass forward rolling reductions of 25%, 50%, 75% and 90%. The samples were then cooled in air.

Deformed samples were cut in half along the rolling direction and prepared for metallographic examination. In the partial deformation test, the samples were also soaked at a temperature of 1100°C and subjected to a single-pass forward rolling reduction of 90%. Half-way through the rolls, the rolling experiment was terminated, the upper roll raised and the half-rolled specimen air cooled. Deformed samples were then cut in half along the rolling direction and samples were prepared for metallographic examination.

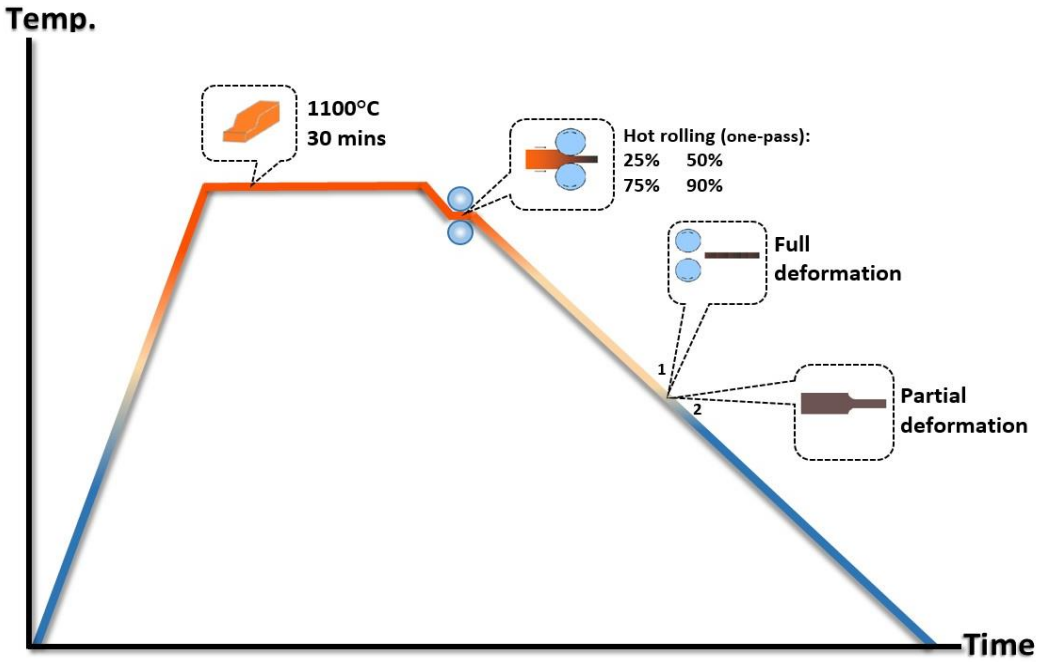

Figure 3.2: Thermal cycle of hot-rolling test.

3.2.3 Metallography

In order to track dendritic structures and their behaviour during hot-rolling, metallographic examinations were carried out on the as-cast and as-rolled samples. Optical microscopy was conducted following an picric acid etch to reveal micro-segregation of alloying elements as proposed by Samuels [8]. The dendritic structures of as-cast and as-rolled medium-carbon steel specimens were revealed by a reagent consisting of 80 ml of saturated aqueous picric acid, in addition to few drops of HCl and drops of teepol. Specimens were immersed into this solution at 68°C, whereupon the surface was covered by a black surface layer. Depending on the conditions of each sample, the duration of etching ranged between 5 and 10min. Then, cross-sectional areas of the tested samples were examined using optical microscopy. Tens and sometime hundreds, depending on the area of investigation, of digital photographs were taken for each prepared cross-sectional area using Leica Camera at magnification

of 50 times. The micrographs were then stitched together in order to provide a full picture of the entire specimen. The same metallographic procedure was used for samples after rolling in order to reveal changes in dendritic structures after different deformations applied on the investigated materials.

3.2.4 Dendrite Arm Spacing

Dendrite arm spacing and especially secondary dendrite arm spacing has been linked to the mechanical properties of most cast alloys as shown by Campbell [152], Totten [153] and Flemings [37]. For this reason, dendrite arm spacings were measured in this study.

The as-cast and as-rolled specimens etched with a picric acid and examined under the microscope, were used for the measurement of primary as well as the secondary dendrite arm spacings. Samples were sectioned from the slab section at intervals of 5 to 10 mm from the surface to the quarter thickness in the direction towards the centre of slab. Samples were collected from all identical locations of slab cross-sections to study the variation of dendrite arm spacing across all faces. The dendrite arm spacing was measured by image analysing software developed by Griesser [154] . On average, 30 measurements at magnifications of 32 and 50 times were recorded at each location and the average dendrite arm spacing is reported. Primary dendrite arm spacing was measured on the faces of specimens sliced in the transverse section, parallel to the casting direction, of the as-cast samples. At each location, an average of 30 measurements was used as the value of primary dendrite arm spacing. Secondary dendrite arm spacing was measured by averaging the distance between adjacent side branches in the longitudinal section of a primary arm. 30 values of λ_2 were measured on average for each selected position. The same procedures were used to measure secondary dendrite arm spacing following hot-rolling of the samples.

3.2.5 Electron Probe Micro-Analysing

Qualitative and quantitative mass analyses using EPMA were carried out on the dendritic and inter-dendritic regions of as-cast sample collected from near centreline region where dendritic structures are well-oriented and formed almost in stable and uniform shape. The same analyses were also carried out on the and as-rolled specimens after applying hot-deformation. In order to investigate the variation in alloying element concentrations between dendritic and inter-dendritic regions of as-cast, parallel line-

scans across each region were performed. The analyses were carried out using A JEOL JXA-8500F HYPERPROBE with a SCHOTTKY field emission source and a CAMECA SX-50 EPMA instrument. The EPMA used is a fully automated instrument employing four wavelength dispersive spectrometers (WDS) and one silicon drift detector energy dispersive x-ray (SDD-EDS) analyser for the detection and non-destructive analysis of most elements ($Z \geq 4$) in the periodic table. Quantitative analysis was carried out on the bulk matrix and areas of micro-segregation. X-ray elemental line scans are carried out across areas of dendritic and inter-dendritic. Colour-gradient quantitative WDS elemental distribution maps, mainly manganese and carbon were generated and SE and BSE images captured of the dendritic and inter-dendritic regions. Table 3.2 shows basic quantitative and qualitative settings and conditions for the EPMA. The instrument is equipped with a liquid nitrogen trap to reduce contamination during light element analysis. This study was performed using the JEOL JXA-8500F Field-Emission SEM-EPMA HYPERPROBE (WDS & SDD-EDS) at UNSW. Prior to performing EPMA analysis, all specimens were cut, ground, and polished using standard metallographic techniques.

Table 3.2: Conditions and Basic Settings for the Microprobe

Measurements	Quantitative point analysis conditions	Qualitative point analysis conditions
Analysed elements	Manganese (Mn)	Carbon (C) , Manganese (Mn)
Analysing crystal material	Lithium fluoride	Lithium fluoride
Acceleration voltage	20 kV	20 kV
Electron beam current	$1.5e^{-7}$A	$1.5e^{-7}$A
Pre-set value for the probe diameter	0 (focused)	0 (focused)
Dwell time per measurement point	20 ms	20 ms
Number of measured points	60 to 100	675*675 and 500*900
Intervals	5 µm	X: 4 µm; Y:4 µm and X:3µm; Y: 3µm

3.2.6 Simulation of micro-structural segregation

Simulation of micro-structural segregation was conducted using DICTRA software to investigate variations after reheating prior to hot-rolling. DICTRA simulations are based on multicomponent diffusion assuming finite interface mobility and using thermodynamic data [155-158].

For the purposes of simulation, a steel containing only 0.3 wt. % carbon and 1.2 wt. % manganese was used. The simulations were performed using the thermodynamic database TCFE6 and mobility database MOB2. The cell size used in the simulation was the approximate primary dendrite arm spacing measured from as-cast specimens, i.e., 100 μm.

3.3 Result and Discussion

The evolution of dendritic structures through deformation was studied for the steel composition selected for this work, which eventually develop micro-chemical banding. The characteristics and behaviour of the dendritic structures during a series of hot-rolling experiments were examined. In addition, the change of chemical composition during deformation as well as reheating prior hot-rolling was investigated experimentally and simulated.

3.3.1 As-Cast Structures

In order to study the behavioural changes of dendritic structures during hot-rolling, the morphology of as-cast structures of the steels was initially observed. This includes the quantitative measurement of the primary and secondary dendrites arm spacing of the as-cast structures.

3.3.1.1 Metallography of As-Cast Structures

The characteristic solidification structures observed through the thickness of the slabs is presented in Figure 3.3. The transition from fine zone (chill zone at the top surface) to the columnar zone in as-cast structures occurs during solidification within a few millimetres from the surface. The columnar zone then extends towards the centre of slab. In the centre region, an equi-axed structure forms. These observations of the dendritic structures are very similar to those reported in the literature for similar steels [37, 159, 160]. It is clear from Figure 3.3 that the dendritic structures have different profiles and orientations across the slab thickness. The dendrites at the surface are very fine and randomly-oriented in almost all directions. The primary as well as secondary arm spacing are very fine as shown in Figure 3.3 (a). The dendrites that formed at the quarter thickness of the slab are coarser and the orientations are more aligned. The dendrites that formed near the centreline of the slab are very coarse and are well-aligned. These findings are in agreement with earlier reports in the literature that the formation, orientation and length of the dendritic structures are related to early solidification events [37, 161].

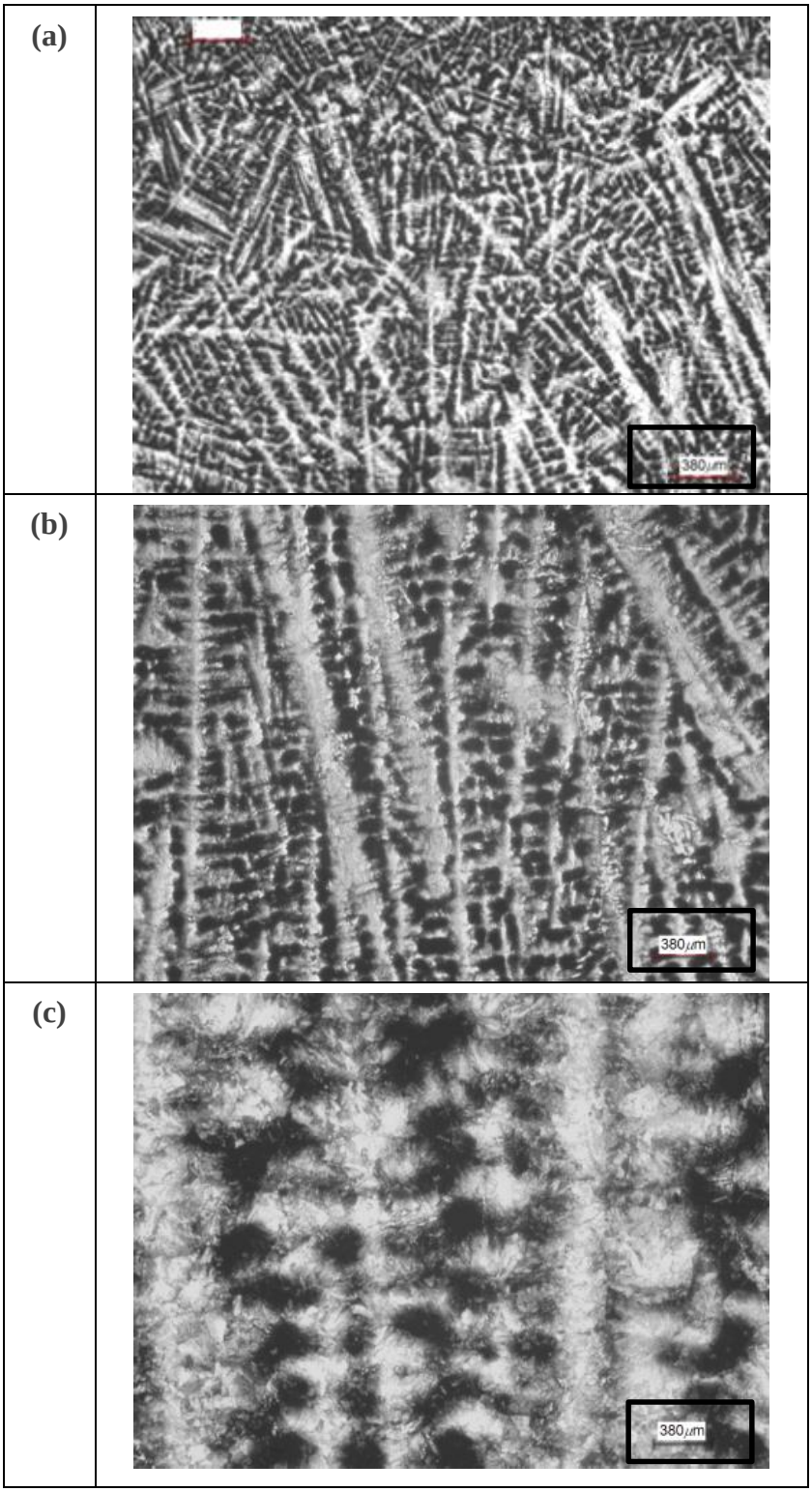

Figure 3.3: Dendritic structures of medium carbon steels through the slab thickness (a) surface, (b) quarter thickness and (c) deep quarter thickness near-centre).

3.3.1.2 Secondary Dendrite Arm Spacing

The as-cast structure and measurement of secondary dendrite arm spacing are presented in Figure 3.4. Figure 3.5 shows presents the typical variation of the experimentally-measured values of the average secondary dendrite arm spacing from the surface of the steel slab to the lower area of quarter thickness. It is evident that the secondary dendrite arm spacing increases from surface to near-centre in the examined medium-carbon steel. The secondary dendrite arm spacing varies from 27 μm in the rear-surface area 160 μm at a distance 160 mm below the surface, in agreement with the findings of PreßLinger *et al.* [50, 162]. This information is particularly relevant to the present investigation because several authors have emphasised the important relationship between secondary dendrite arm spacing and banding in medium-carbon steel [37, 152, 153] and [20]

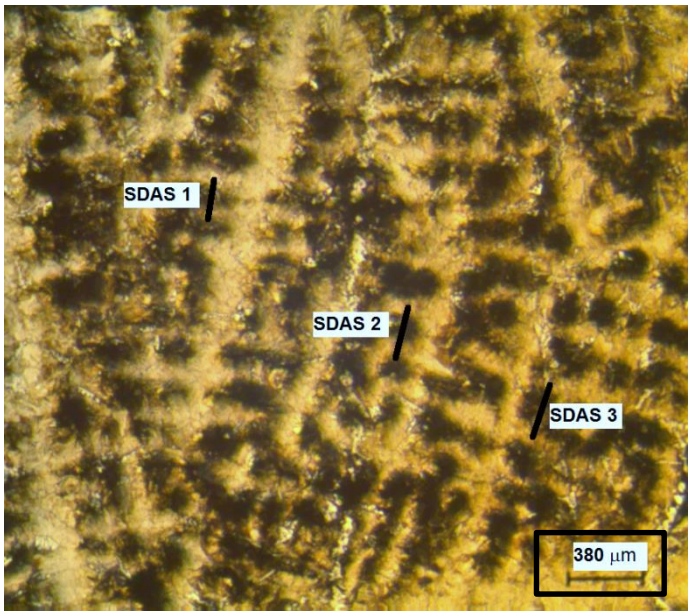

Figure 3.4: Example of secondary dendrite arm spacing measurements.

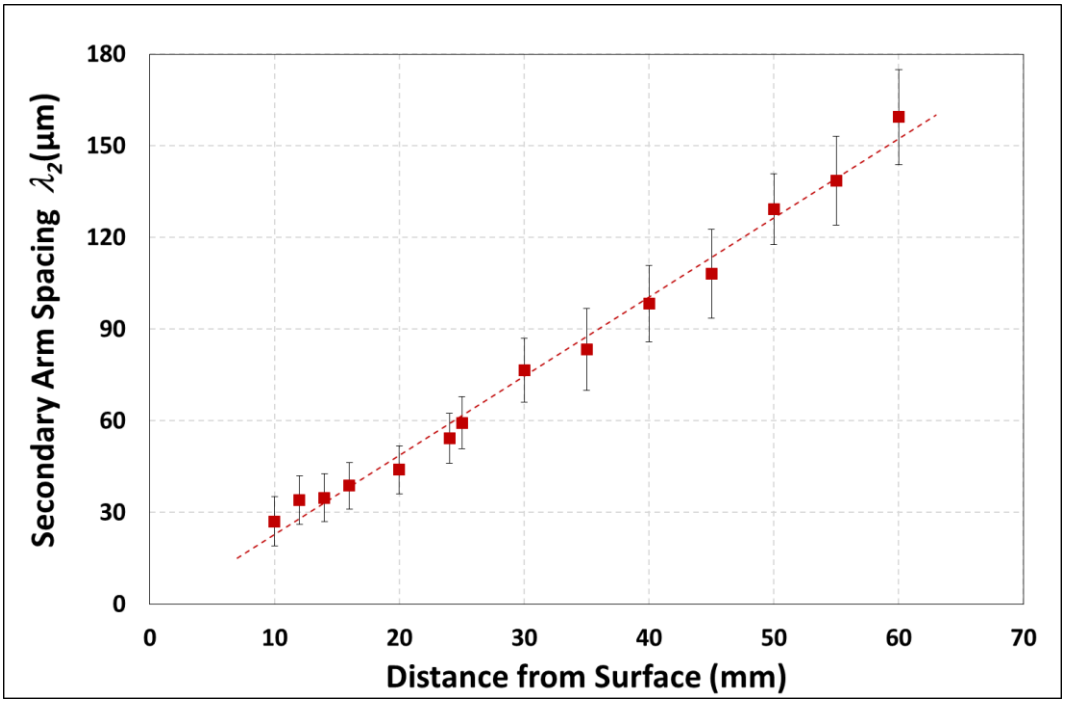

Figure 3.5: Secondary dendrite arm spacing across the slab thickness.

3.3.1.3 Primary Dendrite Arm Spacing

An example of the cast structure and schematic representation of dendrites showing measured primary dendrite arm spacing is presented in Figure 3.6. Primary dendrite arm spacing was determined on samples sliced transversely to the trunks of primary arms. The accuracy of primary dendrite spacing is higher than that of secondary dendrite arm spacing since more primary dendrite arms can be observed and more spacings can be measured. Figure 3.7 presents a typical variation of the experimentally measured values of the average primary dendrite arm spacing from the surface of the steel slab to the quarter thickness. The figure shows that the primary dendrite arm spacing increases from 80 µm in the surface region to 600 µm 60 mm below the surface. These measurements agree well with values reported in the literature [162, 163] for alloys of similar composition.

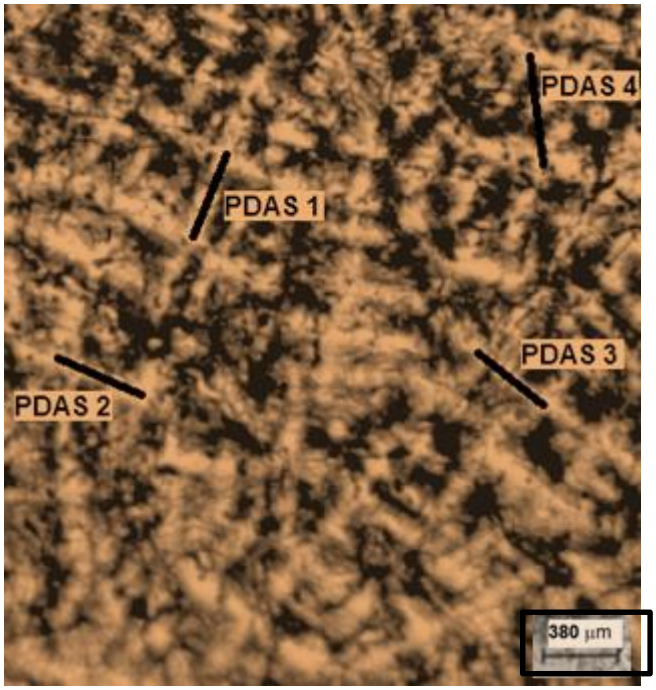

Figure 3.6: Example of primary dendrite arm spacing measurements.

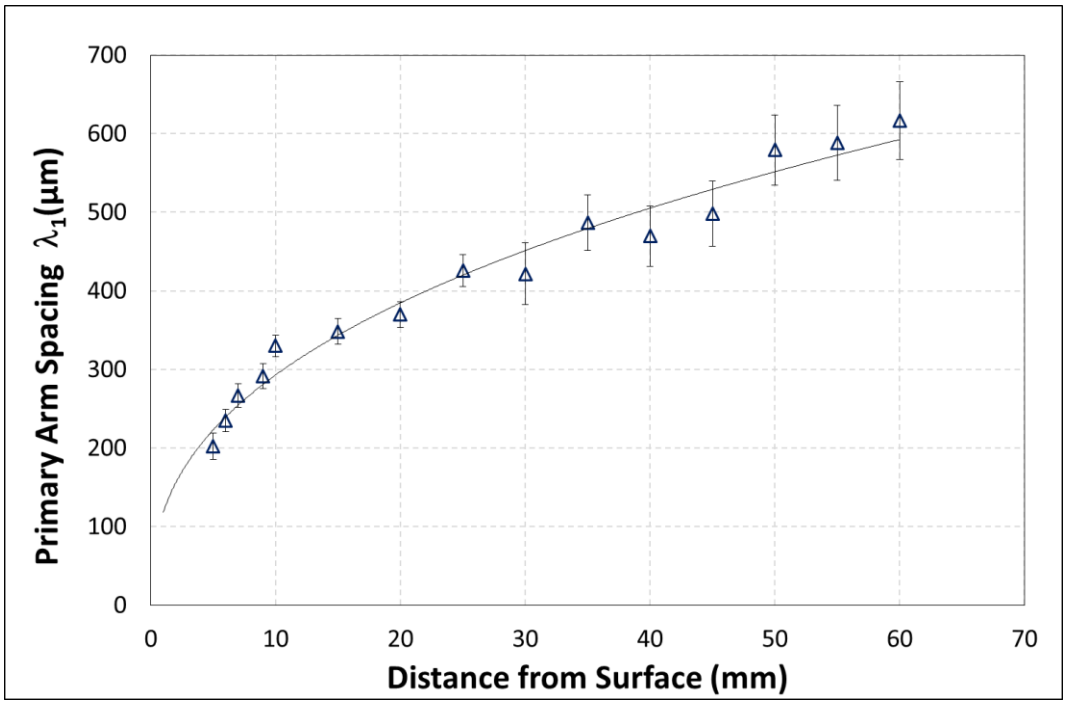

Figure 3.7: Primary dendrite arm spacing across the slab thickness.

3.4 Behaviour of Dendritic Structures during Hot-Rolling

Hot deformation was conducted on a laboratory rolling mill as described above. Samples with an average primary dendrite arm spacing of about 600 µm and a secondary dendrite arm spacing of 160 µm were cut from the bottom regain of the quarter thickness block, in order to investigate the behaviour of this dendritic structure

during hot-rolling. Samples were heated 1100°C, soaked for 30 minutes and then hot rolled at this temperature in a single pass to different reductions of 25, 50, 75 and 90%. The same rolling test conditions were used during partial hot-rolling (partial deformations) on other samples as described above. Samples from the hot-rolling experiments were then sectioned in the rolling direction and examined by metallographic techniques. More than 30 micrographs from each of the rolling reductions were stitched together in order to show full images of the changes occurring in dendrites during the full-rolling experiments. More than 200 micrographs were built together to cover the whole of the partially-rolled sample.

3.4.1 Behaviour during Full-deformation

3.4.1.1 25% Reduction

Figure 3.8 displays a macro-structural image across the width of a sample that was deformed 25%. The primary dendrite arms rotated slightly (bended) about transverse axis, perpendicular to the rolling direction while the secondary dendrite arms together with the inter-dendritic segregations (dark areas in the figure)elongated slightly parallel to the rolling direction.

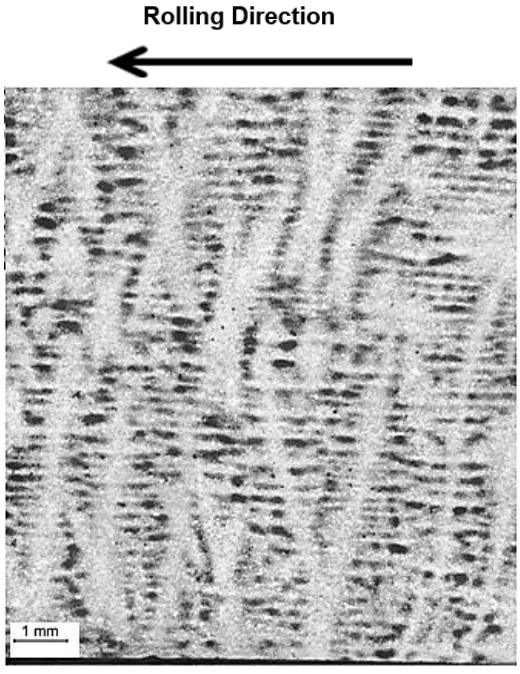

Figure 3.8: A structure image across the width of medium carbon steel sample deformed up to 25%.

3.4.1.2 50% Reduction

Figure 3.9 displays a macro-structural image across the width of a sample that was deformed 50%. The figure shows that the primary dendrite arms rotated further about transverse axis whereas the secondary dendrite arms and the adjacent inter-dendritic regions elongated further parallel to the rolling direction than similar regions in the lower reduction level.

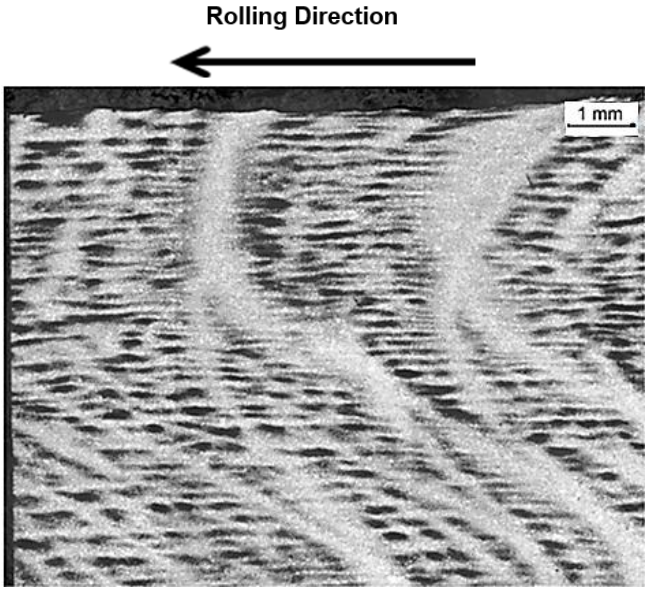

Figure 3.9: A structure image across the width of medium carbon steel sample deformed up to 50%.

3.4.1.3 75% Reduction

Figure 3.10 displays a macro-structural image across the width of a sample that was subjected to 75% reduction. The primary dendrite arms rotated extensively about the axis perpendicular to the rolling direction (transverse axis). In addition, some primary arms start to align with the rolling direction. The secondary dendrite arms and adjacent inter-dendritic regions elongate further parallel to the rolling direction and parallel to each other to form layers, rather than patches of inter-dendritic regions. Some secondary arms and their adjacent inter-dendritic regions become thinner and elongate more than others depending on their location with respect to the rotated primary arms. (For instance, secondary arms located in the middle between two rotated primary dendrite arms, elongate further due the larger distance between primary arms).

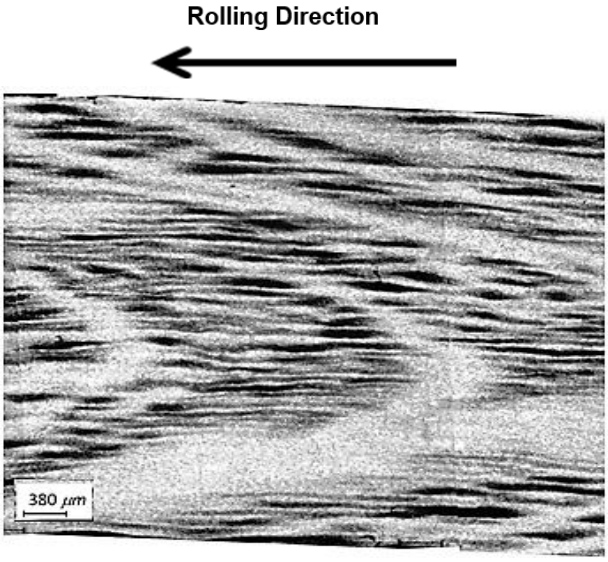

Figure 3.10: A structure image across the width of medium carbon steel sample deformed up to 75%.

Figure 3.11 shows the macro-structure across the width of a sample that was reduced 90%. Dendritic structures are absent at macro and micro scale at this level of reduction. The primary dendrite arms rotated to such a degree that they are now aligned with rolling direction. The inter-dendritic regions and secondary dendrite arms also deformed to the extent that they are fully aligned to the rolling direction. This observation is in agreement with the findings of Pressinger [55] at this level of deformation.

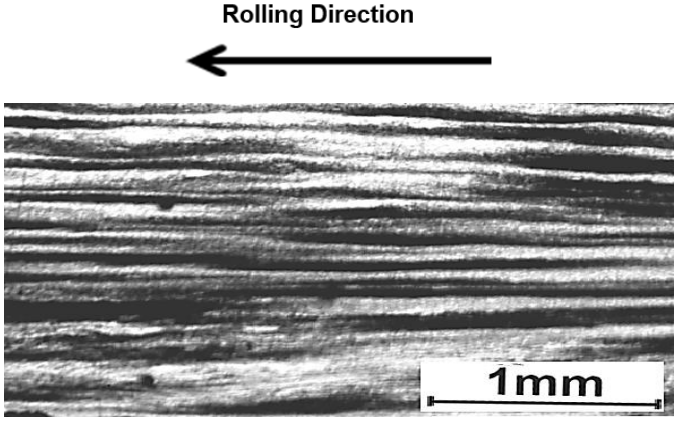

Figure 3.11: A structure image across the width of medium carbon steel sample deformed up to 90%.

In summary: dendritic structures (dendrites and inter-dendritic regions) remain distinguishable in hot-rolled medium carbon steel up to reductions of about 70%. On further reduction the dendrites (low-carbon, low alloyed regions) and the inter-

dendritic regions (high-carbon, high alloyed regions) form alternative layers (micro-chemical banding) parallel to the rolling direction.

3.4.2 Quantifying the Changes of Primary and Secondary Dendrite Arm Spacings during Hot-Rolling

The changes in the dendritic structures that occur during hot-rolling are shown in Figure 3.8 to Figure 3.11. Secondary dendrite arms elongate parallel to the rolling direction and the secondary dendrite arm spacing can be determined as a function of the extent of deformation. However, the primary dendrite arms rotate during hot-rolling and hence, it is not possible determine quantitatively the (deformed) primary dendrite arm spacing.

3.4.2.1 Secondary Dendrite Arm Spacing

Table 3.3 and Figure 3.12 display the quantitative changes occur to the secondary dendrite arm spacing during single pass hot-rolling. The secondary dendrite arm spacing decreases with deformation. A slight decrease in secondary dendrite arm spacing at small reductions is followed by a rapid decrease in secondary dendrite arm spacing after about 50% reduction.

Table 3.3: Secondary Dendrite arm spacing after hot-rolling of the samples.

Deformation Degree	25%	50%	75%	90%
Deformed λ_2(μm)	138.6 ±22.6	125.3 ±19.5	74.94 ±12.48	40.21 ±6.29

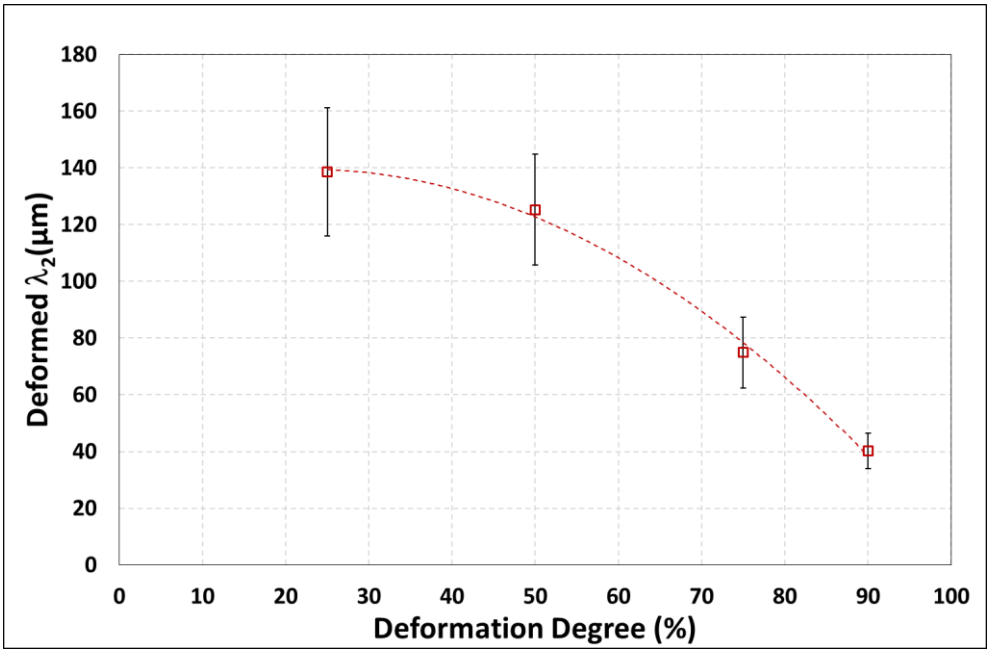

Figure 3.12: Secondary dendrite arm spacing after hot-rolling of the samples.

3.4.3 Partially-Rolled Specimen

In an attempt to better understand the rotation of dendrite arms during hot-rolling, a specimen was only partially rolled and examined metallographically as described above. A section through such a specimen is shown in Figure 3.13. It follows from the figure that the response of the dendritic structures to hot-deformation is at macro-scale, mainly related to the material flow during hot-rolling and the concomitant strain distribution. The primary dendrite arms reveal clear progressive rotation about the transverse axis from the head-end (fully-deformed) to the tail-end (non-deformed) of the sample while the secondary dendrite arms and the associated inter-dendritic regions elongate at increasing rates as a function of the extent of deformation. At the tail-end of the partially-rolled sample, from no reduction to about 30% reduction, little changes occur on the dendritic structures except for a slight rotation of the primary dendrite arms and a slight elongation of the secondary dendrites and associated solute-rich regions. In the mid-way region, from a reduction of about 30% to 66%, significant rotation of primary arms occurs – to an extent of more than 45 degrees about the transverse axis. At the same time, secondary dendrite arms and their adjacent and associated inter-dendritic regions, located between the rotating primary arms, elongate parallel to the rolling direction (roll circumferences). At the head-end of the sample where the reduction is more than 80%, the dendritic structures are not discernible any longer and are replaced by alternating layers of regions (dark) that are solute rich and

regions (white) of low solute content, aligned parallel to the rolling direction. These regions are evidently related to the micro-chemical bands that are observed at micro-scale.

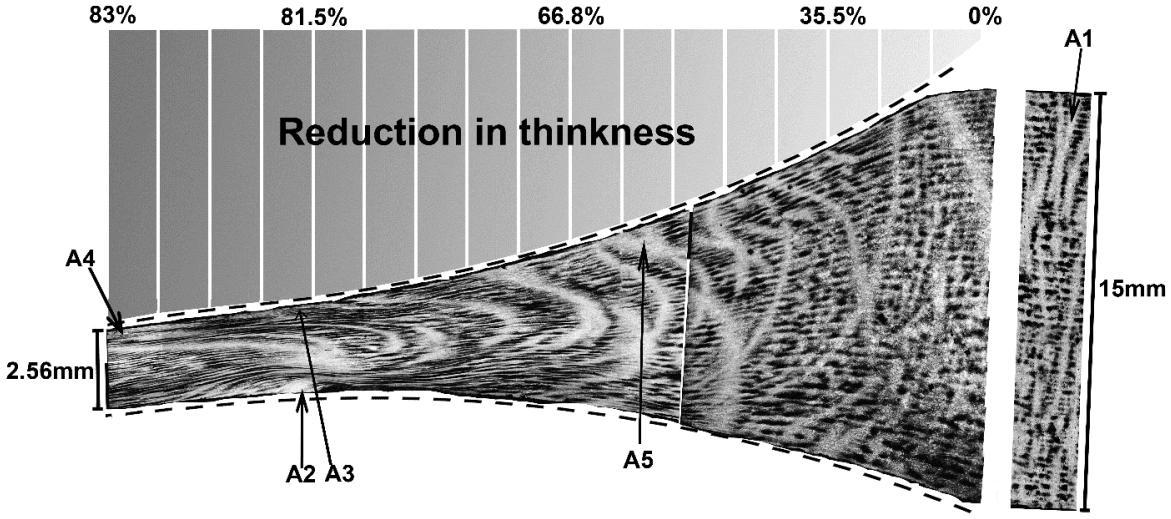

Figure 3.13: A section of a sample partially rolled.

It is interesting to compare the macro-structure with microscopical observations. Figure 3.14 (a) to (d) shows single micrographs taken from different areas of the partially-rolled sample. Figure 3.14 (a) shows the micro structure taken form non-deformed area, while Figure 3.14 (b) shows an area that was deformed 35%. Figure 3.14 (c) and (d) were taken from areas deformed about 80% (bottom region) and 85% respectively. The dendritic and inter-dendritic regions are clearly discernible in Figure 3.14 (a). It is more difficult to identify dendrites at higher reductions, but the distance between the inter-dendritic regions, aligned parallel to the rolling direction can be determined. The spacing of these regions are related to the secondary dendrite arm spacing and also to the formation of micro-chemical bands. Offerman [20] argued that the distance between micro-structural bands (wavelength of the band) in hot rolled medium-carbon steel is related to the primary dendrite arms spacing while Verhoeven [19] and Thompson and Howell [9] proposed that the distance between bands could either be the distance between two elongated secondary dendrite arms or the distance between a rotated primary dendrite arm and an elongated secondary dendrite arm.

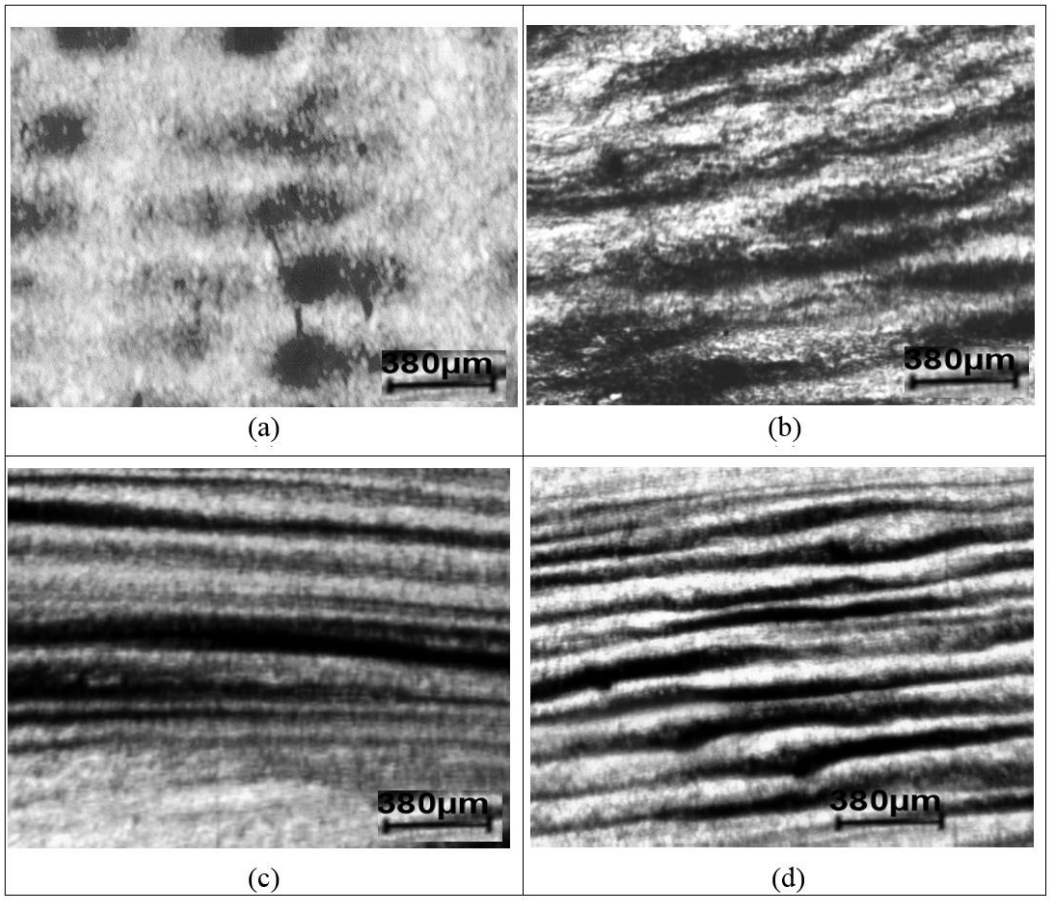

Figure 3.14: Micro-scale graphs of micro-chemical bands from different areas of partially-rolled sample (a) A4, (b) A3, (c) A2 and (d) A1 (white and black areas are dendritic and inter-dendritic regions respectively).

In this study, it is assumed that the distance between the parallel layers of elongated inter-dendritic regions is related to the secondary dendrite arm spacing and these values are shown in Figure 3.15 as a function of the extent of deformation. These values are in good with the deformed secondary dendrite arm spacing measured for the fully deformed specimen shown previously in Figure 3.12.

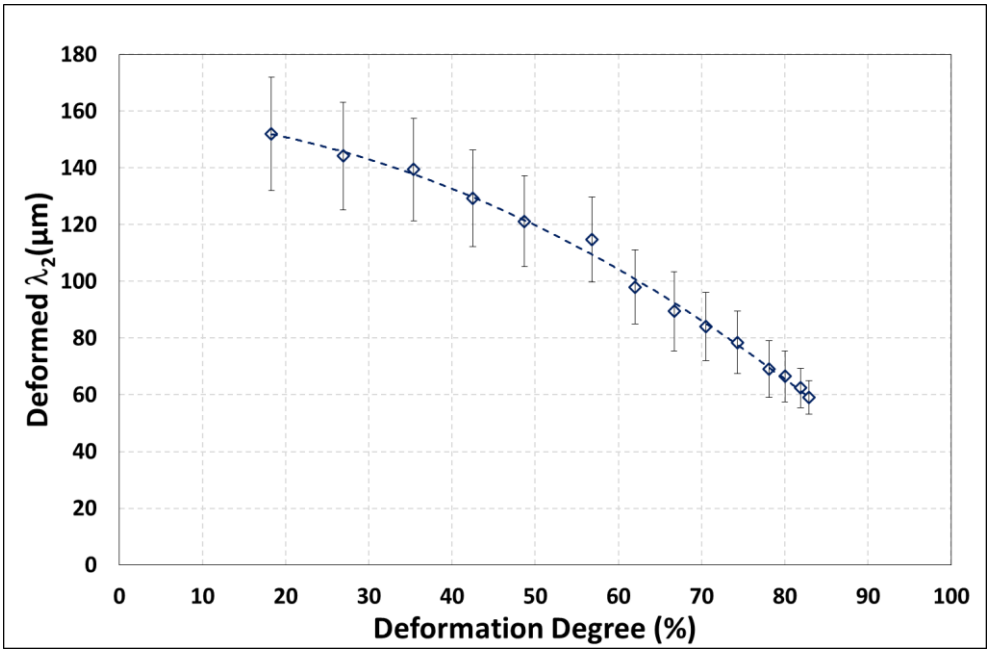

Figure 3.15: Changes in secondary dendrite arm spacing during hot-rolling of the samples.

3.5 Electron Probe Micro-Analyses

3.5.1 Qualitative Assessment

Selected areas indicated by A1 to A4 in Figure 3.13 were examined by EPMA analysis as representative of non-deformed to fully-deformed regions in the partially-rolled medium-carbon steel sample.

3.5.1.1 Non-deformed Area, A1

Figure 3.16 (a) and (b) show an etched sample of a non-deformed (as-cast) area (A1) with its corresponding qualitative manganese segregation map obtained by EPMA. Both images revealed the typical shapes of dendritic structures consisting of primary and secondary arms with regions rich in solute in between (inter-dendritic regions). There is a higher concentration of manganese in the inter-dendritic regions between the dendrite arms while the dendrite arms themselves are manganese depleted. This is in good agreement with the outcome of earlier investigations [164] and [165]. It is also in good agreement with the EPMA and subsequent three dimensional reconstruction mapping of an as-cast steel Domitner *et al.* [166].

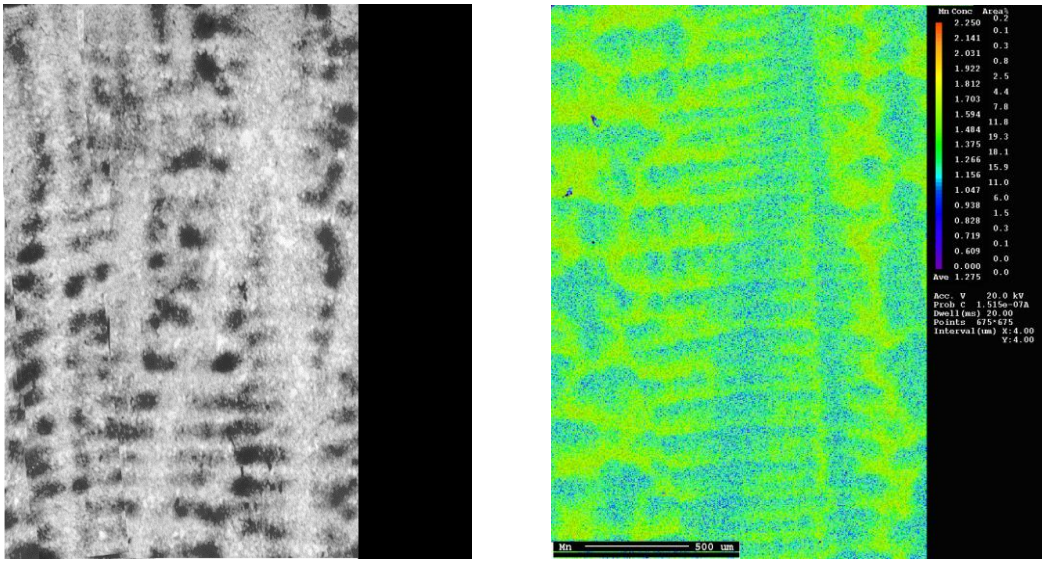

(a) (b)

Figure 3.16: EPMA analyses of the non-deformed region (as-cast). (a) an etched sample (b) a manganese map.

3.5.1.2 Fully-deformed Area, A4

Figure 3.17 (a) and (b) show an etched sample of the fully-deformed region (A4) with its corresponding qualitative of manganese segregation obtained by

EPMA respectively. The bands observed in the optical micrograph are clearly due to the distribution in the dendritic and inter-dendritic regions respectively of alloying element manganese as shown in Figure 3.17 (b). The wavelengths (widths) of these bands are generally 62±6 µm, which is in good agreement with the wavelengths reported by Offerman [20] and, Thompson and Howell [9]. Larger band widths (wavelengths) up to 87±8 µm (indicated by arrows in both images) originated from the presence of rotated (bent) primary dendrite arms.

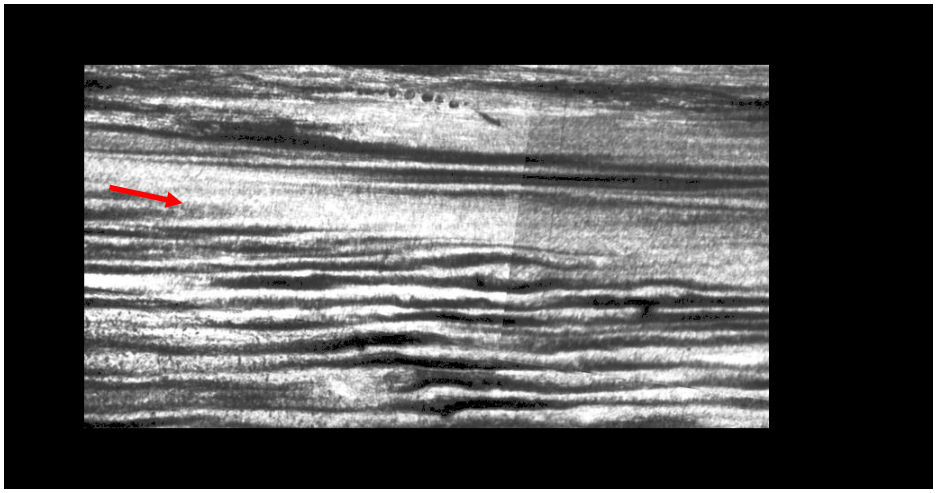

(a)

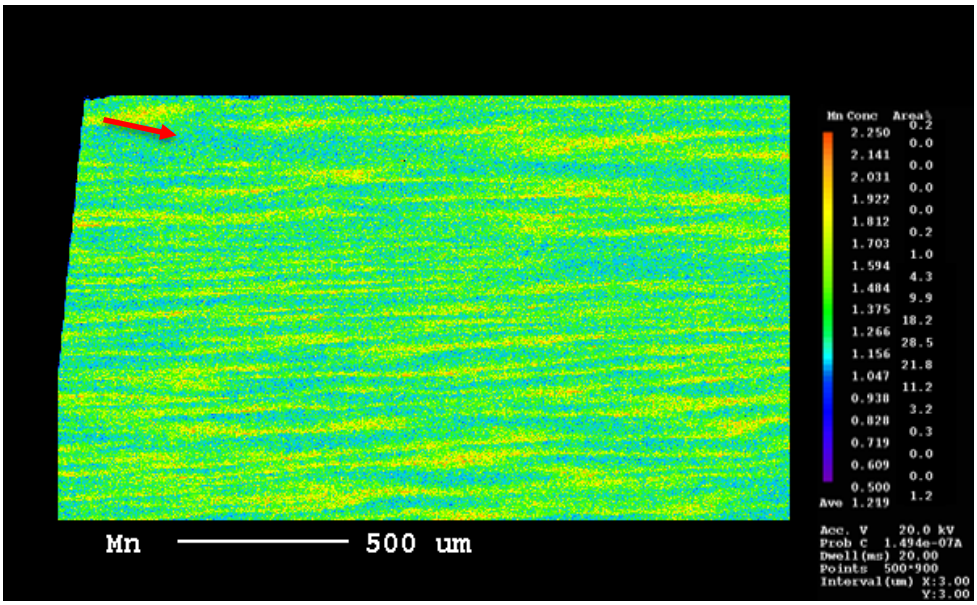

(b)

Figure 3.17: Fully-deformed area of dendritic structures (a) etched sample (b) EPMA manganese map.

Apart from the non-deformed and fully-deformed areas, two partially-deformed areas (A2 and A3) were selected for further investigation form the bottom and top of the sample respectively because the friction between bottom side of the rolled sample and lower-roll is higher than the friction between top surface and upper-roll [167, 168]. Areas A2 and A3 were subject to between 80 and 85% reduction. A2 was in contact with the lower-roll where friction is higher and A3 was in contact with the upper-roll where friction is lower. In addition, Area (A5), which had undergone 50%, reduction was also studied. The behaviour of dendritic structures in these areas are described below.

3.5.1.3 Partially Deformed Area, A5

Figure 3.18 (a) shows an etched sample of a mid-way partially-deformed area (A5). The corresponding qualitative manganese segregation is shown in Figure 3.18 (b). In this 50% deformed region, there is evidence of distinct primary dendrite arms rotation during hot-rolling, following materials flow while secondary dendrite arms and solute-rich regions elongate parallel to the rolling direction (roll circumference).

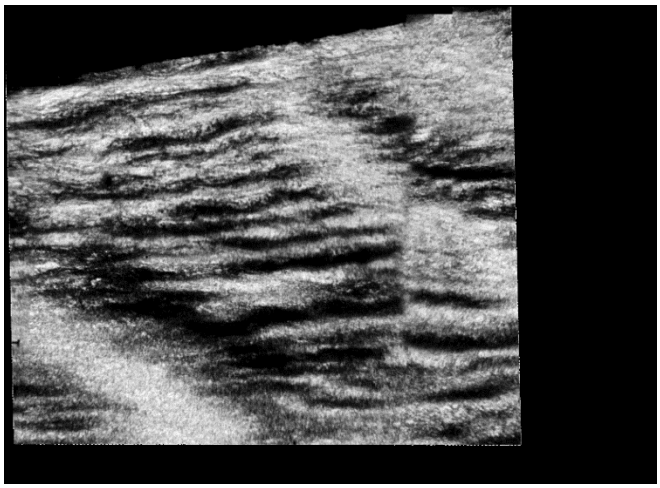

(a)

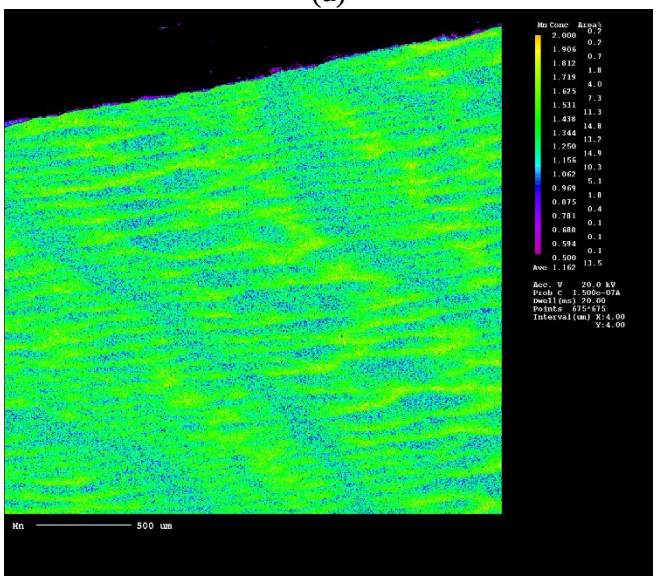

(b)

Figure 3.18: Partially-deformed area (50% deformation) of the dendritic structures from sample A5 (b) EPMA manganese map.

3.5.2 Quantitative Assessment

Selected region from non-deformed to fully-deformed areas of the partially-rolled sample were selected for more detailed EPMA analysis and the compositional changes across dendrite arms and inter-dendritic regions were determined quantitatively.

3.5.2.1 Non-deformed Area

The dendritic segregation in the non-deformed regions of specimen A1 is shown in Figure 3.19. The medium-carbon steel under consideration (Table 3.1) contains 1.2 wt.% Mn while the local manganese varied from about 1.08 to 1.5 wt.%. These findings agree well with the analyses reported by Brooks [6] and Samuels [8].

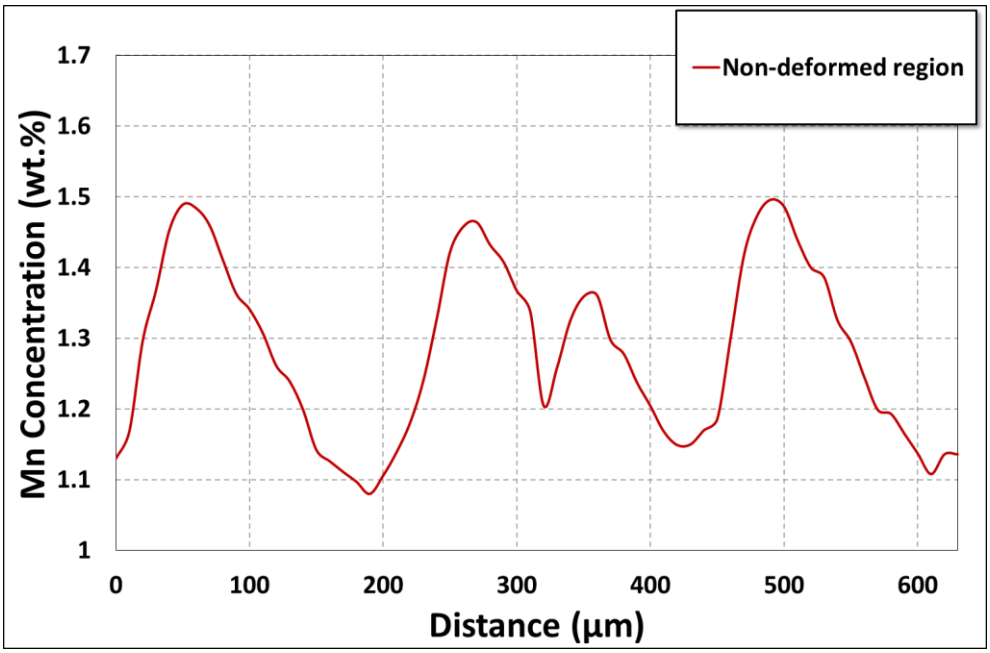

Figure 3.19: Mn concentration across the dendritic and inter-dendritic regions of the non-deformed area A4.

3.5.2.2 Fully-Deformed Area

The magnitude of the dendritic segregation in the fully-deformed (A4) sample was quantitatively measured and shown in Figure 3.20. The local manganese concentration varies from about 1.05 to 1.5 wt.%. This agrees well with the Mn content in the non-deformed area (A4). It also follows that there is a reduction in the primary dendrite arm spacing due to deformation after their rotation. The small peaks in the fully-rolled area result in all probability from elongated secondary dendrite arms and their adjacent inter-dendritic regions. It is evident that deformation does not have much of an influence on the concentration of alloying elements within the bands and solute elements are not redistributed as a result of the mechanical deformation.

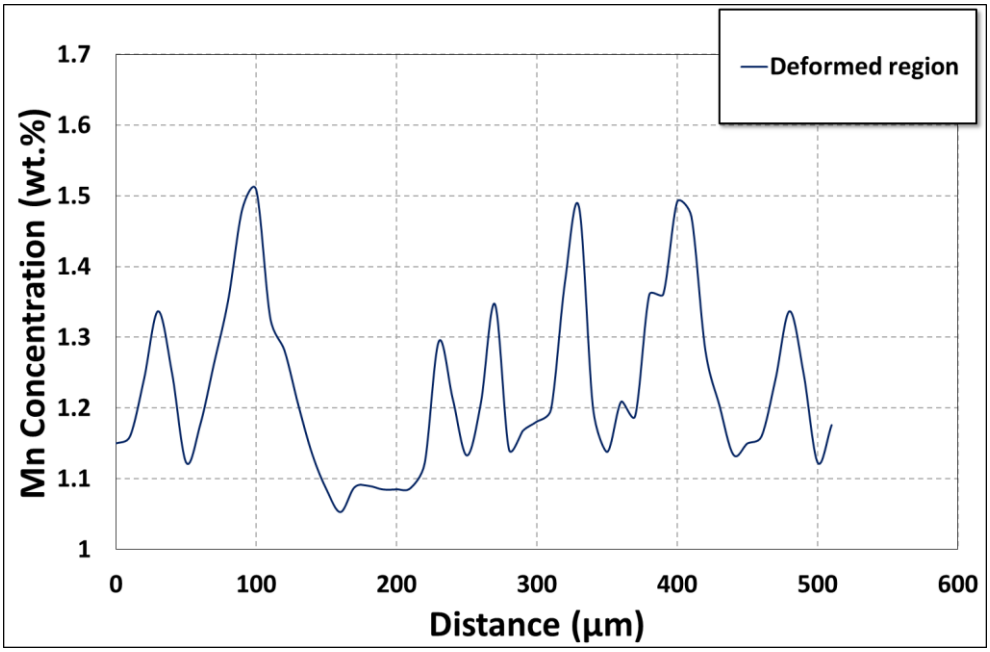

Figure 3.20: Mn concentration across dendritic and inter-dendritic regions of fully-deformed samples area.

3.5.2.3 Dendritic vs. Inter-dendritic Regions

The as-cast structure of the medium-carbon steel investigated exhibits a dendritic structure and the variation in manganese concentration between the dendrites and the inter-dendritic regions originates form the rejection of manganese during the early stages of solidification. The magnitude of this segregation across the dendritic and inter-dendritic regions, indicated by line 1 and line 2 respectively in Figure 3.21, of the non-deformed area was determined quantitatively and is shown in Figure 3.22. It follows that the inter-dendritic regions are enriched in manganese, the manganese concentration being 0.3 to 0.45 wt.% higher in the centre of the inter-dendritic regions whereas there is only a slight variation, between 1.1 and 1.2 wt.%, in manganese concentration across the primary dendrite arm itself This observation agrees well with the findings of Brooks and Samuels [6, 8].

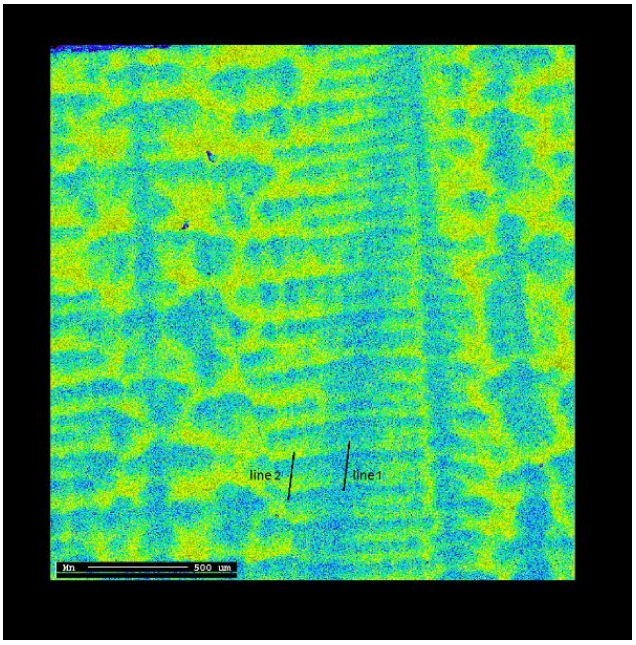

Figure 3.21: EPMA manganese concentration map of a sample taken from an as-cast section of a slab.

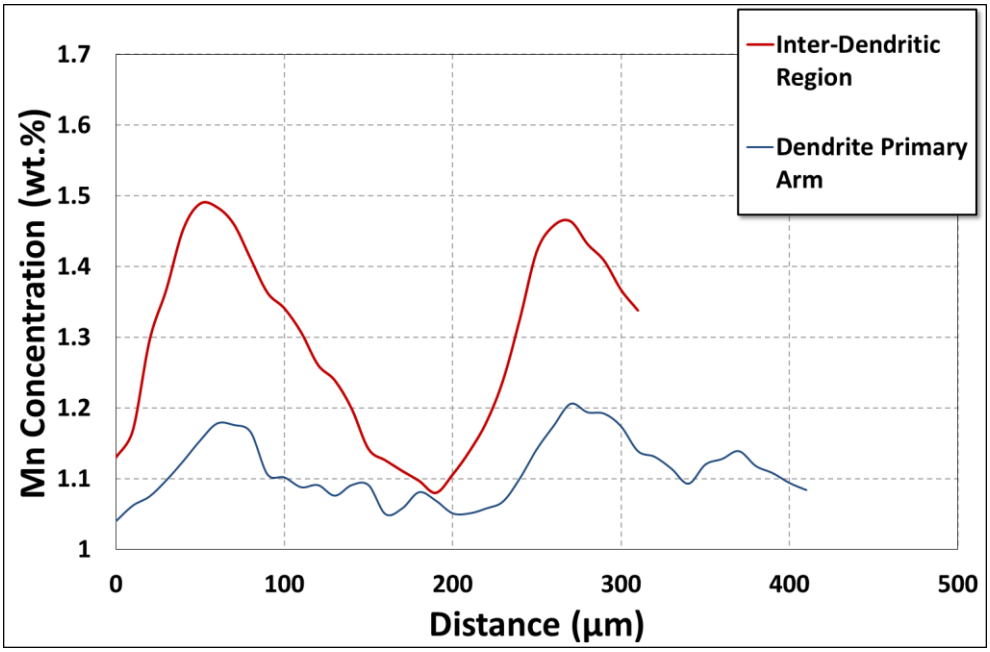

Figure 3.22: Manganese concentration measured by EPMA line-scan analyses across dendritic and inter-dendritic regions of an as-cast sample.

3.6 Effect of Re-heating on Micro-segregation

The sections of the as-cast slab selected for the present investigation have been reheated before rolling and it is therefore necessary to establish if any micro-structural changes had occurred during re-heating of the specimen before it was deformed by rolling. In an attempt to homogenize the chemical composition of slabs in industrial practice, they are usually reheated for several hours at temperatures between 1100 and

1350°C. However, homogenization of large slab is never achieved because of the low diffusion coefficients of most alloying elements in the austenite region and hence, full homogenization requires several days or even weeks [6, 169, 170], a procedure that is completely impractical in the present study, as-cast steel samples were reheated to and soaked in the austenite phase field for half an hour at 1100 °C. The effect of this reheating practice on the concentration of alloying elements prior hot-rolling were investigated by conducting selected EPMA analysis. Manganese concentrations were measured using EPMA line-scan and DICTRA simulation were conducted across the inter-dendritic regions of an as-cast sample prior and after the reheating process.

3.6.1 Manganese Distribution

3.6.1.1 EPMA measurement

Figure 3.23 and Figure 3.24 show manganese concentrations measured by conducting EPMA line-scans across inter-dendritic regions of an as-cast sample prior and after reheating respectively. The differences between the maximum and minimum values of manganese concentration in the as-cast specimens compared to those in reheated specimens were less than ±0.022 wt. % as shown in Figure 3.23 and 3.24. Hence, there is no significant change in manganese concentration during reheating. Similar conclusions were drawn in the literature [6, 20].

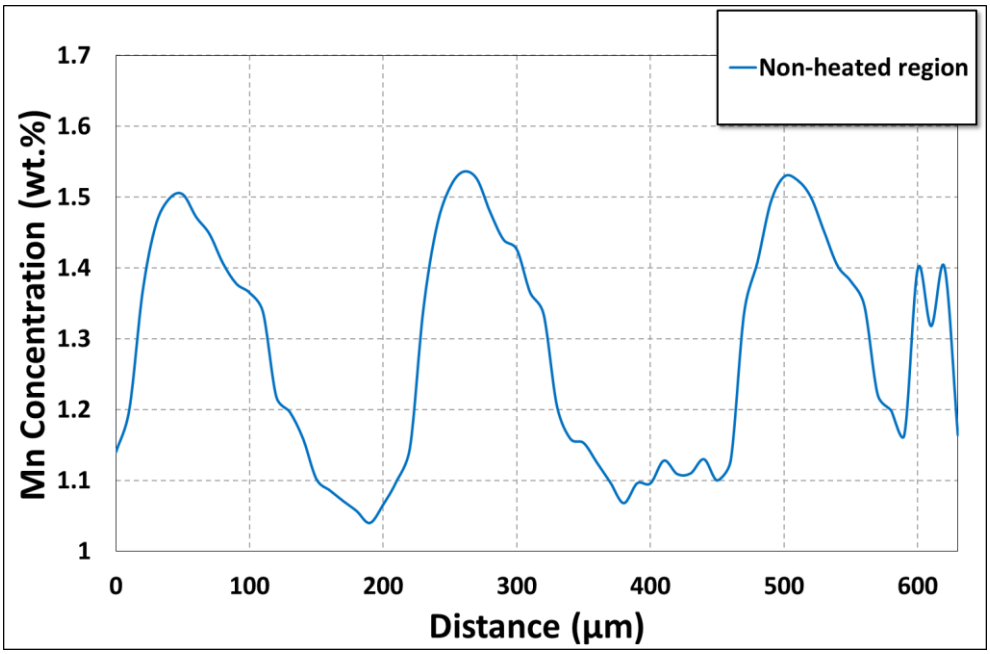

Figure 3.23: Manganese concentration measured by EPMA line-scan across inter-dendritic regions of an as-cast sample prior to reheating.

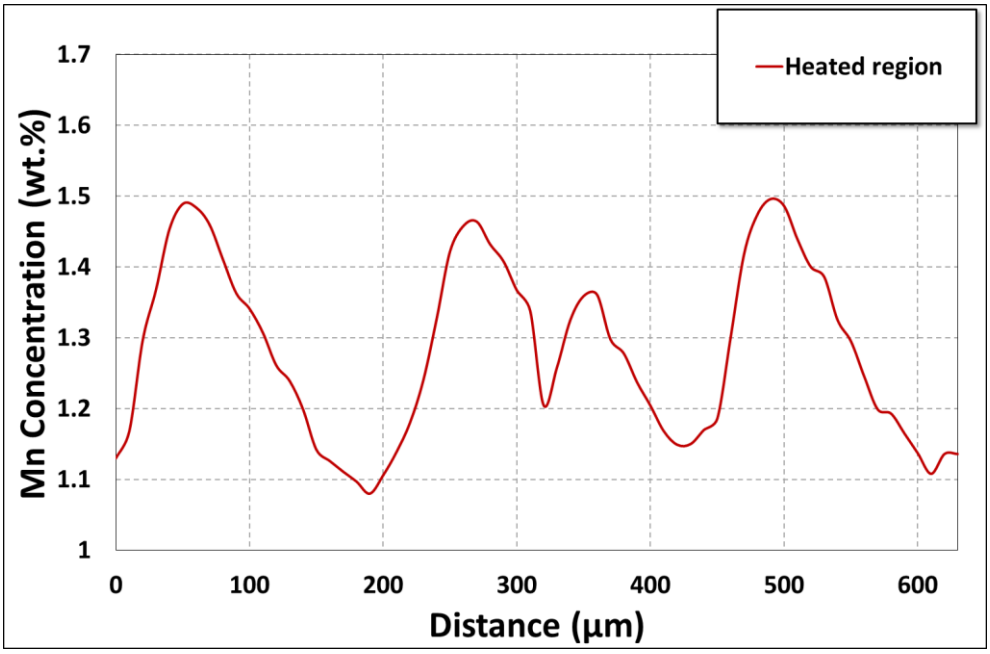

Figure 3.24: Manganese concentration measured by EPMA line-scan across inter-dendritic regions of an as-cast sample after reheating.

3.6.1.2 DICTRA-Simulations

The variations in manganese concentration across inter-dendritic regions of an as-cast sample prior to and following reheating was simulated by the use of DICTRA simulation software. The outcomes of these simulations are shown in Figure 3.25. Notwithstanding the fact that in the simulation the steel it was heated at 1100°C for two hours and 45 minutes, there were no signs of significant manganese segregation since the maximum and minimum values of manganese concentration were different by less than 0.1 wt.%. Moreover, there is good agreement between the experimental measurements and the DICTRA calculations. Both the experimental measurements and the DICTRA-simulations are in good agreement with earlier findings reported in A comparison between the experimentally determined and calculated manganese concentrations are shown in Figure 3.25.

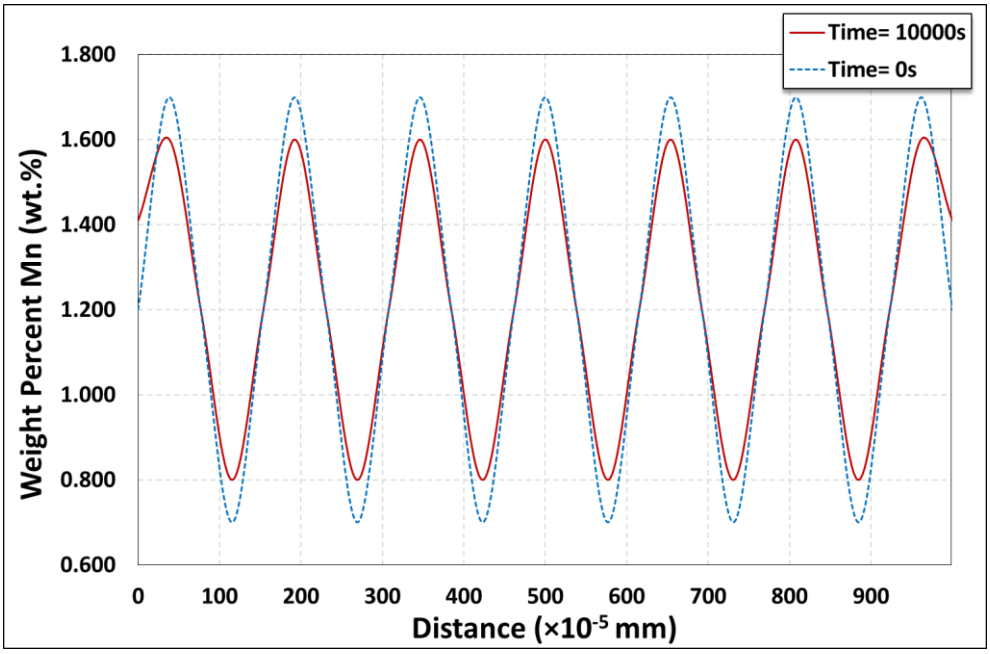

Figure 3.25: A comparison of the variation in manganese concentration simulated by DICTRA across dendritic regions of an as-cast sample before and after reheating.

Such behaviour of dendritic structures are rarely discussed in the literature. However, Flemings [171] and Spencer *et al.* [172] reported dendrite rotation (bending) and distortion during deformation of semisolid dendrites of Sn-15 wt.% Pb alloy. The effect of material flow and strain distribution during hot-rolling plays key role to control the rotation (bending) of primary dendrite arms as well as elongation of secondary dendrite arms and inter-dendritic segregation regions. Pawelski and Gopinathan [173] reported similar bending on screws fixed in different positions in steel specimen and rolled at 950°C to 28.6% deformation. After rolling it was observed that the screws from the longitudinal axis of the specimen bent to the rolling direction. As the flow behaviour of steel in hot-rolling is related strain, Pawelski and Gopinathan observed that there is variation in strain across the rolled specimens. The maximum strain was observed at the centre of the specimen which was almost double the nominal strain. Sakai *et al.* [174] reported similar bending of embedded pin in 2.5-mm thick steel specimen and subjected to hot-rolling at 650, 700, 750, 800 and 850°C to 40%. It was observed that the variation of the effective strain through the thickness and maximum effective strain occurs at the centre of all rolled specimens. Martin *et al.* [47] referred deformation of segregated alloys and dendritic structures its effect on homogenisation to the crystallographic of high and low segregated regions from one side and average concentration regions from other sides. However, this assumption

neglected the effect of material flow during hot-rolling. Verhoeven [19] also referred micro-chemical banding alignment to the rotation of plane during hot-rolling. Bramfitt [175] also studied the effect of hot deformation on the as-cast dendritic structures via observation of dendritic texture in directionally solidified ingots of three commercial steels, AISI 1010, Fe-3.4% Si, and Type 430 stainless steel were hot-rolled at 1010°C. Bramfitt [175] reported that the strong dendritic (100) orientation of both the Fe−Si and Type 430 alloys was completely destroyed by the heavy reductions typical of the commercial hot-rolling of ingots. The AISI 1010 steel, which had very little of the dendritic <100> orientation in the ingot stage, had a combination of two weak textures after hot-rolling: (100) [011] and (110) [110]. Similarly, with the other two steels, which had a strong dendritic <100> orientation in the ingot stage, hot-rolling resulted in weak textures: (110) [001] with a rotation of this orientation of ±45 degrees about the [001] rolling direction, followed by (110) [001] rotated ±35 degrees about the [110] in the transverse direction.

3.7 Conclusions

- Primary dendrite arms rotate progressively around the transverse axis during hot-rolling.
- Secondary dendrite arms, with their adjacent areas of inter-dendritic segregation elongate progressively parallel to the rolling direction.
- When the reduction exceeds 80% the primary as well as the secondary arms, with the associated inter-dendritic regions, align parallel to the rolling direction, thereby forming layers of low and high concentration of allying elements respectively.
- The secondary dendrite arm spacing changes from about 160 μm in the as-cast (undeformed) condition to about 40 μm at 90% reduction.
- Reheating the as-cast slab prior hot-rolling for relatively short times does not cause a redistribution of manganese.

Chapter 4. Variations of Mechanical Properties of Dendritic and Inter-dendritic Regions in Medium-Carbon Steel

4.1 Introduction

This chapter deals with the mechanical properties of dendritic and inter-dendritic regions in as-cast medium carbon steel. The mechanical properties of these different regions in the slab are essential input parameters for the finite element models, described in Chapter 5, that were used in this study to simulate the microstructural changes during hot-rolling that lead to the formation of micro-structural bands. An attempt was made to determine the mechanical properties of the dendritic and inter-dendritic regions respectively of the as-cast medium-carbon steel under investigation by the use of two different approaches.

In the first approach, a nano-indentation technique was used to assess the mechanical properties of the dendritic and inter-dendritic regions respectively because it is not possible to section specimens large enough for bulk mechanical testing,.

In the second approach, it was assumed that different areas in the industrially-produced slab might be taken as representative of dendrites and inter-dendritic regions respectively. For these assessments, samples were taken from two different regions of the slab. A block sample was cut from one half of a medium-carbon slab that was produced on an industrial production line. One set of samples were cut from an area close to the top of the slab. These samples were to dendrite structures. A second set of samples were taken from the area close to the centreline to represent inter-dendritic segregated regions. In all cases samples were machined into hot-tensile specimens for assessing the high-temperature mechanical of the two different regions. Testing temperatures were selected to simulate industrial finishing rolling conditions. Following the hot-tensile tests, the fracture surfaces were studied using a defocused-beam line-scan in an EPMA in order to measure the chemical composition variations in specimens sectioned from the near-surface area, the quarter thickness and at the centreline.

Specimens from the two regions were also prepared for sectioning by focused ion-beam milling in order to measure the chemical compositional variations across dendritic and inter-dendritic regions in the as-cast medium carbon steel under investigation.

4.2 Experimental Work

4.2.1 Test material and specimen

Specimens were selected from an as-cast medium-carbon steel of composition shown in Table 3.1.

Samples taken from the quarter-thickness region was cut into 10×10×10 mm sections for nano-indentation tests. The face perpendicular to the casting direction was prepared in the same way as specimens for metallurgical examination. In order to reveal the dendritic structure and segregation of micro-alloyed elements, specimens were etched in picric acid. It often required several polishing and etching cycles to achieve optimum results. The etching reagent consists of 80 ml of saturated aqueous picric acid, in addition to a few drops of HCl and teepol respectively. Specimens were immersed into this solution at 68°C, when the surface was covered by black smut. On removal of the smut, the process was repeated between 5 to 10 times until the dendritic structure was clearly revealed.

Specimens for hot-tensile tests were of cylindrical shape, 6-mm diameter and 100-mm in length. The specimens were machined with the transverse axis perpendicular to the dendritic growth direction, as shown in Figure 4.1. Specimens were selected from the top and bottom regions (region 1 and region 2 respectively) of the columnar dendritic zone of the slab to represent dendrites. Specimens sectioned from the centreline were to represent inter-dendritic regions. Sectioning of the specimens is schematically shown in Figure 4.1.

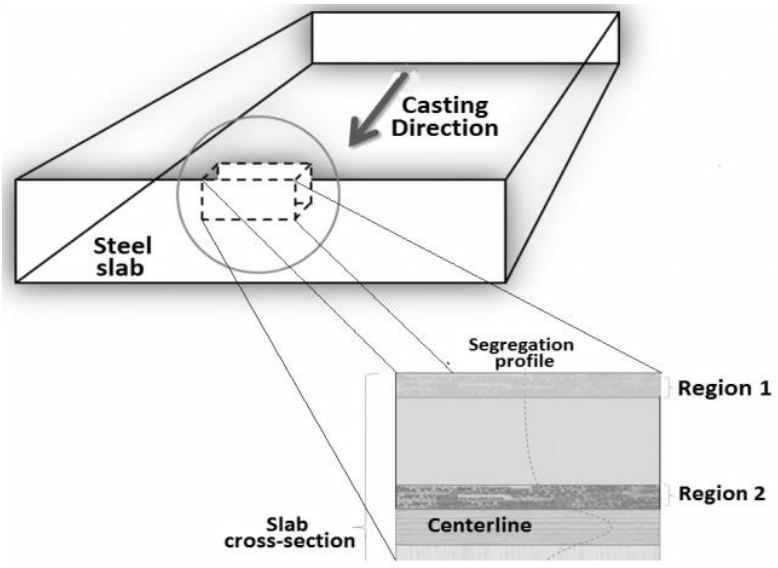

Figure 4.1: Sample location in the slab.

4.2.2 Nano-Indentation procedure

The mechanical properties of both segregated (inter-dendritic) and non-segregated (dendritic) regions were determined at room temperature by using a UMIS-2000 nano-indenter, which continuously measures force and displacement as an indentation is made. The indenter in this particular instrument is a Berkovich diamond three-sided pyramid (E_i=1140 GPa, ν_i= 0.07) with a nominal angle of 65.3° and an area-to-depth function which is the same as that of a Vickers indenter. As-cast specimens were etched in picric acid to reveal the dendritic structure prior to performing nano-indentation, optical microscopy and AFM. A matrix of 120 indentations was made on etched samples with a maximum load of 30 mN, the indentations being separated by 10 μm and an average value for each region was determined.

From the data obtained during unloading of the indentation, elastic displacements can be determined and from these measurements the elastic modulus, *E*, can be calculated. Furthermore, by removing the elastic contribution from the total displacement, the hardness, *H*, can be calculated [176]. A schematic diagram of a typical loading unloading curve is shown in Figure 4.2.

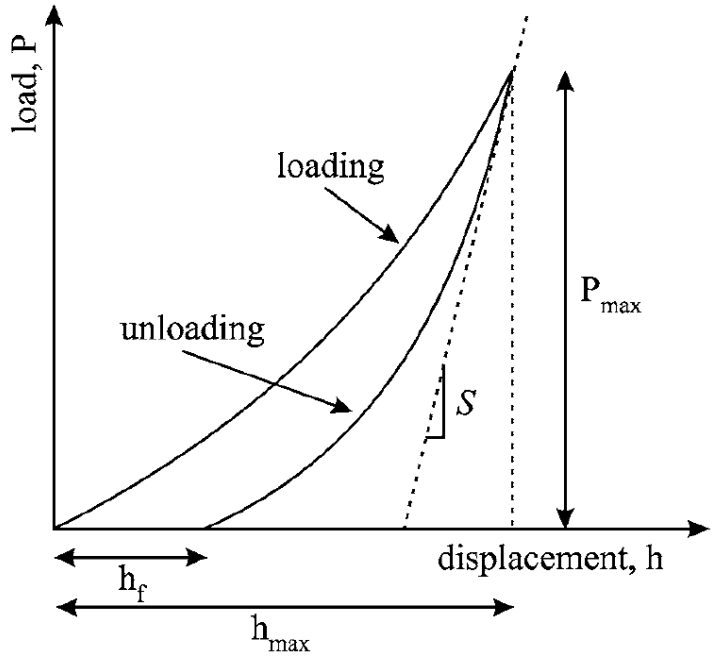

Figure 4.2: Schematic representation of a loading-unloading curve for a nano-indentation measurement [176].

Because this technique has been use to estimate the mechanical properties of the steel under consideration from, essentially, a hardness test, it is pertinent to refer to important considerations in the use of this test. The displacement plotted in this figure

represents the total displacement of the indenter relative to the initial position. This value has both elastic and plastic components of displacement. An important observation concerns the shape of the hardness impression after the indenter is unloaded and the material has elastically recovered [69]. In metals the impression formed by a conical indenter is still conical, but with a larger included tip angle. Doerner and Nix [177] observed that during the initial stages of unloading, the area of contact remains constant as the indenter is unloaded. The unloading stiffness is then related to the elastic modulus and the projected area of the contact, *A*, through the following relationship:

$$S = \left(\frac{dP}{dh}\right)_{P=P_{max}}^{unloading} = \frac{2}{\sqrt{\pi}} E_r \sqrt{A} \qquad 4.45$$

where E_r is the reduced elastic modulus as defined in the following equation:

$$\frac{1}{E_r} = \frac{\left(1-v^2\right)}{E} + \frac{(1-v_i^2)}{E_i} \qquad 4.46$$

where E and v are the Young's modulus and Poisson's ratio for the specimen and E_i and v_i are the parameters for the nano-indenter material (E_i=1140 GPa, v_i= 0.07). To determine the contact area at peak load, Oliver and Pharr [69] proposed a new method of analysis, since the behaviour of materials when indented by a Berkovich indenter cannot be described using the flat punch approximation [177]. Sneddon [178] has derived analytical solutions for punches of several geometries, including conical indenters. The cross-sectional area of a conical indenter varies as the square of the depth of contact and its geometry is singular at the tip. Oliver *et al.* [69] argued that a conical indenter provides a better description of the elastic unloading than a Berkovich indenter. The area of contact at peak load is determined by the geometry of the indenter and the depth of contact, h_c. The indenter geometry can be described by an area function $F(h)$ which relates the cross-sectional area of the indenter to the distance from its tip, h. Given that the indenter itself does not deform significantly, the projected contact area at peak load can be calculated from the relation:

$$A = F(h_c) \qquad 4.47$$

In addition to the elastic modulus, the hardness, *H*, defined as the applied load divided by the projected area of contact between the indenter and the sample can now be calculated:

$$H = \frac{P_{max}}{A} \quad 4.48$$

The hardness is often used for estimating other mechanical properties of metals [179-182].

There have been attempts to obtain a general expression relating to the 0.2% offset yield strength of metals to hardness [183, 184]. A good correlation between the 0.2% offset yield strength and hardness for different steels in the quenched and tempered condition has been established but the reasons for the correlation were neither investigated, nor was the treatment extended to other metals. It has also been shown that the yield stress of a material could be given by the following relation:

$$\sigma_y = \frac{H}{3} \quad 4.49$$

which has been verified experimentally to some degree subject to an assumption of the strain hardening coefficient, *n*, being equal to zero [179]. However, some studies have taken into consideration the influence of strain hardening in other materials[185, 186]. Cahoon et *at* [179] developed a general expression to correlate the 0.2% offset yield strength with hardness for various materials that would include the strain hardening coefficient since it seems reasonable that this coefficient would affect the yield strength versus hardness correlation. This proposed expression showed that the 0.2% offset yield strength of a material can be calculated by the expression

$$\sigma_y = \left(\frac{H}{3}\right)(0.1)^{(m-2)} \quad 4.50$$

where *H* is the Diamond pyramid hardness and *m* is Meyer's hardness coefficient.

4.2.3 Hot Tensile Test equipment and procedure

One of the most commonly used techniques to assess the mechanical properties of steels are tensile tests in transient mode or under steady state. Although a transient test is considered more realistic in simulating high temperature steel behaviour, steady state tests are more commonly used because they are easier to perform and provide the stress–strain curves directly [77, 80, 84].

Although hot-rolling is a compression process, mechanical properties at high temperature such as the elastic modulus, yield strength and ductility are obtained from hot-tensile tests since they are approximately equal to those in compression for ductile materials such as steel at high temperature. Hot tensile testing usually provides sufficient data to determine the mechanical properties of steel at high temperature. [100-103, 187-192].

Hot-tensile tests were conducted using a Gleeble 3500, which is a fully integrated digital closed loop control thermal and mechanical testing system, as shown in Figure 4.3 and Figure 4.4. The Gleeble 3500 has a digital control system, which provides all the signals necessary to control thermal and mechanical test variables simultaneously through the digital closed-loop thermal and mechanical servo systems. The Gleeble 3500 mechanical system is an integrated hydraulic servo system capable of exerting as much as 20 tons of static force in compression or 10 tons in tension. In the tensile rig of the Gleeble, tension is applied by using two loading rods as shown in Figure 4.4.

During testing, the force, *F*, measured by a load cell and the displacement of the stroke were recorded and converted to engineering stress (σ_E) as

$$\sigma_E = \frac{F}{A_0} \qquad 4.51$$

where is A_0 is initial area of the specimen.

and engineering strain (ε_E) as

$$\varepsilon_E = \frac{l - l_0}{l_0} = \frac{\Delta l}{l_0} \qquad 4.52$$

Engineering stress and strain are then converted to true stress (ε_T) and true strain (σ_T) by the following equations:

$$\varepsilon_T = ln\,(1 + \varepsilon_E) \qquad 4.53$$

$$\sigma_T = \sigma_E\,(1 + \varepsilon_E) \qquad 4.54$$

It is important to note that these equations were only used to convert engineering stress and strain to true stress and strain up to the point of necking, the limit of their respective validity.

All the hot tensile tests were conducted at isothermal temperatures and the air temperature inside the rig of the Gleeble 3500 was measured with two thermocouples welded at the centre of specimen.

Strain-control was used in the tensile tests, which were conducted at a strain rate of 0.05/s. The experimental process was controlled by some predefined programming options using QuikSim Software. All the data obtained from the tests (i.e., force, stroke, strain, temperature and time) were recorded by a computer and could be monitored during testing.

Test temperatures of 800, 900, 1000 and 1100 ºC were selected to simulate finishing rolling temperatures in industry. The tensile load was applied when the test temperature was reached on heating and it continued until failure. However, stress-strain data up to necking obtained from the hot tensile testing provides sufficient data to determine the required mechanical properties at high temperature. The measured true stress-strain data before necking were then fitted using polynomial curves of TableCurve® 2D Software.

Figure 4.3: Gleeble 3500 machine.

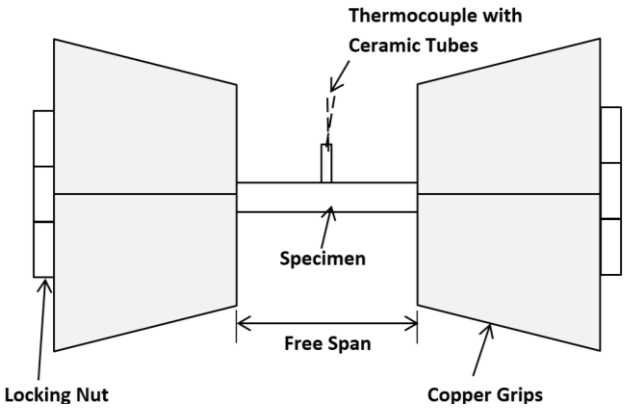

Figure 4.4: Tensile test set-up in Gleeble Machine

4.2.4 Electron Microprobe Analysis

Quantitative analyses using EPMA were carried out on the dendritic and inter-dendritic regions of as-cast sample collected from the near centreline region where dendritic structures formed almost in a uniform shape and in a direction perpendicular to the macroscopic surface. The same analyses were also carried out on the tips of fractured tensile specimens from the near surface region (region 1) and near centreline region (region 2). This was performed using the JEOL JXA-8500F Field-Emission SEM-EPMA HYPERPROBE (WDS & SDD-EDS) at UNSW.

In order to perform EPMA tests on tensile specimens, the tips of these specimens were cut, ground, and polished using metallographic techniques. Line-scan tests were performed along the tip of these specimens after fracture, as illustrated in Figure 4.5. Line-scans were conducted using a defocused electron beam, 100µm in diameter at five spots from the centre to the edge of a specimen. Other line-scans were performed across primary dendrite arms as well as inter-dendritic regions. The weight percent of analysed elements is determined using the instrument's software ZAF correction factors [193]. Standard samples with 1% and 2% manganese (balance Fe) were used for calibration. The conditions and basic settings for the EPMA analysis are listed in Table 4.1.

Table 4.1: Conditions and Basic Settings for the Microprobe

Measurements	**Quantitative point analysis (Linescan) conditions**
Analyzed element	Manganese (Mn)
Analyzing crystal material	Lithium fluoride
Acceleration voltage	20 kV
Electron beam current	40 nA
Pre-set value for the probe diameter:	100µm (defocused)
Dwell time per measurement point:	20 ms
Number of measured points:	5 points per sample

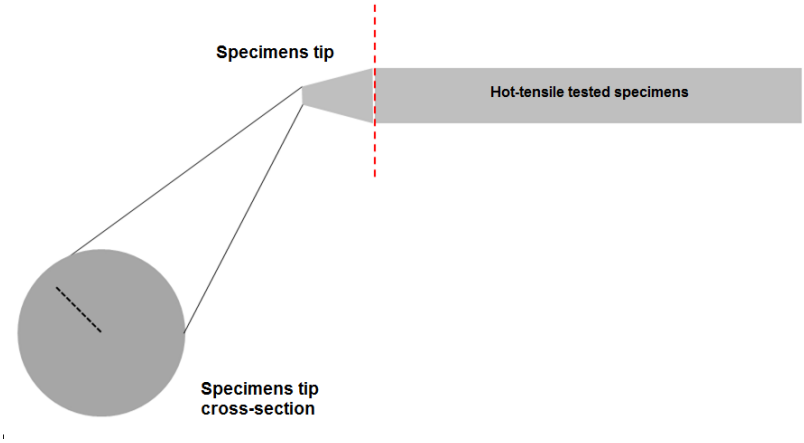

Figure 4.5: Schematic of hot-tensile tested sample from region 1 and 2 prepared for EPMA.

4.3 Results and Discussions

4.3.1 Nano-Indentation results

Typical loading-unloading indentation curves for the dendritic structures of as-cast medium-carbon steel sample are shown in Figure 4.6. Indentation curves with deviant shapes were excluded from the interpretation. These deviant shaped curves were either a result of indentations with underlying particles that were present in segregated region, indentations on particle whereby the indenter slid off, or they were due to surface roughness of the sample. Average indentation curves for the segregated regions are shown as thick dark lines while thick dotted lines indicate the non-segregated regions (dendrites).

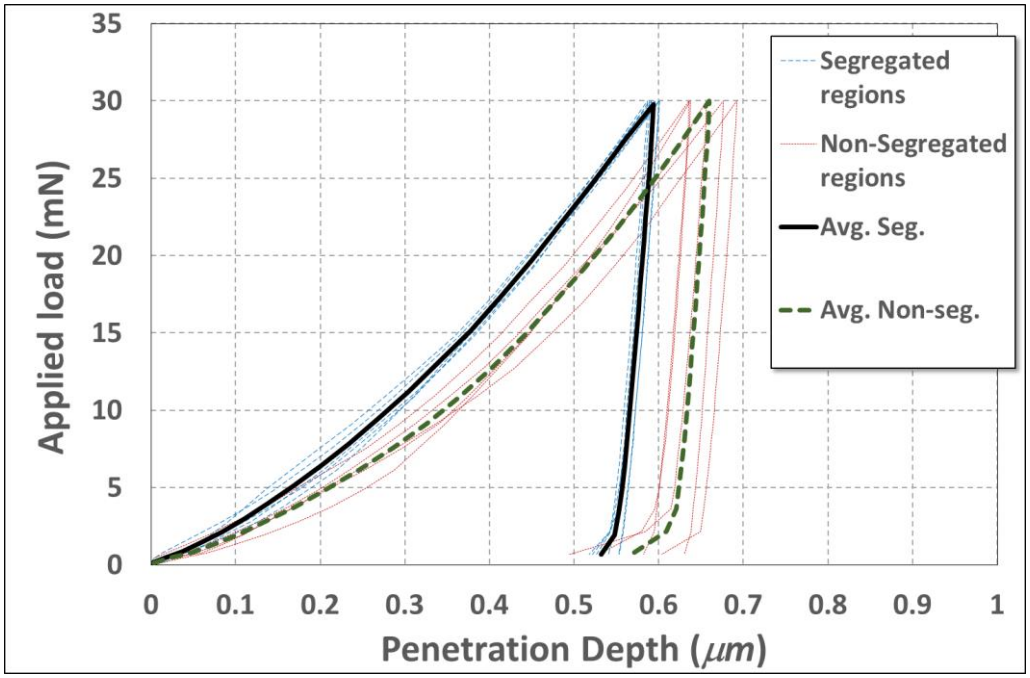

Figure 4.6: Examples of Indentation loading-unloading curves for segregated and non-segregated regions of as-cast medium carbon steel.

Using dark-field optical microscopy, most indentations in the matrix material could be tracked, whereas indentations in segregated regions were difficult to track. After locating the position of the indentations in the matrix material under dark field optical microscopy, it was possible to switch to bright field and take photographs for further interpretation. The microstructures of the dendritic and inter-dendritic areas where the indentations were made are shown in Figure 4.7.

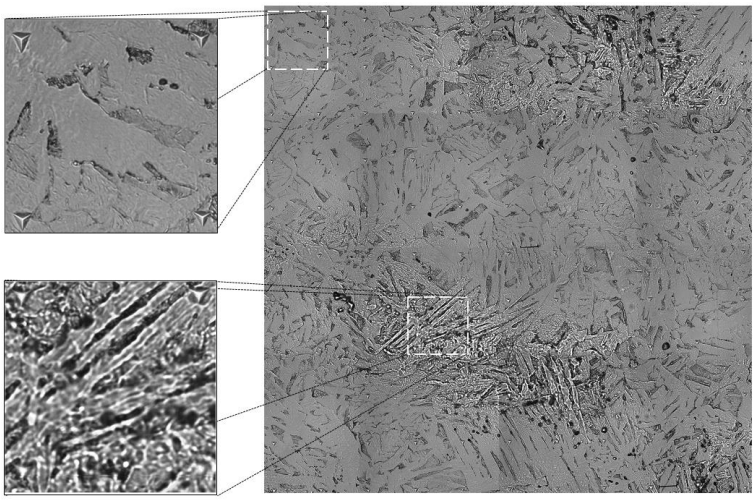

Figure 4.7: Nano-indentations image (the indentations were separated by 10 µm).

Average elastic moduli and hardness values at room temperature for the segregated and non-segregated regions respectively of the as-cast medium-carbon steel are given in Table 4.2.

The elastic moduli were determined from a linear fit to the initial points of unloading of the indentation curves and the hardness values were determined from the maximum force and depth of the penetrations. These procedures are outlined in the instruction manual of the instrument used. The data in Table 4.2 exhibits a relatively small scatter for indentations in the matrix (non-segregated regions), but the data for the segregated display much wider scatter. The elastic modulus of the segregated regions is higher than that of the non-segregated regions and both elastic moduli were within the range reported in the literature for the steel type under discussion, i.e. 190-210 GPa [194-196]. Elastic modulus is not as important as other mechanical properties in the analysis of bulk plasticity. However, it is an important in parameter in the use of Finite Element Modelling techniques [67, 197, 198].

The matrix and segregated regions clearly have different hardness values. The segregated regions are on average 0.4 GPa harder than the matrix (dendrites). Similar observations have been reported in the literature for welds in steel [67, 199, 200].

Table 4.2: Average elastic moduli and hardness values in the segregated and non-segregated regions of slabs.

Region	**Elastic modulus**	**Hardness**	**Yield Strength**
	E (GPa)	*H (*GPa)	σ_y *(MPa)*
Segregated region	208 ± 39	2.54 ± 0.22	846.6± 73.3
Non-segregated region	199 ± 27	2.1 ± 0.19	700.3 ± 63.4

4.3.2 Hot-Tensile Test

Fitted stress–strain curves obtained from the raw data of the Gleeble tests are shown in Figure 4.8 and Figure 4.9 for samples from region 1 (low segregation region near slab surface representing dendritic structures), and region 2 (highly segregated area from the quarter thickness region, representing inter-dendritic structures) at testing temperatures 800, 900, 1000 and 1100°C.

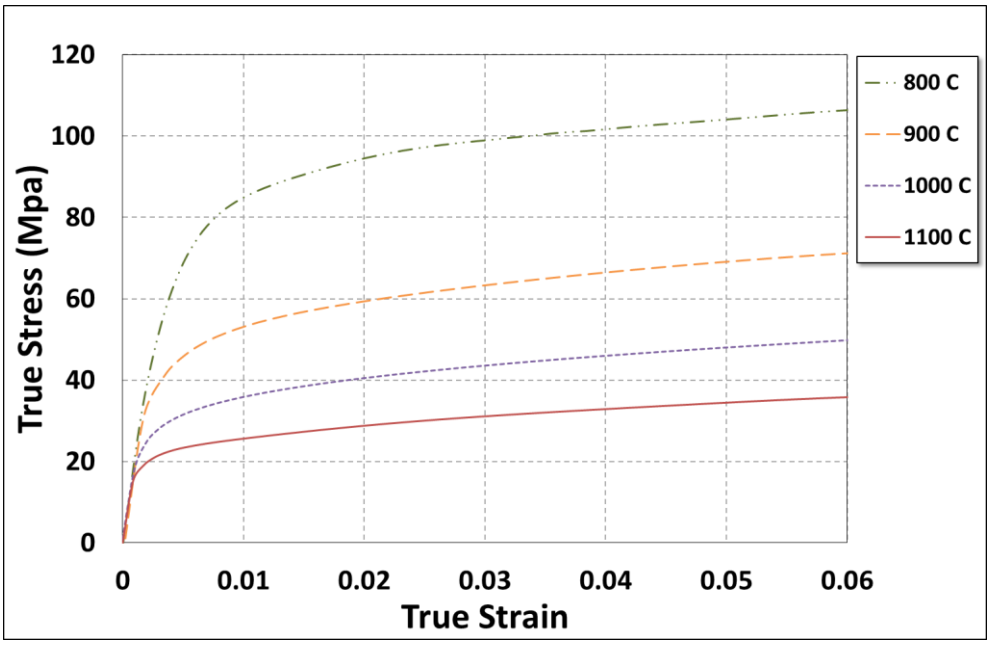

Figure 4.8: Stress–strain curves of region 1 (representing low-segregated region) at temperatures of 800, 900, 1000 and 1100 °C.

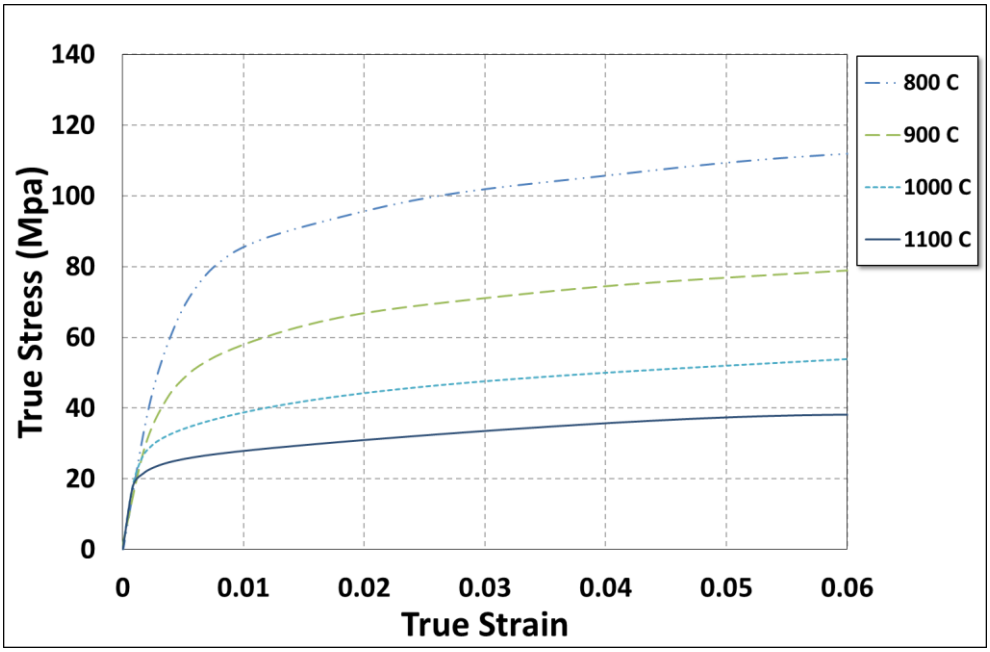

Figure 4.9: Stress–strain curves of region 6 (representing highly segregated region) at temperatures of 800, 900, 1000 and 1100 °C.

4.3.3 Mechanical Properties of Segregated and Non-segregated Regions

Figure 4.11, Figure 4.12 and Figure 4.13 show elastic moduli, yield strength and ductility for regions 1 and 2 (see Figure 4.1) at testing temperatures 800, 900, 1000 and 1100°C respectively.

4.3.3.1 Elastic modulus

The elastic modulus of steel is generally obtained from the initial slope of the stress–strain curve at room temperature as illustrated in Figure 4.10. The elastic modulus is measured as the slope of line AB drawn in the figure.

The elastic modulus is essentially a measurement of the stiffness of a material. Thus it is commonly used in design and engineering applications. The elastic modulus is not very sensitive to the microstructure when subjected to deformation under severe conditions [67], such as hot-rolling. However, finite element modelling has been developed, as discussed in the next chapter, to predict dendrite changes when small incremental changes in mechanical properties are used. Thus, it is important to take the elastic moduli into consideration [197, 198, 201].

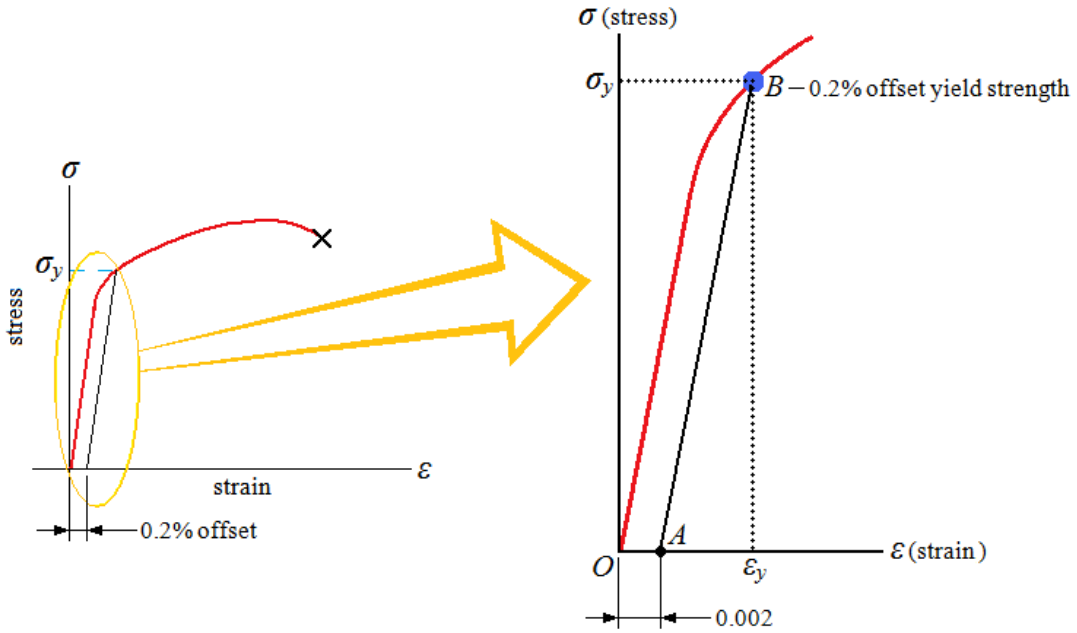

Figure 4.10: Determination of the elastic modulus and yield strength using the offset method from stress-strain curve.

The elastic moduli determined from the hot-tensile tests of the segregated and non-segregated regions determined at high temperature are shown in Table 4.3 and Figure 4.11. There is a significant drop in elastic modulus at 800 ºC of about 25% compared to room temperature for both regions. When the test temperature is increased

to 900 ºC, the non-segregated samples lost approximately 6% more of the value of the elastic modulus, while the segregated samples lost less than 5%. The elastic modulus decreases by 9-10% for both regions at 1000 ºC and to 13% and 15% for non-segregated and segregated regions, respectively at 1100 ºC.

Table 4.3: Elastic Moduli in Segregated and non-segregated regions of the slab.

Temperature (C)	Non-Segregated Regions E-modulus (GPa)	Segregated Regions E-modulus (GPa)
800	156.56 ± 2.07	160.70 ± 1.60
900	147.27 ± 1.59	152.90 ± 1.82
1000	132.45 ± 2.31	138.33 ± 1.96
1100	112.53 ± 3.02	120.33 ± 2.59

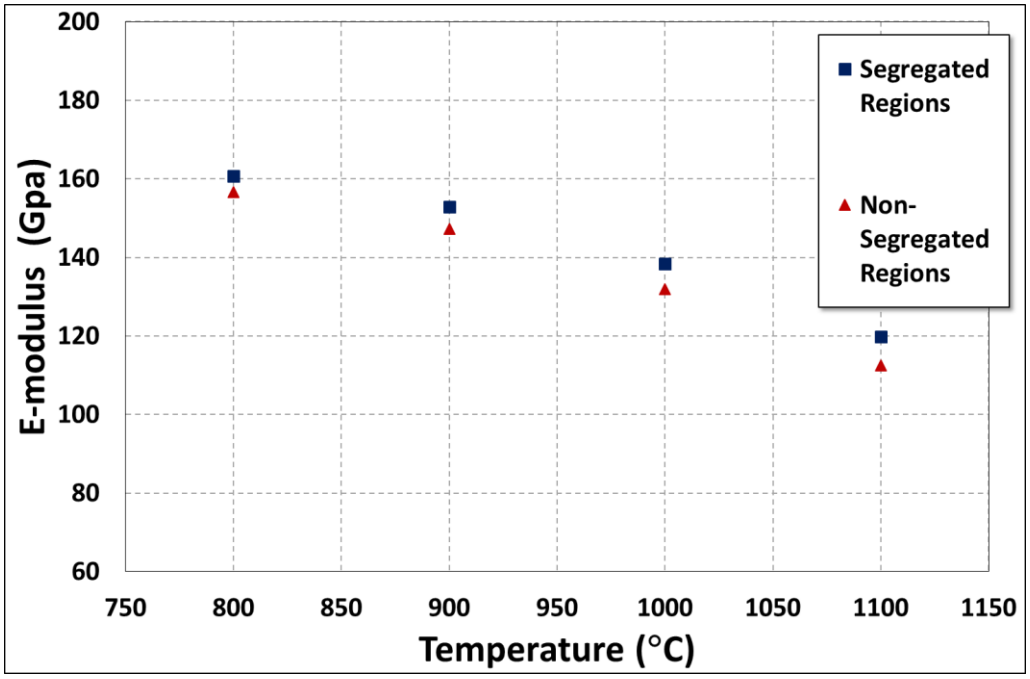

Figure 4.11: Elastic modulus of segregated and non-segregated regions as a function of testing temperature.

4.3.3.2 Yield strength

The yield strengths (0.2 % proof stress) of the segregated and non-segregated regions are shown in Table 4.4 and Figure 4.12. It is evident that the yield strengths of the segregated and non-segregated regions vary by more than 8% at 800ºC. Above 800ºC, the difference in these yield strengths decreases and at 1100ºC the difference is less than 2 MPa.

Table 4.4: Yield Strength (0.2 % off-set) in segregated and non-segregated regions of the slab.

Temperature (°C)	Non-Segregated Regions Yield Strength (MPa)	Segregated Regions Yield Strength (MPa)
800	90.33 ± 4.53	98.44 ± 3.06
900	58.33 ± 2.42	66.24 ± 2.39
1000	38.90 ± 0.82	41.84 ± 2.04
1100	29.00 ± 0.58	30.91 ± 0.56

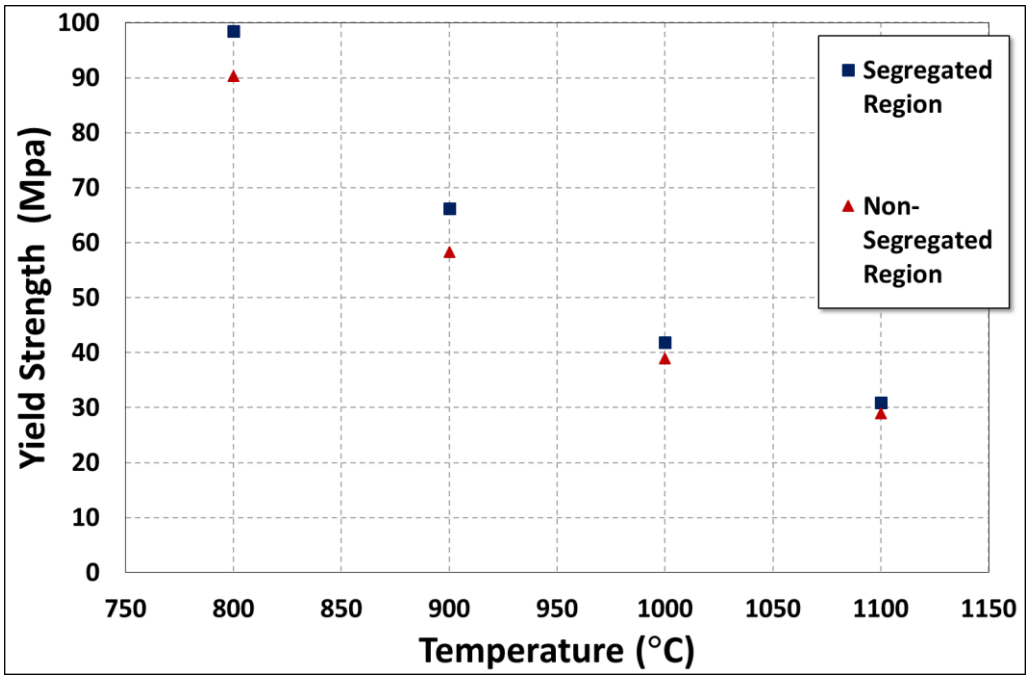

Figure 4.12: Yield strength (0.2% off-set) of segregated and non-segregated regions as a function of testing high temperature.

4.3.3.3 Ductility

Ductility is expressed by the reduction in area from the following equation:

$$R.A\ (\%)\ =\ (A_0 - A_{min})\ /\ A_0\ \times 100 \qquad 4.55$$

The reduction in area of the segregated and non-segregated regions is shown in Figure 4.13. Compared to the segregated regions, non-segregated regions have higher ductility at high temperature. The figure shows that there is variation in ductility between the segregated and non-segregated regions at high temperature and this variation in ductility increases as the temperature increases. This observation indicates

that the difference between the ductility of the segregated and non-segregated regions in the slab could lead to different behaviour of these regions during hot rolling.

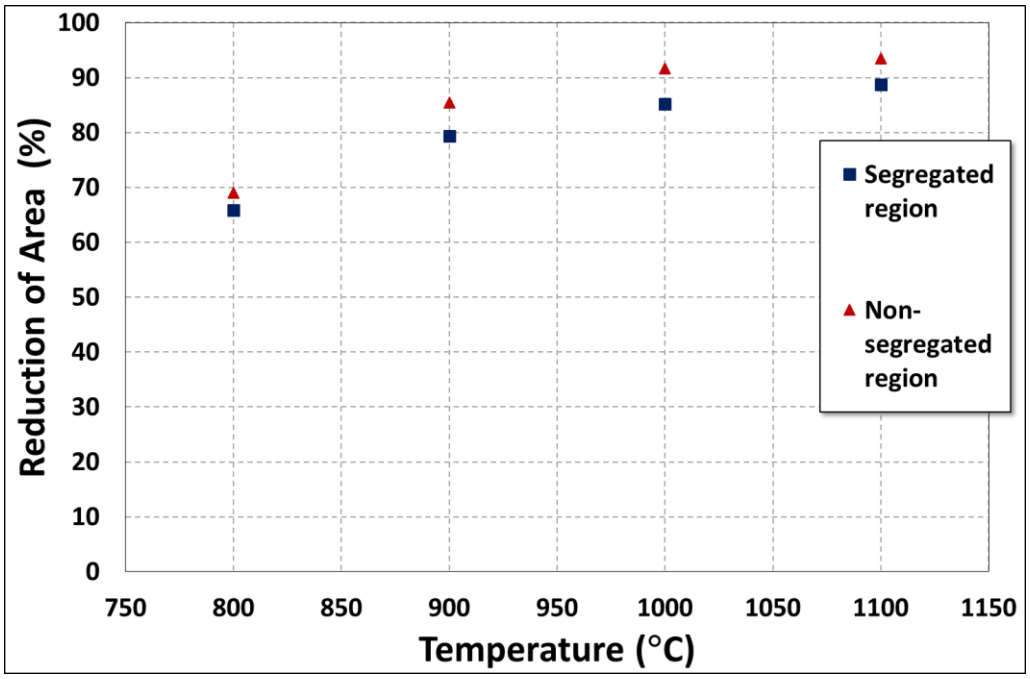

Figure 4.13: Ductility of segregated and non-segregated regions as a function of testing high temperature.

4.3.4 Prediction of Mechanical Properties

Experimental results from this study showed that the mechanical properties of simulated segregated and non-segregated regions in a medium-carbon continuously cast slab were different. Using this experimental data, empirical equations were developed for each region in the slab in order to predict the pertaining mechanical properties at rolling temperatures for use the FE modelling study. Figure 4.14 and Figure 4.15 show the correlations between these empirical equations and the experimental results.

4.3.4.1 Elastic Modulus

The predictive equation to express the elastic modulus as a function of temperature was developed by using the elastic modulus at room temperature for each region, which in this study was measured by using the nano-indentation test.

$$E_T = -4.9\times10^{-11}T^4 + 3.9\times10^{-8}T^3 - 3.22\times10^{-5}T^2 - 0.0265T + E_r \quad 4.56$$

where $800 < T < 1100℃$

E_T is the elastic modulus at high temperature, E_r is the respective elastic modulus at room temperature for the regions under consideration and T is temperature (°C). The predictions of elastic modulus using equation 12 for dendritic and inter-dendritic regions are compared to the experimental measurements in Figure 4.14. The predicted elastic modulus agrees well with the experimental measurements for both dendritic and inter-dendritic regions expect at 800°C for segregated regions.

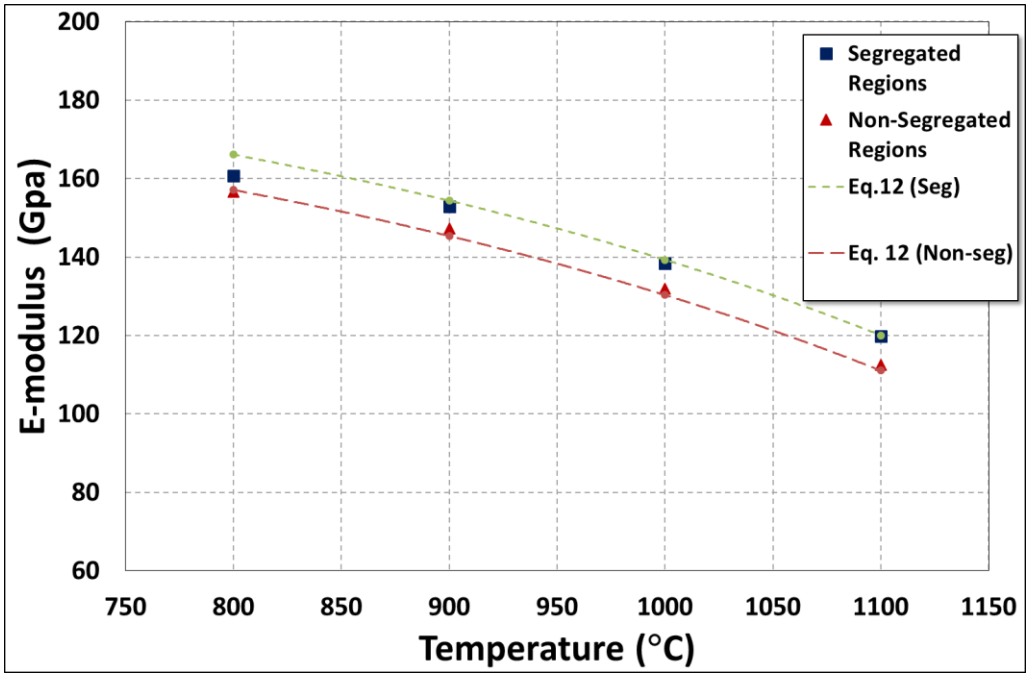

Figure 4.14: Comparison of predicted elastic modulus equation with experimental results.

4.3.4.2 Yield Strength

The predictive equation used to correlate the experimentally determined yield strengths with calculations as a function of temperature:

$$\sigma_{Y_T} = 5\times10^{-3}T^2 + 1.2375T - \sigma_Y \qquad 4.57$$

where $800 < T < 1100℃$

where σ_{Y_T} is yield strength at temperature, σ_Y is yield strength at room temperature of the respective region and T is temperature (°C). The predictions of yield strengths by using equation 13 are compared with the experimentally obtained values of this study in Figure 4.15, showing good agreement except at 1000°C and 1100°C for the segregated regions.

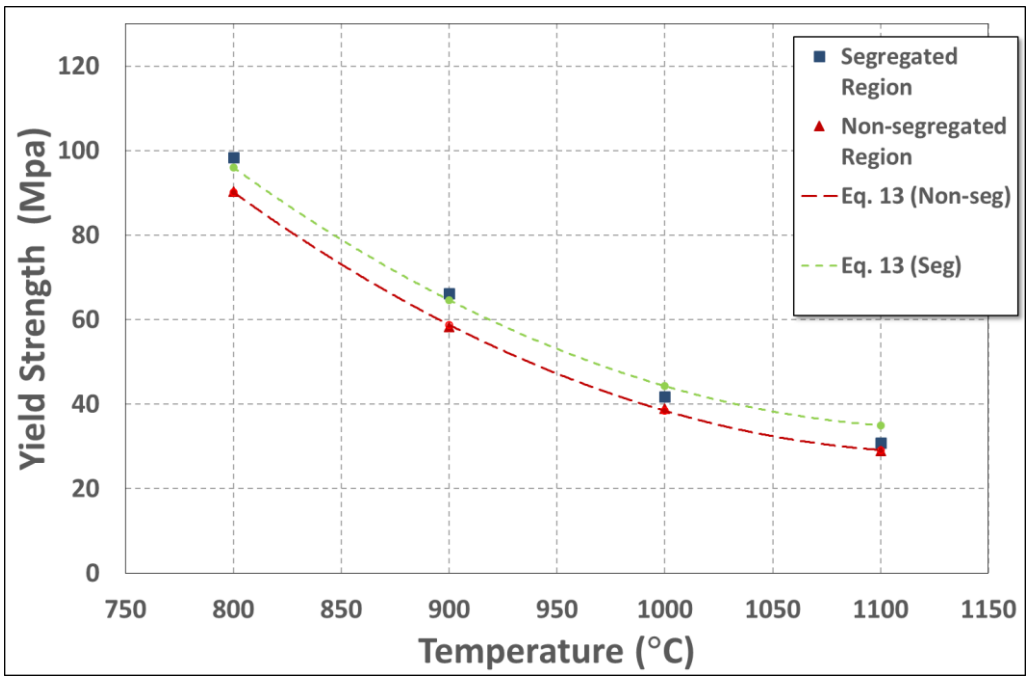

Figure 4.15: Comparison of predicted yield strength equation with experimental results.

4.3.5 Electron Microprobe Analysis

EPMA element mapping was performed to identify the dendritic and inter-dendritic regions as well as to quantify the concentration of alloying elements (mainly manganese) in these regions. The EPMA maps were collected from a 1500 x 1500 µm section of an as-cast sample taken from the quarter thickness of the slab (near the centreline) where dendritic arms have been fully developed and are well-oriented. Details of the way in which EPMA maps were obtained and how quantitative analyses were conducted have been explained in the previous chapter. An example of a Mn concentration map and line scans by EPMA analysis are shown in Figure 4.16. After revealing the dendritic structure, EPMA parallel line-scans were performed across the dendrite primary arm (core) and inter-dendritic regions, as indicated by Lines 1 (across dendrite primary arm) and Line 2 (across inter-dendritic region) in Figure 4.16. By these means manganese element concentrations in both regions were determined quantitatively and the results are shown in Figure 4.17.

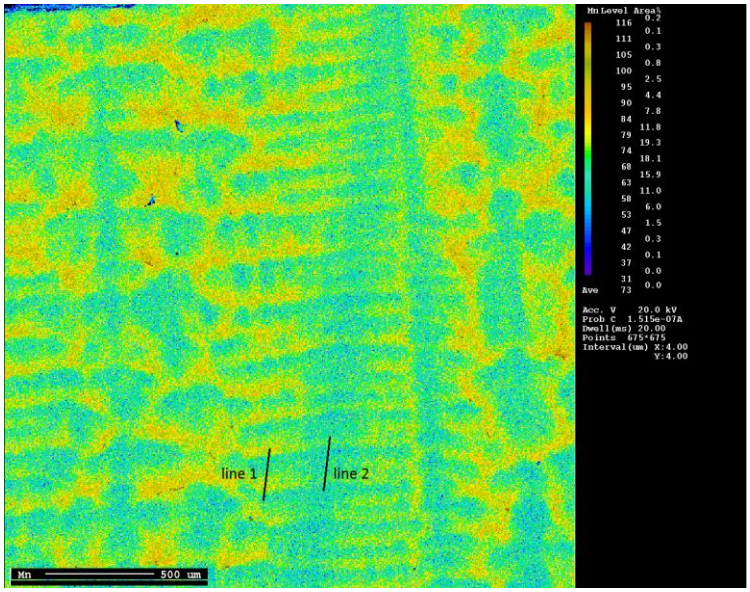

Figure 4.16: Examples of an EPMA manganese concentration line-scan of a sample taken from the quarter thickness of a slab.

Figure 4.17 clearly shows that the inter-dendritic regions are enriched in manganese, the manganese concentration being 0.3- 0.45 wt. % higher in the centre of inter-dendritic regions whereas there is only slight variations of between 1.1 and 1.2 wt.% in the manganese concentration across the primary dendrite arm itself. . This observation is very common in medium-carbon steel and similar to what have been reported by Brooks and Samuels [6, 8].

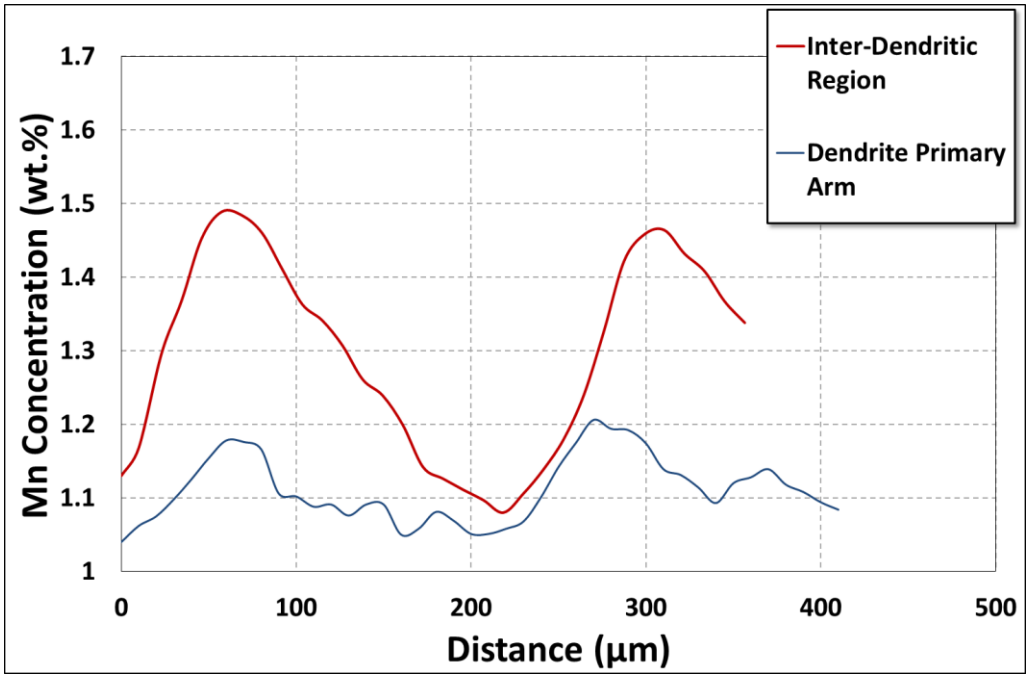

Figure 4.17: Manganese concentration measured by EPMA line-scan across dendritic and inter-dendritic regions of an as-cast sample.

Figure 4.18 shows the manganese concentration using EPMA line-scan with defocused beam performed at five areas across the tip of tensile specimens taken from an area close to the surface of the slab (region 1), which is representative of dendrite arms (low in manganese), and specimens form the quarter thickness (region 2), which is representative of the inter-dendritic regions. Figure 4.18 shows that there is a distinct difference in manganese concentration between these two regions. The manganese concentration is almost uniform across the specimens except for one location on the specimen taken form near surface region. Moreover, there is generally good agreement between the manganese concentrations of the dendritic structures (shown in Figure 3.22) and the manganese concentrations across the representative tips of tensile specimen.

The tip of the tested specimen was selected because it is at this location that necking deformation and fracture occur and it also has relatively small cross-sectional area, which has a more homogeneous chemical composition compared to the other areas across the specimen since the heat generated during deformation, could possibly reduce the local peaks in alloying element concentrations.

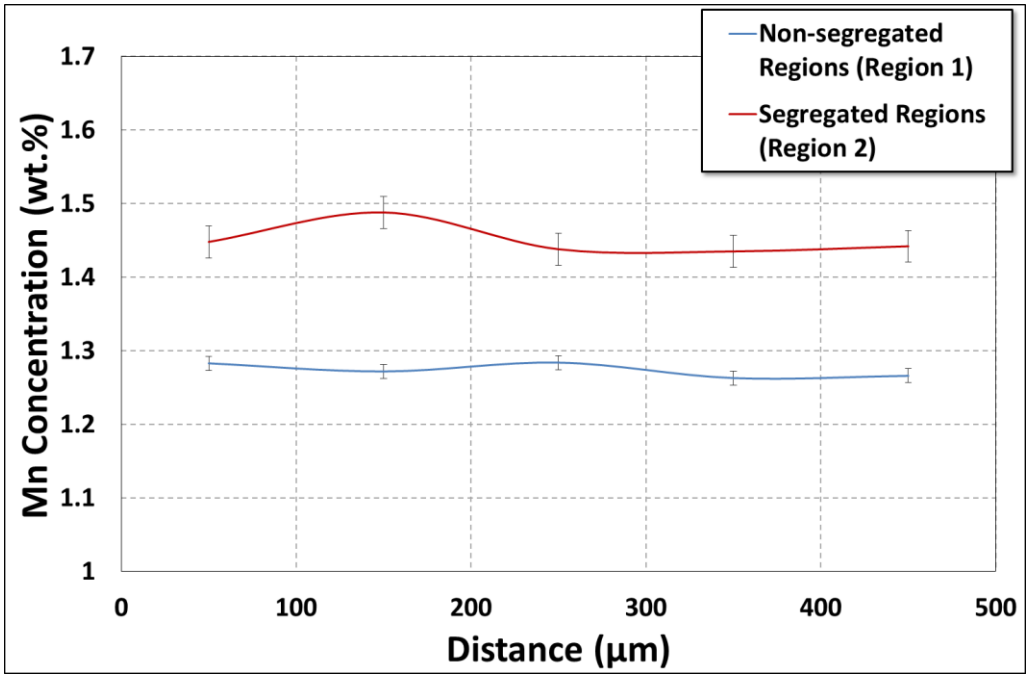

Figure 4.18: Manganese concentration measured by EPMA defocused beam line-scan across tip of tensile tested sample from top and bottom region of as-cast slab sample.

Following Preßlinger [50], the EPMA results provide insights into the maximum concentration (C_{max}) and the minimum concentration (C_{min}) of manganese. From these data, the required segregation coefficients (C_{max}/C_{min}) were calculated for the dendritic and inter-dendritic regions from Figure 3.22. These values are compared in Figure 4.19 to those obtained by Preßlinger [50]. The correlation is generally good although the values are slightly different since the initial manganese concentration in the two steels were different. The initial manganese concentration of the steel used in this study was 1.27wt. % while that of the Preßlinger study was1.5 wt.%.

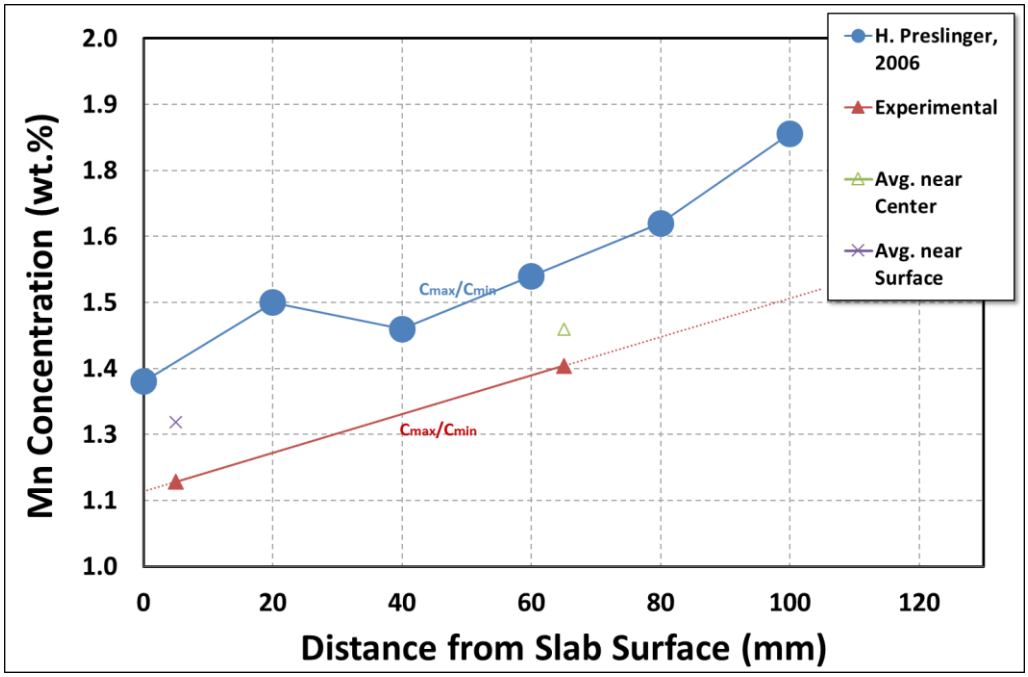

Figure 4.19: Measured and calculated manganese concentration and segregation coefficients across the steel slab and compared to the results of Preßlinger, 2006 [50].

The concentration profiles of manganese measured by EPMA across the samples from the near-surface area of the slab (region 1) and quarter thickness (region 2) were compared to the manganese concentration profile of dendritic and inter-dendritic regions and are shown in Figure 4.20**.** This comparison was made to verify the validity of the assumption that the near-surface region and the centreline region and deep quarter thickness regions as representatives of dendritic and inter-dendritic regions respectively.

It is clear from Figure 4.20 that the manganese concentration in region 1 is close to the maximum value of the manganese concentration in dendrites whereas the manganese concentration in region 2 is close to the maximum manganese concentration in inter-

dendritic regions. This comparison confirms that it is reasonable to assume that region 1 is representative of a primary dendrite arm and region 2 representative of an inter-dendritic region.

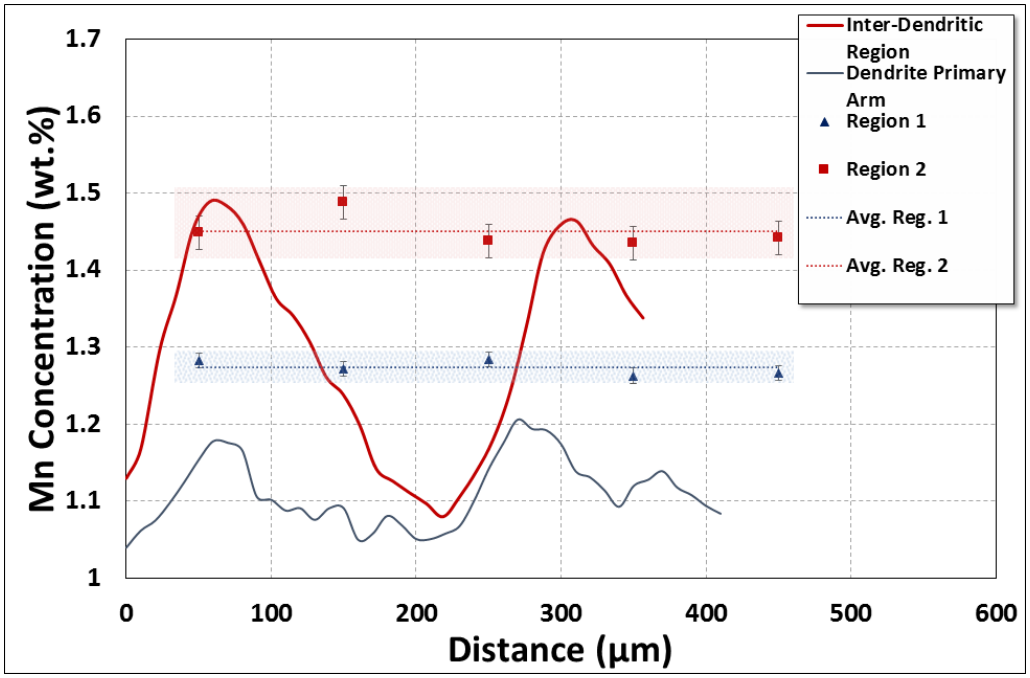

Figure 4.20: Average concentration profile of manganese measured by EPMA for region 1 and region 2, and dendritic structure.

4.4 Conclusions

- Nano-hardness tests at room temperature revealed that there is a discernable difference in mechanical properties between dendritic and inter-dendritic regions in a continuously-cast slab
- There is a significant difference in hardness between the matrix and inter-dendritic regions. Inter-dendritic region is harder by more than 0.4 GPa
- The elastic moduli of inter-dendritic regions are higher than that of the dendritic regions and both elastic moduli were within the range of values reported in the literature
- The assumption that the bulk mechanical properties of specimens sectioned from the near-surface area of the slab are representative of the mechanical properties of dendrites is justified. In similar vein, the mechanical properties of an area close to the centreline can be taken as representative of the mechanical properties of inter-dendritic regions.
- Hot-tensile tests, performed on specimens taken from the near-surface area of the slab representing dendritic regions and specimens from deep thickness near the

centreline representing inter-dendritic regions, revealed that the yield strength and elastic moduli of dendritic and inter-dendritic regions differ by a discernable amount.

Chapter 5. Simulation of Dendritic and Inter-dendritic Regions Behaviour during Hot Rolling of Medium-Carbon Steel

5.1 Introduction

Microstructural banding in medium carbon steel is related to micro-segregation of alloying elements in the form of micro-chemical banding which consist of alternation layers of high and low concentration of alloying elements. Micro-segregation forms during the early stages of solidification and then it is elongated during subsequent hot rolling to form micro-chemical banding. In previous chapters, the formation of elongated micro-segregation and micro-chemical banding were experimentally examined and variations in chemical composition and mechanical properties of lowly segregated and highly segregated regions at elevated temperatures were determined.

In this chapter, two-dimensional symmetric finite element (FE) models were employed to simulate the behaviour of each of these regions during hot rolling of the medium-carbon steel used in this study, due to the difficulties of experimentally analysing this behaviour during hot rolling. Although this simplified model cannot deal with the complex thermal conditions and phase transformations in steel, the behaviour of dendritic structures (segregated and non-segregated regions) that leads to the formation of micro-chemical banding, is the main objective of this part of the present study. The main aim was to track and analyse the distribution of effective stresses and strains in these regions during hot rolling.

5.1.1 General Modelling Approach

A normal modelling approach to solve problems with respect to micro-mechanical modelling is shown in Figure 5.1. For developing a finite element model, experimental results are required to establish a geometrical model that represents the material microstructures or phases. Constitutive equations for each phase are essential to precisely simulate micro-scale behaviour. The equations describing material behaviour under a given set of conditions such as elastic, plastic, visco-elastic behaviour are required to relate stresses and strains for a particular model. Boundary conditions used for the model are to be obtained from experimental results for the purposes of validation. Based on such boundary conditions, behaviour can then be simulated using numerical techniques, e.g. the FEM. If the agreement between the model and

experiments is satisfactory, the model can be used to explain the material behaviour. Otherwise, improvements of the model are required.

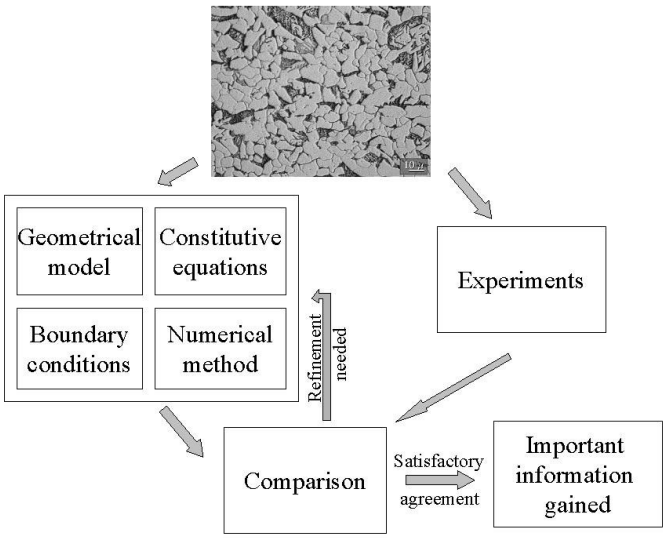

Figure 5.1: Flow chart for micro-mechanical modelling of materials [202].

The main aim of the research described in this part of the study is to investigate the behaviour of dendritic structures (primary dendrite arms, secondary dendrite arms and inter-dendritic (segregated) regions) during hot rolling of medium-carbon steel through developing a two-dimensional finite element (FE) model. This technique is used to simulate the micro-mechanical behaviour of the dendritic structures during plastic deformation process and analyse local distribution of effective stresses and strains at different rolling and material conditions. The behaviour of dendritic structures during hot rolling of the medium-carbon steel under investigation is subsequently correlated to the formation of micro-chemical banding.

5.2 Materials and mechanical properties

The simulations conducted in this study are concerned with the response of dendritic structures of as-cast medium-carbon steel to mechanical deformation. The dendritic structures selected for the simulation studies were obtained from the deep quarter thickness of continuously cast slab (see Figure 3.1). Figure 5.4 is an example of the dendritic structures that was selected for the purposes of the simulation. The dendritic structures consists of three mains features: primary and secondary dendrite arms which are similar in composition and mechanical properties and inter-dendritic regions which vary in chemical composition and mechanical properties. The primary arms align nearly perpendicular to the casting/rolling directions. They are connected to secondary dendrite arms which align parallel to the casting/rolling directions and isolates regions, rich in solute elements have been formed between the secondary dendrites as a result of micro-segregation. The chemical compositions and mechanical properties of each of these regions at room and at high temperatures were assessed and the results were described in Chapters 3 and 4. The dendrite arm spacing in a region selected from the quarter thickness of an industrially produced slab, 300 mm below the surface where dendritic structures are stable and well-oriented, are shown in Table 5.1. It is this structure that was selected for the simulation studies.

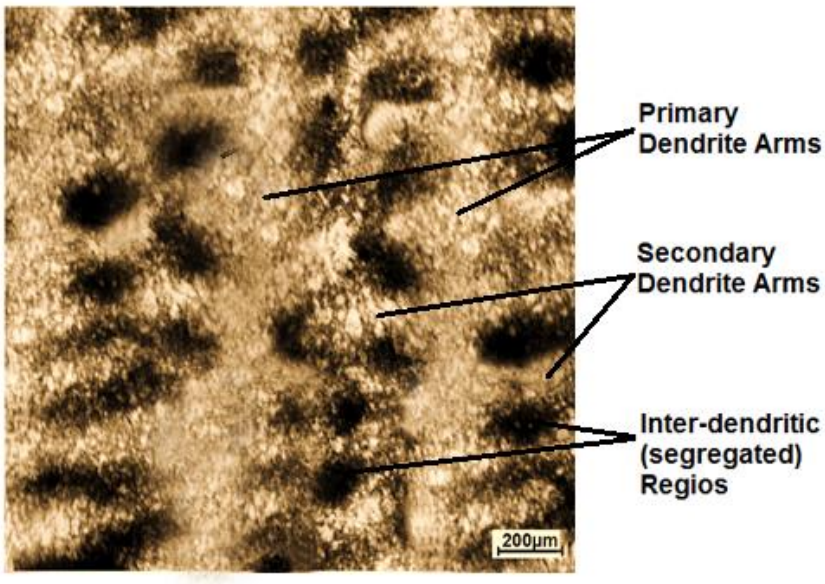

Figure 5.2: dendritic structures of medium-carbon steel obtained from deep quarter thickness of continuously cast slab.

Table 5.1: Dendritic structures measurements.

Dendritic Structure	Spacing	Orientation
Primary Dendrite Arm	λ_1= 310-400µm	Perpendicular to Casting Direction
Secondary Dendrite Arm	λ_2= 180-220µm	Parallel to Casting Direction
Inter-dendritic Segregation	Sg= 100-200 µm	Surrounded between secondary and primary arms

The stress-strain curves for the simulated dendritic regions (steel matrix) and simulated inter-dendritic (segregated) regions were experimentally determined from the uniaxial tensile tests performed at different temperatures as explained in Chapter 4. Because rough rolling is carried out in the temperature range 1100°C to 1250 °C in industrial practice, the stress-strain curves determined at 1100 ºC were selected for further analysis as shown in Figure 5.3.

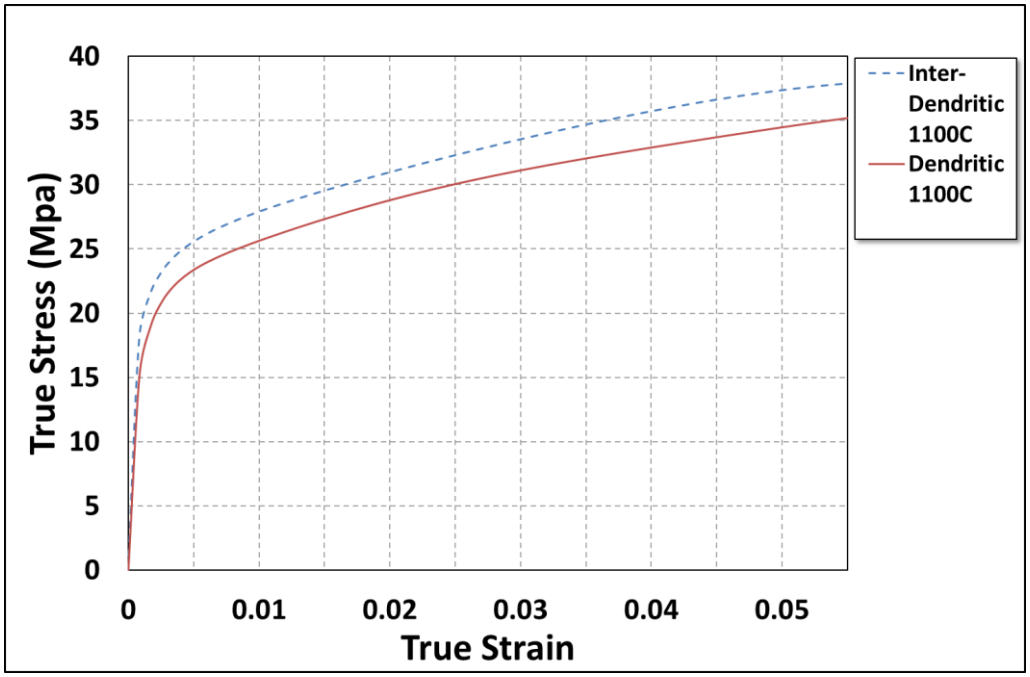

Figure 5.3: Expermintal Stress-Strain curves used in the model.

5.3 Simulation Model and Assumptions

Finite element modelling provides an opportunity to enhance our understanding of the response of dendrites and inter-dendritically segregated areas such as shown in Figure 5.2, to mechanical deformation. In order to study response of this complex morphology to mechanical deformation, the following assumptions were made:

- For the sake of simplicity, an arrangement representing primary arms, secondary dendrite arms and inter-dendritic regions, schematically shown in Figure 5.4 has been adopted. The use of circular shapes instead of dendrites follows the suggestions of earlier approaches recorded in the literature [203-205].
- The mechanical properties of the dendritic and inter-dendritic regions respectively used in FE models were obtained from the calculations and experimental measurements of the mechanical properties of specimens simulating the dendritic and inter-dendritic regions as described in previous chapters.
- The primary dendrite arms are assumed to be of vertically paralleled rectangular shape.
- The primary arms are split by circular micro-segregated regions and secondary arms linked them horizontally.
- An average secondary dendrite arm spacings of 210 µm is assumed.
- An average width of the primary arms is assumed to be 200 µm.
- The diameter of the micro-segregated regions is assumed to be 125 µm.

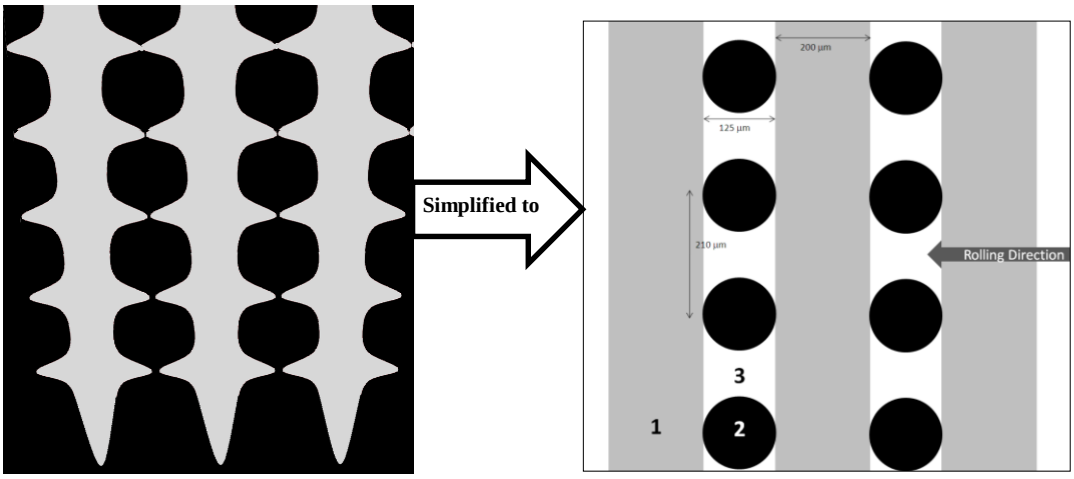

Figure 5.4: Schematic of dendritic structures as (a) commonly presented during solidification process, and (b) simple arrangements of primary dendrite arm (represented by 1), secondary dendrite arms (represented by 3), segregated regions (represented by 2).

- The Von Mises yield criterion is used in plasticity calculations.
- The yield stress in tension was assumed to be equal to the yield stress in compression and the Bauschinger Effect was ignored.
- The flow rule used describes differential changes in the plastic strain components $d\varepsilon^p$ as a function of the current stress state. After yield, the strain increment consists of both elastic, ε^e, and plastic, $d\varepsilon^p$, strains:

$$d\varepsilon = d\varepsilon^e + d\varepsilon^p \quad 5.58$$

- Since e the non-linear plastic strains are much larger than the elastic strains, rigid-plastic models were used in the analysis of the behaviour of the dendritic and inter-dendritic structures during hot rolling process

In the simulation of the behaviour of the dendritic and inter-dendritic structures respectively during hot rolling, the most common and accurate constitutive equation is used, that is given by the well-known power law (for each region): $\sigma = K\varepsilon^n$ where n = strain hardening exponent, $0 < n < 1$ (0 is perfectly plastic and 1 is perfectly elastic) and K = strain hardening coefficient.

- The dendritic structures were built in the model by taking the experimentally measured average sizes of primary and secondary dendrites.
- In order or simplify the modelling exercise, two-dimensional nonlinear approximations were made
- The FE mesh is attached to the material and moves through the rolling gap with the material during rolling. This approach allows stress and strain records to be established at any particular point in the material and to describe the deformation of elements. These model configuration acts as the reference state and the mesh coordinates are updated after every roll-pass.

5.3.1 Boundary conditions

In the rolling model used, contact between the roll and the strand is the main boundary that plays a role in severe nonlinear deformation. During contact, mechanical loads and, sometimes heat are transmitted across the area of contact. In the presence of friction, shear forces are also transmitted [206, 207]. Contact problems are characterized by the gap between the rolls and friction. The size of the gap depends on the displacement of the specimen and determines the degree of reduction, which depends on the contact force as well as the friction coefficient based on the experimental values of hot rolling of medium-carbon steel.

Nonlinear heat transfer is often taken into account in hot-rolling models. However, the main aim of the present model is to distinguish the behaviour of dendrites and inter-dendritic regions during rolling and to determine the stress and strain distribution and hence, the complexity introduced by taking heat-transfer into account has been

avoided. In addition, since the hot rolling is done in the austenite region at constant temperature, phase transformations were not taken into consideration.

5.3.2 Model Description

In order to analyse the deformation of dendritic structures leading to micro-chemical banding during hot rolling, two-levels of model were used, which, as mentioned before, are constructed on macro- and micro-scales respectively. The non-linear FEM software package ANSYS LS-DYNA was used in this study. Deformation of the specimens during hot rolling is simulated by symmetric rigid–plastic finite element methods. In the transient simulation of hot rolling, the specimen is fed into the roll gap gradually with by interfacial friction. The strains are calculated from time-accumulation of computed strain rates. Plane strain rolling is assumed and the rolls are assumed to be rigid. Specimens were designed to have three main parts: a **head** built of a fine-mesh of homogenous material linked to an ultra-fine mesh representing homogenous **dendritic regions** connected to a coarse mesh in the **tail**. The connection areas between the head and dendritic structures, and dendritic structures and tail have a mix of coarse and fine elements in order to facilitate the movement of the specimen during rolling. The head and tail were analysed at macro-level due to their homogeneity while the behaviour of the dendritic structures are analysed on micro-scale. Because of symmetry, only one half of the specimen, containing more than 78500 elements is considered.

5.3.2.1 Macro-Scale Behaviour

Figure 5.5 shows the finite element mesh at the macro-level consisting of 9167 elements of fine meshes in the head of the specimen in the length and thickness directions. The macro-level, homogenous material is connected on one side to the finer elements of the dendritic structures, which will be described below. The tail of specimen has 6291 coarse element meshes in the length and thickness direction, which also represents homogenous material and connected to the dendritic structures form the other side.

The selected elements are traced throughout a rolling step, while they move from the entrance to the exit. The locations, velocities and strain histories for the specified elements are stored for each iteration step. In the simulation, each strain increment is set by a pre-determined time step.

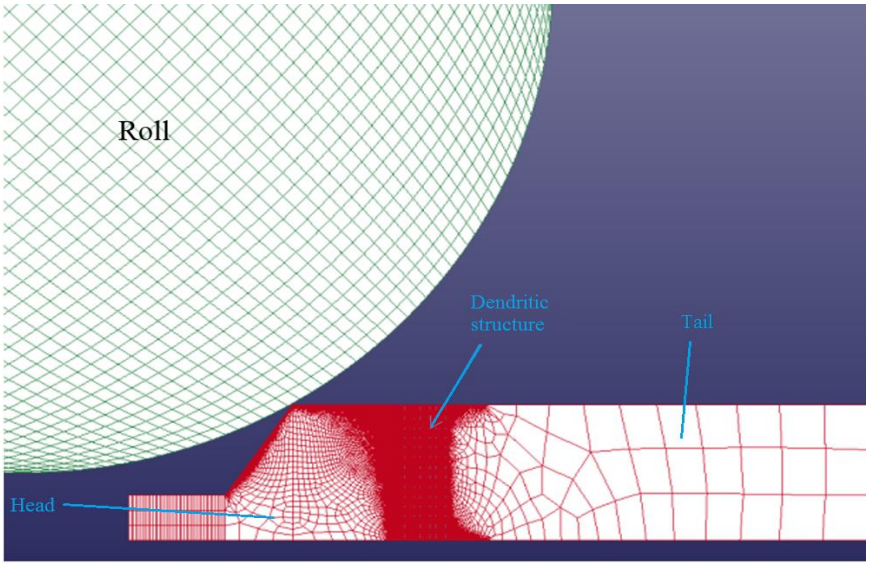

Figure 5.5: Finite Element Mesh of the Macro Cell.

5.3.2.2 Micro-Scale Behaviour

Figure 5.6 shows a part of the micro-level mesh of the dendritic structure. As shown in the figure, cell elements of segregated regions are matched to the primary arms and secondary dendrite arms in the steel matrix. The model consists of more than 63000 elements of ultra-fine meshes for the part of dendritic structures as indicated in Figure 5.5. The dendritic structures are treated across the specimen thickness as a 'unit cell', which contains segregated regions located between two primary arms and two secondary arms on the micro-level scale as shown in Figure 5.6. The dendritic structures comprise 1224 segregated regions, 1207 secondary dendrite arms and 16 primary dendrite arms. Each segregated region has 9 elements, the adjacent secondary dendrite arm 13 elements and 2265 primary dendrite arms. For the sake of simplicity, the shape of the segregated regions is considered to of circular shape. It is assumed that there is perfect bonding between the segregated regions and the dendritic arms (matrix); that there is no interfacial sliding between the segregated regions and the matrix and that no failure occurs, neither in the dendritic regions nor in inter-dendritic (segregated) regions. These assumptions allow each region to be described by the power law to the maximum targeted reduction. By this technique it is possible to simulate the behaviour of real dendritic structures as well as to provide full records of stresses and strains created when the specimen (at macro-scale) is subjected to high reductions. The velocities and coordinates were applied at the macro-level and the global movement of the specimen and the deformation histories were traced at micro-scale.

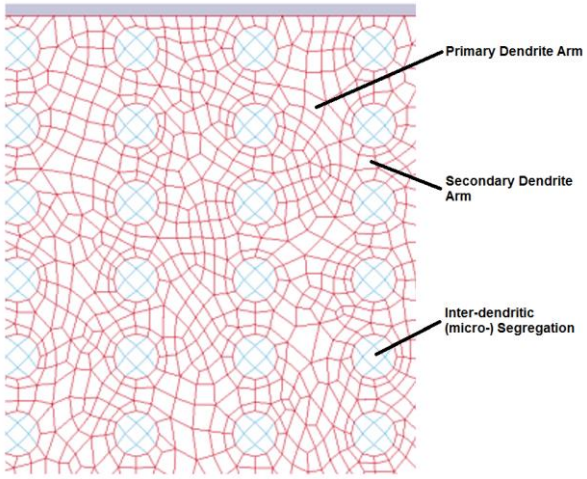

Figure 5.6: fine mesh of part of dendritic structures.

5.3.2.3 Model Conditions

The rolling and material parameters that were used in the models to simulate the laboratory rolling-mill operations, described in Chapter 3, as well as the average dendritic structure geometry are shown in Table 5.2.

Table 5.2: Basic rolling and material conditions.

Roll Diameter (mm)	D= 110.00
Initial thickness of specimen (mm)	H= 15.00
Roll Speed (RPM)	V_R= 30.10
Roll Speed (mm/s)	V_R= 173.28
Friction Factor	m=0.3

Four different models were run with parameters shown in Table 5.3. These data were obtained from experimentally measured values of medium-carbon steel.

Table 5.3: Rolling Reductions and dendritic structure details for the four models.

	Model 1	**Model 2**	**Model 3**	**Model 4**
Primary Dendrite Arm Spacing (μm)	λ_1= 225	λ_1= 550	λ_1= 225	λ_1= 225
Secondary Dendrite Arm Spacing (μm)	λ_2= 210	λ_2= 420	λ_2= 210	λ_2= 210
Segregated Region Diameter (μm)	D_{sg}= 125	D_{sg} = 125	D_{sg} = 125	D_{sg} = 125
Specimen Targeted Final Thickness (mm) at:				
25%	11.25	--	--	--
50%	7.50	7.50	--	--
60%	6.00	6.00	6.00	6.00
70%	4.50	--	--	--
Stress-strain Curve Used	Figure 5.3	Figure 5.3	Figure 5.7	Figure 5.7

Model 1 acted as a reference. Different primary and secondary dendrite arm spacing were assumed in in Model 2. In Model 3, the stress-strain curves shown in Figure 5.7 were used for the dendritic and inter-dendritic regions respectively. Model 4 acted as a control model and it was assumed that the inter-dendritic (segregated) and dendritic (primary arm and secondary dendrite arms) regions have exactly the same mechanical properties. The stress-strain curve for this model is also shown in Figure 5.7.

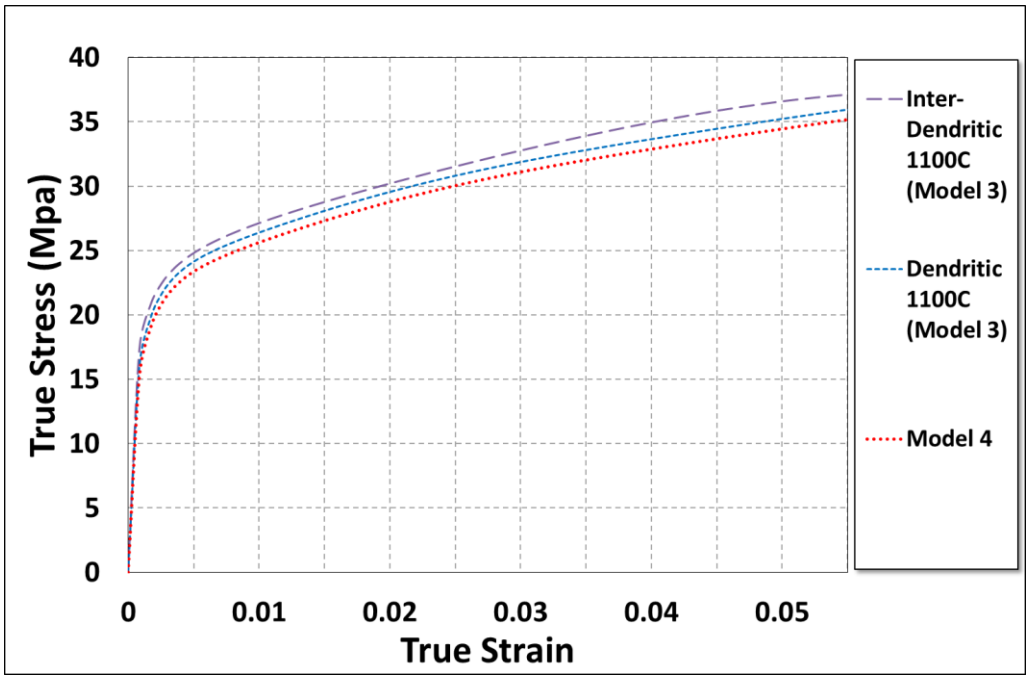

Figure 5.7: Expermintal Stress-Strain curves used in the Model 3 and Model 4.

5.4 Results and Discussions

5.4.1 Macroscopic Behaviour

The response of the dendritic structures during hot rolling are on macroscopic level intimately linked to the stress and strain distribution.

5.4.1.1 Strain Distribution

The effective strain increases from the entry of the roll bite and reaches a value close to the true strain at the exit. The non-uniformity of strain in the longitudinal direction is greater than in the thickness direction. This mainly depends on the reduction and the friction factor (Table 5.2). Since the materials at the head of specimen are the same in all models, Model 1 was used to analyse strain distribution at different reductions applied to this part of specimen. The inhomogeneity of strain across the strip thickness is illustrated in ***Figure*** 5.8 for 25, 50, 60 and 70% rolling reductions. The figure shows the non-uniformity of plastic deformation in the roll gap in both thickness and longitudinal directions as a function of reduction. The surface of the specimen experiences a higher strain and a higher strain rate than the centre. The highest strained zone is close to the entry of the roll gap owing to the sudden change of rolling gap in the vertical direction. Such inhomogeneous deformation in the roll bite has been reported in literature [126, 133, 208-214].

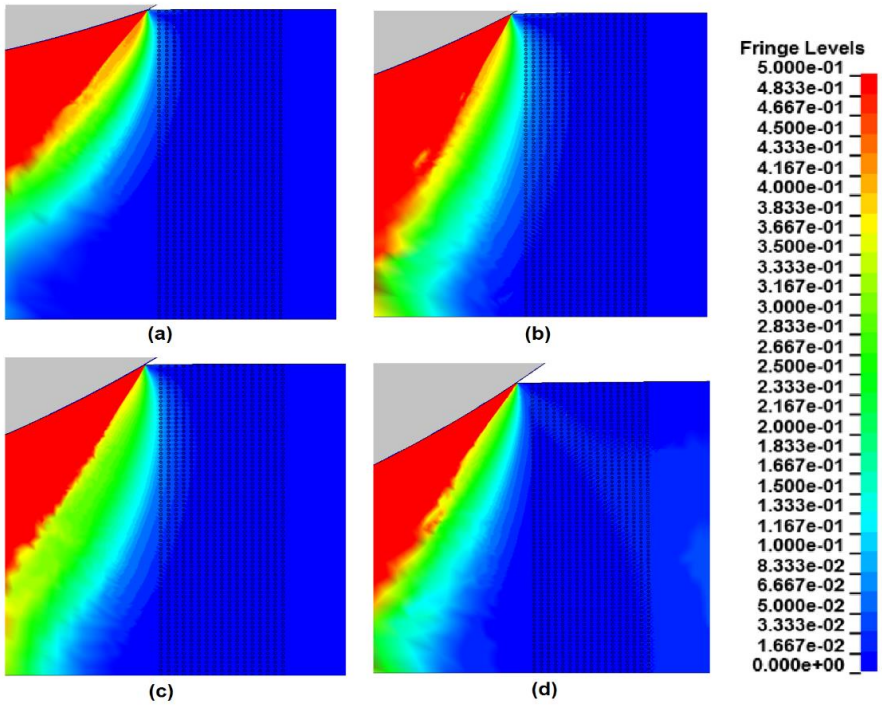

Figure 5.8: Effective strain at different reductions (a) 25%, (b) 50% (c) 60% and (d) 70%.

5.4.1.2 Stress Distribution

Figure 5.9 shows the evolution of effective stress during rolling at 25, 50, 60 and 70% reductions respectively. The variation of the effective stress through the thickness and maximum effective stress occurs at the centre of all rolled specimens. The effective stress increases from the entry of the roll bite and reaches a value close to the true stress at the exit. The non-uniformity of stress in the thickness direction is greater than in the longitudinal direction. Model 1 was used to analyse the stress distributions at different reductions applied on this part of specimen. These findings are in agreement to the earlier research of Wang [208], who reported the non-uniform strain rate and strain lead to non-uniform stress. The same observations were also reported in several studies of uniform materials at macro-scale [133, 210-213].

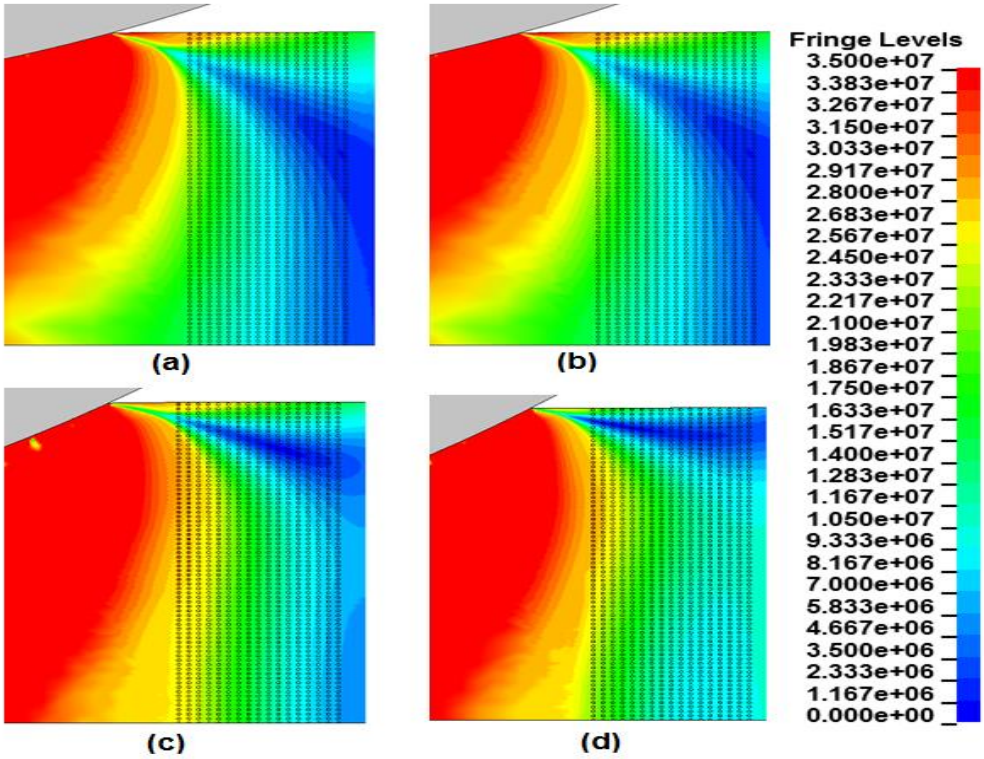

Figure 5.9: Effective stress in different reductions (a) 25%, (b) 50% (c) 60% and (d) 70%.

5.4.1.3 Rotation of Primary Dendrite Arms

Figure 5.10 shows the dendritic structures (primary and secondary dendrite arms and segregated regions) simulated just before entering the roll bite. Upon entering the roll bite, the primary dendrite arms rotate about the rolling direction and change from vertical to an angle with respect to the rolling direction. This rotation is depicted for 25 and 50% reductions in more detail in Figure 5.11 and Figure 5.12 respectively. The

meshes representing primary dendrite arms concave in the direction of material flow of the specimen due to the change in the strain across the specimen thickness. Despite this rotation, they are staying parallel to each other. The secondary dendrite arms and their adjacent segregated regions undergo movement along the rolling direction and are flattened along rolling direction. The primary dendrite arm rotation corresponds to the material flow and the variation of the effective strain across the specimen thickness. The simulated behaviour of dendritic structures during hot rolling at macro-level shown in Figures 5.10 to 5.13, is quite similar to those experimentally found and reported in the previous chapters and are also shown in Figure 5.13 (a) and (b).

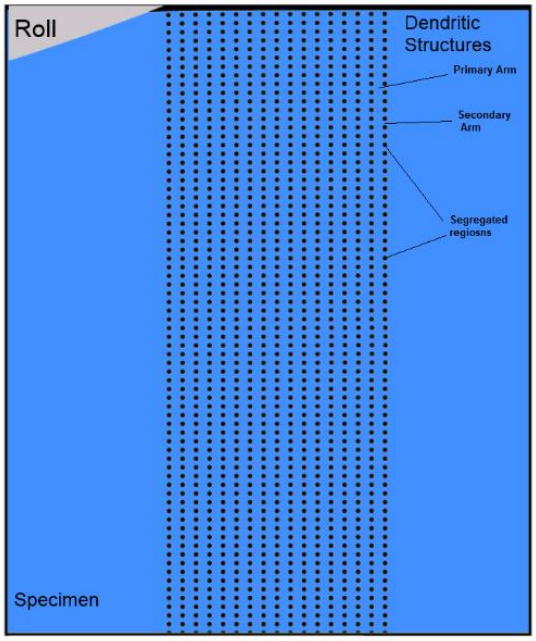

Figure 5.10: Dendrite structures just before entering roll bite.

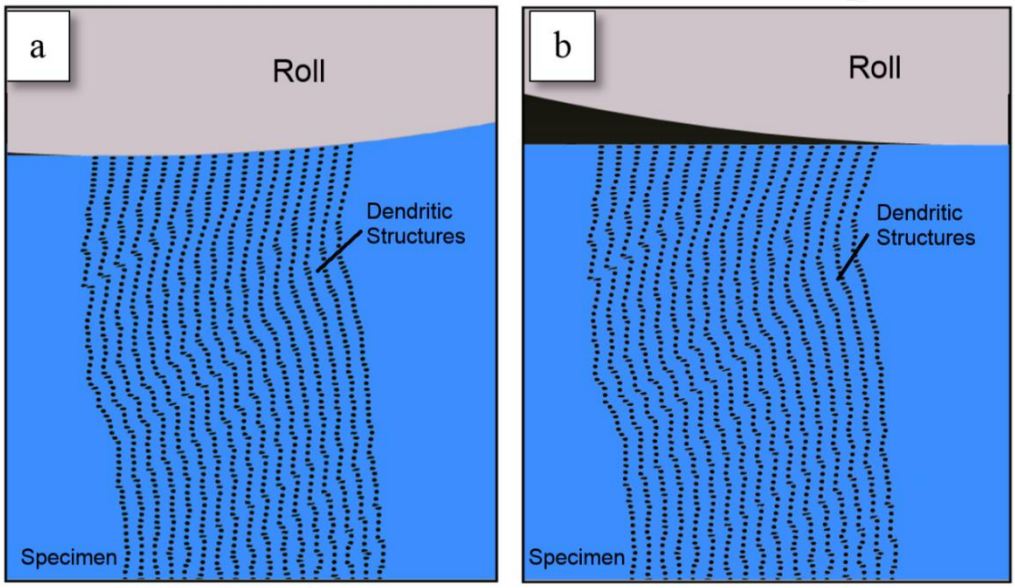

Figure 5.11: Macroscopic behaviour of dendrite structures at 25% reduction: (a) in the maximum deformation zone, and (b) after rolling.

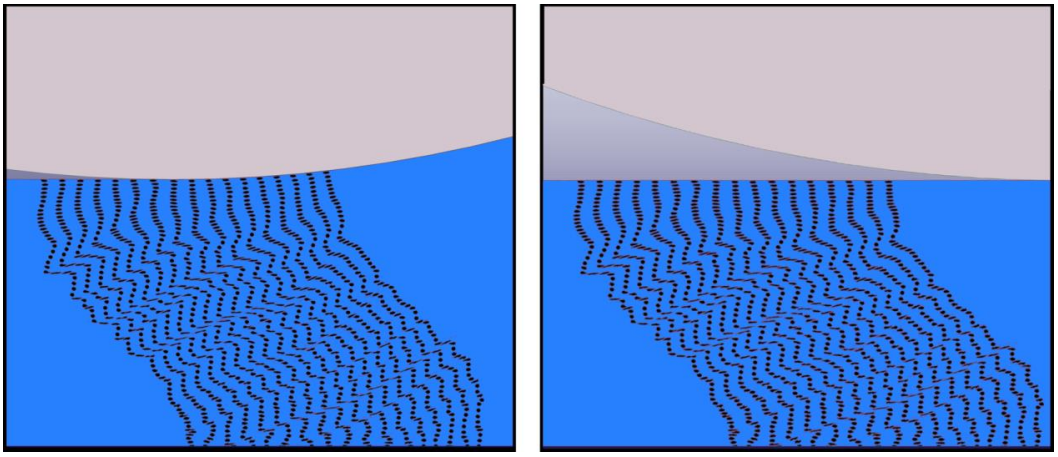

Figure 5.12: Macroscopic behaviour of dendrite structures at 50% reduction: (a) in the maximum deformation zone, and (b) after rolling.

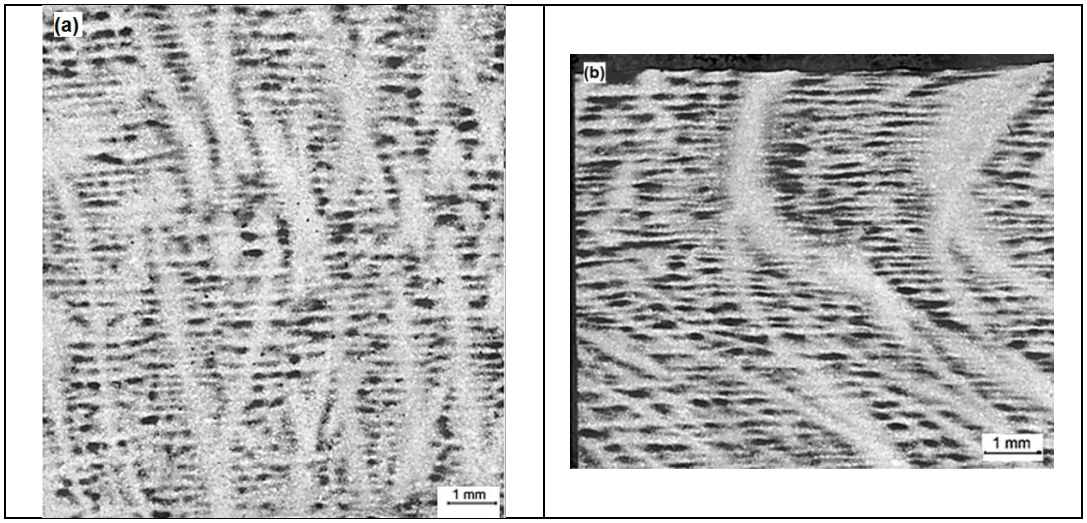

Figure 5.13: Experimental observations of the behaviour of dendrite for (a) 25% reduction and (b) 50% reduction respectively.

Although little information about dendrite arm rotation is available in the literature, Flemings [171] and Spencer *et al.* [172] reported dendrite rotation (bending) and dissertation during deformation of semisolid dendrites of Sn-15% Pb alloy. The effect of material flow and strain distribution during hot rolling plays a key role in controlling the rotation (bending) of primary dendrite arms as well as the elongation of secondary dendrite arms and the inter-dendritic segregation regions between the secondary dendrite arms. Pawelski and Gopinathan [173] reported bending on screws fixed in different positions in steel specimen and rolled at 950°C to 28.6% deformation. After rolling it was observed that the screws from the longitudinal axis of the specimen bent into the rolling direction. The flow behaviour of steel during hot rolling is related to the imposed strain and Pawelski and Gopinathan have shown that there is variation in the strain across a rolled specimen with the maximum strain at the centre of the specimen almost double the nominal strain. Sakai *et al.* [174] reported similar bending of an embedded pin in a 2.5-mm thick steel plate subjected to hot rolling to 40% at temperatures between at 650 and 850°C to 40%.

The rotation of primary dendrite arms about the rolling axis decreases with increasing specimen reduction as shown in Figure 5.14. While the primary dendrite arms rotate by about 5 degrees about rolling direction at 25% reduction in thickness, the rotation angle decreases rapidly to reach about 53 and 65 at 60 and 70% of reductions respectively. By extrapolating these data for higher deformations, the rotation angles of the primary dendrite arms obtained from the models showed excellent agreement with the experimental observations since the primary dendrite arms start to align with rolling direction at about 75% reduction. These results are also in reasonably good agreement with Pressinger [55]. The rotation of primary dendrite arms at higher reductions, say up to 90%, agrees well with experimental observations. At this level of reduction, the primary dendrite arm structure is completely destroyed and they are aligned in the rolling direction to form micro-chemical bands.

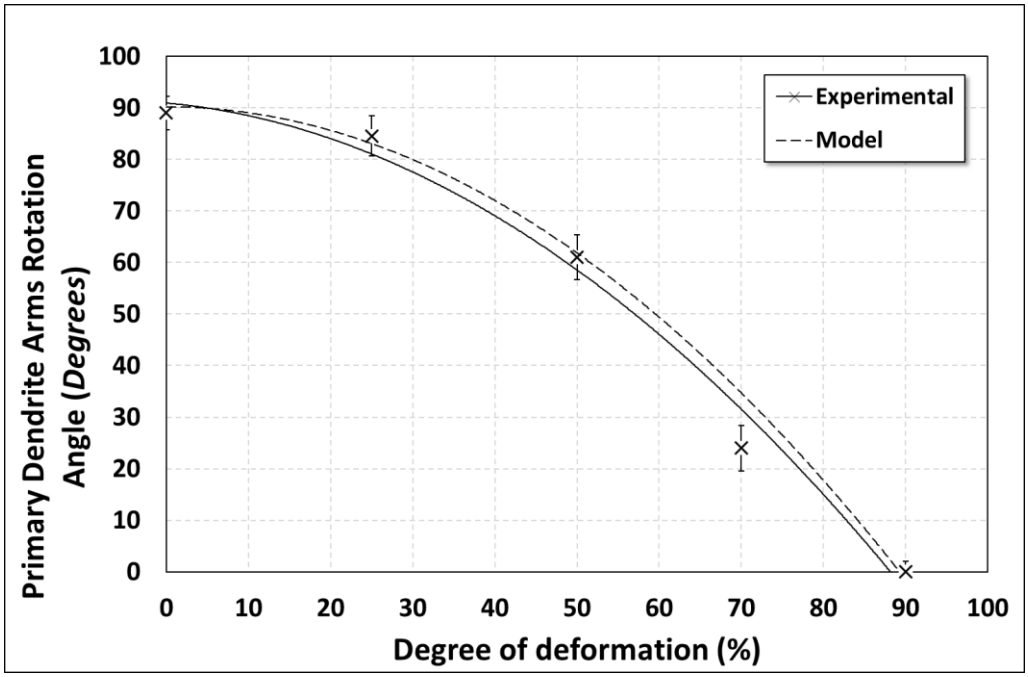

Figure 5.14: Change in primary dendrite arms rotation angle about rolling axis as function of reduction.

5.4.2 Microscopic Behaviour

5.4.2.1 Behaviour of dendritic structures

Figure 5.15 to Figure 5.17 are microscopic views of simulated dendritic structures during rolling to different reductions. As shown in Figure 5.15 (a), (b) and (c) for specimens of Model 1 rolled to 25, 50 and 60% respectively, the secondary dendrite arms and adjacent inter-dendritic segregated regions are elongated and flattened in the rolling direction quite apart from the rotation of the primary dendrite arms about the rolling direction. The elongation of secondary dendrite arms and inter-dendritic regions generally increase at higher reductions until the dendritic structures disappear in the affected areas as shown in the specimen with 60% reduction.

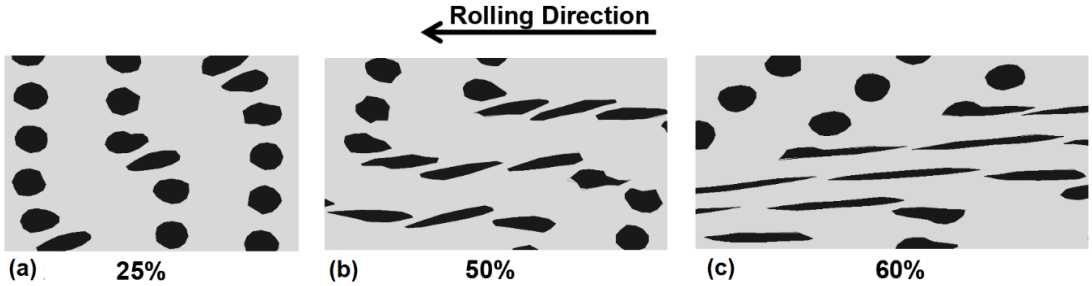

Figure 5.15: Microscopic view of dendritic structures during hot rolling at (a) 25% (b) 50% and (c) 60% reductions using Model 1.

The same arguments apply to the specimens of Model 2 rolled to 50 and 60% respectively. The spacing between the inter-dendritic regions are larger because of the

initial larger dendritic arm spacing assumed in Model 2 as shown in Figure 5.16 (a) and (b) respectively.

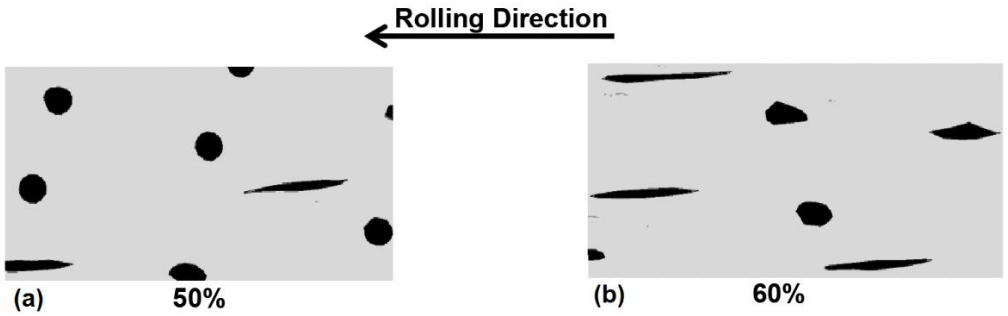

Figure 5.16: Microscopic view of dendritic structures hot rolled to (a) 50% and (b) 60% reduction using Model 2.

The slight change in mechanical properties of the dendritic regions and inter-dendritic segregated regions used in Model 3 resulted in the simulated structures shown in Figure 5.17 (a).

Model 4 was a control model and it was assumed that the mechanical properties of the dendritic regions and inter-dendritic segregated regions are exactly the same as shown in Figure 5.7 above. In this instance, the behaviour of the inter-dendritic regions is completely different as shown in Figure 5.17 (b) and the response to hot rolling is akin to that of homogeneous material.

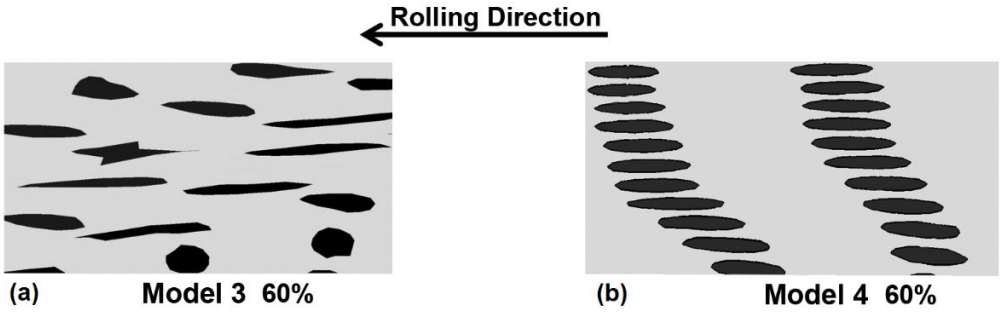

Figure 5.17: Microscopic view of dendritic structures during hot rolling at 60% reductions in (a) Model 3 and (b) Model 4.

There is variation in the effective strain in the through-thickness of the specimen and in these highly strained regions, the secondary arms are elongated more than their adjacent segregated regions due to the variation in mechanical properties between secondary arms (softer) and inter-dendritic segregated regions (harder).

5.4.2.2 Effective Strain Distribution

5.4.2.2.1 Model 1: Basic Conditions

Figure 5.18 and Figure 5.19 show the effective strain contour upon entering the dendritic structures the roll bite and halfway through rolling respectively to 25, 50 and 60% reductions and using Model 1. It follows that the strain is partitioned between inter-dendritic segregated regions and dendritic regions and local bands of high and low strains respectively are formed. The high strain bands initiate at the contact point between strand and roll and propagate toward the centre of the specimen through the softer dendritic regions (primary and secondary dendrite arms) that are located between the harder inter-dendritic regions. More strain partitioning occurs as the strand move through the rolls as shown in Figure 5.18 (c) Figure 5.19 (c). Detailed examination of the strain partitioning shown in Figure 5.20 to Figure 5.22 indicates that high strain bands propagate through the dendritic regions.

It is interesting to note that strain partitioning during deformation has been observed in multiphase steels and that the cause of strain partitioning has been attributed to microstructural inhomogeneity and the concomitant differences in micro-mechanical properties of the respective phases [137, 215-220]. Moreover, Sun [137] suggested that the microstructural inhomogeneity of dual phase steels is the key to plastic strain localization during deformation. In similar vein, Paul [218] argued that strain incompatibility between the softer ferrite matrix and the harder martensite phase arises during tensile straining because of the difference in flow characteristics of the two phases. Local deformation in ferrite is constrained by adjacent martensite islands, which results in local stress partitioning.

Strain partitioning and the formation of local stain bands due to the inhomogeneity of the dendritic structures are exacerbated in specimens deformed to 50 and 60% reductions as shown from Figure 5.18 (b) and (c) and Figure 5.19 (b) and (c) for dendritic structures upon entering the roll bite and halfway through the roll gap respectively. It is evident that the severity of strain partitioning and localization increase with increased reductions.

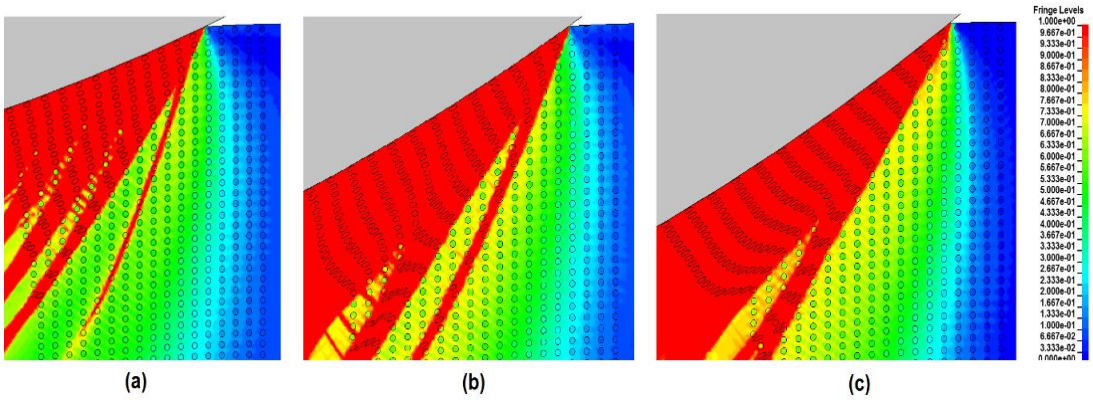

Figure 5.18: Strain contours (indicated by fringe levels) in part of the dendritic structures upon entering the roll bite (a) 25% Reduction, (b) 50% Reduction, and (c) 60% Reduction.

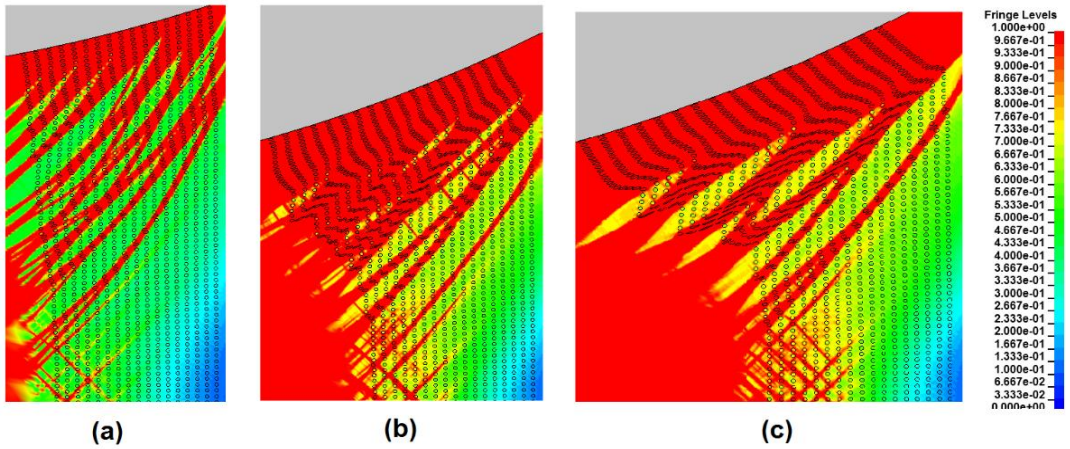

Figure 5.19: Strain contour (indicated by fringe levels) in the dendritic structures halfway through the rolling gap (a) 25% Reduction, (b) 50% Reduction, and (c) 60% Reduction.

In order to quantify the local strains and strain partitioning, the strains present in the strand at the point of maximum deformation in the roll bite was analysed at different reductions. The outcomes of this analysis are shown in Figure 5.20, Figure 5.21 and Figure 5.22 for reductions of 25, 50 and 60% respectively

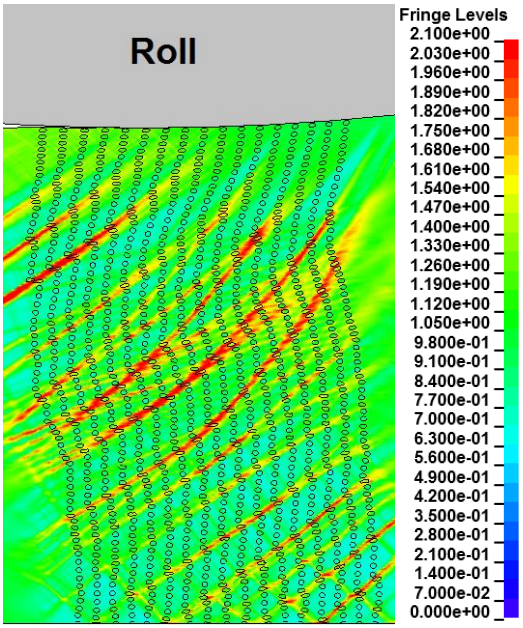

Figure 5.20: Strain contour (indicated by fringe levels) in the dendritic structures at the point of maximum deformation in the roll bite (25% Reduction).

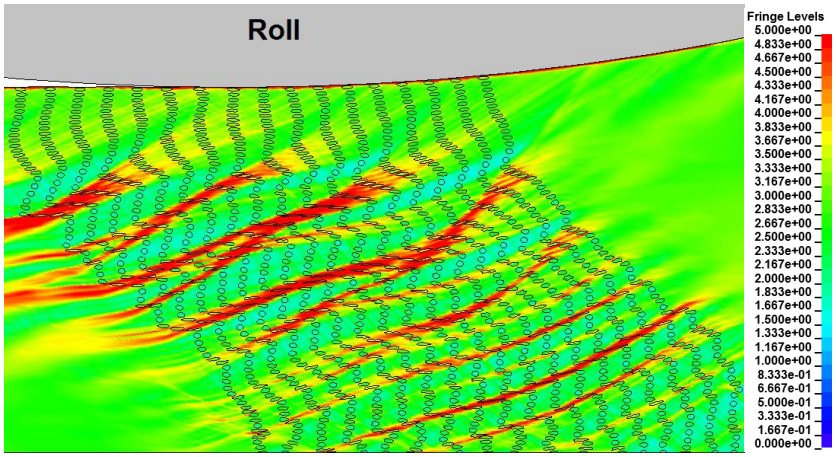

Figure 5.21: Strain contour (indicated by fringe levels) in the dendritic structures at the point of maximum deformation in the roll bite (50% Reduction).

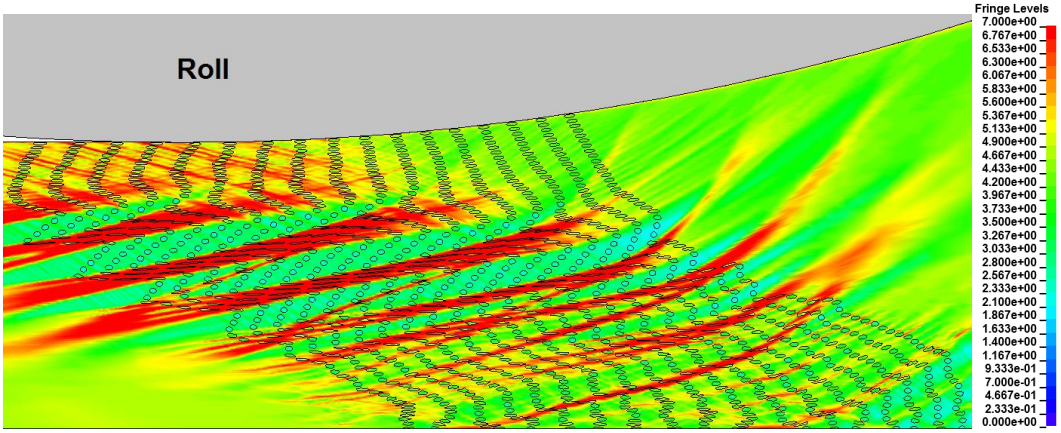

Figure 5.22: Strain contour (indicated by fringe levels) in the dendritic structures at the point of maximum deformation in the roll bite (60% Reduction).

Closer scrutiny of the strain bands, at higher magnification reveals that the strain in the secondary dendrite arm is much higher than the strain in the adjacent inter-dendritic regions as shown in Figure 5.23, Figure 5.24 and Figure 5.25 for reductions of 25, 50 and 60% respectively. These figures also show the flattening and transforming of the secondary arms from circles to ellipsoids at higher reductions.

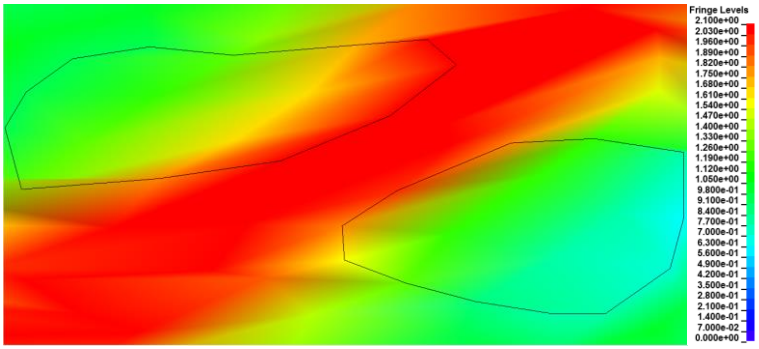

Figure 5.23: Strain contour (indicated by fringe levels) on the dendritic and segregated regions at maximum deformation zone between rolls at 25% reduction.

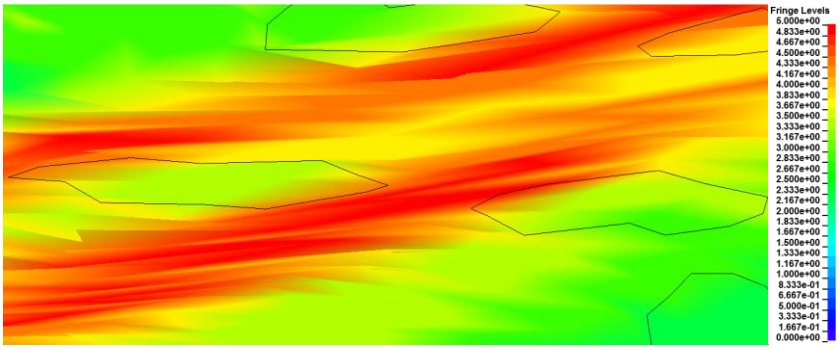

Figure 5.24: Strain contour (indicated by fringe levels) on the dendritic and segregated regions at maximum deformation zone between rolls at 50% reduction.

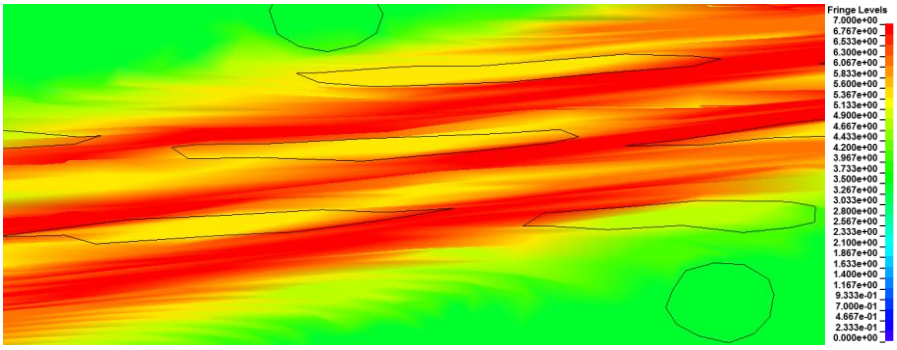

Figure 5.25: Strain contour (indicated by fringe levels) on the dendritic and segregated regions at maximum deformation zone between rolls at 60% reduction.

Figure 5.26 shows the effective strain distributions in the secondary dendrite arms and the adjacent inter-dendritic segregated regions located in a highly strained band at 25% reduction. It is evident that the softer secondary dendrite arms strain more than the harder segregated regions.

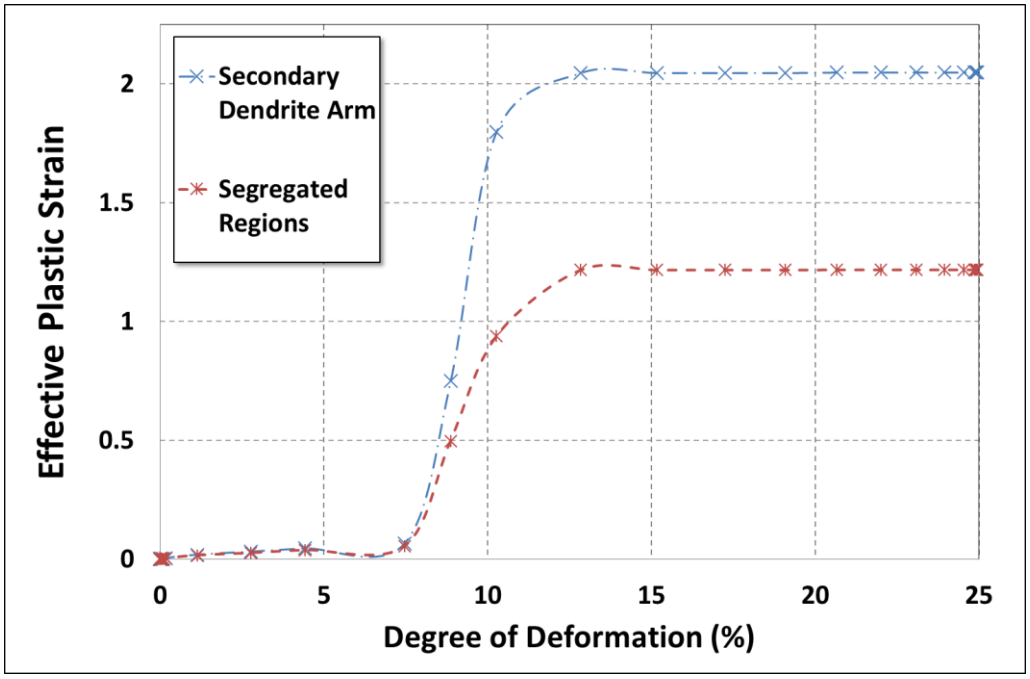

Figure 5.26: Effective plastic strain of the secondary dendrite arms and the segregated regions following a single pass to 25% reduction.

Figure 5.27 shows, in similar vein, the effective plastic strain in the secondary arms and segregated regions respectively following 50% reduction.

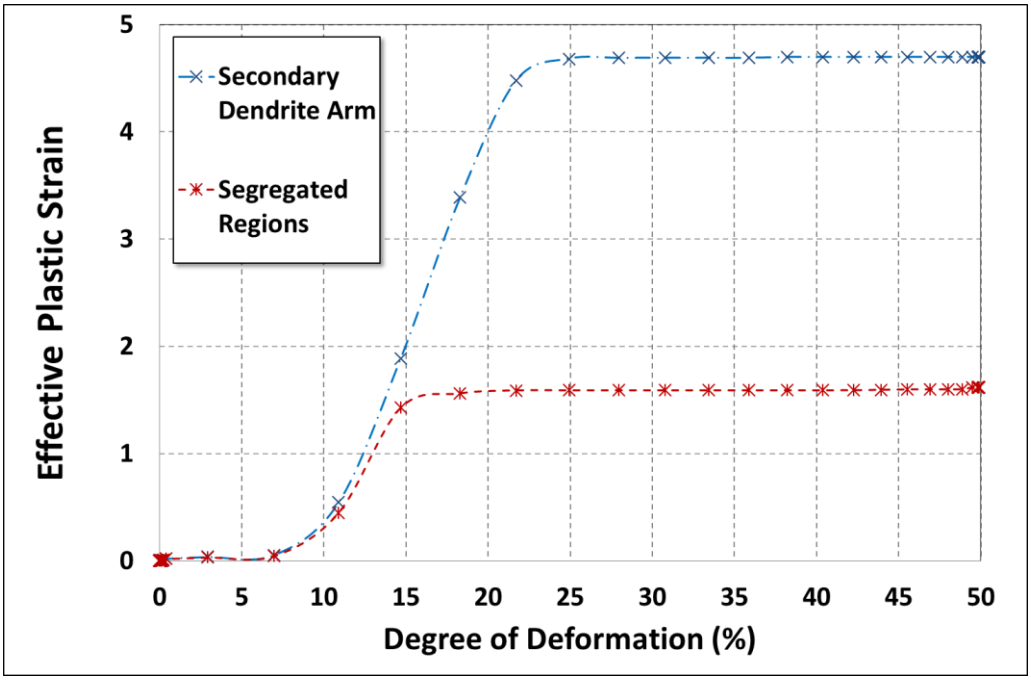

Figure 5.27: Effective plastic strain of the secondary dendrite arms and the segregated regions following a single pass to 50% reduction.

Figure 5.28 shows the effective plastic strain of the secondary arms and the segregated regions respectively following reduction to 60%.

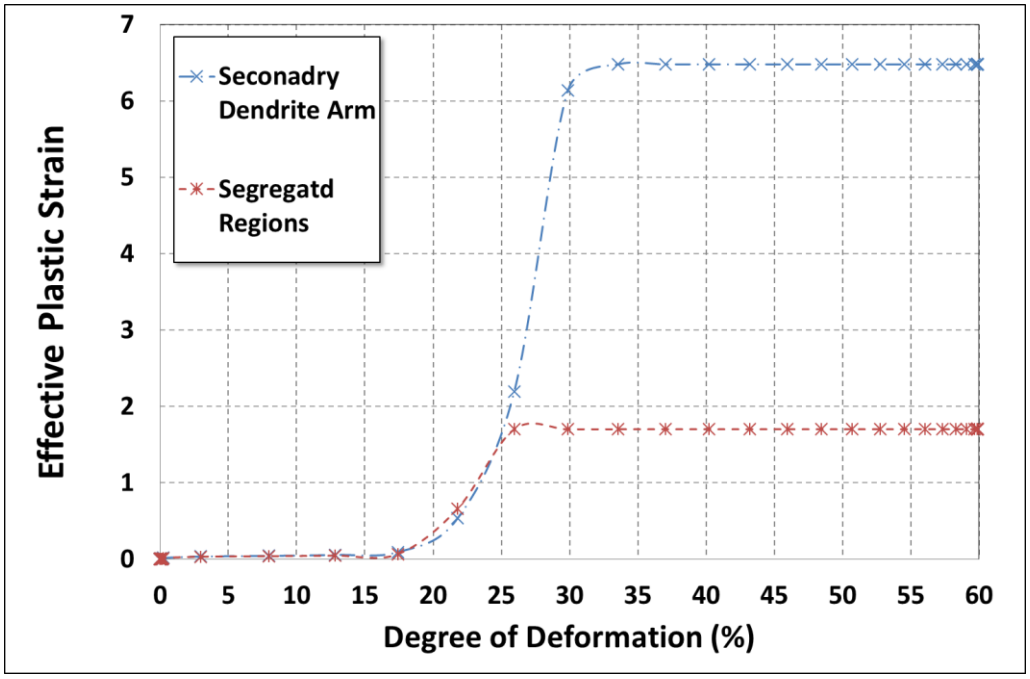

Figure 5.28: Effective plastic strain of the secondary dendrite arms and the segregated regions following a single pass to 60% reduction.

5.4.2.2.2 Model 2: The Effect of Dendrite Arm Spacing

In Model 2 the effect of larger primary and secondary dendrite arm spacing has been considered. The effective strain distributions in the dendritic and the inter-dendritic segregated regions respectively are presented in

Figure 5.29 (a) and (b) for single pass 50 % and 60% reductions respectively.

Although the primary and secondary arm dendrite spacing are double those in Model 1, the same local strain partitioning and strain bands development have been observed.

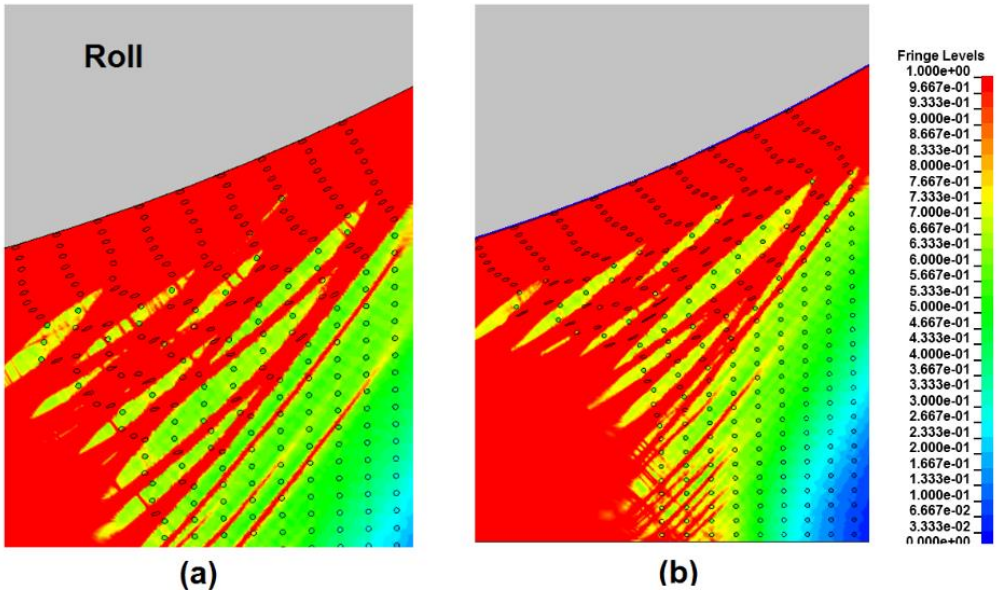

Figure 5.29: Strain contour (indicated by fringe levels) in the segregated regions halfway through the roll bite (a) 50% reduction and (b) 60% reduction.

Details of the strain in the secondary dendrite arm is much higher than the strain in adjacent inter-dendritic regions as shown in Figure 5.30 and Figure 5.31 for reductions of 50 and 60% respectively. These figures, relevant to the maximum deformation zone, also show the flattening and transforming of the secondary arms from circles to ellipsoids increase at higher reductions. However, the spaces between elongated regions are greater than for the same reduction in Model 1.

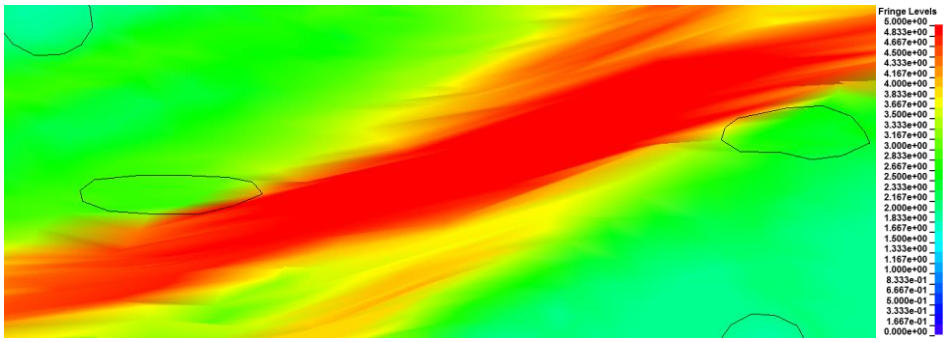

Figure 5.30: Strain contour (indicated by fringe levels) of the dendritic and segregated regions in the zone of maximum deformation at 50% reduction.

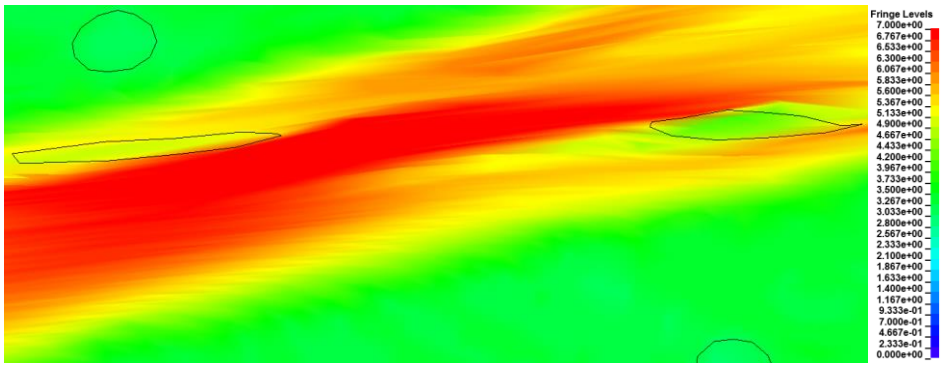

Figure 5.31: Strain contour (indicated by fringe levels) on the dendritic and segregated regions in the zone of maximum deformation at 50% reduction.

Figure 5.32 shows the effective plastic strain in the secondary dendrite arms and segregated regions located in the same strained bands following 50% reduction. The softer secondary dendrite arms strain more than the harder segregated regions as before.

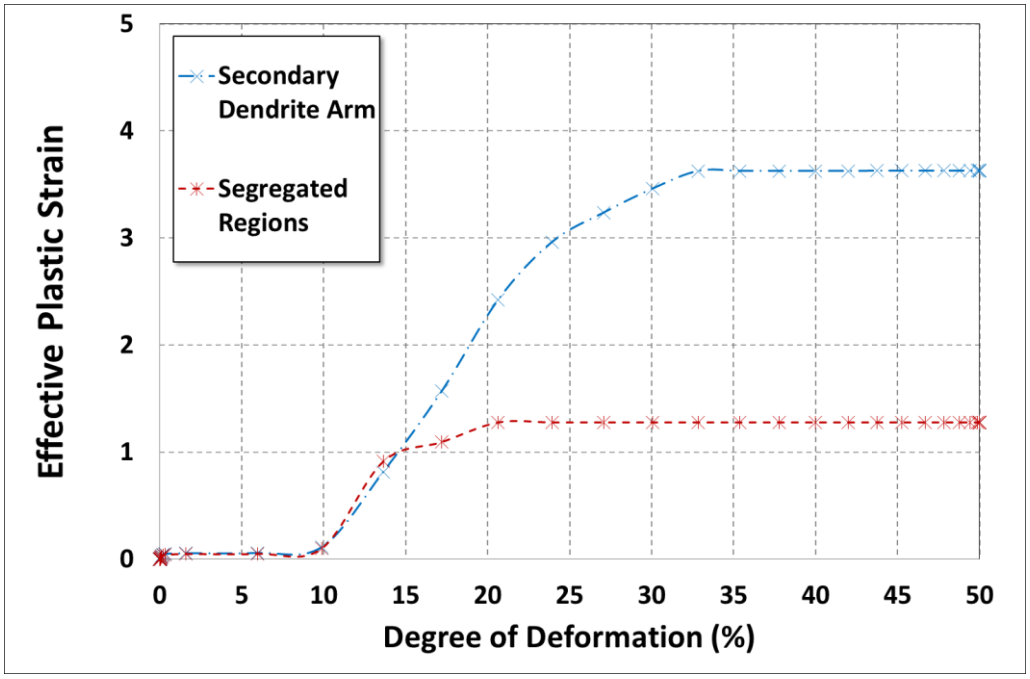

Figure 5.32: Effective plastic strain of secondary dendrite arms and segregated regions following a single pass to 50% reduction.

Figure 5.33 shows the effective plastic strain of secondary dendrite arms and segregated regions following a single pass to 60% reduction. It is apparent also in this instance, that as the deformation increases, the secondary arms experience more strain than the adjacent segregated regions located in the same strained band.

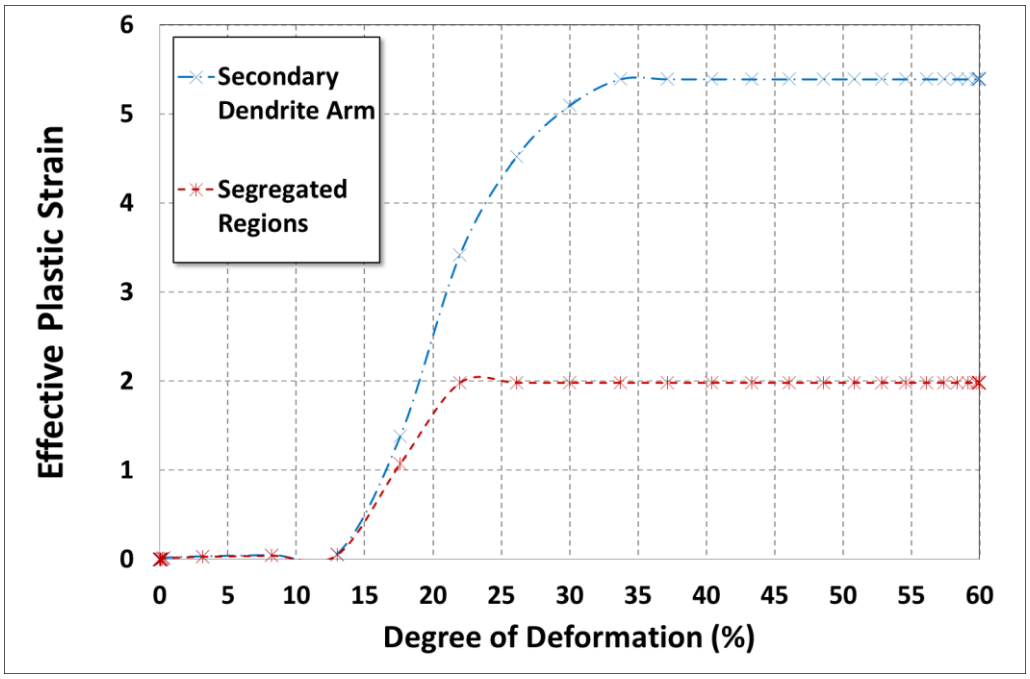

Figure 5.33: Effective plastic strain of the secondary dendrite arms and segregated regions following a single pass to 60% reduction.

5.4.2.2.3 Model 3: Effect of Slight Variation in Mechanical Properties

In this model, small variations in the mechanical properties of dendritic and inter-dendritic regions were assessed (see Table 5.3). The effective strain distributions in the dendritic and the inter-dendritic segregated regions are presented in Figure 5.34 (a) for a single pass to 60% reduction upon entering the roll bite and in Figure 5.34 (b) for a reduction of 60% halfway through the roll bite.

Although the difference in mechanical properties between dendritic and inter-dendritic regions in this model is very small, the same local strain partitioning and strain bands formation that occurred in Model 1, also occurred in this instance.

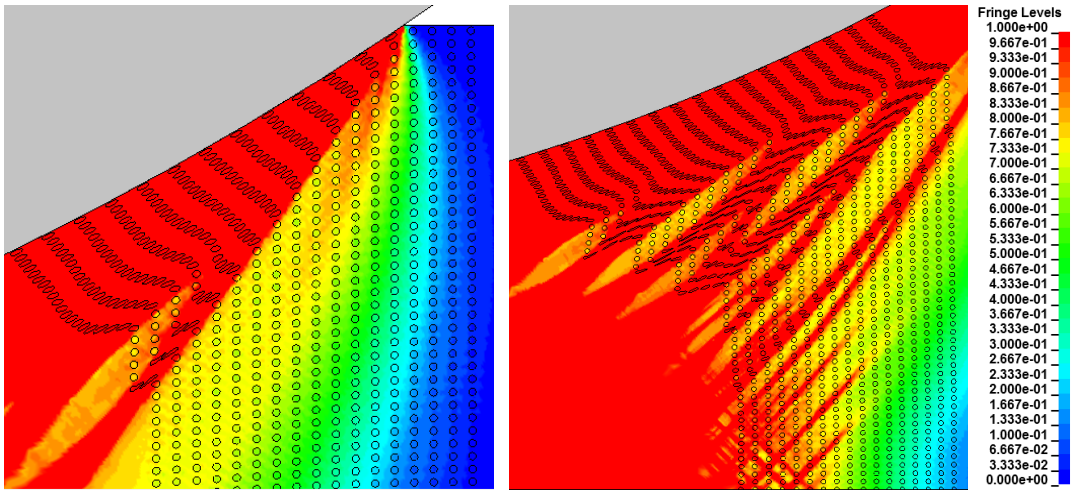

(a) **(b)**

Figure 5.34: Strain contour (indicated by fringe levels) using Model 3 (a) upon entering the roll bite and (b) halfway through the roll bite, 60% Reduction.

Strains at the zone of maximum deformation in the roll bite are shown in Figure 5.35.

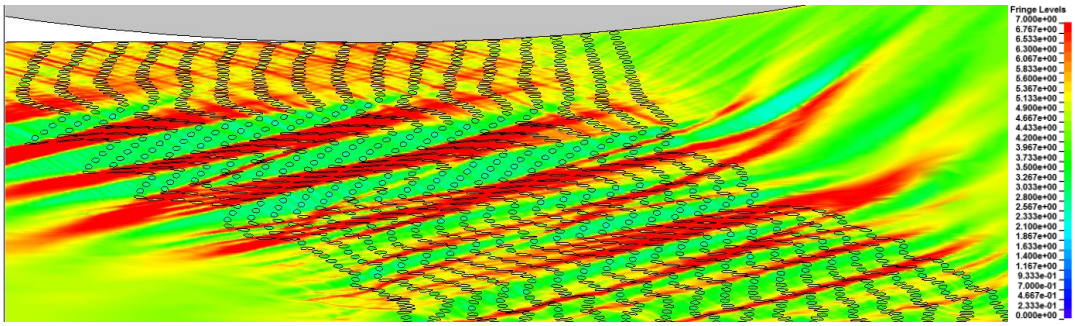

Figure 5.35: Strain contour (indicated by fringe levels) derived from using Model 3 at the zone of maximum deformation (60% Reduction).

Figure 5.36 is a higher magnification of the strain bands and it show in detail that the strain in the secondary dendrite arm is much higher than the strain in the adjacent inter-dendritic regions. The figure also shows the flattening and transformation of the

secondary arms from circles to ellipsoids as higher reductions are applied. This observation is the same as in Model 1.

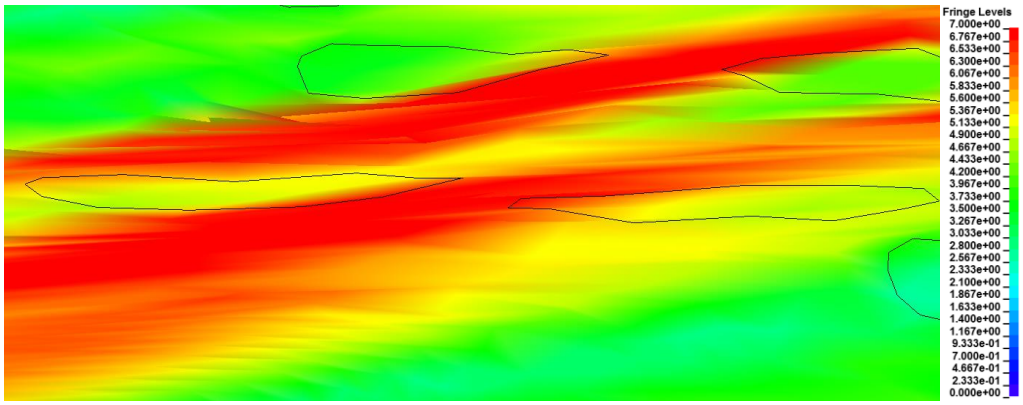

Figure 5.36: Strain contour (indicated by fringe levels) from Model 3 of the dendritic and segregated regions at the zone of maximum deformation between the rolls at 60% reduction.

Figure 5.37 shows quantitatively the effective plastic strain of the secondary arms and segregated regions located in the same strained bands during a single pass to 60% reduction using Model 3. It is apparent that as deformation increases, the secondary arms experience more strain than by adjacent segregated regions located in the same highly strained band. The effective plastic strain of the secondary dendrite arms was about 2.7 while the strain for the segregated regions amounted to about 5.1.

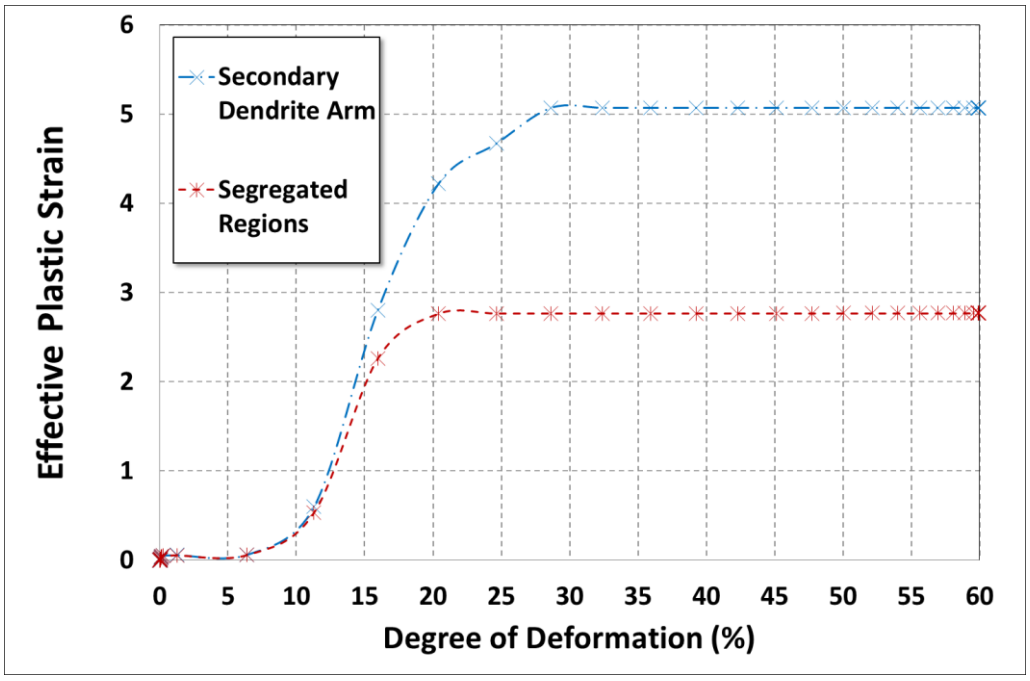

Figure 5.37: Effective plastic strain of the secondary dendrite arms and the segregated regions located in highly strained bands during a single pass to 60% reduction (Model 3).

5.4.2.2.4 Model 4: No Variation in Mechanical Properties- Control Model

In this control model the mechanical properties of the dendrite arms and inter-dendritic regions were exactly the same. This model assumption was made to check the sensitivity of the finite element model to changes in mechanical properties of the respective phases. The effective strain distributions in the dendritic and the inter-dendritic segregated regions using these boundary conditions are presented in Figure 5.38 for a single pass 60% up on entering roll bite. Since there is no difference in the mechanical properties of the respective phases, the dendritic regions and inter-dendritic regions should behave as if they are a uniform homogeneous material during hot rolling, and they do. Hence, the conclusion can be drawn that the differences in behavior of the different phases in the previous models are real and that the strain bands develop as a result of these differences.

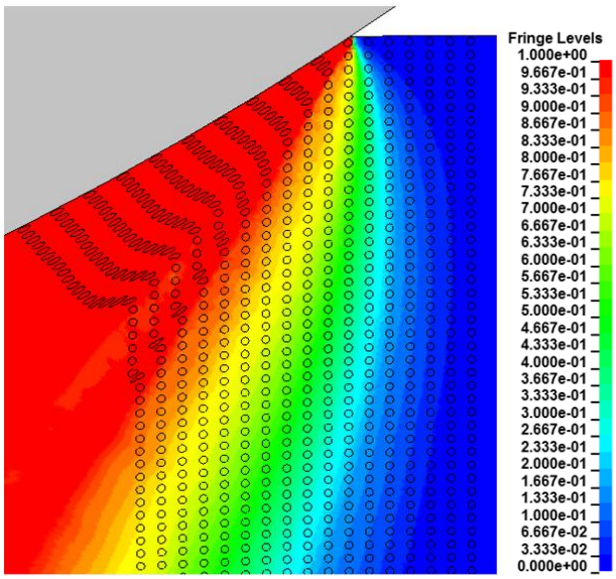

Figure 5.38: Strain contours (indicated by fringe levels) from Model 3 in the segregated region upon entering the roll bite.

Higher magnifications of the strain inside the dendritic structures shown in Figure 5.39, confirm that the secondary dendrite arms and the adjacent inter-dendritic regions in the zone of maximum deformation, experience the same strain during rolling. The figure also shows the flattening and transforming of the segregated regions and secondary dendrite arms from circles to ellipsoids at increased reductions.

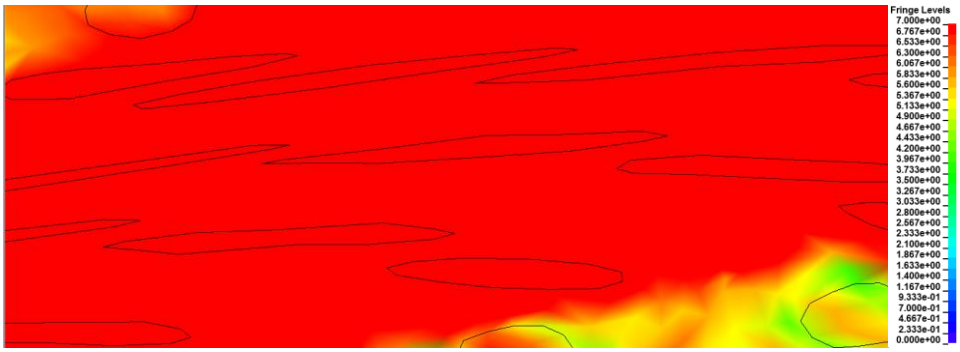

Figure 5.39: Strain contour (indicated by fringe levels) on the dendritic and segregated regions at maximum deformation between rolls (60% reduction, Model 4).

Figure 5.40 shows quantitatively, using Model 4, the effective plastic strain of the secondary dendrite arms and the segregated regions respectively during a single pass to 60% reduction. It is apparent that as deformation increases, the secondary arms experience almost similar strain of adjacent segregated regions. The strain for secondary dendrite arms and segregated regions was about 3.33 and 3.40 respectively.

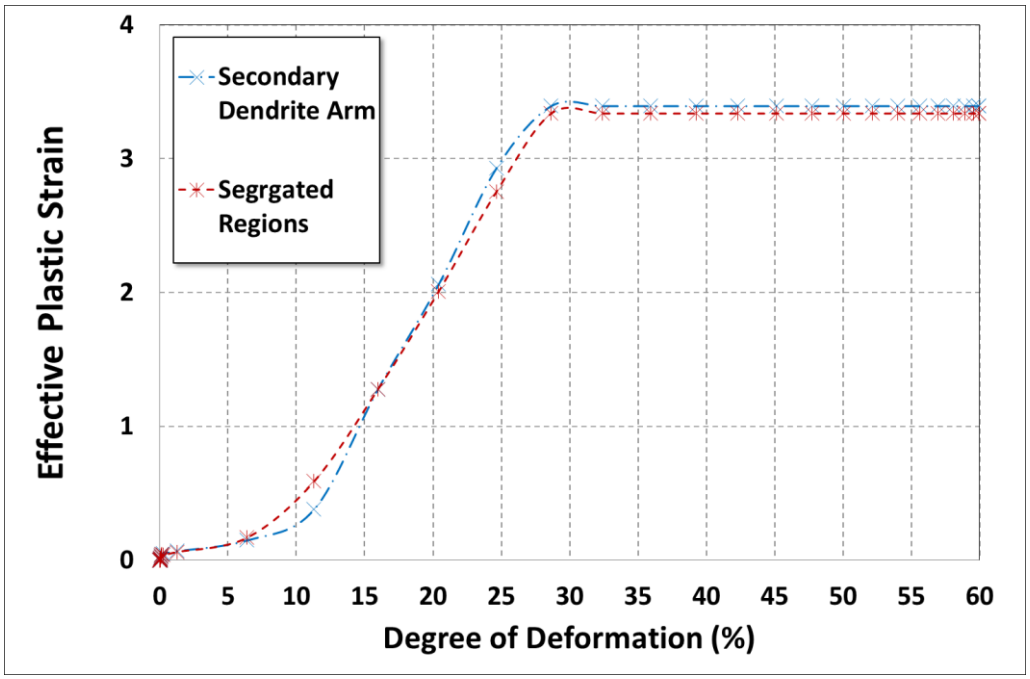

Figure 5.40: Effective plastic strain of secondary dendrite arms and the segregated regions located in highly strained bands during a single pass to 60% reduction (Model 4).

5.4.2.3 Effective Stress distribution

5.4.2.3.1 Model 1: Basic Conditions

Figure 5.41 (a), (b) and (c) shows the effective stress contours calculated by Model 1 upon dendritic structures entering the roll bite at 25, 50 and 60% reductions

respectively. It follows that the segregated regions across the thickness of specimen experience higher stresses than the dendritic regions in the same stress zone.

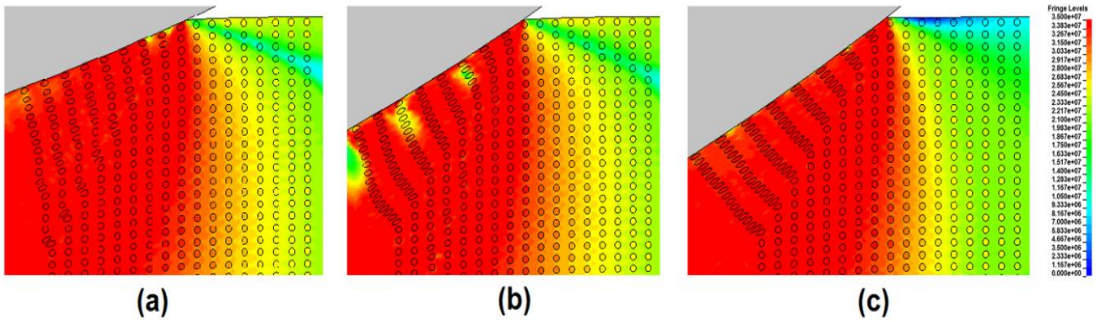

Figure 5.41: Stress contours (indicated by fringe levels in Pa) in the dendritic structures upon entering the roll bite (a) 25% reduction, (b) 50% reduction and (c) 60% reduction (Model 1).

Higher magnifications of the stress distribution inside the dendritic structures in the zone of maximum deformation zone show in more detail that the inter-dendritic regions experience higher stresses than the adjacent dendritic regions as shown in Figure 5.42 (a), (b) and (c).

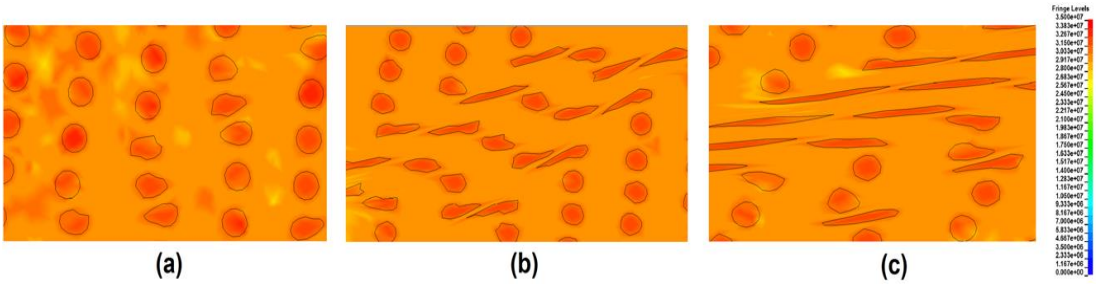

Figure 5.42: Stress contours (indicated by fringe levels in Pa) in the dendritic structures in the zone of maximum deformation (a) 25% reduction, (b) 50% reduction and (c) 60% reduction (Model 1).

This local stress distribution at each reduction is shown in Figure 5.43, Figure 5.44 and Figure 5.45 for 25, 50 and 60% reductions respectively.

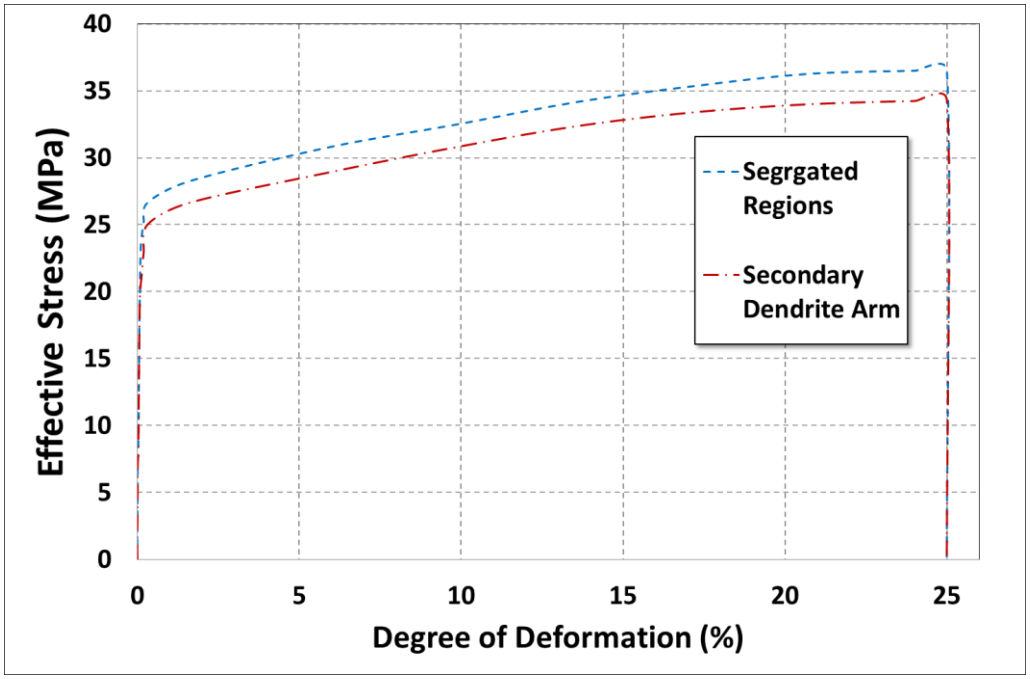

Figure 5.43: Effective stress of secondary dendrite arms and segregated regions during a single pass to 25% reduction (Model 1).

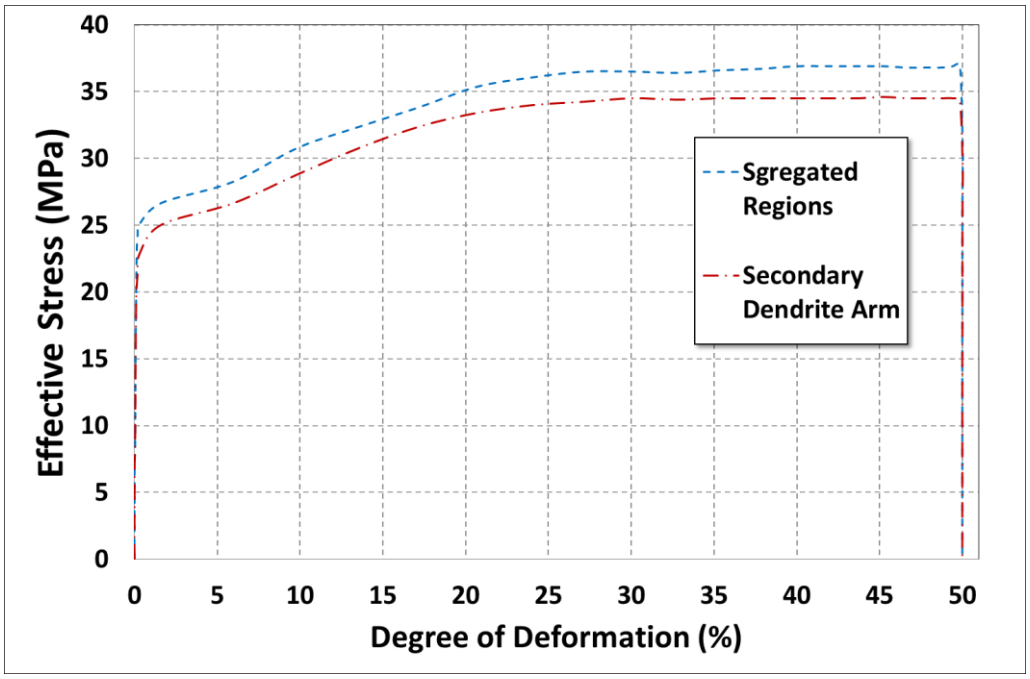

Figure 5.44: Effective stress of secondary dendrite arms and segregated regions during a single pass to 50% reduction (Model 1).

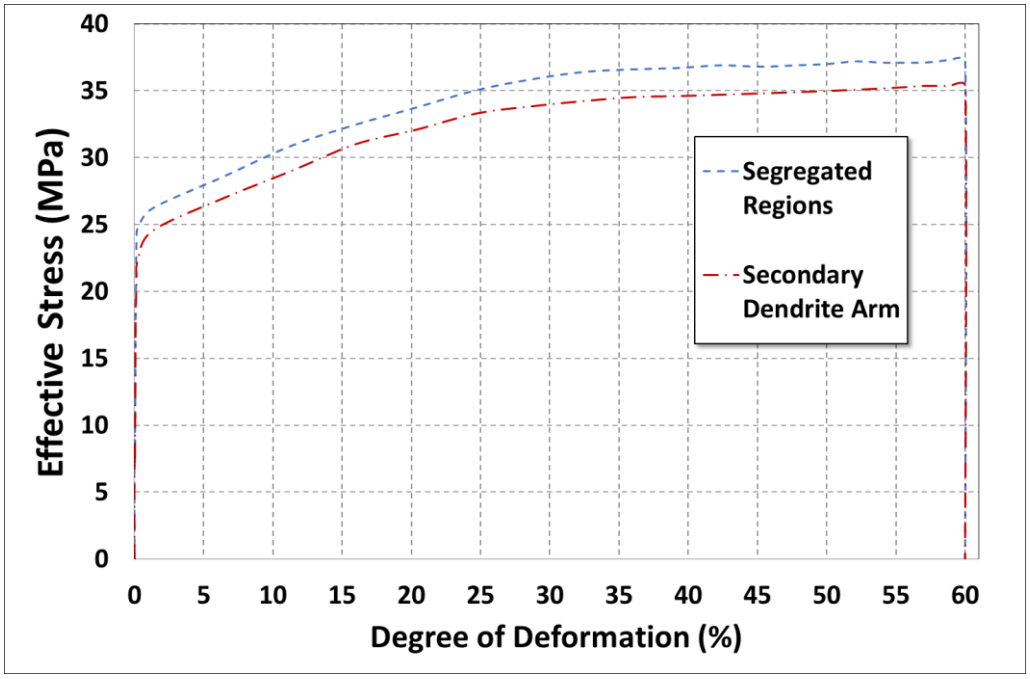

Figure 5.45: Effective stress of secondary dendrite arm and segregated regions during a single pass to 60% reduction (Model 1).

5.4.2.3.2 Model 2: Effect of Dendrite Arm Spacing

This model assumed larger spacing of primary dendrite and secondary arms – see Table 5.3. The effective stress distributions in the dendritic and the inter-dendritic segregated regions are presented in Figure 5.46 (a) and (b) for a single pass of 50 % and 60% reductions respectively. The same information is shown at higher magnification in Figure 5.47. The segregated regions across the thickness of specimen experience higher stresses than the dendritic regions in the same stress zone. The same information is also provided in quantitative form in Figure 5.48 and Figure 5.49.

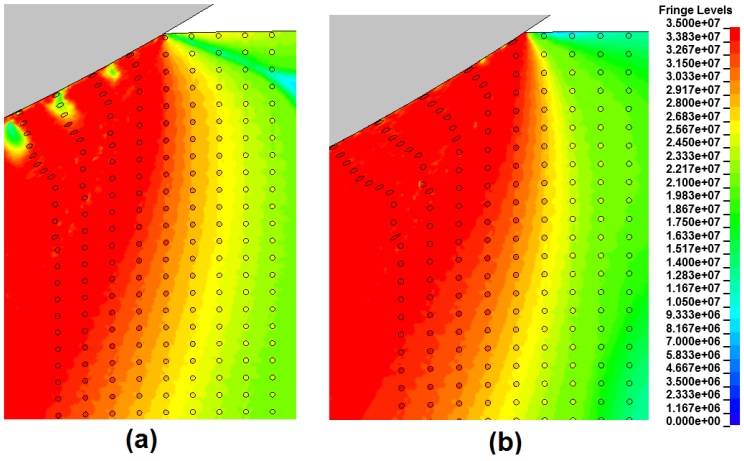

Figure 5.46: Stress contour (indicated by fringe levels in Pa) in the dendritic structures upon entering roll the bite (a) 50% reduction and (b) 60% reduction (Model 2).

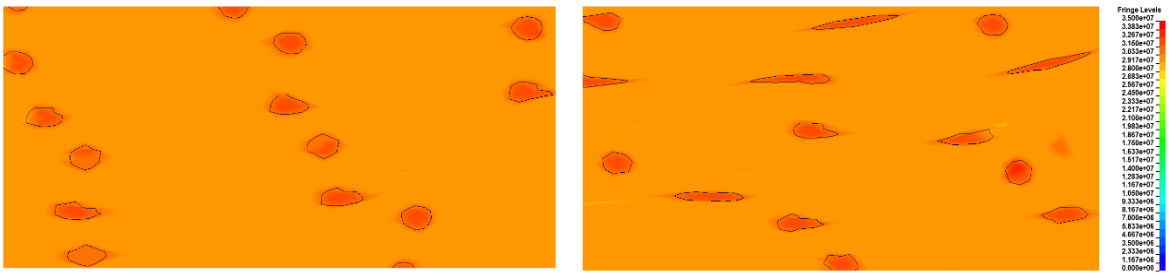

Figure 5.47: Stress contour (indicated by fringe levels in Pa) in the dendritic structures at maximum deformation in the roll bite (a) 50% reduction and (b) 60% reduction (Model 2).

This local stress distribution occurring through dendritic structures during rolling, effective stress was quantitatively analysed at each reduction as can be seen from Figure 5.48 and Figure 5.49 for 25, 50 and 60% reductions respectively. The figures clearly also show that the effect of arm spacing is insignificant and dendritic and inter-dendritic regions follow similarly stress-strain relationship initially defined based on the mechanical properties of each region at high temperature. Since both of dendritic and inter-dendritic regions are ductile material at high temperatures and no failure assumed to happen during rolling, they follow their stress-strain curves until deformations of the specimen complete.

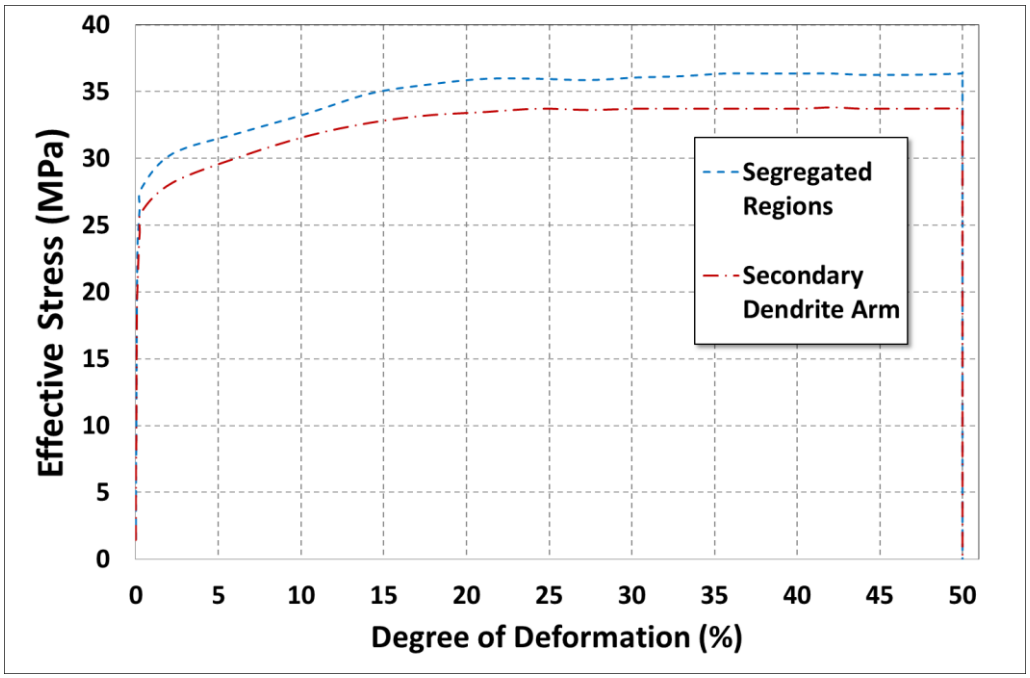

Figure 5.48: Effective stress of secondary dendrite arm and segregated regions respectively during a single pass to 50% reduction (Model 2).

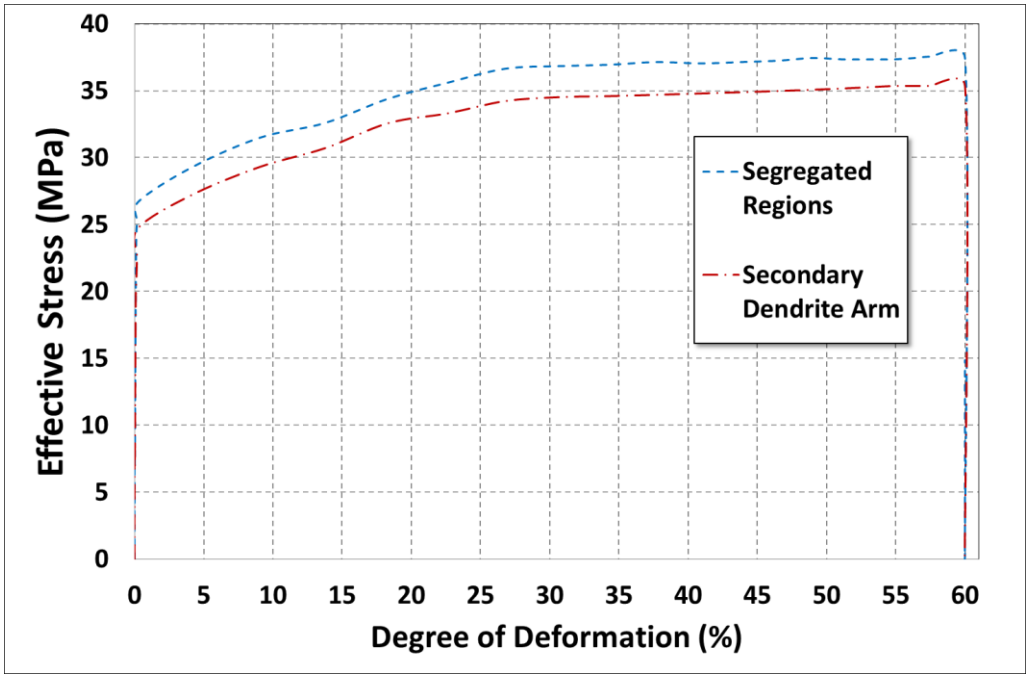

Figure 5.49: Effective stress of secondary dendrite arms and segregated regions respectively during a single pass to 60% reduction (Model 2).

5.4.2.3.3 Model 3: Effect of Slight Variation in Mechanical Properties

In this model a slight difference in mechanical properties between dendritic regions and inter-dendritic regions was imposed (See Table 5.3). The effective stress distributions in the dendritic and the inter-dendritic segregated regions are presented in Figure 5.50 for a single pass of 60% reduction. The segregated regions across the thickness of specimen experience higher stresses than the dendritic regions in the same stress zone. This is more clearly shown at higher magnification in Figure 5.51and quantified in Figure 5.52. The figure also shows that the stresses inside the segregated regions are lower than those predicted by Models 1 and 2.

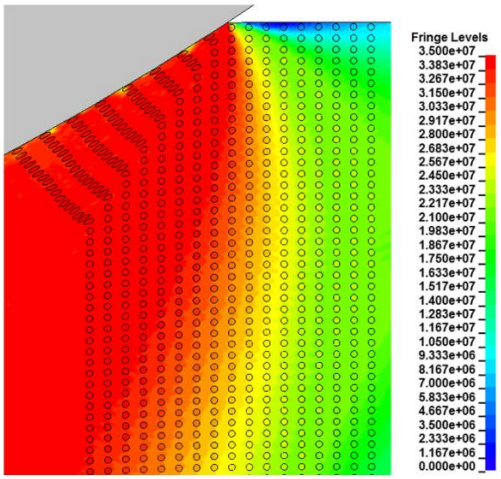

Figure 5.50: Stress contour (indicated by fringe levels in Pa) in the dendritic structures upon entering roll bite for a single pass of 60% reduction (Model 3).

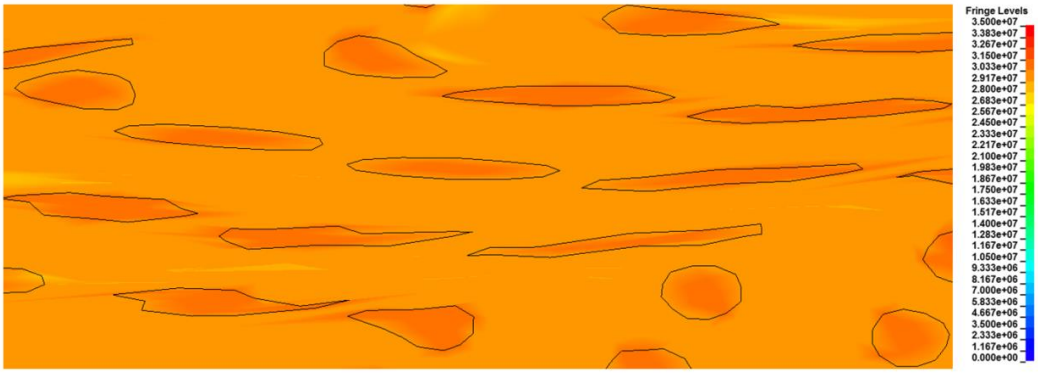

Figure 5.51: Stress contour (indicated by fringe levels in Pa) in the dendritic structures at maximum deformation under rolls 60% reduction (Model 3).

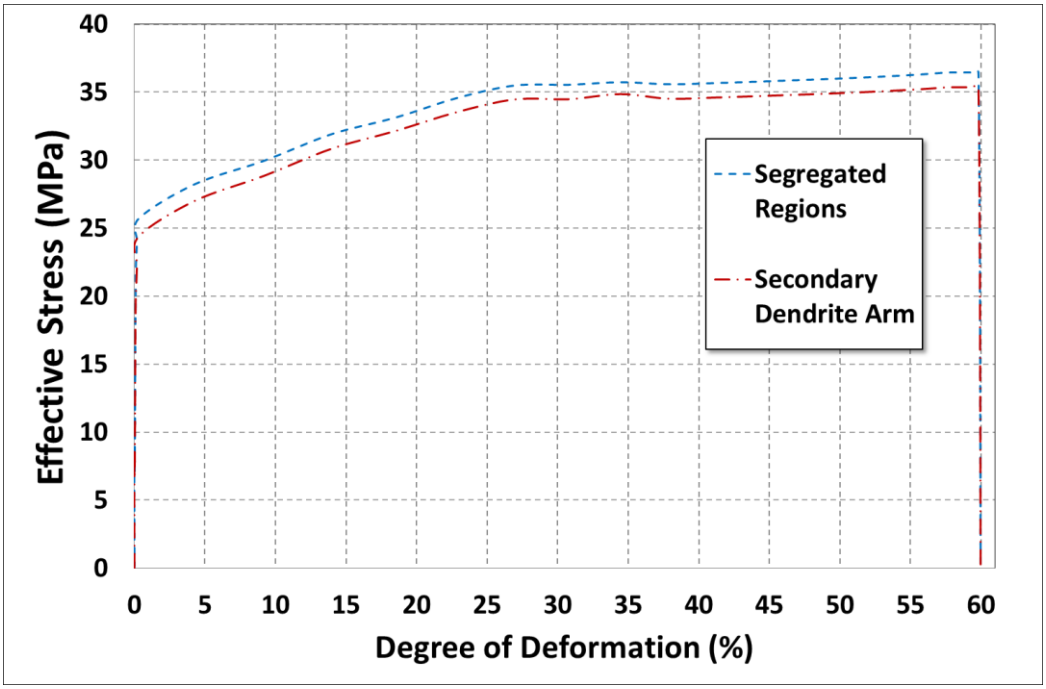

Figure 5.52: Effective stress of secondary dendrite arms and segregated regions respectively during a single pass to 60% reduction (Model 3).

5.4.2.3.4 Model 4: No Variation in Mechanical Properties

The mechanical properties of the dendritic regions and inter-dendritic regions were assumed to be the same in this control model, Model 4 and the effective stress distributions are shown in Figure 5.53 for a single pass of 60% reduction at the zone of maximum deformation in the roll bite and quantified information is provided in Figure 5.54. These figures clearly shows that the secondary dendrite arm and adjacent inter-dendritic regions experience the same strain during rolling as would be expected.

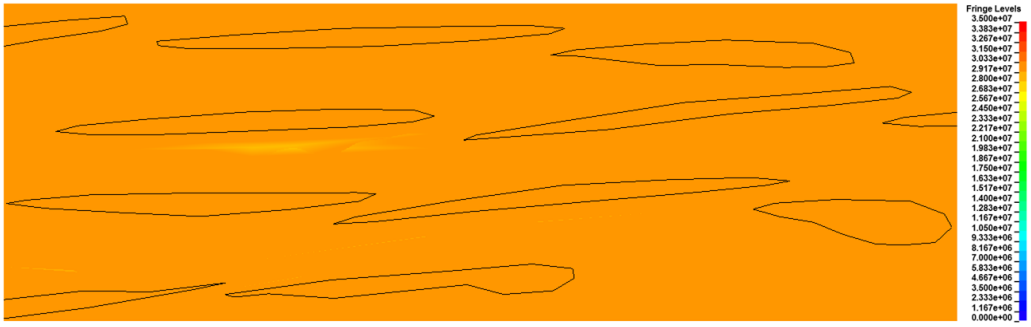

Figure 5.53: Stress contour (indicated by fringe levels in Pa) in the dendritic structures at maximum deformation under rolls 60% reduction (Model 4).

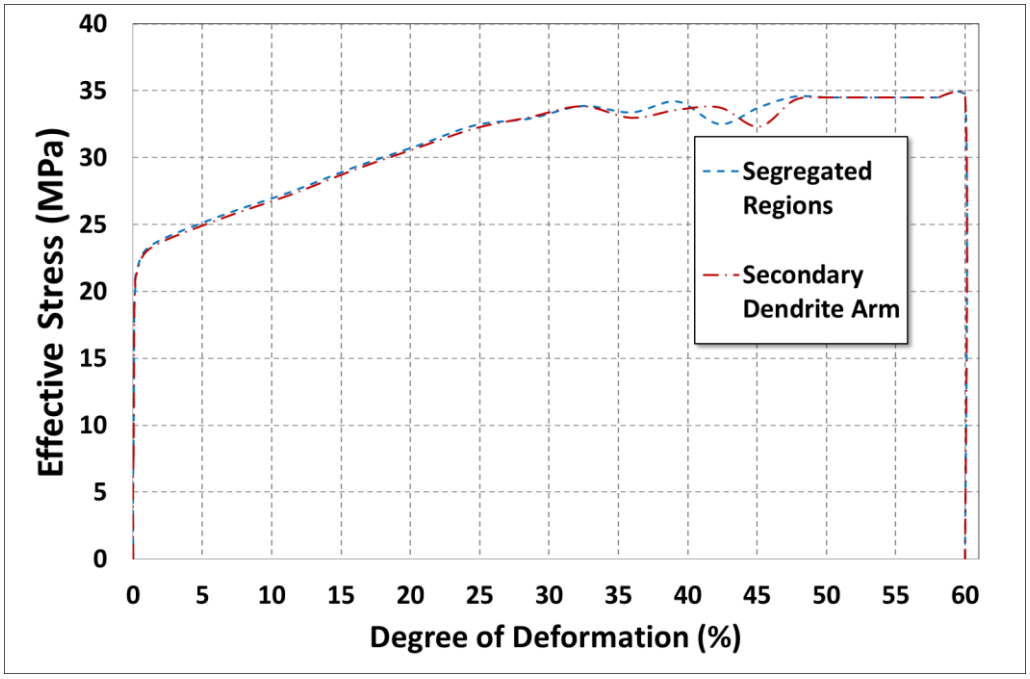

Figure 5.54: Effective stress of secondary dendrite arms and the segregated regions during a single pass to 60% reduction (Model 4).

In summary, the assumptions made in Models 1 to 3 with respect to different dendrite arm spacing and the difference in mechanical properties of the respective regions lead to stress and strain partitioning. The plastic strain in the segregated regions is lower than in the adjacent dendritic regions and hence, the dendritic regions elongate more than the segregated regions during hot deformation. The maximum stress within the segregated regions is higher than the yield stress of dendritic regions and hence, the stress in the dendrites reaches their yield stress before that of the segregated regions and hence deform more easily. The control model, Model 4 in which the same mechanical properties have been assigned to dendritic and inter dendritic confirms the absence of the stress and strain partitioning.

It is pertinent to compare at this stage, the findings of the present study to earlier findings reported in the literature. Wilson [221] reported strain localization during rolling of aluminium alloy sheets. Strain partitioning and localization have been modelled [137, 218-229] during tensile deformation of multiphase steels and other composite materials, mainly at room temperature. Paul [218] found that strain incompatibility between the softer ferrite matrix and the harder martensite phase in dual-phase steel arises from the difference in flow characteristics of the respective phases. Inhomogeneities at microstructural-level are the main cause of strain incompatibility, strain partitioning and finally shear band localization during tensile deformation. The local deformation in the ferrite phase is constrained by adjacent martensite islands, which locally results in stress development in the ferrite phase. Tomota *et al.* [222] calculated the flow stress of $\alpha - \gamma$ Fe–Cr–Ni alloys consisting of two ductile phases on the basis of a continuum model where the internal stress produced by the inhomogeneous distribution of plastic strain is taken into account. Sodjit and Uthaisangsuk [220] found that under tensile deformation several short interrupted shear bands form in the dual phase structure with a small martensite contents, but that long, continuous and pronounced localizing bands appear in DP structure a high fraction of martensite. Ishikawa *et al.* [229] made similar observations ferrite-pearlite steels.

5.4.2.4 Comparison between Experimental Observations and Model Predictions

The as-cast structure of the medium-carbon steel under investigation is shown in Figure 5.2. Primary and secondary dendrite arms can clearly be identified and the presence of inter-dendritic regions between the dendrite arms is evident. This as-cast structure has been modelled as shown in Figure 5.6 for the purposes of finite element analysis aimed at predicting the response of this complex microstructure to hot rolling. Figure 5.55 shows another variant of two adjacent segregated regions in the as-cast structure interspaced by a secondary dendrite arm. The modelled response of the two adjacent segregated regions with respect to the secondary dendrite arm to hot rolling is shown in Figure 5.56 to 5.59 for different rolling reductions. These predictions are then compared to experimental observations at the same degree of reduction.

Both circular segregated regions are elongated gradually along the rolling direction and deformed from a circular to an elliptic shape. They are elongated gradually as

higher reduction is applied which is responsible for the large deformation of segregated regions. As the rolling reduction increases, the profiles of segregated regions changed progressively which corresponds to the rise of the effective strain. It can be seen from the figures, after 25% rolling reduction, segregated regions are elongated by about 65% for upper region and 80% for lower region. The upper segregated region vertically is pulled down due to reduction while lower segregated region is pushed up and horizontally shifted at the same time. At 50% reduction, segregated regions are elongated by more than 140% to 170% for upper and lower segregated regions respectively. Upper region is pulled down further and lower region is raised up and shifted further. Segregated regions are elongated further by about 300% to 400% for upper and lower regions respectively at 60% reduction. At this stage, the two regions are placed in one level and aligned in the rolling direction and close to link to each other to form one long segregated region. Models that extend beyond 60% rolling reduction are difficult to deal with since they require extremely fine meshes to accurately simulate the behaviour of the dendritic structures, which require excessive computational capacity. Thus, extrapolation of the behaviour of upper and lower segregated regions is used based on the similar input data. It is expected for upper and lower segregated regions to latch on each other at about 65 to 75% reductions as shown in Figure 5.59. These model predictions compared to the experimental observation of the equivalent area using metallographic techniques (Figure 5.56 to 5.59) are in agreement with the rolling reduction experiments reported by Preßlinger [55] as well as the experimental results shown in Chapter 3. Since the segregated regions are harder than secondary dendrite arm, the upper and lower regions disrupt secondary dendrite arm by their shear force into two parts and each part joins a different primary dendrite arm.

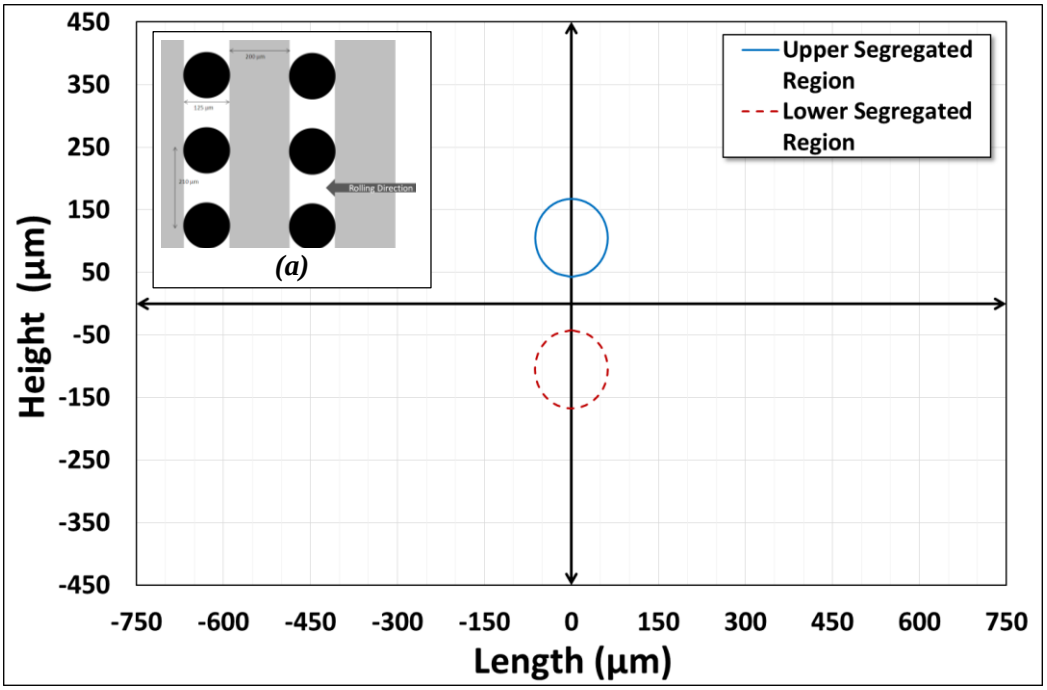

(b)

Figure 5.55: Modelling the as-cast structure. (a) Position of secondary dendrite arms (3) with respect to the inter-dendritic regions (3) in the modelling exercise. (b) Close-up of two inter-dendritic regions (termed upper and lower) separated by a secondary dendrite arm

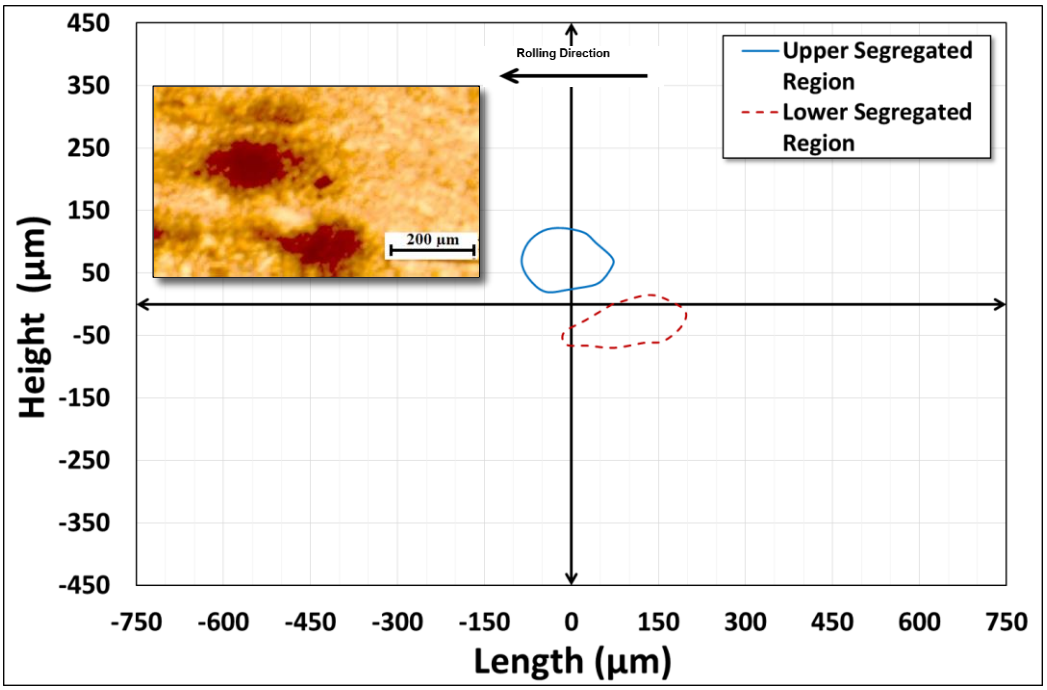

Figure 5.56: Model predictions of the response to hot-rolling of the inter-dendritic (segregated) regions following 25% rolling reduction. These predictions are compared to the experimental observation of the equivalent area are using metallographic techniques.

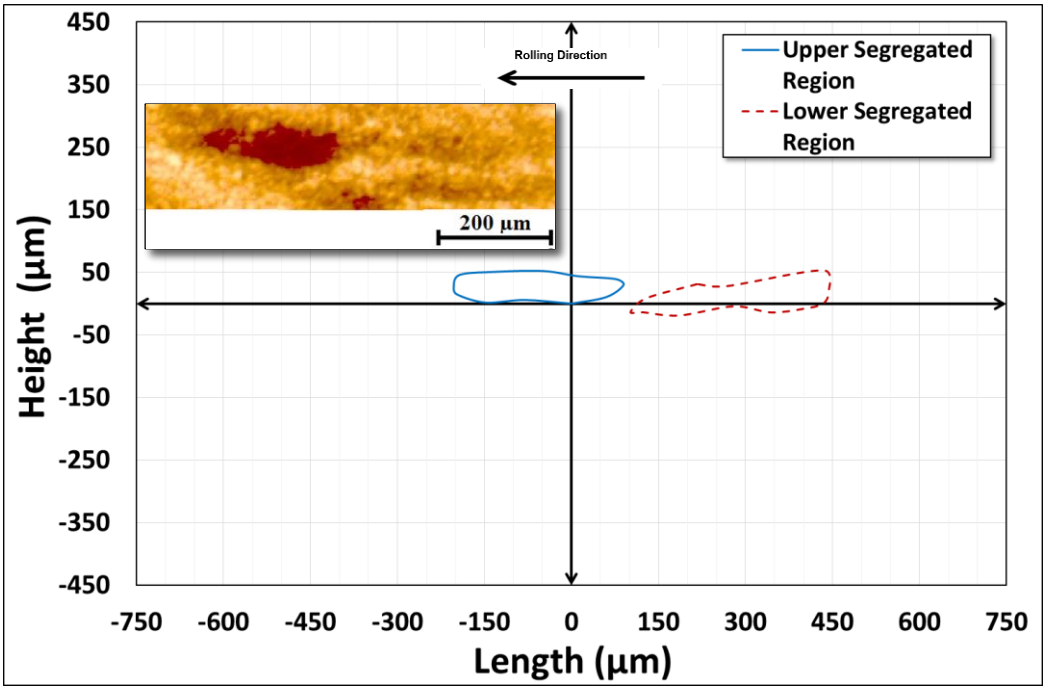

Figure 5.57: Model predictions of the response to hot-rolling of the inter-dendritic (segregated) regions following 50% rolling reduction. These predictions are compared to the experimental observation of the equivalent area using metallographic techniques.

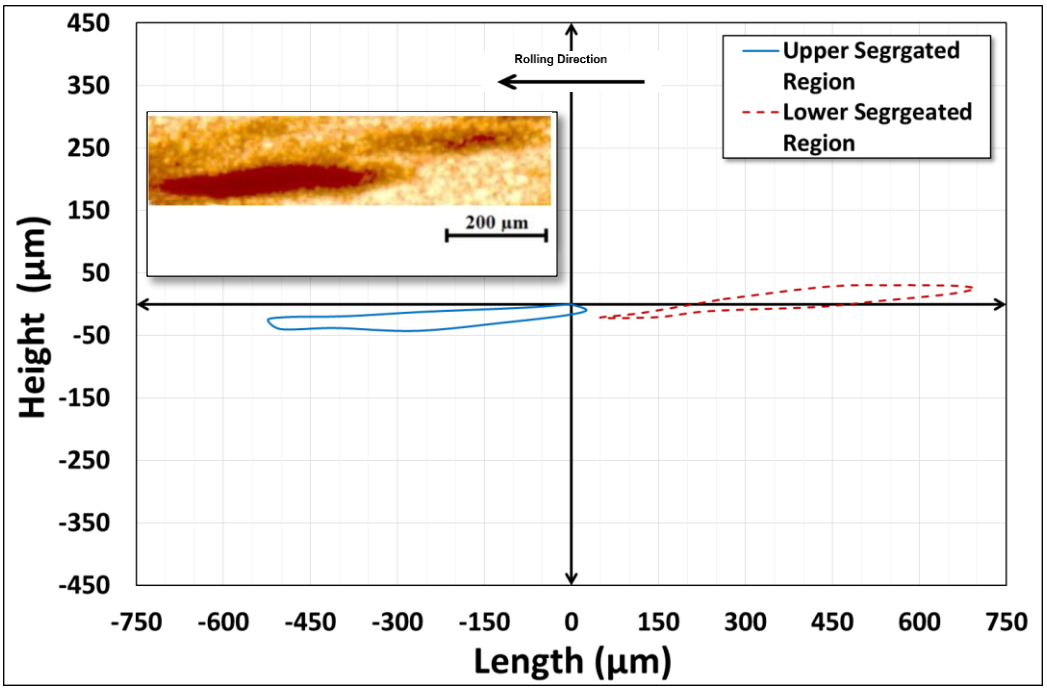

Figure 5.58: Model predictions of the response to hot-rolling of the inter-dendritic (segregated) regions following 50% rolling reduction. These predictions are compared to the experimental observation of the equivalent area using metallographic techniques.

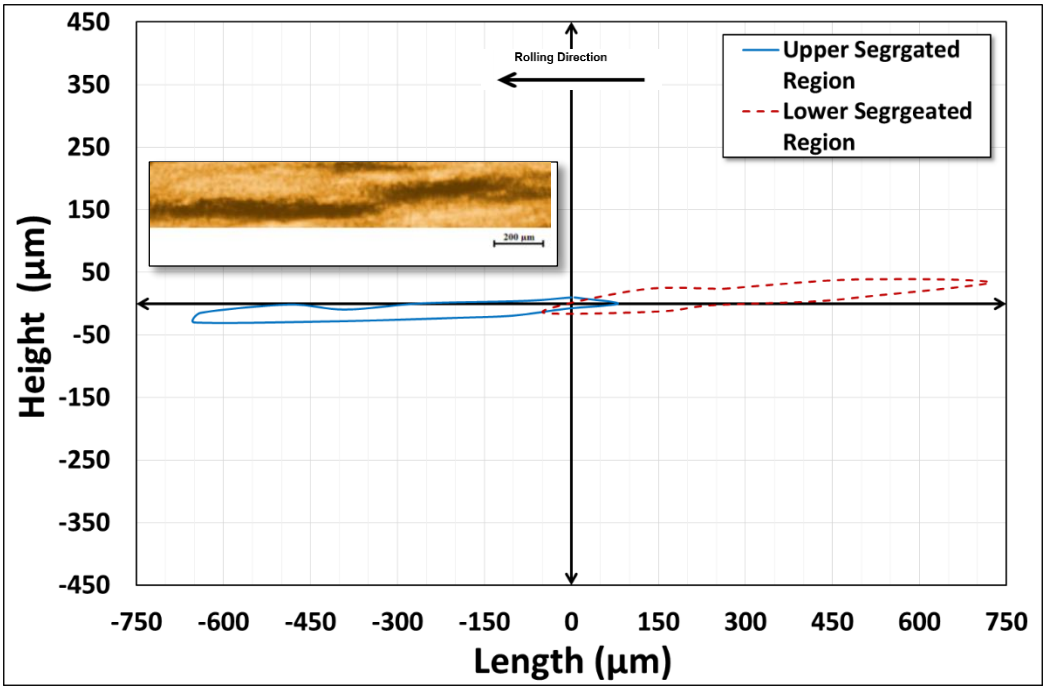

Figure 5.59: Model predictions of the response to hot-rolling of the inter-dendritic (segregated) regions following 60% rolling reduction. These predictions are compared to the experimental observation of the equivalent area using metallographic techniques.

5.5 Summary and Conclusions

- Two-dimensional finite-element models were developed to simulate the response of dendritic structures to hot rolling for medium carbon steel.
- The dendritic structures comprise primary dendrite arms perpendicular to the rolling direction, secondary dendrite arms perpendicular to the direction of the primary arms and inter-dendritic (segregated) regions between the secondary dendrite arms.
- The inter-dendritic regions were modelled as circular shapes interspaced by secondary dendrite arms in the as-cast structure
- Equivalent plastic strain and von-Mises equivalent stress distributions were determined in this complex structure under a variety of conditions as a function of rolling reduction.
- Shear bands and strain localization developed within the roll bite due to differences in the mechanical properties of the dendritic and inter-dendritic regions.
- The secondary arms experienced larger elongations than the segregated regions within strain bands due to the lower yield point of the dendrite arms.

- During hot rolling the primary dendrite arms rotate about the rolling direction and align with the rolling direction at rolling reductions of more than 70%. Secondary dendrite arms located between two segregated regions experience significant thinning during rolling until the segregated regions latch onto each other at about 70% rolling reduction.
- At rolling reductions between 65 and 75%, the primary and secondary dendrite arms and inter-dendritic regions pre-existing in the as-cast structure are destroyed and transformed into distinctive micro-chemical bands that align parallel to the rolling direction.
- The consequence of this response is that the segregated, inter-dendritic regions, which were roughly of circular shape in the as-cast structure, are transformed into essentially continuous bands parallel to the rotated dendrite arms. Hence, severe deformation by hot-rolling leads to the formation of parallel micro-chemical bands.

Chapter 6. In-situ Study of Microstructural Banding Formation of Medium-Carbon Steel

6.1 Introduction

It was argued in earlier chapters that microstructural banding is commonly observed in hot-rolled medium-carbon steel, manifested by alternating bands of ferrite and pearlite aligned in the rolling direction. It was shown that this kind of banding results from micro-segregation of alloying elements initially present in the inter-dendritic regions during the early stages of solidification. These inter-dendritic regions are elongated and flattened in the rolling direction, roughly parallel to dendrites during subsequent hot-rolling, forming regions of micro-chemical banding of high and low solute content. Apart from the steel composition, the cooling rate and the austenite grain size determines the extent of banding. It was also shown that slow cooling results in strong microstructural banding while banding does not form at high cooling rates. Microstructural banding doesn't seem to form when the austenite grain size is much larger than the micro-chemical band width [1-3, 9, 20, 23]. Earlier research emphasized the importance of ferrite nucleation and hence, large austenite grains lead to a limited number of ferrite nucleation sites [1-4, 6, 20].

In order to further explore the details of the formation of banding, an attempt was made to directly observe the austenite to ferrite and pearlite phase transformations. By the use of high-temperature laser-scanning confocal microscopy, observations have been made in real time and the progression of austenite decomposition has been observed *in-situ*. Heat treatments that would lead to the formation of microstructural banding in hot-rolled medium-carbon steel have been simulated by conducting heat treatments within the high-temperature microscope such that *in-situ* observations could be made.

6.2 Experimental Work

6.2.1 Material and Sample Preparation

Samples of medium-carbon steel hot-rolled to 90% reduction in thickness were longitudinally cut along the rolling direction and prepared for *in-situ* heat treatment in a high-temperature laser-scanning confocal microscope (HTLSCM).

6.2.2 High-temperature laser-scanning confocal microscopy

The principles of laser-scanning confocal microscopy (LSCM) was established by Minski and initially used for biological sciences applications. However, it was not until the 1990's when Emi and co-workers combined LSCM with infrared heating that renewed interest was developed in high temperature microscopy of metals. Experimental studies conducted by using this technique include the morphology of solidification; the analysis of the progress of delta-ferrite to austenite interfaces in low carbon steels; inclusion agglomeration, inclusion engulfment; crystallization in oxide melts; dissolution of alumina inclusions in slag; kinetics of the peritectic transformation and other solidification phenomena [230].

Read *et al.* [9] described the technique used in this study as follows: laser light is focused by an objective lens on to the object, and the reflected beam is focused onto a photo detector via a beam splitter, as shown in Figure 6.1.

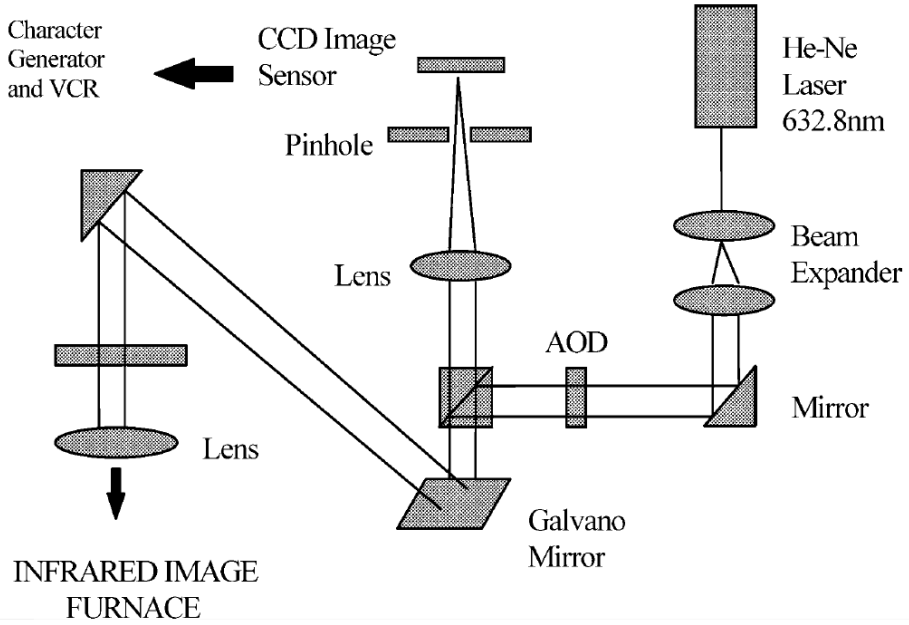

Figure 6.1: Schematic representation of the laser-scanning confocal microscope [230].

A helium-neon laser beam laser with wavelength 632.8 nm is deflected and scanned in two dimensions in the horizontal direction at a rate of 15.7 kHz and by an acoustic optical device (AOD) and in the vertical direction at 60 Hz by glavano-mirror, 45° polarized by a polarizing half mirror, and delivered through a long focal length objective lens on to the surface of the specimen. The reflected beam rom the surface of the sample enters a charge-coupled device (CCD) sensor after being further 45° polarized by the half mirror, and going through a modulated beam splitter and a pinhole. The pinhole serves to shut out any stray radiation from the unfocused area of the sample surface. The high intensity of the coherent laser beam (0.5 μm in diameter) is such that even the small difference in emissivity between the liquid and solid steel is clearly distinguishable. Signals from the charge-coupled device are displayed on a cathode ray tube recorded on video and stored in a computer for further processing. Signals can be obtained from planes located at different vertical distances from the specimen surface by vertically adjusting the microscope, and are stored and reproduced as a quasi-three-dimensional image as shown in Figure 6.2. It is therefore possible to identify both concave and convex features on the sample. The resolution obtained is 0.25 μm with a maximum magnification is 1350X.

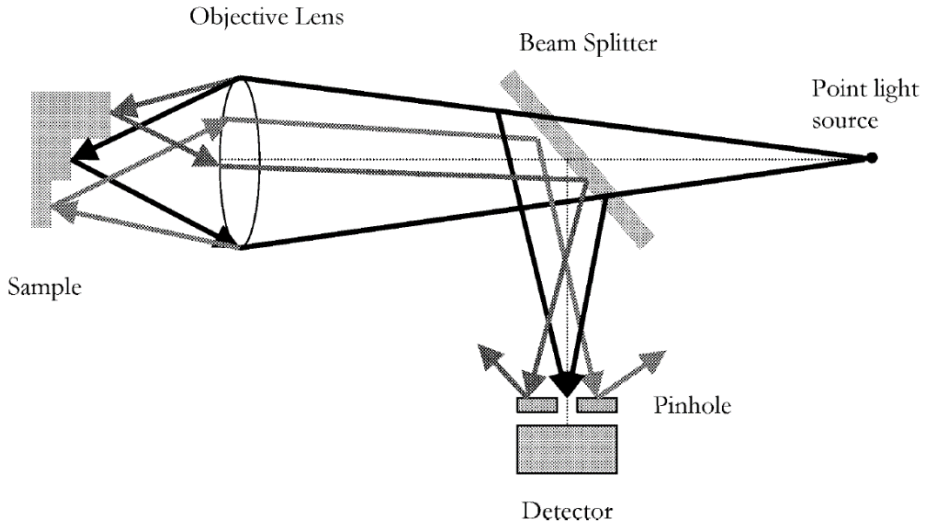

Figure 6.2: Confocal nature of the optics [230].

A schematic diagram of an infrared imaging furnace is shown in Figure 6.3 [230]. Specimens are placed at the upper focal point in a high-purity alumina crucible in the upper half of the gold-plated ellipsoidal cavity of an infrared imaging furnace. The top of the cavity has a viewing port covered by an airtight transparent quartz plate. At the lower focal point in the lower half of the cavity, separated from the upper part by a

transparent quartz plate, a 1.5 kW-halogen lamp is used to heat the specimen by radiation. Ultra-high-purity argon gas is bled into the upper cavity to prevent oxidation of the specimen. The temperature of the furnace can be measured with a thermocouple welded to the platinum container that holds the alumina crucible and simultaneously recorded with the image on computer at a rate of 30 frames per second. Hard copies of the video frames can be made or they can be subject to digital video analysis on a computer.

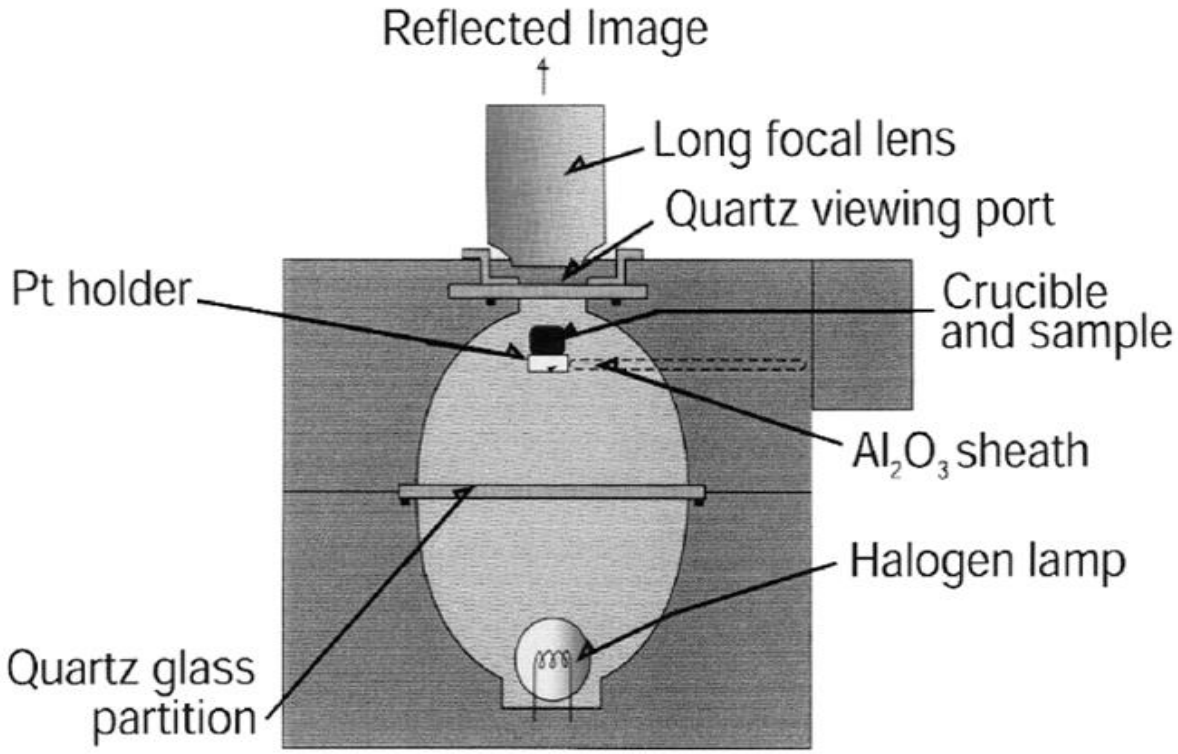

Figure 6.3: Infrared imaging furnace and specimen position [230].

Specimen holders consist of 5 mm diameter round holders, made from a polymeric end-piece, alumina 2-bore tube with an outer silica support tube and a platinum holder welded to a B type thermocouple wire as shown in Figure 6.4. In this study, the actual temperature of the specimen was estimated by using the same techniques as Reid *et al*. [9] and the following results were obtained:

Specimen temperature = Control temperature + 40°C

The control temperature is the temperature recorded in the video clips.

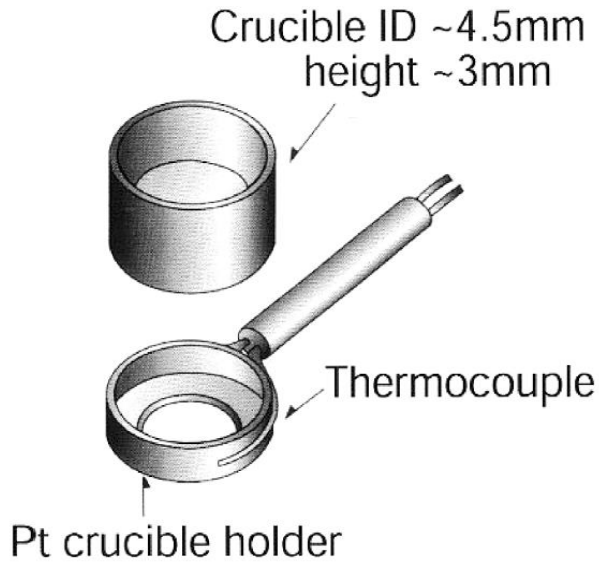

Figure 6.4: Laser-scanning confocal microscope specimen crucible and holder [230].

6.2.3 Sample Preparation and Setup

Specimens were prepared to fit into 5-mm diameter alumina crucibles. The surfaces of the specimens were ground and polished using standard metallographic techniques. The sample and the holder were then inserted into the furnace chamber as shown in Figure 6.3. This part of the furnace is atmosphere controlled to avoid oxidation of the specimen at elevated temperatures. The top half of the microscope chamber is filled with ultra-high purity argon gas. To further purify the inert gas, a Super-Clean^{TM} gas filter is placed in the gas train and the purified gas is then passed through a stainless steel tube filled with titanium turnings, held at a temperature of 900°C to further remove any remaining oxygen. In order to ensure high integrity of the inert atmosphere in the furnace, the microscope chamber is vacuum flushed with argon gas at least ten times. A Rapidox 2100 Cambridge Sensotec oxygen sensor determines the partial pressure of oxygen during the flushing period and during the experiment.

6.2.4 Thermal Cycle

Samples of medium-carbon steel hot-rolled to 90% reduction in thickness were heated at a heating rate of 100°C/min in the infrared imaging furnace of the laser-scanning confocal microscope to a temperature of 1100°C. Two different test conditions were then applied. In the first test condition, the samples were held for 5 minutes and then cooled at a cooling rate of 30°C/min to room temperature. This thermal cycle, which simulated an industrial rolling process, is shown in Figure 6.5. In the other test

condition, the samples were held for short time (about one minute) and rapidly cooled to 800°C to minimise decarburization of the sample. The sample was then slowly cooled at a cooling rate of 30°C/min to room temperature. This thermal cycle is shown in Figure 6.6.

Microstructural changes, including the pertaining phase transformations were observed and recorded upon heating and cooling of the specimens.

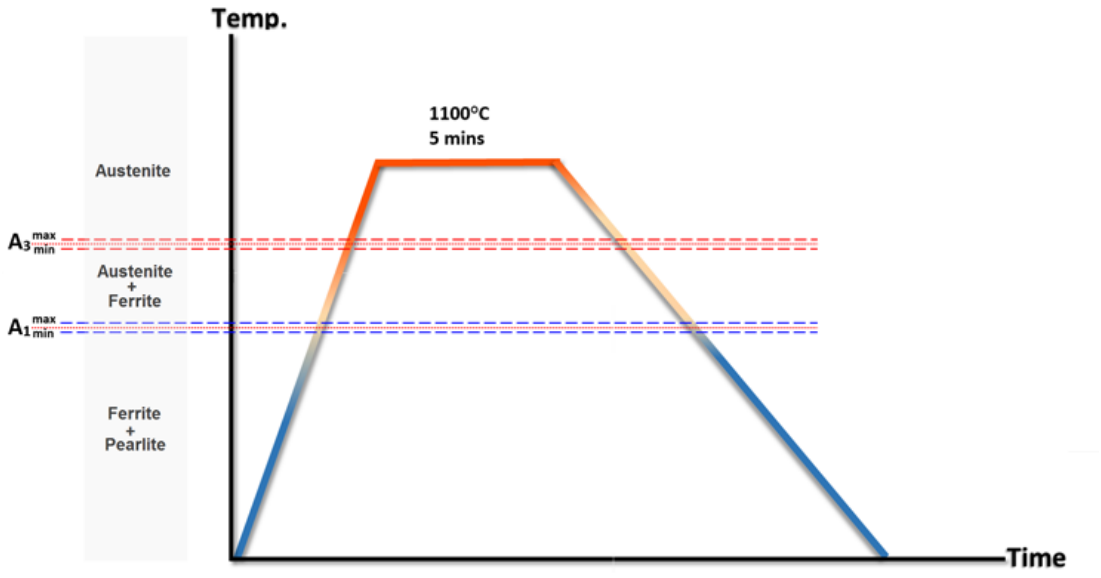

Figure 6.5: Thermal cycle of heat treatment (test condition 1).

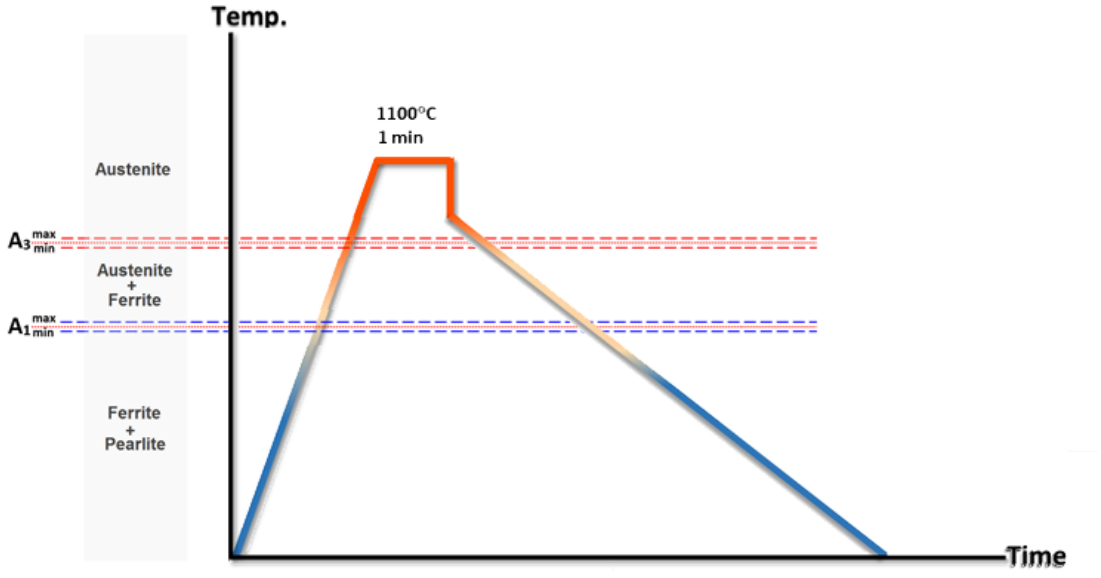

Figure 6.6: Thermal cycle of heat treatment (test condition 2).

6.2.5 Determination of Phase Transformation Temperatures

The micro-structure of the hot-rolled medium-carbon steel used in this study contains micro-chemical bands of low and high alloying content respectively (formed from dendritic and inter-dendritic regions) and hence, the temperature at which the austenite decomposition will occur is different for the different bands. In addition, the differences in alloying element in the bands result in different decomposition kinetics – see Chapter 3.

The respective chemical compositions of these bands have been determined (Chapter 3) and hence, it was possible to predict the phase transformation temperature for each region using Thermo-Calc software with TCFE6 databases [231].

6.2.6 Metallography

Hot-rolled specimens were observed by optical microscopy before and after observation in the high-temperature microscope. Micro-structural banding in hot-rolled specimens were revealed by examining cross-sectional areas etched in picric acid (following Samuels [8]) using optical microscopy. Many digital photographs were taken from each prepared cross-sectional area using a Leica Camera at a magnification of 50 times and the corresponding micrographs were ten 'stitched' together.

Following heat treatment and observation in the high-temperature microscope, cross-sectional areas of the specimens so examined were analysed using optical microscopy. Many digital photographs were taken for each prepared cross-sectional area using the Leica Camera at the same magnification with corresponding micrographs 'stitched' together. Sample were then slightly polished and etched with 2% nital and again the cross-sectional areas of the tested samples were examined using optical microscopy. Again, corresponding micrographs were 'stitched' together.

6.3 Results and Discussions

6.3.1 Isothermal Soaking in the Austenite Phase

6.3.1.1 Test condition 1

During isothermal soaking in the single-phase austenite region in test condition 1, the grain structure becomes visible as a result of thermal grooving as shown in Figure 6.7. Austenite grains evolved and stabilized in less than 2 minutes at isothermal holding at 1100°C as shown in Figure 6.7. The austenite grains grow over the segregated (micro-chemical) bands of high and low solute regions resulting in a stabilised austenite grain size of 95.6 ±10 µm. The traces of the pre-existing pearlite and ferrite bands are still visible (this is an inherent characteristic of confocal microscopy – although the bands are no longer there, the grooves formed earlier by thermal etching remain and can be observed, this being one of the very useful features of confocal microscopy).

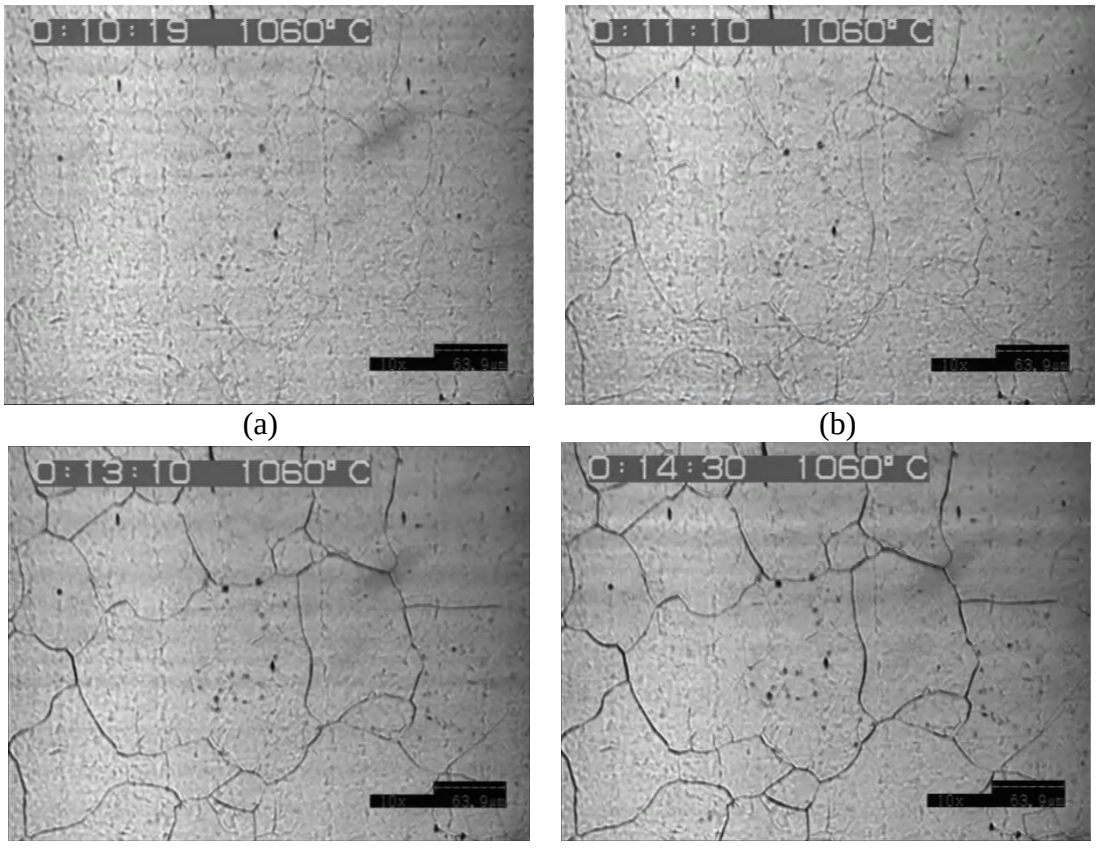

(a) (b)

(c) (d)

Figure 6.7: Progressive austenite grain growth at a (calibrated) temperature of 1100℃ for times of: (a) 40s, (b) 100s, (c) 160s and (d) 240s (test condition 1) (scale bars= 63.9µm).

6.3.1.2 Test condition 2

In similar vein to test condition 2, during isothermal soaking in the single-phase austenite region, the austenite grains evolved and finally stabilized as shown in Figure 6.8 for isothermal holding at 1100°C for about 1 minute. The austenite grains grow over the segregated (micro-chemical) bands of high and low solute regions and the stabilised austenite grain size was 92.1 ±11 µm.

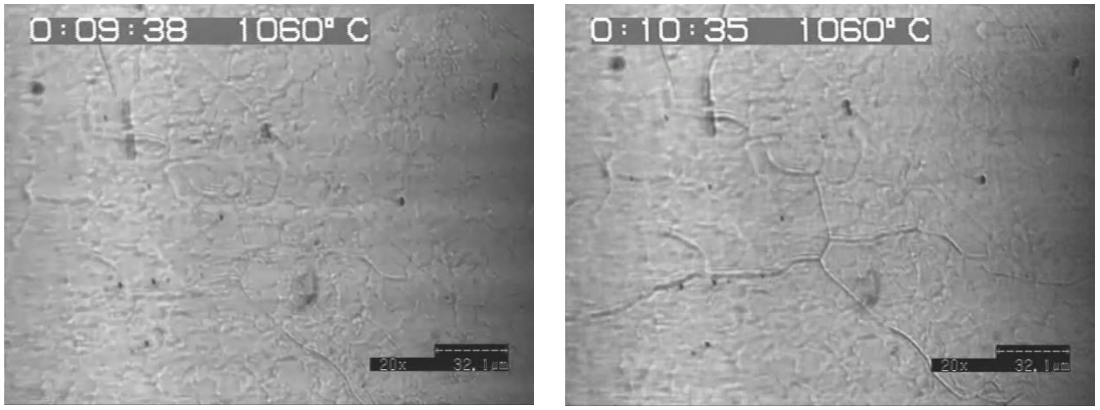

(a) (b)

Figure 6.8: Progressive austenite grain growth at a (calibrated) temperature of1100 ℃ for times of: (a) 0s, and (b) 60s (test condition 2) (scale bars= 32.1µm).

6.3.2 Cooling from Austenite

6.3.2.1 Test condition 1

For specimens cooled at a rate of 30°C per minute following a 5 minute soak at 1100°C, the first discernible transformation upon cooling was the transformation of austenite to ferrite at temperatures between about 725 °C and 698 °C as shown in Figure 6.9 (a) to (h). These figures were photographically enhanced to reveal the ferrite growth within a single austenite grain, which was about 151 µm in diameter. Ferrite nucleated on a grain boundary on the surface of the sample as shown in Figure 6.9 (b) and grew progressively until the austenite grain was completely transformed to ferrite as shown in Figure 6.9 (h).

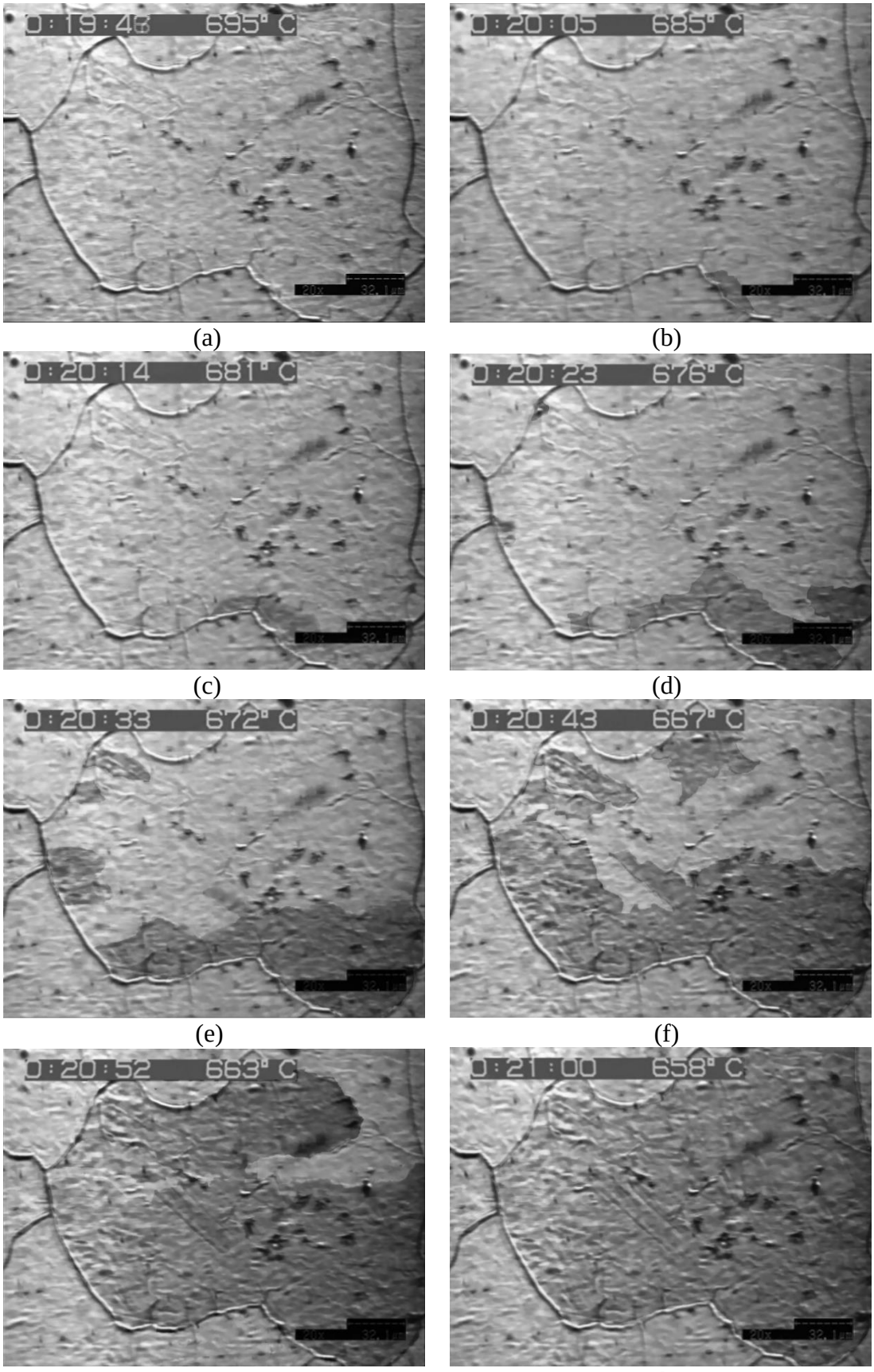

(a) (b)

(c) (d)

(e) (f)

(g) (h)

Figure 6.9: Ferrite nucleation and growth in a single austenite grain during cooling at a rate of 30°C/min (test condition 1) (scale bars= 32.1µm).

It is interesting to note that only the austenite to ferrite transformation was observed. However, it is most likely that the specimen surface was subjected to decarburization, especially during annealing at 1100°C, and subsequent analysis showed that this was the case, notwithstanding the care taken to ensure that the oxygen potential is as low as experimentally possible. The specimen has been cross-sectioned to determine whether or not there is a decarburized layer on the surface. Figure 6.10 shows this cross-section. It is evident that the surface that had been observed in the high-temperature microscope had been decarburized.

Figure 6.10: Cross sectional view of the tested sample at room temperature (test condition 1).

6.3.2.2 Test condition 2

For specimens cooled at a rate of 30°C per minute following a one minute soak at 1100°C and rapidly cooled to 800°C (Test condition 2), the first discernible transformation upon cooling was the formation of ferrite at temperatures between about 695 °C and 665 °C as shown in Figure 6.11 (a) to (f). These figures were photographically enhanced to reveal the ferrite growth within a single austenite grain. Ferrite nucleated on a grain boundary on the surface of the sample as shown in Figure 6.11 (b) and grew progressively until the austenite grain was completely transformed to ferrite as shown in Figure 6.11 (h) followed by nucleation and growth of new grains/phases on the surface.

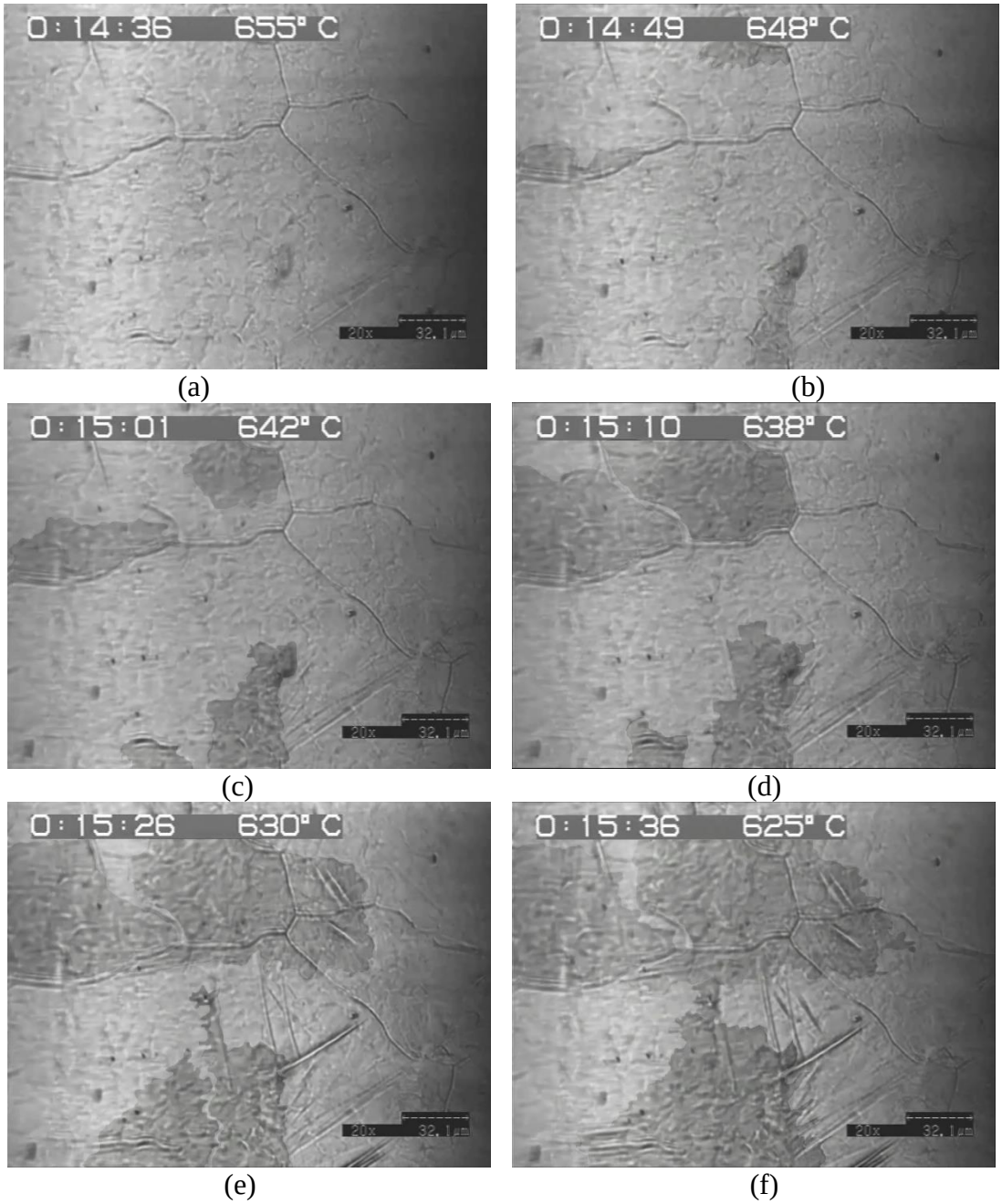

(a) (b)

(c) (d)

(e) (f)

Figure 6.11: Ferrite nucleation and growth in a single austenite grain during cooling at rate of 30°C/min (test condition 2) (scale bars= 32.1µm).

For this test condition, apart from the austenite to ferrite transformation another transformation was observed. Decarburization of the specimen surface was reduced, especially during annealing for only one minute at 1100°C. Similar to the first test condition the specimen has been cross-sectioned to determine whether or not there is a decarburized layer on the surface. Figure 6.12 shows this cross-section and it follows that the surface had not been decarburized to the same extent as the one that had been annealed for 5 minutes.

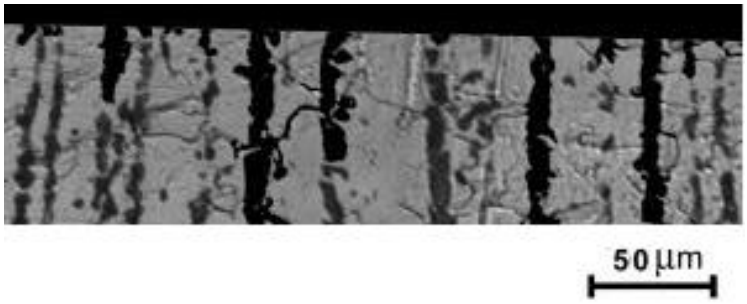

Figure 6.12: Cross sectional view of the tested sample at room temperature (test condition 2).

6.3.3 Second Phase Transformation

6.3.3.1 Test condition 1

Evidence was found of a second transformation occurring beneath the surface at a (calibrated) temperature of 618°C. At this temperature a change in the surface morphology was observed and bands formed beneath the surface. Although the surface layer due to decarburization, is totally ferrite, volumetric changes as a result of band formation below the surface leads to undulations on the surface, which are discernible in the confocal microscope. No undulations of the surface were observed below a temperature of 600 °C. Figure 6.12 showed this decarburised layer. However, it is also clear that the bands extend to just below the surface and hence, it is not surprising that surface undulations could be observed when these bands formed. These bands are shown in the plane of observation in Figure 6.13 (a) and (b) at a temperature of 410°C and room temperature respectively. Figure 6.13 (c) shows the bands formed in single austenite grain at room temperature.

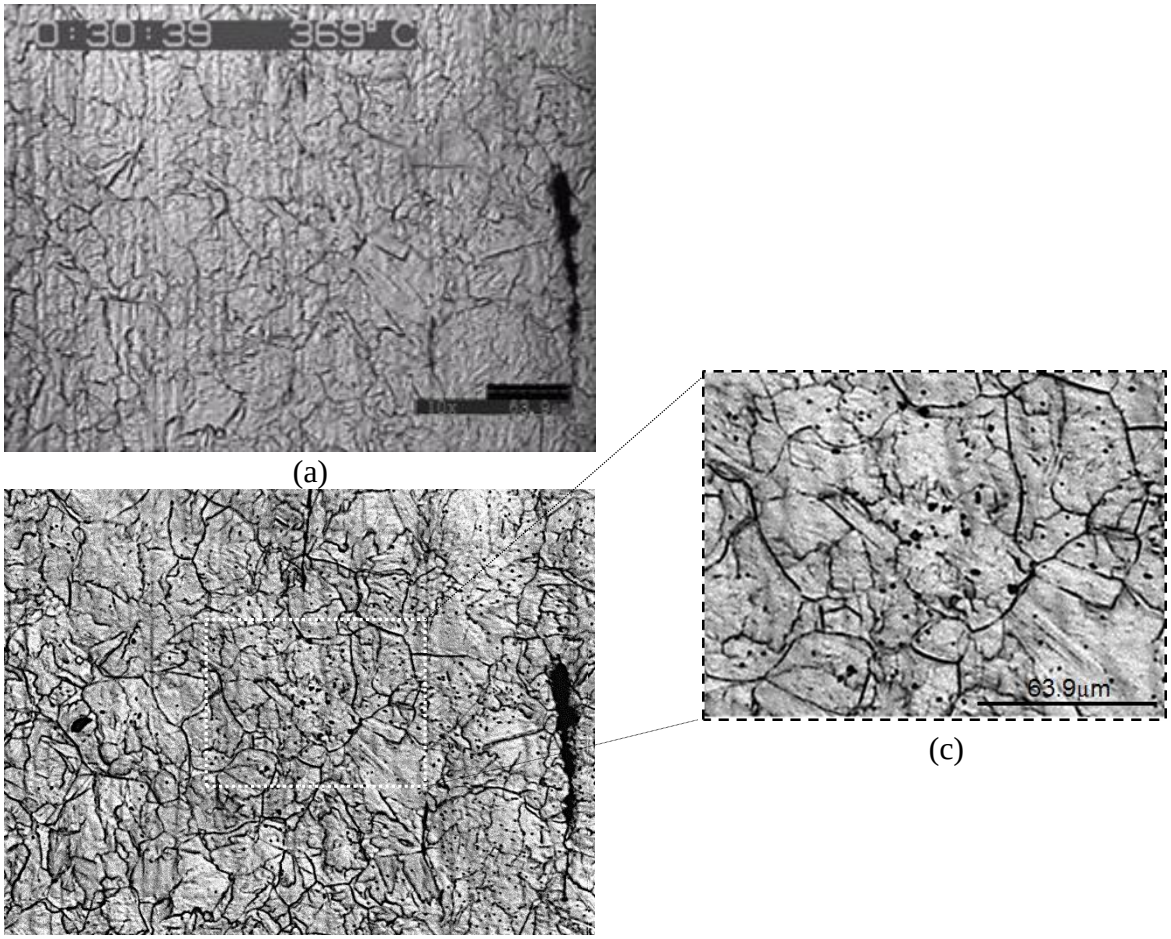

Figure 6.13: (a) Bands observed at high temperature during the test (b) the same area at room temperature, and (c) single austenite grain at room temperature just after the test (scale bars= 63.9µm).

The pearlite/ferrite bands were located about 15µm below the surface of observation as shown in Figure 6.14. In this instance, the specimen (annealed for 5 minutes) was progressively ground, polished and etched and the figure shows the plane of observation and a plane 15µm below the surface. The first pearlite/ferrite bands revealed by etching, 15µm below the surface, were identical to the weakly imaged bands observed on the sample surface (Figure 6.13).

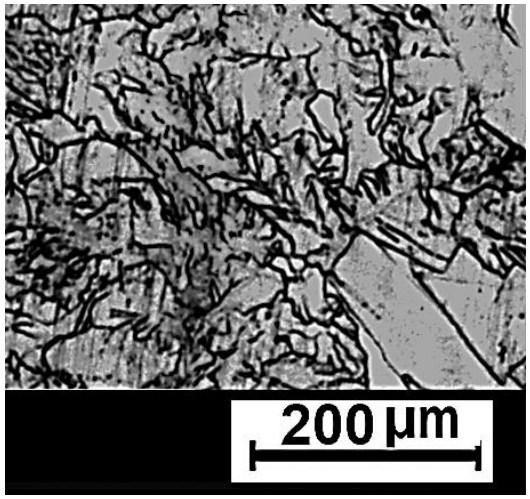

(a)

(b)

Figure 6.14: (a) absence of pearlite/ferrite bands on the surface after 2% nital etching, and (b) the first pearlite/ferrite bands found underneath the decarburized layer (15µm below the surface).

6.3.3.2 Test condition 2

During cooling from the austenitic region in this condition, ferrite nucleates on austenite grain boundaries and grows progressively within austenite grains as was earlier in Figure 6.11. The pearlite phase then filled in the gaps between the ferrite phases forming pearlite/ferrite band on the surface as can be observed in Figure 6.15 (a) and (b). Band 1 and band 2 indicated in Figure 6.15 (a) formed at about 663°C following ferrite nucleation on austenite grains. The progressive nucleation of ferrite on austenite grains results similarly in the formation of Band 3, indicated in Figure 6.15 (b).

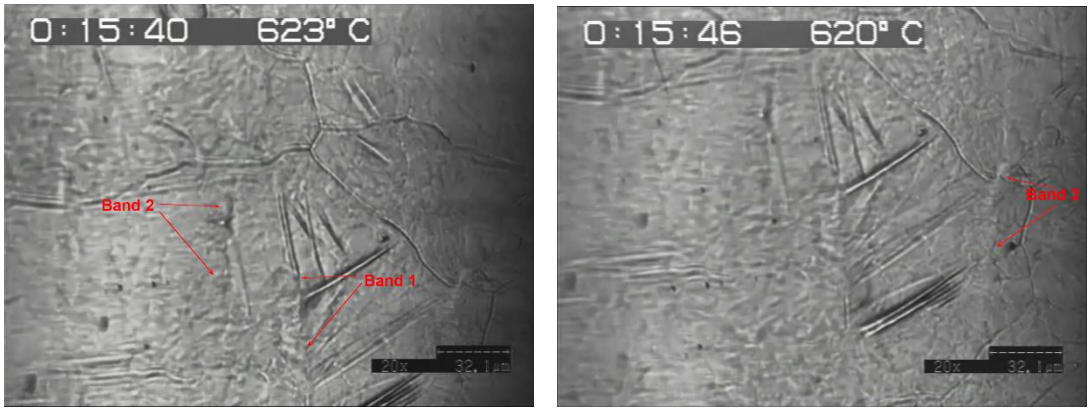

(a) (b)

Figure 6.15: Bands formed on the surface at high temperature during the test condition 2 (scale bars= 32.1µm)..

Further cooling below 631°C revealed surface undulations of pearlite/ferrite on the surface of the specimen since volumetric changes accompany band formation as shown in Figure 6.16 (a) to (d). Evidence was found of a second transformation occurring on the surface at this temperature: a change in surface morphology was observed and bands formed on the surface, which are discernible under the confocal microscope.

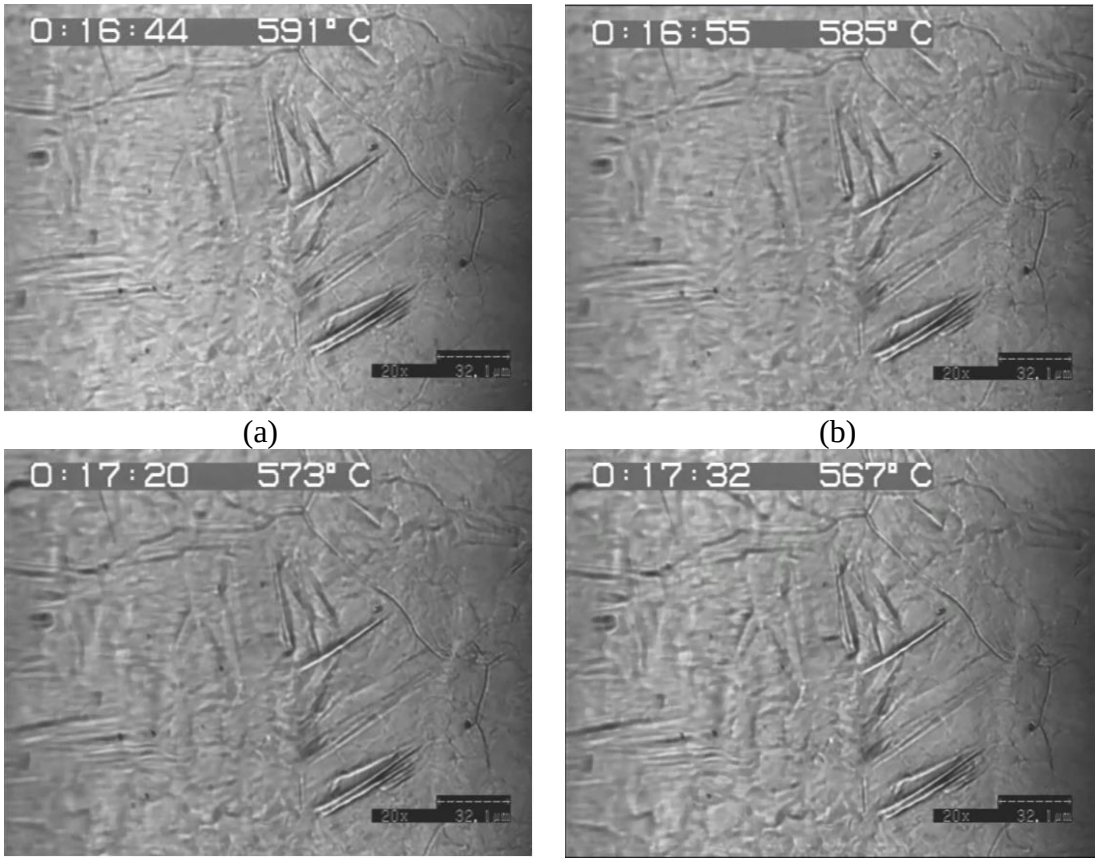

(a) (b)

(c) (d)

Figure 6.16: Morphology of pearlite/ferrite revealed on the surface (scale bars= 32.1µm).

The morphology (undulations) of pearlite/ferrite bands observed on the surface as shown in Fig. 16 (c) was compared to the pearlite/ferrite bands revealed by etching. In this instance, the specimen was etched without polishing and the figure shows the observation on the surface. The pearlite/ferrite bands revealed by etching, on the surface without polishing, were identical to the bands observed on the sample surface for the working area as well as wider area on the sample as shown from Figure 6.17 (b) and (c).

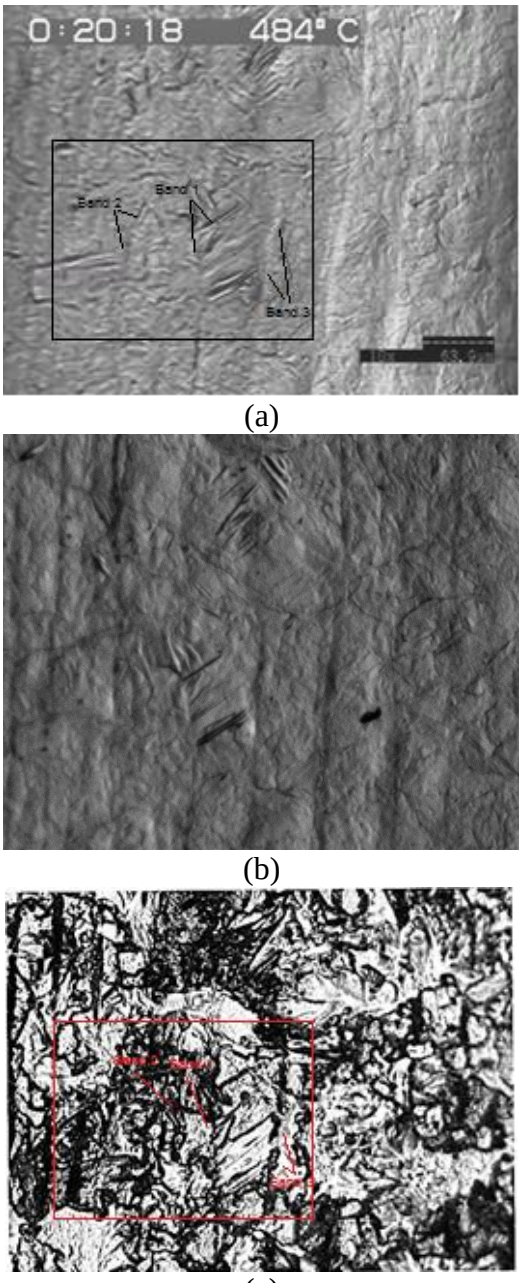

(a)

(b)

(c)

Figure 6.17: (a) Bands observed at high temperature during the test (b) the same area at room temperature and (c) pearlite/ferrite bands revealed on the (unpolished) surface after applying 2% nital etching on the same area (scale bars= 63.9µm).

The austenite grain size shown in Figure 6.9 was about 151 μm in diameter, the average austenite grain size was 95.6 ±10 μm for the specimen of test condition 1. By comparison, the (deformed) dendrite arm spacing after rolling was about 60 μm. Hence, the austenite grain size is about twice the dendrite arm (micro-chemical) spacing. Offerman [20] as well as Thompson and Howell [9] argued that when the austenite grain size is two to three times larger than the chemical band spacing, only a few nucleation sites are available for the nucleation of ferrite, leading to a significant difference in ferrite nucleation rate between regions with a high and a low A_3 transition temperature. Offerman [20] suggested that the case of hot rolled steel is different since the shape and size of austenite grains change due to hot deformation.

Verhoeven [19] found that formation of pearlite/ferrite banding depends on the primary dendrite arm spacing. For hot rolled steel, this spacing should depend on the spacing between the deformed and elongated primary and secondary arms since the spacing between (micro-chemical) bands after rolling are formed by alternation of primary dendrite arms (rotated) and secondary dendrite arms and their adjacent segregated regions (elongated) or by alternation of secondary dendrite arms and their adjacent segregated regions (elongated).

6.4 Conclusions

- Following austenite formation, continued heating led to growth of austenite grains.
- During cooling from austenite, ferrite nucleates on austenite grain boundaries and grow progressively into the austenite grains. The pearlite phase then fills the gaps between the ferrite phases. In the initial experiments, a thin layer on the surface of observation was decarburised.
- For short soaking times in austenite, pearlite/ferrite band formation could be observed on the surface. However, for longer soaking times in austenite, pearlite/ferrite band formation could still be observed just below the surface even though the surface was decarburised since the volumetric changes accompanying the band formation led to surface undulation on the surface under observation.
- The banding observed in the high-temperature microstructure were similar to those detected by optical microscopy following the same heat treatment.

Chapter 7. Conclusion and Future Work

7.1 General Conclusions

An investigation of micro-chemical and microstructural banding during hot rolling of medium-carbon steel led to the following conclusions:

- Primary dendrite arms rotate progressively around the transverse axis during hot-rolling, while the secondary dendrite arms and the adjacent areas of inter-dendritic segregation elongate progressively parallel to the rolling direction.
- When the reduction exceeds 70%, the primary as well as the secondary dendrite arms, with the associated inter-dendritic regions, align parallel to the rolling direction, thereby forming layers of low and high concentration of alloying elements respectively.
- The secondary dendrite arm spacing changes from about 160 μm in the as-cast (undeformed) condition to about 40 μm following 90% reduction
- Reheating the as-cast slab prior to hot-rolling for relatively short times does not cause a redistribution of manganese.

The variations of mechanical properties of dendritic and inter-dendritic regions in medium-carbon steel was investigated and reported in Chapter 4. The most important conclusions are:

- Nano-hardness tests (instrumented indentation tests) at room temperature revealed that there is a discernible difference in mechanical properties between dendritic and inter-dendritic regions in a continuously-cast slab. Inter-dendritic region is harder by more than 0.4 GPa. In addition, the elastic moduli of the inter-dendritic regions are higher than that of the dendritic regions and both elastic moduli were within the range of values reported in the literature.
- Hot-tensile tests, performed on specimens taken from the near-surface area of the slab (representing dendritic regions) and specimens from the deep-thickness area close to the centreline (representing inter-dendritic regions), revealed that the yield strength and elastic moduli of dendritic and inter-dendritic regions differ by a discernible amount at the hot-rolling temperatures typically used in industry. The manganese concentration of specimens taken from the quarter thickness of a slab was the same as that in the inter-dendritic regions and hence, it is reasonable to assume that specimens taken from the quarter thickness area of the slab can be used to simulate the mechanical properties of the inter-dendritic regions. This

finding also strengthens the relationship between micro-segregation and dendritic arm spacing.

Chapter 5 described the development of a two-dimensional finite-element model used to simulate the response of dendritic structures to hot-rolling of medium-carbon steel. The dendritic structures comprise primary dendrite arms perpendicular to the rolling direction, secondary dendrite arms perpendicular to the direction of the primary arms and inter-dendritic (segregated) regions between the secondary dendrite arms. This structure was simulated by simulating the inter-dendritic regions as circular shapes interspaced by secondary dendrite arms in the as-cast structure and equivalent plastic strain and von-Mises equivalent stress distributions were determined in this complex structure under a variety of conditions as a function of rolling reduction. The key findings of this part of the investigation can be summarized as follows:

- Shear bands and strain localization developed within the roll-bite due to differences in the mechanical properties of the dendritic and inter-dendritic regions.
- The secondary dendrite arms experienced larger elongations than the segregated regions within strain bands due to the lower yield point of the dendrite arms.
- During hot-rolling the primary dendrite arms rotate about the rolling direction and align with the rolling direction at rolling reductions of more than 70%.
- Secondary dendrite arms located between two segregated regions experience significant thinning during rolling until the segregated regions latch onto each other at about 70% rolling reduction.
- At rolling reductions between 65 and 75%, the primary and secondary dendrite arms and inter-dendritic regions pre-existing in the as-cast structure are destroyed and transformed into distinctive micro-chemical bands that align parallel to the rolling direction.
- The consequence of this response is that the segregated, inter-dendritic regions, which are roughly of circular shape in the as-cast structure, are transformed into essentially continuous bands parallel to the rotated dendrite arms. Hence, severe deformation by hot-rolling leads to the formation of parallel micro-chemical bands

An attempt was made to directly observe the austenite to ferrite and pearlite phase transformations by *in-situ* heat treatments within a high-temperature laser-scanning confocal microscopy as described in Chapter 6. The main observations were:

- Following austenite formation, continued heating led to grain growth of austenite grains.
- During cooling from the austenitic region, ferrite grains nucleate on austenite grain boundaries and grow progressively within austenite grains. The pearlite phase then fills in the gaps between the ferrite phases. In the initial experiments a thin layer near the surface of observation was decarburised, but pearlite/ferrite band formation just below the surface could still be observed even though the surface was decarburised since the volumetric changes accompanying the band formation led to surface undulations on the surface under observation.
- The banding observed in the high-temperature microstructure were similar to those detected at room temperature by optical microscopy following the same heat treatment that was used in the microscope.

7.2 Future work

Based on the findings of the present study, the following suggestions are made for future research:

i. It was shown in this study that the progressive rotation of primary and secondary dendrite arms, with their adjacent inter-dendritic areas lead to micro-chemical banding. These initial results require further investigation and refinement of the experimental techniques used as well as the modelling exercise.

ii. The use instrumented indentation techniques (nano-indentation) in this study revealed that there is a discernible difference in mechanical properties between dendritic and inter-dendritic regions in a continuously-cast slab at room temperature. It would be very useful to extend such measurements to temperatures between 800 and 1000°C.

iii. The two-dimensional finite-element models used in this study should ideally be extended to three-dimensional finite-element analysis.

The *in-situ* observation of banding during the cooling of austenite should be refined and isothermal heat treatments, similar to those conducted in earlier research, should be conducted.

References

1. Krauss, G., *Steels: Heat Treatment and Processing Principles (ASM International*. Materials Park, OH, 1990: p. 218.

2. Krauss, G., *Solidification, segregation, and banding in carbon and alloy steels.* Metallurgical and Materials Transactions B, 2003. **34**(6): p. 781-792.

3. Krauss, G., *Steels: processing, structure, and performance*. 2005: Asm Intl.

4. Majka, T.F., Matlock, D.K., and Krauss, G., *Development of microstructural banding in low-alloy steel with simulated Mn segregation.* Metallurgical and Materials Transactions A, 2002. **33**(6): p. 1627-1637.

5. Majka, T.F., Matlock, D.K., Krauss, G., and Lusk, M.T. *Analysis of tensile deformation behavior and microstructural evolution in an artificially banded SAE 5140*. 2000.

6. Brooks, C.R., *Principles of the Austenitization of Steels*. 1992: Elsevier Science Publishers LTD.

7. Joo, M.S., Suh, D.W., and Bhadeshia, H., *Mechanical Anisotropy in Steels for Pipelines.* ISIJ International, 2013. **53**(8): p. 1305-1314.

8. Samuels, L.E., *Light microscopy of carbon steels*. 1999: ASM International.

9. Thompson, S.W. and Howell, P.R., *Factors influencing ferrite/pearlite banding and origin of large pearlite nodules in a hypoeutectoid plate steel.* Materials Science and Technology, 1992. **8**(9): p. 777-784.

10. Bhadeshia, H., *Ferrite formation in heterogeneous dual-phase steels= Formation de ferrite dans les aciers hétérogènes biphasés.* Scripta metallurgica, 1983. **17**(7): p. 857-860.

11. Bhadeshia, H., *Alternatives to the ferrite-pearlite microstructures*, in *Proceedings of the International Conference on Microalloying in Steels*, J.M. RodriguezIbabe, I. Gutierrez, and B. Lopez, Editors. 1998, Transtec Publications Ltd: Zurich-Uetikon. p. 39-50.

12. Bhadeshia, H., *Phase transformations contributing to the properties of modern steels.* TECHNICAL SCIENCES, 2010. **58**(2).

13. Bhadeshia, H., Bhadeshia, H., and Honeycombe, R.W.K., *Steels: microstructure and properties*. 2006: Butterworth-Heinemann.

14. Verhoeven, J.D., *Steel Metallurgy for the Non-metallurgist*. 2007: ASM International.

15. Wilson, P., Murty, Y., Kattamis, T., and Mehrabian, R., *Effect of homogenization on sulphide morphology and mechanical properties of rolled AISI 4340 steel.* Metals Technology, 1975. **2**(1): p. 241-244.

16. Luiten, E.E.M., *Beyond energy efficiency: Actors, networks and government intervention in the development of industrial process technologies*. 2001, Utrecht University. p. pp 129-161.

17. Morita, Z., Emi, T., Zaidan, K.-s., and Section, K.S.K.K.T.I., *An Introduction to Iron and Steel Processing*. 1997, Tokyo, Japan The Foundation.

18. Flemings, M.C. and Nereo, G.E., *Macrosegregation: part I.* Trans. Metall. Soc. AIME, 1967. **239**: p. 1449–1461.

19. Verhoeven, J.D., *A review of microsegregation induced banding phenomena in steels.* Journal of materials engineering and performance, 2000. **9**(3): p. 286-296.

20. Offerman, S.E., Van Dijk, N.H., Rekveldt, M.T., Sietsma, J., and Van Der Zwaag, S., *Ferrite/pearlite band formation in hot rolled medium carbon steel.* Materials Science and Technology, 2002. **18**(3): p. 297-303.

21. Bastien, P.G., *The mechanism of formation of banded structures.* Institute of Materials, 1 Carlton House Terrace, London, SW 1 Y 5 DB, UK, 2001., 2001: p. 95-115.

22. Caballero, F.G., Garcia-Junceda, A., Capdevila, C., and Garcia, D.E.A., *Evolution of microstructural banding during the manufacturing process of dual phase steels.* Materials transactions, 2006. **47**(9): p. 2269-2276.

23. Grossterlinden, R., Kawalla, R., Lotter, U., and Pircher, H., *Formation of pearlitic banded structures in ferritic-pearlitic steels.* Steel research, 1992. **63**(8): p. 331-336.

24. Jatczak, C.F., Girardi, D.J., and Rowland, E.S., *On banding in steel.* Transactions of American Society for Metals, 1956: p. 279.

25. Rivera-Díaz-Del-Castillo, P.E.J., Van Der Zwaag, S., and Sietsma, J., *A model for ferrite/pearlite band formation and prevention in steels.* Metallurgical and Materials Transactions A, 2004. **35**(2): p. 425-433.

26. Sietsma, J. and Van Der Zwaag, S., *A Model for Ferrite/Pearlite Band Formation and Prevention in Steels.* Metallurgical and Materials Transactions A, 2004. **35**(2): p. 425-433.

27. Jaegle, E.A., *Modelling of Microstructural Banding during Transformations in Steels*, in *Department of Materials Science & Metallurgy*. 2007, University of Cambridge: Cambridge.

28. Bor, A.S., *Effect of Pearlite Banding on Mechanical Properties of Hot-rolled Steel Plates.* ISIJ international, 1991. **31**(12): p. 1445-1446.

29. Grange, R.A., *Effect of microstructural banding in steel.* MET TRANS, 1971. **2**(2): p. 417-426.

30. Stauffer, A.C., Koss, D.A., and McKirgan, J.B., *Microstructural banding and failure of a stainless steel.* Metallurgical and Materials Transactions A, 2004. **35**(4): p. 1317-1324.

31. Owen, W.S., Cohen, M., Averbach, B.L., and Ship Structure Committee Washington, D.C., *The Influence of Ferrite Banding on the Impact Properties of Mild Steel.* Welding Journal, 1958. **23**.

32. Kirkaldy, J.S., Brigham, R.J., Domian, H.A., and Ward, R.G., *A study of banding in Skelp by electron-probe microanalysis.* Canadian Metallurgical Quarterly, 1963. **2**: p. 233–241.

33. Losert, W., Shi, B.Q., and Cummins, H.Z., *Evolution of dendritic patterns during alloy solidification: Onset of the initial instability.* Proceedings of the National Academy of Sciences of the United States of America, 1998. **95**(2): p. 431.

34. Flinn, R.A., *Fundamentals of metal casting*. 1963: Addison-Wesley.

35. Kurz, W. and Fisher, D.J., *Fundamentals of solidification.* Trans Tech Publications Ltd, Trans Tech House, 4711, Aedermannsdorf, Switzerland, 1986. 244, 1986.

36. Dantzig, J. and Rappaz, M., *Solidification*. 2009 621 pages

37. Flemings, M.C., *Solidification processing*. Materials Science and Engineering Series 1974.

38. Reed-Hill, R.E. and Abbaschian, R., *Physical Metallurgy Principles*. Third ed. 1994, Boston, MA, USA: PWS

39. Scheil, E., *Bemerkungen zur schichtkristallbildung.* Zeitschrift für Metallkunde, 1942. **34**(3): p. 70-72.

40. Brody, H.D. and Flemings, M.C., *Solute Reditribution in Dendritic Solidification.* Trans. AIME, 1966. **236**: p. 615.

41. Purdy, G.R. and Kirkaldy, J.S., *Homogenization by diffusion.* Metallurgical and Materials Transactions B, 1971. **2**(2): p. 371-378.

42. Rappaz, M., *Modelling of microstructure formation in solidification processes.* International Materials Reviews, 1989. **34**(1): p. 93-124.

43. Kirkwood, D.H., *Microsegregation.* Materials Science and Engineering, 1984. **65**(1): p. 101-109.

44. Cornelissen, M.C.M., *Mathematical model for solidification of multicomponent alloys.* Ironmaking and Steelmaking, 1986. **13**(4): p. 204.

45. Battle, T.P., *Mathematical modelling of solute segregation in solidifying materials.* International Materials Reviews, 1992. **37**(1): p. 249-270.

46. Cole, G.S., *Inhomogeneities and their control via solidification.* Metallurgical and Materials Transactions B, 1971. **2**(2): p. 357-370.

47. Martin, J.W., Doherty, R.D., and Cantor, B., *Stability of microstructure in metallic systems*. 2nd ed. 1997: Cambridge University Press.

48. Kattamis, T.Z., Coughlin, J.C., and Flemings, M.C., *Influence of coarsening on dendrite arm spacing of aluminum-copper alloys.* AIME MET SOC TRANS, 1967. **239**(10).

49. Pierer, R. and Bernhard, C., *On the influence of carbon on secondary dendrite arm spacing in steel.* Journal of materials science, 2008. **43**(21): p. 6938-6943.

50. Preßlinger, H., Ilie, S., Reisinger, P., Schiefermüller, A., Pissenberger, A., Parteder, E., and Bernhard, C., *Methods for assessment of slab centre segregation as a tool to control slab continuous casting with soft reduction.* ISIJ International, 2006. **46**(12): p. 1845-1851.

51. Stead, J.E., Journal of Society of the Chemical Industry, 1913. **33**: p. 173-84.

52. Oberhoffer, P., Stahl und Eisen, 1913. **33**: p. 1569-1574.

53. Howe, H.M., *The metallography of steel and cast iron*. 1916: McGraw-Hill book company, inc.

54. Korda, A.A., Mutoh, Y., Miyashita, Y., Sadasue, T., and Mannan, S.L., *In situ observation of fatigue crack retardation in banded ferrite-pearlite microstructure due to crack branching.* Scripta materialia, 2006. **54**(11): p. 1835-1840.

55. Preßlinger, H., Mayr, M., Tragl, E., and Bernhard, C., *Assessment of the primary structure of slabs and the influence on hot-and cold-rolled strip structure.* Steel research international, 2006. **77**(2): p. 107-115.

56. Samuels, L.E., *Optical microscopy of carbon steels*. 1980: American Society for Metals.

57. Owen, W.S., Whitmore, D.H., Cohen, M., and Averbach, B.L., *Relation of Charpy Impact Properties to Microstructure of Three Ship Steels'.* Welding Research Supplement, 1957: p. 503 - 511.

58. Heiser, F.A. and Hertzberg, R.W., J. Iron Steel Institute, 1971. **209** p. 975-980.

59. Li, T., *Banding in nickel-base superalloys and steels*. 2007, The University of British Columbia.

60. Rao, G.R., Lee, E.H., Boatner, L.A., Chin, B.A., and Mansur, L.K., *Multiple ion implantation effects on hardness and fatigue properties of Fe---13Cr---15Ni alloys* 1*. Journal of nuclear materials, 1992. **191**: p. 748-753.

61. Tasan, C.C., Hoefnagels, J.P.M., and Geers, M.G.D., *Microstructural banding effects clarified through micrographic digital image correlation.* Scripta materialia, 2010. **62**(11): p. 835-838.

62. Spitzig, W.A., *Effect of sulfide inclusion morphology and pearlite banding on anisotropy of mechanical properties in normalized C-Mn steels.* Metallurgical and Materials Transactions A, 1983. **14**(1): p. 271-283.

63. Maier, P., Richter, A., Faulkner, R., and Ries, R., *Application of nanoindentation technique for structural characterisation of weld materials.* Materials characterization, 2002. **48**(4): p. 329-339.

64. Seah, M., *Interface adsorption, embrittlement and fracture in metallurgy: A review.* Surface Science, 1975. **53**(1): p. 168-212.

65. Druce, S., Gage, G., and Jordan, G., *Effect of ageing on properties of pressure vessel steels.* Acta Metallurgica, 1986. **34**(4): p. 641-652.

66. Beere, W.B. and Buswell, J.T., *The effect of heat treatment on phosphorus segregation in a submerged-arc weld metal.* ASTM SPECIAL TECHNICAL PUBLICATION, 1999. **1325**: p. 317-332.

67. Peng, X.N., Peng, Y., Wei, J.S., and Tian, Z.L., *Analysis of Microstructure and Micro Mechanical Properties for Weld Joints of 1000MPa Class Steel by Nanoindentation Technique.* Applied Mechanics and Materials, 2012. **217**: p. 1987-1993.

68. Oliver, W.C. and Pharr, G.M., *Measurement of hardness and elastic modulus by instrumented indentation: Advances in understanding and refinements to methodology.* Journal of materials research, 2004. **19**(01): p. 3-20.

69. Oliver, W.C. and Pharr, G.M., *Improved technique for determining hardness and elastic modulus using load and displacement sensing indentation experiments.* Journal of materials research, 1992. **7**(6): p. 1564-1583.

70. Ohmura, T., Tsuzaki, K., and Matsuoka, S., *Nanohardness measurement of high-purity Fe–C martensite.* Scripta materialia, 2001. **45**(8): p. 889-894.

71. Li, X. and Bhushan, B., *A review of nanoindentation continuous stiffness measurement technique and its applications.* Materials characterization, 2002. **48**(1): p. 11-36.

72. Fischer-Cripps, A.C., *Nanoindentation*. Vol. 1. 2011: Springer.

73. Trenkle, J.C., Packard, C.E., and Schuh, C.A., *Hot nanoindentation in inert environments.* Review of Scientific Instruments, 2010. **81**(7): p. 073901-073901-13.

74. Korte, S., Stearn, R.J., Wheeler, J.M., and Clegg, W.J., *High temperature microcompression and nanoindentation in vacuum.* Journal of materials research, 2012. **27**(1): p. 167.

75. Duan, Z.C. and Hodge, A.M., *High-temperature nanoindentation: New developments and ongoing challenges.* JOM, 2009. **61**(12): p. 32-36.

76. Chen, J., Young, B., and Uy, B., *Behavior of high strength structural steel at elevated temperatures.* Journal of Structural Engineering, 2006. **132**(12): p. 1948-1954.

77. Qiang, X., Bijlaard, F.S., and Kolstein, H., *Elevated-temperature mechanical properties of high strength structural steel S460N: Experimental study and recommendations for fire-resistance design.* Fire Safety Journal, 2013. **55**: p. 15-21.

78. Qiang, X., Bijlaard, F.S., and Kolstein, H., *Deterioration of mechanical properties of high strength structural steel S460N under steady state fire condition.* Materials & Design, 2012. **36**: p. 438-442.

79. Qiang, X., Bijlaard, F.S., and Kolstein, H., *Deterioration of mechanical properties of high strength structural steel S460N under transient state fire condition.* Materials & Design, 2012. **40**: p. 521-527.

80. Qiang, X., Bijlaard, F.S., and Kolstein, H., *Post-fire mechanical properties of high strength structural steels S460 and S690.* Engineering Structures, 2012. **35**: p. 1-10.

81. Knobloch, M., Pauli, J., and Fontana, M., *Influence of the strain-rate on the mechanical properties of mild carbon steel at elevated temperatures.* Materials & Design, 2013.

82. Wang, W.-y., Liu, B., and Kodur, V., *Effect of Temperature on Strength and Elastic Modulus of High-Strength Steel.* Journal of Materials in Civil Engineering, 2012. **25**(2): p. 174-182.

83. Kodur, V., Dwaikat, M., and Fike, R., *High-temperature properties of steel for fire resistance modeling of structures.* Journal of Materials in Civil Engineering, 2010. **22**(5): p. 423-434.

84. Ufuah, E. *Characterization of elevated temperature mechanical properties of butt-welded connections made with HS steel grade S420M*. in *Proceedings of the World Congress on Engineering*. 2012.

85. Luecke, W.E., McColskey, J.D., McCowan, C.N., Banovic, S.W., Fields, R.J., Foecke, T., and Siewert, T.A., *Mechanical properties of structural steels*. 2005: US Department of Commerce, Technology Administration, National Institute of Standards and Technology.

86. Koster, W., *The Temperature Dependence of the Elasticity Modulus of Pure Metals.* Zeitschrift für Metallkunde, 1948. **39**: p. 1-9.

87. Schneider, R. and Lange, J. *Constitutive equations of structural steel S460 at high temperatures*. in *Nordic steel construction conference*. 2009.

88. Outinen, J., Kaitila, O., and Mäkeläinen, P., *High-temperature Testing of Structural Steel and Modelling of Structures at Fire Temperatures: Research Report*. 2001: Helsinki University of Technology.

89. Outinen, J. and Maekelaeinen, P., *Mechanical properties of structural steel at elevated temperatures and after cooling down.* Fire and materials, 2004. **28**(2-4): p. 237-251.

90. Schneider, R. and Lange, J., *Constitutive equations and empirical creep law of structural steel S460 at high temperatures.* Journal of Structural Fire Engineering, 2011. **2**(3): p. 217-230.

91. Schneider, R. and Lange, J. *Material and creep behaviour of S460 in case of fire-experimental investigation and analytical modeling*. in *International conference application of structural fire engineering, Cost, Prague*. 2011.

92. Outinen, J., Kesti, J., and Mäkeläinen, P., *Fire design model for structural steel S355 based upon transient state tensile test results.* Journal of Constructional Steel Research, 1997. **42**(3): p. 161-169.

93. Mäkeläinen, P., Outinen, J., and Kesti, J., *Fire design model for structural steel S420M based upon transient-state tensile test results.* Journal of Constructional Steel Research, 1998. **48**(1): p. 47-57.

94. Wagoner, R.H. and Chenot, J.-L., *Metal forming analysis*. 2001: Cambridge University Press.

95. Kalpakjian, S. and Schmid, S., *Manufacturing Engineering & Technology*. 2013: Pearson Education.

96. Rao, S.S., *The finite element method in engineering*. 2005: Butterworth-heinemann.

97. Champion, E.R., *Finite element analysis in manufacturing engineering*. 1992: McGraw-Hill.

98. Rowe, G.W., Sturgess, C.E.N., and Hartley, P., *Finite-Element Plasticity and Metalforming Analysis*. 2005: Cambridge University Press.

99. Groover, M.P., *Fundamentals of Modern Manufacturing: Materials, Processes, and Systems, 5th Edition*. 2012.

100. Bower, A.F., *Applied Mechanics of Solids*. 2011: Taylor & Francis.

101. Chen, W.F. and Han, D.J., *Plasticity for Structural Engineers*. 2007: J. Ross Pub.

102. Kelly, P., *Solid Mechanics*. 2012, The University of Auckland.

103. Roylance, D., *Mechanical Properties of Materials.* Massachusetts Institute of Technology study, Cambridge, 2008.

104. Roylance, D., *Mechanics of Materials*. 1996: Wiley.

105. Roylance, D., *Yield and Plastic Flow.* Massachusetts Institute of Technology study, Cambridge, 2001.

106. DoITPoMS. *Stress Analysis and Mohr's Circle*. 2008 [cited 2014 09/04].

107. Pietrzyk, M. and Lenard, J.G., *Thermal-mechanical modelling of the flat rolling process*. 1991: Springer.

108. Pietrzyk, M., Cser, L., and Lenard, J., *Mathematical and physical simulation of the properties of hot rolled products*. 1999: Elsevier.

109. Ginzburg, V.B., *High-quality steel rolling: theory and practice*. 1993: CRC Press.

110. Haslach Jr, H.W. and Armstrong, R.W., *Deformable bodies and their material behavior*. 2004: John Wiley & Sons Incorporated.

111. Ginzburg, V.B., *Steel-rolling technology: theory and practice*. 1989: M. Dekker.

112. Ginzburg, V.B. and Ballas, R., *Flat rolling fundamentals*. 2000: CRC Press.

113. Roberts, W.L. and Roberts, W., *Cold rolling of steel*. 1978: M. Dekker New York.

114. Roberts, W.L., *Hot rolling of steel*. 1983: CRC Press.

115. Muñiz, A.R., *Non-Linear Finite Element Method Simulation and Modeling of the Cold and Hot Rolling Processes*. 2007, Virginia Polytechnic Institute and State University.

116. Crisfield, M.A., Remmers, J.J., and Verhoosel, C.V., *Nonlinear finite element analysis of solids and structures*. 2012: John Wiley & Sons.

117. Lemaitre, J. and Chaboche, J.L., *Mechanics of Solid Materials*: Cambridge University Press.

118. Shida, S., *Effect of Carbon Content, Temperature, and Strain Rate on Compression Flow Stress of Carbon Steels.* Hitachi Research Report, 1974: p. 1-9.

119. Grober, H., *Finite element simulation of hot flat rolling of steel.* Numiform 86. Numerical Methods in Industrial Forming Processes, 1986: p. 225-229.

120. Micari, F., *Three-dimensional coupled thermo-mechanical analysis of hot rolling processes.* Journal of Materials Processing Technology, 1992. **34**(1): p. 303-310.

121. Dawson, P.R. and Thompson, E.G., *Finite element analysis of steady-state elasto-visco-plastic flow by the initial stress-rate method.* International Journal for Numerical Methods in Engineering, 1978. **12**(1): p. 47-57.

122. Li, G.-J. and Kobayashi, S., *Rigid-plastic finite-element analysis of plane strain rolling.* Journal of Engineering for Industry, 1982. **104**(1): p. 55-63.

123. Mori, K., Osakada, K., and Oda, T., *Simulation of plane-strain rolling by the rigid-plastic finite element method.* International Journal of Mechanical Sciences, 1982. **24**(9): p. 519-527.

124. Hwu, Y.-J. and Lenard, J., *A finite element study of flat rolling.* Journal of Engineering Materials and Technology, 1988. **110**(1): p. 22-27.

125. Dixit, U. and Dixit, P., *Finite-element analysis of flat rolling with inclusion of anisotropy.* International Journal of Mechanical Sciences, 1997. **39**(11): p. 1237-1255.

126. Zhou, S., *An integrated model for hot rolling of steel strips.* Journal of Materials Processing Technology, 2003. **134**(3): p. 338-351.

127. Chen, W., Samarasekera, I., Kumar, A., and Hawbolt, E., *Mathematical modelling of heat flow and deformation during rough rolling.* Ironmaking & steelmaking, 1993. **20**(2): p. 113-125.

128. Tseng, A.A. and Wang, S.R., *Effects of interface resistance on heat transfer in steel cold rolling.* Steel research, 1996. **67**(2): p. 44-51.

129. Sellars, C., *Modelling microstructural development during hot rolling.* Materials Science and technology, 1990. **6**(11): p. 1072-1081.

130. Colás, R., *A model for the hot deformation of low-carbon steel.* Journal of Materials Processing Technology, 1996. **62**(1): p. 180-184.

131. Roucoules, C. and Hodgson, P., *Post-dynamic recrystallisation after multiple peak dynamic recrystallisation in C–Mn steels.* Materials Science and technology, 1995. **11**(6): p. 548-556.

132. Busso, E.P., *A continuum theory for dynamic recrystallization with microstructure-related length scales.* International Journal of Plasticity, 1998. **14**(4): p. 319-353.

133. Liu, Y. and Lin, J., *Modelling of microstructural evolution in multipass hot rolling.* Journal of Materials Processing Technology, 2003. **143**: p. 723-728.

134. Choi, K.S., Liu, W.N., Sun, X., and Khaleel, M.A., *Microstructure-based constitutive modeling of TRIP steel: Prediction of ductility and failure modes under different loading conditions.* Acta Materialia, 2009. **57**(8): p. 2592-2604.

135. Sun, X., Choi, K.S., Soulami, A., Liu, W.N., and Khaleel, M.A., *On key factors influencing ductile fractures of dual phase (DP) steels.* Materials Science and Engineering: A, 2009. **526**(1): p. 140-149.

136. Paul, S.K., *Micromechanics based modeling of Dual Phase steels: Prediction of ductility and failure modes.* Computational Materials Science, 2012. **56**: p. 34-42.

137. Sun, X., Choi, K.S., Liu, W.N., and Khaleel, M.A., *Predicting failure modes and ductility of dual phase steels using plastic strain localization.* International Journal of Plasticity, 2009. **25**(10): p. 1888-1909.

138. Uthaisangsuk, V., Prahl, U., and Bleck, W., *Micromechanical modelling of damage behaviour of multiphase steels.* Computational Materials Science, 2008. **43**(1): p. 27-35.

139. Nygårds, M. and Gudmundson, P., *Micromechanical modeling of ferritic/pearlitic steels.* Materials Science and Engineering: A, 2002. **325**(1): p. 435-443.

140. Luo, C. and Ståhlberg, U., *Deformation of inclusions during hot rolling of steels.* Journal of Materials Processing Technology, 2001. **114**(1): p. 87-97.

141. Luo, C. and Ståhlberg, U., *An alternative way for evaluating the deformation of MnS inclusions in hot rolling of steel.* Scandinavian journal of metallurgy, 2002. **31**(3): p. 184-190.

142. Melander, A., *A finite element study of short cracks with different inclusion types under rolling contact fatigue load.* International Journal of Fatigue, 1997. **19**(1): p. 13-24.

143. Hwang, Y. and Chen, D., *Analysis of the deformation mechanism of void generation and development around inclusions inside the sheet during sheet rolling processes.* Proceedings of the Institution of Mechanical Engineers, Part B: Journal of Engineering Manufacture, 2003. **217**(10): p. 1373-1381.

144. Yu, H., Liu, X., and Li, X., *FE analysis of inclusion deformation and crack generation during cold rolling with a transition layer.* Materials Letters, 2008. **62**(10): p. 1595-1598.

145. Yu, H.-l., Liu, X.-h., Bi, H.-y., and Chen, L.-q., *Deformation behavior of inclusions in stainless steel strips during multi-pass cold rolling.* Journal of Materials Processing Technology, 2009. **209**(1): p. 455-461.

146. Yu, H.-L., Bi, H.-Y., Liu, X.-h., and Tu, Y.-F., *Strain distribution of strips with spherical inclusion during cold rolling.* Transactions of Nonferrous Metals Society of China, 2008. **18**(4): p. 919-924.

147. Rappaz, M. and Voller, V., *Modeling of micro-macrosegregation in solidification processes.* Metallurgical and Materials Transactions A, 1990. **21**(2): p. 749-753.

148. Llovet Ximenes, X., *Electron probe microanalysis: principles and applications.* Capítol del llibre: Handbook of instrumental techniques for materials, chemical and biosciences research, Centres Científics i Tecnològics. Universitat de Barcelona, Barcelona, 2012. Part I. Materials technologies (MT), MT. 4, 12 p., 2012.

149. Pouchou, J.-L., *X-Ray microanalysis of stratified specimens.* Analytica chimica acta, 1993. **283**(1): p. 81-97.

150. Pouchou, J.-L., *X-ray microanalysis of thin surface films and coatings.* Microchimica Acta, 2002. **138**(3-4): p. 133-152.

151. Grote, K.H. and Antonsson, E.K., *Springer Handbook of Mechanical Engineering*. 2009: Springer.

152. Campbell, J., *Castings*. 2003: Elsevier Science.

153. Totten, G.E., Funatani, K., and Xie, L., *Handbook of Metallurgical Process Design*. 2006: Taylor & Francis.

154. Griesser, S. and O'LEARY, P., *A new approach for the automatic evaluation of the solidification structure in steel using orientational entropy filtering.* Journal of microscopy, 2013. **253**(2): p. 161-165.

155. Borgenstam, A., Höglund, L., Ågren, J., and Engström, A., *DICTRA, a tool for simulation of diffusional transformations in alloys.* Journal of phase equilibria, 2000. **21**(3): p. 269-280.

156. Bos, C. and Sietsma, J., *A mixed-mode model for partitioning phase transformations.* Scripta materialia, 2007. **57**(12): p. 1085-1088.

157. Sietsma, J. and van der Zwaag, S., *A concise model for mixed-mode phase transformations in the solid state.* Acta Materialia, 2004. **52**(14): p. 4143-4152.

158. Dmitrieva, O., Ponge, D., Inden, G., Millán, J., Choi, P., Sietsma, J., and Raabe, D., *Chemical gradients across phase boundaries between martensite and austenite in steel studied by atom probe tomography and simulation.* Acta Materialia, 2011. **59**(1): p. 364-374.

159. Bower, T. and Flemings, M., *Formation of the chill zone in ingot solidification.* AIME MET SOC TRANS, 1967. **239**(2): p. 216-219.

160. Pierer, R., Rauter, W., and Bernhard, C., *The Importance of Solidification Structure with Respect to Hot Tearing during Continuous Casting of Steels.* Supplemental Proceedings: Materials Properties, Characterization, and Modeling, Volume 2: p. 251-258.

161. Fredriksson, H. and Åkerlind, U., *Materials processing during casting*. 2006: John Wiley & Sons Inc.

162. Ganguly, S. and Choudhary, S., *Quantification of the Solidification Microstructure in Continuously-Cast High-Carbon Steel Billets.* Metallurgical and Materials Transactions B, 2009. **40**(3): p. 397-404.

163. Cicutti, C., Bilmes, P., and Boeri, R., *Estimation of primary dendrite arm spacings in continuous casting products.* Scripta materialia, 1997. **37**(5): p. 599-604.

164. Senk, D., Erdem, E., and Stratemeier, S., *Statistical analysis of EPMA results for numerical modelling of micro-segregation in steel.* International Journal of Cast Metals Research, 2009. **22**(1-4): p. 94-98.

165. Senk, D., Emmerich, H., Rezende, J., and Siquieri, R., *Estimation of Segregation in Iron Manganese Steels.* Advanced Engineering Materials, 2007. **9**(8): p. 695-702.

166. Domitner, J., Kharicha, A., Wu, M., and Ludwig, A., *Application of microprobe analysis to the reconstruction and characterization of dendritic structures.* Metallurgical and Materials Transactions A, 2013. **44**(2): p. 607-616.

167. Panjkovic, V., *Friction and the Hot Rolling of Steel*. 2014: Taylor & Francis.

168. Richelsen, A.B., *Numerical analysis of asymmetric rolling accounting for differences in friction.* Journal of Materials Processing Technology, 1994. **45**(1–4): p. 149-154.

169. Ward, R., *Effect of annealing on the dendritic segregation of manganese in steel.* Journal of the Iron and Steel Institute, 1965. **203**: p. 930-932.

170. Brooks, C.R., *Principles of the Heat Treatment of Plain Carbon and Low Alloy Steels*. 1996: ASM International.

171. Flemings, M., *Behavior of metal alloys in the semisolid state.* Metallurgical Transactions A, 1991. **22**(5): p. 957-981.

172. Spencer, D., Mehrabian, R., and Flemings, M., *Rheological behavior of Sn-15 pct Pb in the crystallization range.* Metallurgical Transactions, 1972. **3**(7): p. 1925-1932.

173. Pawelski, O. and Gopinathan, V., *Comparison of material flow and deformation resistance of HSLA steel deformed by hot rolling and by flat compression under simulated conditions.* Journal of Mechanical Working Technology, 1981. **5**(3): p. 267-280.

174. Sakai, T., Saito, Y., Hirano, K., and Kato, K., *Deformation and recrystallization behavior of low carbon steel in high speed hot rolling.* Transactions of the Iron and Steel Institute of Japan, 1988. **28**(12): p. 1028-1035.

175. Bramfitt, B., *Effect of hot rolling on the dendritic texture of directionally solidified steel ingots.* Metallurgical Transactions, 1970. **1**(9): p. 2495-2505.

176. Mussert, K., Vellinga, W.P., Bakker, A., and Van Der Zwaag, S., *A nano-indentation study on the mechanical behaviour of the matrix material in an AA6061-Al2O3 MMC.* Journal of materials science, 2002. **37**(4): p. 789-794.

177. Doerner, M. and Nix, W., *A method for interpreting the data from depth-sensing indentation instrurnents.* J. Mater. Res, 1986. **1**(4).

178. Sneddon, I.N., *The relation between load and penetration in the axisymmetric Boussinesq problem for a punch of arbitrary profile.* International Journal of Engineering Science, 1965. **3**(1): p. 47-57.

179. Cahoon, J., Broughton, W., and Kutzak, A., *The determination of yield strength from hardness measurements.* Metallurgical Transactions, 1971. **2**(7): p. 1979-1983.

180. Tabor, D., *The hardness of metals*. 2000: Oxford university press.

181. Tabor, D., *The hardness and strength of metals.* J. Inst. Met, 1951. **79**(1): p. 1-18.

182. Pavlina, E. and Van Tyne, C., *Correlation of yield strength and tensile strength with hardness for steels.* Journal of materials engineering and performance, 2008. **17**(6): p. 888-893.

183. Atkins, A. and Tabor, D., *Plastic indentation in metals with cones.* Journal of the Mechanics and Physics of Solids, 1965. **13**(3): p. 149-164.

184. Devenpeck, M. and Weinstein, A., *Experimental investigation of workhardening effects in wedge flattening with relation to nonhardening*

theory. Journal of the Mechanics and Physics of Solids, 1970. **18**(3): p. 213-218.

185. Marcinkowski, M., Fisher, R., and Szirmae, A., *Effect of 500 C Aging on the Deformation Behavior of an Iron-chromium Alloy.* Trans. Aime, 1964. **230**(6).

186. Speich, G. and Warlimont, H., *Yield strength and transformation substructure of low-carbon martensite.* J IRON STEEL INST, 1968. **206**(4): p. 385-392.

187. Vable, M., *Intermediate mechanics of materials*. 2008: Oxford University Press New York.

188. Vable, M., *Mechanics of Materials Book*. 2002, Oxford University Press.

189. Callister, W.D., *Materials Science And Engineering: An Introduction*. 2007: John Wiley & Sons.

190. ASTM-International, *Annual Book of ASTM Standards: Metals test methods and analytical procedures. Metals-mechanical testing ; elevated and low temperature tests ; metallography*. 2011: ASTM International.

191. Vable, M., *Mechanics of Materials*. 2012, Michigan Technological University.

192. Roylance, D., *Stress-strain curves.* Massachusetts Institute of Technology study, Cambridge, 2001.

193. Clarke, G., Daczko, N., and Nockolds, C., *A method for applying matrix corrections to X-ray intensity maps using the Bence–Albee algorithm and Matlab.* Journal of Metamorphic Geology, 2001. **19**(6): p. 635-644.

194. Totten, G.E., Xie, L., and Funatani, K., *Handbook of Mechanical Alloy Design*. 2003: Taylor & Francis.

195. Harvey, P.D. and Metals, A.S.f., *Engineering properties of steel*. 1982: American Society for Metals.

196. Key-to-Metals-Database, *Steel Properties*. 2013, Key-to-Metals AG: Zurich.

197. NPL-Manual, *Manual for the Calculation of Elastic-Plastic Materials Models Parameters*. 2007, Queen's Printer: Scotland, UK.

198. Ling, Y., *Uniaxial true stress-strain after necking.* AMP Journal of Technology, 1996. **5**: p. 37-48.

199. Choi, Y., Yong Choo, W., and Kwon, D., *Analysis of mechanical property distribution in multiphase ultra-fine-grained steels by nanoindentation.* Scripta materialia, 2001. **45**(12): p. 1401-1406.

200. Noren, T.M. and Pfeiffer, C., *Applied Steel Welding Metallurgy*. 1961: Elektriska Svetsningsaktiebolaget.

201. Szwaja, N., *Elastic and Elasto-Plastic Finite Element Analysis of a Tension Test Specimen With and Without Voids*. 2012, Rensselaer Polytechnic Institute.

202. Nygårds, M., *Microstructural finite element modeling of metals*, in *Department of Solid Mechanics*. 2003, Royal Institute of Technology: Stockholm.

203. Qiao, J.W., Zhang, T., Yang, F.Q., Liaw, P.K., Pauly, S., and Xu, B.S., *A Tensile Deformation Model for In-situ Dendrite/Metallic Glass Matrix Composites.* Scientific reports, 2013. **3**.

204. Abdeljawad, F. and Haataja, M., *Continuum Modeling of Bulk Metallic Glasses and Composites.* Physical Review Letters, 2010. **105**(12): p. 125503.

205. Zhu, Z., Zhang, H., Hu, Z., Zhang, W., and Inoue, A., *Ta-particulate reinforced Zr-based bulk metallic glass matrix composite with tensile plasticity.* Scripta materialia, 2010. **62**(5): p. 278-281.

206. Belytschko, T., Liu, W.K., Moran, B., and Elkhodary, K., *Nonlinear Finite Elements for Continua and Structures*. 2013: Wiley.

207. Crisfield, M., *Non-linear Finite Element Analysis of Solids and Structures, Volume 2: Advanced Topics, 1997.* Baffins Lane, Chichester, West Sussex PO19 1UD, England: John Wiley & Sons Ltd, 1997. **2**.

208. Wang, S. and Tseng, A., *Macro-and micro-modelling of hot rolling of steel coupled by a micro-constitutive relationship.* Materials & Design, 1995. **16**(6): p. 315-336.

209. Phaniraj, M.P., Behera, B.B., and Lahiri, A.K., *Thermo-mechanical modeling of two phase rolling and microstructure evolution in the hot strip mill: Part I. Prediction of rolling loads and finish rolling temperature.* Journal of Materials Processing Technology, 2005. **170**(1): p. 323-335.

210. Shahani, A., Setayeshi, S., Nodamaie, S., Asadi, M., and Rezaie, S., *Prediction of influence parameters on the hot rolling process using finite element method and neural network.* Journal of Materials Processing Technology, 2009. **209**(4): p. 1920-1935.

211. Shahani, A., Nodamaie, S., and Salehinia, I., *Parametric study of hot rolling process by the finite element method.* Sharif University of Technology Transaction B: Mechanical Engineering, 2008. **16**(2): p. 130-139.

212. Lin, J. and Dean, T., *Modelling of microstructure evolution in hot forming using unified constitutive equations.* Journal of Materials Processing Technology, 2005. **167**(2): p. 354-362.

213. Hwang, S. and Joun, M., *Analysis of hot-strip rolling by a penalty rigid-viscoplastic finite element method.* International Journal of Mechanical Sciences, 1992. **34**(12): p. 971-984.

214. Serajzadeh, S., Karimi Taheri, A., Nejati, M., Izadi, J., and Fattahi, M., *An investigation on strain inhomogeneity in hot strip rolling process.* Journal of Materials Processing Technology, 2002. **128**(1): p. 88-99.

215. Berbenni, S., Favier, V., Lemoine, X., and Berveiller, M., *Micromechanical modeling of the elastic-viscoplastic behavior of polycrystalline steels having different microstructures.* Materials Science and Engineering: A, 2004. **372**(1): p. 128-136.

216. Bai, Y. and Wierzbicki, T., *A new model of metal plasticity and fracture with pressure and Lode dependence.* International Journal of Plasticity, 2008. **24**(6): p. 1071-1096.

217. Al-Abbasi, F. and Nemes, J., *Micromechanical modeling of dual phase steels.* International Journal of Mechanical Sciences, 2003. **45**(9): p. 1449-1465.

218. Paul, S.K., *Effect of martensite volume fraction on stress triaxiality and deformation behavior of dual phase steel.* Materials & Design, 2013. **50**(0): p. 782-789.

219. Al-Abbasi, F. and Nemes, J.A., *Characterizing DP-steels using micromechanical modeling of cells.* Computational Materials Science, 2007. **39**(2): p. 402-415.

220. Sodjit, S. and Uthaisangsuk, V., *Microstructure based prediction of strain hardening behavior of dual phase steels.* Materials & Design, 2012. **41**(0): p. 370-379.

221. Wilson, D. and Rodrigues, P.M., *On the directionality of strain localization when stretching aluminum alloy sheets in biaxial tension.* Metallurgical and Materials Transactions A, 1986. **17**(2): p. 367-370.

222. Tomota, Y., Kuroki, K., Mori, T., and Tamura, I., *Tensile deformation of two-ductile-phase alloys: Flow curves of α-γ Fe□ Cr□ Ni alloys.* Materials Science and Engineering, 1976. **24**(1): p. 85-94.

223. Al-Abbasi, F. and Nemes, J., *Micromechanical modeling of the effect of particle size difference in dual phase steels.* International journal of solids and structures, 2003. **40**(13): p. 3379-3391.

224. Sodjit, S. and Uthaisangsuk, V., *Microstructure based prediction of strain hardening behavior of dual phase steels.* Materials & Design, 2012. **41**: p. 370-379.

225. Cannmo, P., Runesson, K., and Ristinmaa, M., *Modelling of plasticity and damage in a polycrystalline microstructure.* International Journal of Plasticity, 1995. **11**(8): p. 949-970.

226. Sodjit, S. and Uthaisangsuk, V., *High Strength Dual Phase Steels and Flow Curve Modeling Approach*. 2011, TSME-ICOME.

227. Gänser, H.-P., Fischer, F., and Werner, E., *Large strain behavior of two-phase materials with random inclusions.* Computational Materials Science, 1998. **11**(3): p. 221-226.

228. Sodjit, S. and Uthaisangsuk, V., *A micromechanical flow curve model for dual phase steels.* Journal of Metals, Materials and Minerals, 2012. **22**(1): p. 87-97.

229. Ishikawa, N., Parks, D.M., Socrate, S., and Kurihara, M., *Micromechanical modeling of ferrite-pearlite steels using finite element unit cell models.* ISIJ International, 2000. **40**(11): p. 1170-1179.

230. Reid, M., Phelan, D., and Dippenaar, R., *Concentric solidification for high temperature laser scanning confocal microscopy.* ISIJ International, 2004. **44**(3): p. 565-572.

231. Andersson, J., Helander, T., Höglund, L., Shi, P., and Sundman, B., *Thermo-Calc & DICTRA, computational tools for materials science.* Calphad, 2002. **26**(2): p. 273-312.